UNIVERSITÀ DEGLI STUDI DI MODENA E REGGIO EMILIA

DIPARTIMENTO DI INGEGNERIA "ENZO FERRARI"

PhD SCHOOL

INDUSTRIAL AND ENVIRONMENTAL ENGINEERING

INGEGNERIA INDUSTRIALE E DEL TERRITORIO

XXXII CYCLE

Development of Cost-effective Methodologies to Incorporate Chemistry-relevant Fuel Properties Modelling in 3D-CFD Combustion and Soot Emission Simulations of Gasoline Internal Combustion Engines

Advisor:
Prof. Stefano Fontanesi

Candidate:
Marco Del Pecchia

PhD School Director:
Prof. Alberto Muscio

Ogni singola lettera, parola e pagina di questa tesi sono dedicati a te papà.

L'inchiostro fresco di stampa su queste pagine sbiadirà lentamente col passare del tempo

e con esso il lavoro frutto di anni di sacrifici e impegno.

Il tempo di certo non potrà però celare la passione e l'amore che ne sono stati il combustibile.

Abbiamo iniziato insieme quest'avventura, la vita purtroppo ha voluto che tu non possa vederne la conclusione.

Nei momenti più difficili e bui, però, sei sempre stato la ragione che mi ha spinto a rialzarmi.

Per questo, le parole che seguiranno sono tanto mie quanto tue.

Non potrò mai ringraziarti abbastanza. Vinciamo noi, Sempre

"There is not a law under which any part of this universe is governed which does not come into play and is touched upon in these phenomena. There is no better, there is no more open door by which you can enter into the study of natural philosophy than by considering the physical phenomena of a candle"

Michael Faraday

Christmas Lectures at the Royal Institution, 1859

The Chemical History of a Candle

Index

Abstract

Nowadays, the leading driver pushing the technological development of the new era of internal combustion engines is the continuous strive for the increase of efficiency and pollutants emissions reduction. The increasing complexity of new combustion systems is made possible thanks to the evolution of 3D-CFD. At the same time, the introduction of new technical solutions pushed the in-cylinder combustion process to operate in challenging conditions which are particularly demanding under the modelling standpoint, considered the high degree of accuracy required. In this scenario, the integration of chemistry-based methodologies in 3D-CFD simulations is a powerful tool to quantitatively estimate the underlying phenomena linked to fuel chemistry which are responsible for local mixture reactivity and, in turn, for the combustion process evolution. The correct estimation of combustion-relevant fuel properties such as laminar flame speed, ignition delay and sooting tendency is a key factor to model, respectively, flame propagation characteristics, end-gas reactivity and soot emission formation in gasoline engines. The need for a quantitative estimation of the aforementioned phenomena has recently promoted a widespread use of methodologies aiming to directly solve chemistry at a cell-wise level in the computational grid. While the main advantage of this approach is the possibility to directly solve chemistry cell by cell, its main drawback is the non-negligible increase in computational cost. In the present work, a comprehensive methodology is developed to integrate detailed chemistry-based information in in-cylinder simulations retaining a high chemistry-fidelity at a feasible computational cost, for the automotive industry standard. In particular, dedicated methodologies are proposed to model flame propagation characteristics, auto-ignition phenomena, sooting tendency and the main chemico-physical properties of gasoline at thermodynamic and mixture quality conditions typically experienced in current production gasoline direct injection engines. The proposed methodologies rely on detailed off-line chemistry-based simulations, carried out in a chemistry solver, to quantitatively estimate the aforementioned properties. This approach is validated on a optically-accessible gasoline direct-injection research engine on different injection strategies at a full-load operating point, with a particular focus on soot engine-out emissions. Due to the increasing limitations imposed on particulate matter by the current regulations worldwide, accurate CFD-based methodologies are needed to predict soot formation in gasoline direct engines. Therefore, a customized version of the Sectional Method model, based on a tabulated constant pressure reactors approach, is used in 3D-CFD simulations for this purpose. The predictive capabilities of the proposed chemistry-based comprehensive methodology is proved twice. Firstly, the improved description of the combustion process development is validated thanks to in-cylinder experimental data. In the second place, an experimental-CFD comparison, in terms of engine-out Particulate Mass, Particulate Number and Particle Size Distribution Function, proves the capability of the proposed methodology, not only to describe the dependence of the sooting tendency on the injection strategy, but also to quantitatively predict soot characteristic quantities at the exhaust with a good agreement.

🇮🇹

Oggigiorno, i fattori principali che influenzano lo sviluppo dei motori a combustione interna di nuova generazione sono la continua ricerca di un aumento di efficienza e di riduzione delle emissioni inquinanti allo scarico. Il progressivo aumento della complessità dei nuovi sistemi di combustione è resa possibile grazie all'evoluzione di modelli 3D-CFD. D'altro canto, l'introduzione di nuove soluzioni tecniche ha progressivamente spinto il motore a combustione interna ad operare in condizioni particolarmente complesse da modellare, considerato l'elevato grado di accuratezza richiesto. In questo scenario, l'integrazione di metodologie basate su calcoli di cinetica chimica in simulazioni 3D-CFD costituisce uno strumento potente, che consente di stimare l'impatto dei processi chimici legati ai processi di ossidazione del combustibile. Questi ultimi caratterizzano la reattività locale della miscela che, a sua volta, influenza l'evoluzione del processo di combustione. Ad esempio, la corretta stima di proprietà del combustibile rilevanti per la combustione come la velocità laminare di fiamma, il ritardo all'accensione e la propensità a formare particolato è fondamentale per modellare, rispettivamente, la propagazione del fronte di fiamma, la reattività degli end-gas e la formazione di particolato nei motori benzina. La necessità di stimare quantitativamente i fenomeni sopraindicati ha recentemente portato alla diffusione di metodologie atte alla risoluzione diretta della cinetica chimica nella griglia computazionale portando, però, ad un aumento non trascurabile del costo computazionale. In questo lavoro, è stata sviluppata una metodologia per integrare informazioni basate sulla cinetica chimica di dettaglio in simulazioni interno cilindro, mantenendo un'elevata accuratezza dal punto di vista chimico ad un ridotto costo computazionale per gli standard dell'industria dell'autoveicolo. In particolare, sono proposte metodologie dedicate alla modellazione della propagazione del fronte di fiamma, delle proprietà di autoaccensione, della propensità alla formazione di particolato e delle principali proprietà chimico-fisiche, alle condizioni termodinamiche e di stratificazione della miscela tipici dei motori benzina ad iniezione diretta di produzione. Le metodologie proposte si affidano a simulazioni di cinetica chimica, effettuate con un solutore chimico, per stimare quantitativamente le proprietà precedentemente descritte. Questo approccio è validato in un motore monocilindrico di ricerca ad accesso ottico, alimentato a benzina con iniezione diretta, su diverse strategie di iniezione in un punto operativo a pieno carico. Il presente lavoro si concentra, in particolar modo, sulla formazione di particolato. Infatti, a causa delle stringenti limitazioni imposte sul particolato da diverse legislazioni mondiali, sono necessarie accurate metodologie CFD al fine di predire la formazione di particolato nei motori a combustione interna alimentati a benzina. A tal fine, una versione modificata del Metodo delle Sezioni, basato su una tabulazione in reattori a pressione costante, viene adottata nelle simulazioni 3D-CFD. Le capacità predittive dell'approccio onnicomprensivo proposto sono validate doppiamente. In primo luogo, il miglioramento della capacità descrittiva dell'evoluzione del processo di combustione è validata grazie a misure sperimentali interno cilindro. Successivamente, un confronto CFD-sperimentale, basato sulla massa, il numero e la distribuzione delle particelle di particolato, evidenzia la validità della metodologia proposta, non solo per la capacità di predire la dipendenza della formazione di particolato dalla strategia di iniezione, ma anche per quanto riguarda la possibilità di predire quantitativamente le grandezze caratteristiche del particolato allo scarico in modo soddisfacente.

Introduction

The threat of climate change and global warming have pushed the European Union (EU) to set very challenging targets in order to firmly decrease the anthropogenic greenhouse gas (GHG) emissions, as published in the Official Journal of the EU [1]. According to a proposal for the regulation by the European parliament and council [2], the road transport was responsible for 22% of EU GHG emissions in 2015. Although several viable alternatives to conventional internal combustion engines are being discussed [3,4,5], currently about 95% of the energy used for transport is provided by petroleum-derived liquid fuels [6]. Further into details, nearly 40% of global transport energy is used in passenger cars, which are essentially (~80%) powered by spark ignition (SI) engines running on gasoline [6]. Despite the tightening on the emission regulations worldwide and the progressive increase of Battery Electric Vehicles (BEV) presence in the market share, the Organization of the Petroleum Exporting Countries ($OPEC$) forecast that between 2016 and 2040 transportation sector will still account for two out of three additional barrels consumed and gasoline demand will be around three-quarters of the amount of 2016 [7]. In this framework, a continuous development of internal combustion engines (ICE) is mandatory to meet the target set by the EU Parliament to reduce overall GHG emissions at least 50% below 1990 levels by 2050 [1]. The degree of complexity of ICEs has been increasing by the introduction of a series of technologies aimed at improving the overall fuel efficiency of SI engines, such as Direct Injection (DI) of fuel into the combustion chamber [8], downsizing combined with turbo-charging [9] and Exhaust Gas Recirculation (EGR) systems [10]. Boosting and downsizing caused an increase of the average operating pressure and temperature in the combustion chamber, which indeed promotes the onset of abnormal combustion phenomena such as knock. This last is now a major obstacle for the increase of ICE efficiency [11,12,13]. Besides potentially leading to engine failures [14], knock limits compression ratio and charge leaning [15,16]. In particular, charge leaning has become technically feasible thanks to the introduction of Gasoline Direct Injection (GDI) systems and the possibility to use in-cylinder stratified fuel-air mixture strategies. This allowed to progressively increase ICE efficiency but introduced additional problems associated with Coefficient Of Variation (COV) increase in Indicated Mean Effective Pressure ($IMEP$), evidence of combustion stability issues [17]. The introduction of Turbulent Jet Ignition (TJI) [18,19] further pushed the boundaries of technological development, enabling Ultra-Lean (UL) operation using radical turbulent jets emerging from a pre-chamber combustor as the ignition source for main chamber combustion in SI engines. Beside pushing combustion system towards flammability limits, TJI technology further widened the possible thermodynamic and mixture quality states encountered by flames due to the high temperature, locally rich and highly diluted mixture present in the pre-chamber [20,21,22]. The political pressure to increase sustainability of road transportation also brought to the approval of the Renewable Energy Directive ($REDII$) [23]. Such directive imposes that at least 10% of the energy used in transportation must be bio-based by 2020 and forces fuel suppliers to a minimum market share equal to 6.8% of low-emissions and renewable fuels, including advanced biofuels, by 2030 [23]. In the light of this scenario, biofuels have increasingly gained the attention of researchers and designers in the automotive industry, as a feasible solution to move towards cleaner powertrains, in compliance with the EU regulations. Furthermore, since fuel composition and properties can deeply affect ICE performance and emissions [24], fuel properties have become an additional control parameter. Engine manufacturers are therefore tending towards a comprehensive development of fuel and engine in the design of new combustion systems [6]. Another important concern for Original Equipment Manufacturers (OEM) is the aerosol carbonaceous-based solid phase emitted by ICE, named Particulate Matter (PM) or more commonly referred to as "soot". This pollutant is gaining ever increasing attention due to the many issues caused by its high concentration in largely populated urban areas. Studies presented by the International Agency for Research on Cancer ($IARC$) have pushed the World Health Organization (WHO) to declare PM carcinogenic to humans [25]. Other studies, not only suggested that a reduction of fine particulate matter ($PM_{2.5}$) concentration should lead to a reduction of harming effects associated with PM [26] but also concluded that exposure to soot poses the greatest risk of cancer of all air pollutants [27]. In particular, average road transportation contribution to $PM_{2.5}$ concentration was quantified around 39% in the largest European capitals [28]. According to [29], urban air pollution is the cause of nearly four million deaths annually. While being particularly harming for human health, soot is also reported to non-negligibly contribute to global warming with a radiation power comparable to CO_2 one [30]. Compared to Port Fuel Injection (PFI) technology, GDI is known to emit a higher Particulate Number (PN) of $PM_{2.5}$ [31,32,33,34,35], especially in the most efficient operating points, in terms of fuel consumption, such as low engine speeds and medium to high loads. As a consequence, stringent emission regulations were introduced worldwide to limit PM and PN emissions [36]. The major concern related to GDI technology is the higher number of ultrafine particles, which is even higher than those of Diesel engines equipped with Diesel Particulate Filter (DPF) [37]. With the aim of reducing soot engine-out emissions, the EU introduced the EURO6 regulations. In particular, from the euro6c stage, entered into force on September 2017, GDI units must meet the 4.5 mg/km and 6.0×10^{11} #/km, for PM and PN respectively [36]. Such limits represent a non-trivial challenge for engine manufacturers. Based on this overview it is straightforward to understand the complexity arising when designing modern ICE combustion system, with such a high number of requests and boundaries. In the last decade, the computational power increase at feasible costs and maturity reached by numerical models in predicting reacting and turbulent flows for ICE applications has made Multi-dimensional Computational Fluid Dynamics ($3D$-CFD) simulations a common practice in the design workflow of most automotive OEMs [38]. Advanced combustion [39,40], knock [41,42,43,44,45] and soot emission models [46,47,48,49] have proven to be powerful and reliable tools to optimize combustion chamber design and engine control strategies with the aim of increasing engine efficiency and reduce engine-out emissions. All the aforementioned models rely on chemistry-based information, which constitute essential input parameters for the correct estimation of the corresponding in-cylinder phenomena. Turbulent combustion simulation in SI engines relies on flamelet combustion models, such as $ECFM$-$3Z$ [39] and G-equation [40], which are widely adopted in the scientific community. Despite the representation of the combustion process is based on two different approaches, both models require laminar flame speed s_L as an input in order to properly estimate turbulent combustion rate. s_L, which plays a key role in the overall burn rate and thus the overall efficiency and emissions of the engine, depends on absolute pressure p, unburnt temperature T_u, equivalence ratio ϕ and EGR. It is thus a fundamental property of a combustible mixture, making it an important target for combustion modelling [50], which is strongly dependent on the characteristic chemical kinetics oxidation pathways specifically related to the fuel considered. Similarly, knock models rely on the prediction of end-gas reactivity during the combustion process, which is usually estimated via ignition delay time τ_{ig} calculations based on chemical kinetics mechanisms [16]. As for s_L, τ_{ig} is dependent on specific thermodynamic and mixture quality conditions $(p^*, T_u^*, \phi^*, EGR^*)$ and fuel chemical kinetics. Soot emission predictions are also known to be a non-trivial challenge due to the complexities associated with soot chemistry modelling [51]. For instance, Particle Inception is influenced by chemistry-based processes responsible for the formation of a solid phase from gas phase species, commonly known as Polycyclic Aromatic Hydrocarbons (PAH). Furthermore, fuel composition is known to deeply affect s_L [6], τ_{ig} [52] and soot formation [53]. For this reason, the definition of appropriate fuel surrogates, able to model real fuels is mandatory for an accurate description of all combustion-relevant chemical kinetics-based processes. The integration of chemistry-based methodologies able to give a reliable and quantitative description of the aforementioned properties, in all the possible in-cylinder conditions experienced by flames, has become a topic of ever increasing relevance in the recent years. Recently developed methodologies, aiming to directly solve chemistry at a cell-wise level in the computational grid, have become increasingly popular. While the main advantage of this approach is the possibility to directly solve chemistry cell by cell, its main drawback is the non-negligible increase in computational cost, which prevents them from becoming a best practice in the industry. For this reason, the aim of the present research activity is the development of cost-effective methodologies able to introduce chemistry-relevant information needed by $3D\text{-}CFD$ models, retaining a similar level of chemistry-fidelity guaranteed by on-line detailed chemistry approach. The present thesis is specifically structured so that each chapter and the relative subchapters discuss in detail specific aspects of chemistry-based modelling integration in $3D\text{-}CFD$ simulations. The first two chapters provide the fundamentals of CFD and combustion chemistry. In the third chapter, a novel approach to fuel surrogate formulation is proposed, with the aim of matching the main chemico-physical properties, combustion-relevant and sooting characteristics with a unique fuel surrogate. The fourth chapter specifically focuses on the development of polynomial-based correlations to provide accurate s_L estimations in in-cylinder combustion calculations depending on local $(p^*, T_u^*, \phi^*, EGR^*)$ conditions. Unlike the previous chapters, the fifth and last chapter constitutes a sort of comprehensive validation of the methodologies outlined previously. In particular, the development of a $3D\text{-}CFD$ methodology to quantitatively predict GDI soot using a customized version of the Sectional Method soot model [46,47,48,49], based on a tabulated constant pressure (CP) reactor-based approach, is discussed. For validation purposes, a single-cylinder optically accessible GDI unit is modelled and CFD results are compared with dedicated experimental engine-out soot measurements, in terms of PM, PN and Particle Size Distribution Function $(PSDF)$, for three different injection strategies. Finally, conclusions and possible future enhancements are drawn.

Chapter 1: Fundamentals of CFD

1.1 Introduction to CFD

Governing equations describing the flow motion are named “Navier-Stokes” equations. They are based on three fundamentals of fluid physics, i.e. mass conservation (also known as continuity), momentum conservation (also known as Newton’s second law) and energy conservation (also known as first law of thermodynamics). An important assumption is that fluid is considered as a “continuum”, since the analysis are carried out on “macroscopic” scales (i.e. bigger than 1μm) and fluid molecular structure and motion can be ignored and disregarded. Fluid behaviour is described in terms of macroscopic properties such as velocity, pressure, density, temperature and their spatial and temporal derivatives, all considered as average values over a huge number of single molecules which can be approximated as a point in space (or a single fluid particle), defined as the smallest fluid element which is not influenced by the single molecules behaviour. A fluid element of size δx_i, δx_j, δx_k, with generic coordinates and volume δV is considered and a sketch is reported in Fig. 1.1.

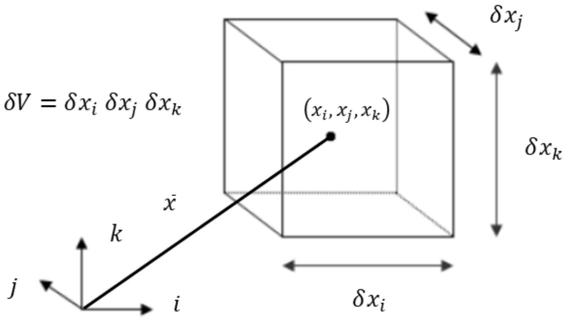

Figure 1.1 Finite control volume.

All the fluid properties are functions of both time and space:

$$p = p(x_i, x_j, x_k, t) \tag{1.1}$$

$$\rho = \rho(x_i, x_j, x_k, t) \tag{1.2}$$

$$T = T(x_i, x_j, x_k, t) \tag{1.3}$$

$$\bar{u} = \bar{u}(x_i, x_j, x_k, t) \tag{1.4}$$

This dependency will not be further remarked for the sake of simplicity.

1.2 Mass Conservation

Mass conservation equation is based on the balance between fluid mass entering and exiting the domain, i.e. the fluid element or “control volume”. The net rate of mass increase/decrease over time is:

$$\frac{\partial}{\partial t}(\rho \cdot \delta x_i \cdot \delta x_j \cdot \delta x_k) = \frac{\partial \rho}{\partial t} \delta x_i \cdot \delta x_j \cdot \delta x_k \tag{1.5}$$

Mass flow through a surface is the product of density, area and velocity component normal to the surface. It is positive if mass flow is entering and negative if exiting. The net balance of the contributions through each surface bounding the element is illustrated in Fig. 1.2.

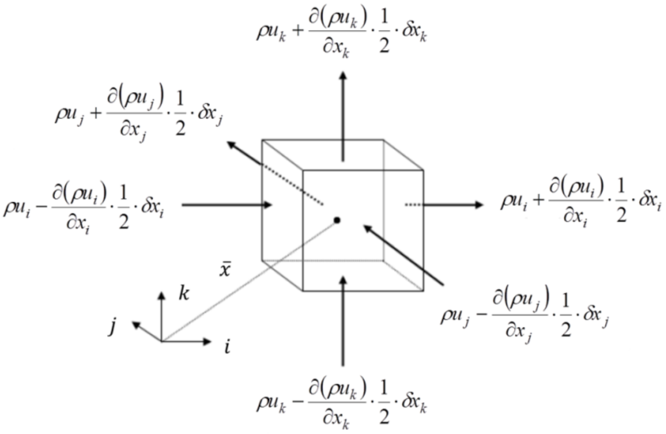

Figure 1.2. Contributions to the momentum equation on the control volume.

$$\begin{gathered}
\left[\rho u_i - \frac{\partial(\rho u_i)}{\partial x_i}\cdot\frac{1}{2}\cdot\delta x_i\right]\cdot\delta x_j\cdot\delta x_k - \left[\rho u_i + \frac{\partial(\rho u_i)}{\partial x_i}\cdot\frac{1}{2}\cdot\delta x_i\right]\cdot\delta x_j\cdot\delta x_k + \\
\left[\rho u_j - \frac{\partial(\rho u_j)}{\partial x_j}\cdot\frac{1}{2}\cdot\delta x_j\right]\cdot\delta x_i\cdot\delta x_k - \left[\rho u_j + \frac{\partial(\rho u_j)}{\partial x_j}\cdot\frac{1}{2}\cdot\delta x_j\right]\cdot\delta x_i\cdot\delta x_k + \\
\left[\rho u_k - \frac{\partial(\rho u_k)}{\partial x_k}\cdot\frac{1}{2}\cdot\delta x_k\right]\cdot\delta x_i\cdot\delta x_j - \left[\rho u_k + \frac{\partial(\rho u_k)}{\partial x_k}\cdot\frac{1}{2}\cdot\delta x_k\right]\cdot\delta x_i\cdot\delta x_j
\end{gathered} \tag{1.6}$$

Equating the two expressions and dividing by the control volume δV a compact notation is obtained:

$$\frac{\partial\rho}{\partial t} + \nabla\cdot(\rho u) = 0 \tag{1.7}$$

Which represents the compact form of the $3D$ continuity, or mass conservation, equation for a compressible fluid. The first term on the left is the rate of density (i.e. mass per unit volume) increase/decrease within the control volume, while the second is the algebraic sum of the fluxes entering/exiting the volume through the bounding surfaces and is also named “convective term”, i.e. due to the fluid motion.

1.3 Momentum Equation

Following Newton’s Second Law, the acceleration a of a body is parallel and directly proportional to the net force F and inversely proportional to the mass m, i.e. $F = ma$. Also here, the variation of a physical quantity is caused by both the temporal variation of the quantity and the net flow through the surface bounding the control volume. Similarly to mass, the momentum variation for a fluid element can be expressed as:

$$\rho\bar{u} \Rightarrow \frac{\partial}{\partial t}(\rho\bar{u}) + \nabla\cdot\rho\bar{u}\bar{u} = \rho\bar{f} + \nabla\cdot\bar{\Pi} \tag{1.8}$$

The first term represents the rate of increase of momentum per unit volume. The second term represents the variation of momentum due to convection through the control volume surface. The term can be further developed as follows.

$$\bar{u}\frac{\partial\rho}{\partial t} + \rho\frac{\partial\bar{u}}{\partial t} + \rho\bar{u}\cdot\nabla\bar{u} + \bar{u}\cdot\nabla\rho\bar{u} = \bar{u}\left(\frac{\partial\rho}{\partial t} + \nabla\rho\bar{u}\right) + \rho\left(\frac{\partial\bar{u}}{\partial t} + \bar{u}\nabla\bar{u}\right) \tag{1.9}$$

$$\nabla\cdot\rho\bar{u}\bar{u} = \rho\bar{u}\cdot\nabla\bar{u} + \bar{u}(\nabla\cdot\rho\bar{u}) \tag{1.10}$$

Using the above expression in the momentum equation, and using the continuity equation, the following expression is obtained.

$$\rho\frac{D\bar{u}}{Dt} = \rho\bar{f} + \nabla\cdot\bar{\Pi} \tag{1.11}$$

In Fig. 1.3, a sketch of the forces acting on the control volume is illustrated.

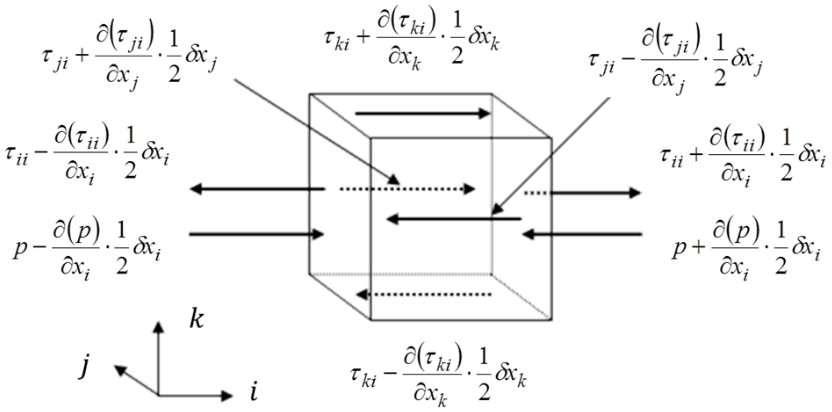

Figure 1.3 Sketch of force acting on a finite control volume.

As for the forces acting on the fluid we usually distinguish between mass forces f and surface forces, where the first type is grouped in a single term called the "mass force source". Mass forces act "remotely" and act on the whole fluid mass. A typical example is gravity, for which the force per unit mass is the gravitational acceleration vector. The second term represents the surface forces acting on the fluid element. Stresses can be split in normal stresses and shear stresses, and are grouped in the tensor. The expression for the momentum conservation is of general use, and loses its generality only when peculiar expression are defined for the stress tensor: for example, for many gases and liquids a correlation between stresses and rate of deformation was observed. Fluids exhibiting that behaviour are usually referred to as Newtonian Fluids.

1.4 Energy Equation

The energy equation is derived from the first law of thermodynamics, expressed as:

$$\frac{dE}{dt} = \frac{dQ}{dt} + \frac{dL}{dt} \tag{1.12}$$

As before, energy variation in time for a fluid particle and per unit volume can be expressed as the product of density and energy material derivative:

$$\rho \frac{DE}{Dt} \tag{1.13}$$

The work done on the fluid particle in the infinitesimal time interval is that exerted by the forces acting on the element surface times the velocity component parallel to the forces themselves. The work can be derived from the previous equations. Considering the work along the i-direction we get:

$$\begin{aligned}
&\left[\left(pu_i - \frac{\partial(pu_i)}{\partial x_i}\cdot\frac{1}{2}\delta x_i\right) - \left(\tau_{ii}u_i - \frac{\partial(\tau_{ii}u_i)}{\partial x_i}\cdot\frac{1}{2}\delta x_i\right)\right]\delta x_j \delta x_k + \\
&\left[-\left(pu_i + \frac{\partial(pu_i)}{\partial x_i}\cdot\frac{1}{2}\delta x_i\right) + \left(\tau_{ii}u_i + \frac{\partial(\tau_{ii}u_i)}{\partial x_i}\cdot\frac{1}{2}\delta x_i\right)\right]\delta x_j \delta x_k + \\
&\left[-\left(\tau_{ji}u_i - \frac{\partial(\tau_{ji}u_i)}{\partial x_j}\cdot\frac{1}{2}\delta x_j\right) + \left(\tau_{ji}u_i + \frac{\partial(\tau_{ji}u_i)}{\partial x_j}\cdot\frac{1}{2}\delta x_j\right)\right]\delta x_i \delta x_k + \\
&\left[-\left(\tau_{ki}u_i - \frac{\partial(\tau_{ki}u_i)}{\partial x_k}\cdot\frac{1}{2}\delta x_k\right) + \left(\tau_{ki}u_i + \frac{\partial(\tau_{ki}u_i)}{\partial x_k}\cdot\frac{1}{2}\delta x_k\right)\right]\delta x_i \delta x_j
\end{aligned} \tag{1.14}$$

Summing the three previous equations and dividing by δV, we get the total work exerted on the fluid particle by the surface forces. The work by the mass forces, mainly due to the variation of potential energy, is described, as for the momentum equations, by a scalar source term S_E, "source of energy per unit volume" in the considered time interval. The final expression is:

$$\left[-\nabla\cdot\left(p\bar{u}\right)\right] + \left[\begin{array}{l} \frac{\partial(u_i\tau_{ii})}{\partial x_i} + \frac{\partial(u_i\tau_{ji})}{\partial x_j} + \frac{\partial(u_i\tau_{ki})}{\partial x_k} + \frac{\partial(u_j\tau_{ij})}{\partial x_i} + \frac{\partial(u_j\tau_{jj})}{\partial x_j} + \frac{\partial(u_j\tau_{kj})}{\partial x_k} + \\ + \frac{\partial(u_k\tau_{ki})}{\partial x_i} + \frac{\partial(u_k\tau_{kj})}{\partial x_j} + \frac{\partial(u_k\tau_{kk})}{\partial x_k} \end{array}\right] + S_E \tag{1.15}$$

The heat exchanged by the fluid particle with the environment is now considered. Vector $\bar{q}$ is heat flux exchanged through conduction. With reference to Fig. 1.4, the overall heat flux can be obtained by summing all the contributions (positive if entering, negative if exiting) through the element bounding surfaces. For example, the contribution along the direction is:

$$\left[\left(q_i - \frac{\partial q_i}{\partial x_i}\cdot\frac{1}{2}\delta x_i\right) - \left(q_i + \frac{\partial q_i}{\partial x_i}\cdot\frac{1}{2}\delta x_i\right)\right]\cdot\delta x_j \delta x_k = -\frac{\partial q_i}{\partial x_i}\cdot\delta x_i \delta x_j \delta x_k \tag{1.16}$$

The overall flux due to conduction exchanged by the fluid element per unit volume is equal to:

$$-\nabla\cdot\bar{q} = -\frac{\partial q_i}{\partial x_i} - \frac{\partial q_j}{\partial x_j} - \frac{\partial q_k}{\partial x_k} \tag{1.17}$$

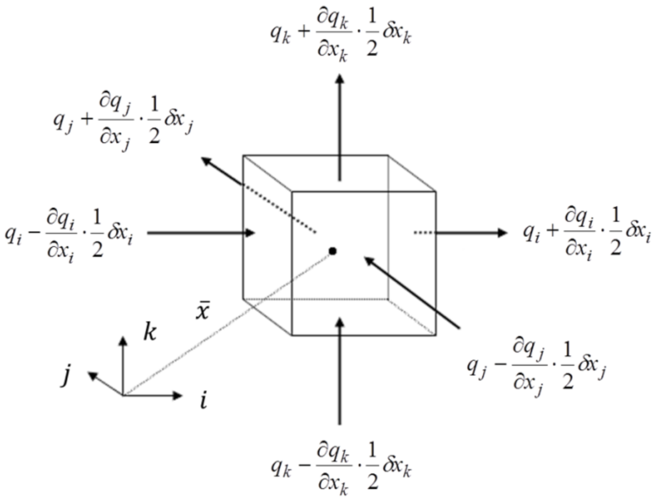

Figure 1.4. Sketch of energy fluxes on finite control volume.

The application of the Fourier's Law for heat conduction allows to link the thermal flux to the local temperature gradient, which in compact notation is expressed as:

$$\bar{q} = -k\nabla T \tag{1.18}$$

Where k is the "heat transfer coefficient". Combining the above expressions we get a new formulation for the heat exchange due to conduction by the fluid element per unit volume, defined as:

$$-\nabla \cdot \bar{q} = \nabla \cdot (k\nabla T) \tag{1.19}$$

Substituting the above expressions we derive the energy equation for a fluid particle:

$$\rho \frac{DE}{Dt} = -\nabla \cdot (p\bar{u}) + \frac{\partial(u_i \tau_{ii})}{\partial x_i} + \frac{\partial(u_i \tau_{ji})}{\partial x_j} + \frac{\partial(u_i \tau_{ki})}{\partial x_k} +$$

$$\frac{\partial(u_k \tau_{ki})}{\partial x_i} + \frac{\partial(u_k \tau_{kj})}{\partial x_j} + \frac{\partial(u_k \tau_{kk})}{\partial x_k} +$$

$$\frac{\partial(u_j \tau_{ij})}{\partial x_i} + \frac{\partial(u_j \tau_{jj})}{\partial x_j} + \frac{\partial(u_j \tau_{kj})}{\partial x_k} +$$

$$\nabla \cdot (k\nabla T) + S_E \tag{1.20}$$

1.5 Set of Equations

The previously described equations are implemented in each control volume so that a system of five scalar equations is obtained: one equation of mass conservation, three equations for the momentum and, finally, one equation for the energy. These partial differential equations describe the $3D$ motion of a fluid. The unknowns are pressure, density, three velocity components and temperature. In order to close the system, a further equation is required. For example, if the assumption of "ideal gas" is adopted for the fluid, the relative well-known state equation can be adopted:

$$\frac{p}{\rho} = RT \tag{1.21}$$

where R is the gas constant. It is important to remind that in the case of uncompressible fluids (liquids and/or low-speed gases) density can be considered to be constant, which means that no connection exists between energy equation on one side and mass and momentum equations on the other side, since temperature, which defines the internal energy, is not dependent on density itself. Under that assumption, the flow field is computed only through the continuity and momentum equations, while energy equation can be solved subsequently, once the velocity vector and the pressure field are known throughout the computational domain.

⬡ 1.6 Transport Equation for a Generic Variable

Repeating the previous rationale for a generic variable χ, we get a similar equation describing the transport of χ within the fluid flow-field:

$$\frac{\partial(\rho\chi)}{\partial t} + \nabla\cdot(\rho\cdot\chi\cdot\bar{u}) = \nabla\cdot\left(\Gamma_{\chi}\cdot\nabla\chi\right) + S_{\chi} \tag{1.22}$$

The first term defines the temporal variation of χ within the control volume δV; the remaining three terms quantify the variation of χ by means of different phenomena. Clearly, χ within the control volume will change if any fluid particles crossing the fluid element at the given time drag the variable χ into or out of δV. This effect is expressed by the second term, which is named convective transport, i.e. due to the motion of the fluid particles. Nevertheless, even a still fluid can transport any variable χ by means of diffusion, i.e. due to molecular agitation, and this transport is quantified by the third term, named diffusive transport, where the constant Γ_{χ} is referred to as "diffusivity of χ". The fourth term quantifies the so-called sources of χ; within this term, both "positive or production" and "negative or dissipation" sources are included. In common practice, the term S_{χ} defines the quantity of χ which is generated or destroyed within the control volume in the time interval t; it is important to remark that these are not flows entering into or exiting from δV; they are internal variations which have nothing to deal with either transport or diffusion through the elements surrounding the considered control volume.

⬡ 1.7 RANS Simulations and 2 Equations k-ε Model

The Reynolds-Averaged Navier-Stokes equations ($RANS$) are derived from the time-averaging operation performed on the Navier-Stokes original set of equations. Time-averaging is based on the decomposition of a generic fluctuating variable into a mean part and a fluctuation around the mean value. The resulting set of equations expresses the time-averaged behaviour, or in case of quasi-periodic flows such as those in internal combustion engines, phase-averaged flow realizations. $RANS$ equations need closure terms to model the Reynolds Stresses, i.e. the product terms between velocity fluctuations. In this context, the two-equations k-ε turbulence model is developed and it is still nowadays the most widespread and used model for turbulent flows in commercial CFD software. The idea is that of introducing two transport equation for k and ε. These have the form of:

$$\frac{\partial(\bar{\rho}k)}{\partial t} + \nabla\cdot(\bar{\rho}k\bar{u}) = \nabla\cdot\left(\frac{\mu_t}{\sigma_k}\nabla k\right) + 2\mu_t\tilde{S}_{ij}\tilde{S}_{ij} - \bar{\rho}\varepsilon \tag{1.23}$$

$$\frac{\partial(\bar{\rho}\varepsilon)}{\partial t} + \nabla \cdot (\bar{\rho}\varepsilon\bar{u}) = \nabla \cdot \left(\frac{\mu_t}{\sigma_\varepsilon}\nabla\varepsilon\right) + C_{1\varepsilon}\frac{\varepsilon}{k}2\mu_t\tilde{S}_{ij}\tilde{S}_{ij} - C_{2\varepsilon}\frac{\varepsilon}{k}\bar{\rho}\varepsilon \tag{1.24}$$

The modeled equations give a relation for the energy transfer represented by the energy-cascade process, which is determined by the problem-dependent large-scale motions. The equations above, represent the Turbulent Kinetic Energy (k) and its dissipation rate (ε) process at a small scale. The origin of the model comes from experimental observations: at high Reynolds numbers, the energy dissipation rate and the turbulent kinetic energy undergo variations in time which are more or less proportional. An increase of k corresponds to an increase of ε of equal intensity, and vice versa; the same happens for decreasing rates. This fact, from a mathematical perspective, is converted into a direct proportionality between the productive and dissipative terms of k and ε. This assumption is called "turbulent equilibrium hypothesis". The mentioned time correlation which stands between k (defined in m^2/s^2) and the dissipation rate ε (m^2/s^3) represents the inverse of the time-scale of the large scale eddies, i.e. it indicates the turn-over frequency of the large-scale eddies, measured in s^{-1}. One major advantage of k-ε model is that it is based on the Boussinesq assumption typical of eddy viscosity turbulence models. It allows to simplify the evaluation of the turbulent stresses, reducing computational times and explaining why such models are the most used from an industrial point of view for the analysis of turbulent flows. Another advantage is their considerable robustness: from a computational point of view they are, surely, highly stable and efficient. Conversely, some inner simplifications in the transport equations can lead to poor accuracy in the representation. Major error sources in two-equation models are the turbulent equilibrium assumption and the Boussinesq hypothesis. As for the turbulent equilibrium assumption, this is sufficiently true only for free-flows at high Reynolds numbers. Boussinesq hypothesis introduces the concept of eddy viscosity in perfect analogy with the molecular; the definition as a scalar, implicitly, imposes an isotropic condition to the eddy viscosity. This assumption leads to a linearity between the strain rate and the Reynolds stresses, which is never verified, except for very simple flows, far from solid walls; for complex fields, highly distorted, where geometry effects are relevant (bended pipes, etc.), a linear relation is wrong. $3D$-CFD simulations presented hereafter are based on a $RANS$ approach, coupled to a two-equation k-ε ReNormalization Group (RNG) model [54] for turbulence description, adapted for compressible flows. Such version of the k-ε model is particularly suitable for the application to internal combustion engines [55]. Transport equations 1.25-1.26 respectively for k and ε are briefly reported hereafter, as implemented in the adopted in $STAR$-CDv2019.1, along with the model constants.

$$\frac{\partial}{\partial t}(\rho k) + \frac{\partial}{\partial x_j}\left(\rho u_j k - \left(\mu + \frac{\mu_t}{\sigma_k}\right)\frac{\partial k}{\partial x_j}\right) = \mu_t\left(2S_{ij}S_{ij} - \frac{g_i}{\sigma_{h,t}}\frac{1}{\rho}\frac{\partial\rho}{\partial x_i}\right) - \rho\varepsilon - \frac{2}{3}\left(\mu_t\frac{\partial u_i}{\partial x_i} + \rho k\right)\frac{\partial u_i}{\partial x_i} \tag{1.25}$$

$$\frac{\partial}{\partial t}(\rho\varepsilon) + \frac{\partial}{\partial x_j}\left(\rho u_j\varepsilon - \left(\mu + \frac{\mu_t}{\sigma_\varepsilon}\right)\frac{\partial\varepsilon}{\partial x_j}\right) = C_{\varepsilon 1}\frac{\varepsilon}{k}\left[2\mu_t S_{ij}S_{ij} - \frac{2}{3}\left(\mu_t\frac{\partial u_i}{\partial x_i} + \rho k\right)\frac{\partial u_i}{\partial x_i}\right] - C_{\varepsilon 3}\frac{\varepsilon}{k}\mu_t\frac{g_i}{\sigma_{h,t}}\frac{1}{\rho}\frac{\partial\rho}{\partial x_i} -$$

$$C_{\varepsilon 2}\rho\frac{\varepsilon^2}{k} + C_{\varepsilon 4}\rho\varepsilon\frac{\partial u_i}{\partial x_i} - \frac{C_\mu\eta^3\left(1-\frac{\eta}{\eta_0}\right)}{1+\beta\eta^3}\frac{\rho\varepsilon^2}{k} \tag{1.26}$$

With:

- $\mu_t = C_\mu\rho\frac{k^2}{\varepsilon}$ which is the turbulent viscosity
- $\eta = S\frac{k}{\varepsilon}$
- $S = \sqrt{2S_{ij}S_{ij}}$
- $S_{ij} = \frac{1}{2}\left(\frac{\partial u_i}{\partial x_j} + \frac{\partial u_j}{\partial x_i}\right)$ which is the "mean strain"

C_μ	σ_k	σ_ε	$\sigma_{h,t}$	$C_{\varepsilon 1}$	$C_{\varepsilon 2}$	$C_{\varepsilon 3}$	$C_{\varepsilon 4}$	η_0	β
0.085	0.719	0.719	0.9	1.42	1.68	1.42*	-0.387	4.38	0.012

Table 1.1. k-ε RNG model constants.

*$C_{\varepsilon 3} = 1.42$ for $-\frac{g_i}{\sigma_{h,t}}\frac{1}{\rho}\frac{\partial\rho}{\partial x_i} > 0$, otherwise zero.

The implemented formulation comes from open literature [56]. Compared to the standard k-ε model, the RNG version is considered more general and accurate and its distinctive feature consists in the last term of the dissipation equation, which is a modeled form of a term arising from the RNG analysis, taking into account the effect of the mean flow distortion on turbulence.

Chapter 2: Fundamentals of Combustion Chemistry

⬡ 2.1 Fundamental Definitions

Combustion is the oldest technology of mankind; it has been used for more than one million years. At present, about 90% of our worldwide energy support (e.g. transportation, electrical power generation, heating) is provided by combustion. The quantitative treatment of combustion processes requires some understanding of fundamental concepts and definitions, which are described in this section. A *chemical reaction* is the exchange and/or rearrangement of *atoms* between colliding *molecules*. In the course of a chemical reaction, as the one in Eq. 2.1, the atoms (relevant in combustion: C, H, O and N) are conserved; i.e. they are not created or destroyed.

$$\mathrm{HCN} + \mathrm{OH} \rightarrow \mathrm{CN} + \mathrm{H_2O} \tag{2.1}$$

On the other hand, molecules e.g. (HCN, OH, CN, $\mathrm{H_2O}$) are not conserved. Reactant molecules are rearranged to become product molecules, with simultaneous release of heat. A primary interest in the heat of reaction sets combustion engineering apart from chemical engineering. Atoms and molecules are conveniently counted in terms of *amount of substance* or *mole numbers* (unit: [mol]). 1 mol of a compound corresponds to $6.023 \cdot 10^{23}$ particles (atoms, molecules, etc.) Accordingly, the *Avogadro*'s constant is $N_A = 6.023 \cdot 10^{23} mol^{-1}$. The *mole fraction* x_i of the species i denotes the ratio of the mole number n_i of species i to the total mole number $n = \sum n_i$; in equations:

$$x_i = \frac{n_i}{n} \tag{2.2}$$

The *mass* m is a fundamental property of matter. The *mass fraction* w_i is the ratio of the mass m_i of the species i and the total mass $m = \sum m_i$ of the mixture; in equations:

$$w_i = \frac{m_i}{m} \tag{2.3}$$

The *molar mass* or *molecular weight* MW_i of species i is the mass of 1 mol of this species. The mixture mean molecular weight $\overline{MW}$ denotes an average molecular weight, using the mole fractions as weighting; in equations:

$$\overline{MW} = \sum x_i MW_i \tag{2.4}$$

Frequently w_i and x_i are expressed in percentages. The following relation hold, which can be verified by simple calculations, where S denotes the number of different compounds:

$$w_i = \frac{MW_i n_i}{\sum_{j=1}^{S} MW_j n_j} = \frac{MW_i x_i}{\sum_{j=1}^{S} MW_j x_j} \tag{2.5}$$

$$x_i = \frac{w_i}{MW_i}\overline{MW} = \frac{w_i/MW_i}{\sum_{j=1}^{S} w_j/M_j} \tag{2.6}$$

Densities do not depend on the size (extent) of a system. Such variables are called intensive properties and are defined as the ratio of the corresponding extensive properties, which depend on the extent of the system, and the system volume V. Mass density $\rho = m/V$ and molar density $c = n/V$ are often used as reference quantities in combustion chemistry. It follows that the mean molar mass is given by the expression:

$$\frac{\rho}{c} = \frac{m}{n} = \overline{MW} \tag{2.7}$$

In chemistry, concentrations c of chemical species defined in this way are usually denoted by species symbols in square brackets (e.g. $c_{H_2O} = [H_2O]$). For the gases and gas mixtures in combustion processes, an equation of state relates temperature, pressure and density of the gas. For many conditions it is satisfactory to use the ideal gas equation of state; it follows that:

$$c = \frac{p}{RT} \; and \; \rho = \frac{p\overline{MW}}{RT} = \frac{p}{RT \sum_{i=1}^{S} \frac{w_i}{MW_i}} \tag{2.8}$$

When temperatures are near or less than the critical temperature, or when pressures are near or above the critical pressures, the concentration or density is inadequately predicted using the ideal gas equation of state. The system is better approximated as a *real gas*.

⬡ 2.2 Basic Flame Types

In combustion processes, fuel and oxidizer, typically air, are mixed and burnt. It is useful to identify several combustion categories based upon whether the fuel and oxidizer is mixed first and burnt later (*premixed*) or whether combustion and mixing occur simultaneously (*non-premixed*). Each of these categories is further subdivided based on whether the fluid flow is laminar or turbulent.

- **Laminar Premixed Flames:** In laminar premixed flames, fuel and oxidizer are premixed before combustion and the flow is laminar. Examples are laminar *flat flames* and, under fuel-lean conditions, *Bunsen flames* as shown in Fig. 2.1.

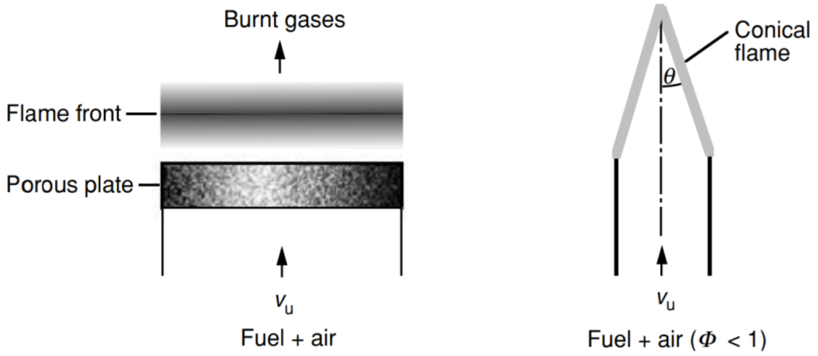

Figure 2.1. Schematic illustration of laminar flat flame (left) and of a Bunsen flame (right), both premixed.

A premixed flame is said to be stoichiometric, if fuel (e.g. a hydrocarbon) and oxidizer (e.g. oxygen O_2) consume each other completely, forming only carbon dioxide (CO_2) and water (H_2O). If there is an excess of fuel, the system is called *fuel-rich*, and if there is an excess of oxygen, it is called *fuel-lean*. Each species symbol in such a chemical reaction equation represents 1 mol. If the reaction equation is written such that it describes exactly the reaction of 1 mol fuel, the mole fraction of the fuel in a stoichiometric mixture can be calculated easily to be

$$\alpha_{st} = \frac{1}{1+v} \tag{2.9}$$

where ν denotes the number of moles of O_2 in the reaction equation. If air is used as an oxidizer, it has to be taken into account that dry air contains only about 21% oxygen (78% nitrogen, 1% noble gas). Thus, for air $x_{N_2} = 3.762x_{O_2}$. It follows mole fractions in a stoichiometric mixture with air are:

$$x_{fuel,st} = \frac{1}{1+v \cdot 4.762} \ ; \ x_{O_2,st} = v \cdot x_{fuel,st} \ ; \ x_{N_2,st} = 3.762 \cdot x_{O_2,st} \tag{2.10}$$

ν denotes, again, the mole number of O_2 in the reaction equation for a complete reaction of 1 mol of fuel to CO_2 and H_2O. Premixtures of fuel and air are characterized by the *air equivalence ratio* (sometimes *air number*) or the reciprocal value, the *fuel equivalence ratio* $\phi = 1/\lambda$ with:

$$\lambda = \left(x_{air}/x_{fuel}\right)/\left(x_{air,st}/x_{fuel,st}\right) = \left(w_{air}/w_{fuel}\right)/\left(w_{air,st}/w_{fuel,st}\right) \tag{2.11}$$

This formula can be written to allow the evaluation of mole fractions in a mixture from ϕ by:

$$x_{fuel} = \frac{1}{1+\frac{4.762 \cdot v}{\phi}} \ ; \ x_{air} = 1 - x_{fuel} \ ; \ x_{O_2} = x_{air}/4.762 \ ; \ x_{N_2} = x_{O_2} \cdot 3.762 \tag{2.12}$$

Accordingly, premixed combustion process can now be divided into three groups:

rich combustion: $\phi > 1 \ , \ \lambda < 1$
stoichiometric combustion: $\phi = 1 \ , \ \lambda = 1$
lean combustion: $\phi < 1 \ , \ \lambda > 1$

The burning of freely burning premixed laminar flat flames into the unburnt mixture can be characterized by the laminar burning velocity s_L which depends only on mixture composition (ϕ or λ), pressure p, unburnt temperature T_u and EGR dilution. If s_L of a flat flame is less than the velocity s_u of the unburnt gases, the flame blows off. Therefore, the inequality $s_L > s_u$ has to be fulfilled for flat flames. Right before the blow-off $s_L \approx s_u$.

- **Turbulent Premixed Flames:** The flow in SI engines is seldom laminar. In this case, premixed flame fronts burn and propagate into a turbulent fluid flow. If turbulence intensity is not too high, curved laminar premixed flame fronts are formed. The turbulent flame can then be viewed as an ensemble of many premixed laminar flames. This is the so-called *flamelet* concept.

- **Laminar Non-premixed Flames:** In laminar non-premixed flames, also called *laminar diffusion flames*, fuel and oxidizer are mixed during the combustion process it-self. The flow is laminar.

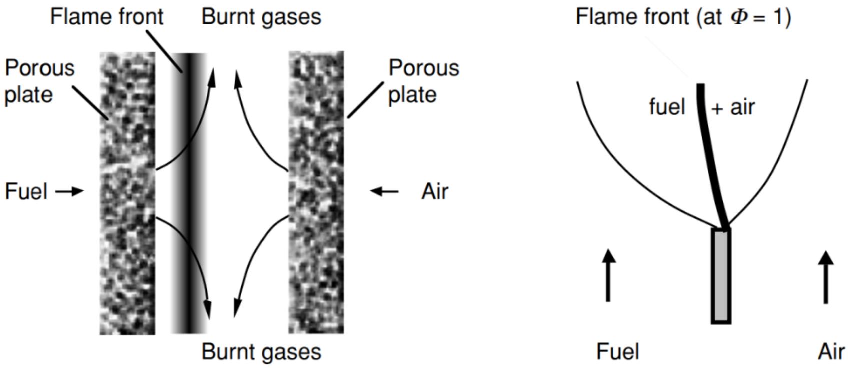

Figure 2.2. Schematic illustration of a laminar counterflow non-premixed flame (left) and a laminar coflow non-premixed flame (right).

Examples include candles, oil lamps and campfires. For research purposes, two important configurations are used: *laminar counterflow* and *laminar coflow non-premixed flames* as shown in Fig. 2.2. Non-premixed flames include more complex chemistry than premixed ones, because the equivalence ratio ϕ covers the whole range from 0 (air) to ∞ (pure fuel). Rich combustion occurs on the fuel side, lean combustion on the air side. The flame front, which is usually characterised by intense luminescence, is fixed to regions near the location of the stoichiometric composition $\phi = 1$, since this is where temperature is the highest. Thus, unlike premixed flames, non-premixed ones do not propagate and, therefore, cannot be characterised by a laminar flame speed.

- **Turbulent Non-premixed Flames:** In this case, non-premixed flames burn in a turbulent flow field, and for low turbulence intensities the so-called *flamelet* concept can be used again. Such kind of flames are mostly used in industrial furnaces and burners. Unless very sophisticated mixing techniques are used, non-premixed flames show a yellow luminescence, caused by glowing soot particles formed by fuel-rich chemical reactions in the rich domains of non-premixed flames.

2.3 Mathematical Description of Premixed Laminar Flat Flames

If a chemically reacting flow is considered, the system at each point in space and time is completely described by specification of pressure p, density ρ, temperature T, flow velocity u and concentration of each species. These properties can be changing in time and space. The changes are the result of fluid flow (convection), chemical reaction, molecular transport (e.g. heat conduction, diffusion and viscosity) and radiation. A mathematical description of flames therefore has to account for each of these properties. Some properties in reacting flows are characterized by the fact that they are conserved. Such properties are energy, mass and momentum. Summation over all the processes that change the conserved properties leads to the conservation equations, which describe the changes in reacting flow; accordingly, these equations are often called the *equations of change*. These equations of change, an extended set of the so-called *Navier-Stokes* equations previously described, are the general starting point for mathematical descriptions of chemically reacting flows. Because all systems are described by the conservation equations, the main difference from one system to another are the boundary conditions and physicochemical conditions. For the purpose of exposing the concepts embodied in these conservation equations, this chapter will develop these conservation equations for a laminar premixed flat flame.

2.3.1 Conservation Equations for Laminar Flat Premixed Flames

Laminar premixed flames on a flat burner constitute a simple yet interesting example for the mathematical treatment of combustion processes. As shown in Fig. 2.3, the burner is usually a porous disk, $\sim 10\ cm$ in diameter, through which premixed fuel and air flow. The gases emerge from the disk and flow into the flame, which appears as a luminous disk levitating a few millimetres above the porous disk. If one assumes that the burner diameter is sufficiently large, effects at the edge of the burner can be neglected as an approximation. Well within the edges, a flat flame front is developed. The properties in this flame (e.g. temperature and gas composition) depend only on the distance from the burner, i.e. only one spatial coordinate z is needed for the description. The conservation equations for this flame are now derived.

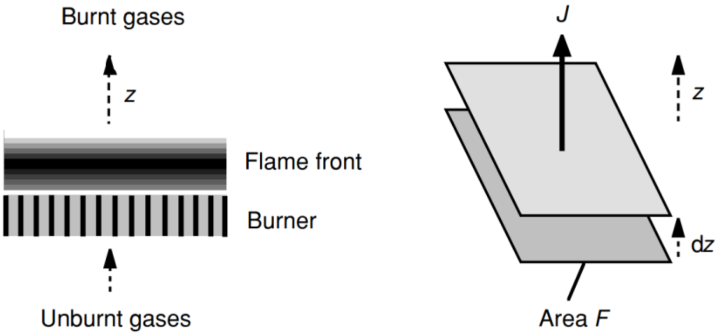

Figure 2.3. Schematic illustration of a laminar premixed flame.

The following assumptions are made in order to simplify the treatment intended:

- The ideal gas law is used
- External forces (e.g. gravitation) are negligible
- The system is continuous; the mean free path of the molecules is small compared to the flame thickness
- The pressure is constant (spatial or temporal fluctuations are weak)
- The kinetic energy of the gas flow is negligible compared to other terms in the energy conservation equation (e.g. shock waves are not considered)
- The reciprocal thermal diffusion effect (*Dufour effect*) can be neglected
- Heat flux caused by radiation of gases and particles is negligible (assumption acceptable when the flame is non-sooting)
- The system is in local thermal equilibrium
- The flame is stationary, i.e., there are no temporal changes. Formally, time-dependent equations are solved under stationary conditions

These assumptions lead to reasonable predictions for laminar flat flames. For any conserved variable E ($z = spatial\ coordinate,\ t = time$) in a one-dimensional system, the general relation holds:

$$\frac{\partial W}{\partial t} + \frac{\partial J}{\partial z} = Q \tag{2.13}$$

where W denotes the density of the conserved variable, J a flux of the conserved variable and Q a source (or sink) of the conserved variable. Eq. 2.13 is a statement that accumulation can be accomplished by influx (or outflux) and by a source (or sink). I t will be shown in the following how the general equation 2.13 appears in the specific cases of conservation of mass, species and enthalpy.

Conservation of the overall mass m of the mixture: In the conservation of total mass, the density W in the conservation equation is given by the *total mass density* ρ. The flux J describes the movement of mass and is given as the product of density and the mean mass velocity (also called *flow velocity*), i.e. $J = \rho u$ (in $kg/(m^2 s)$. The source term in the mass conservation equation is zero, because chemical reactions neither create nor destroy mass ($Q = 0$). Substitution in Eq. 2.13 leads to:

$$\frac{\partial \rho}{\partial t} + \frac{\partial(\rho v)}{\partial z} = 0 \tag{2.14}$$

This equation is called the continuity equation, here for one-dimensional systems.

Conservation of the mass m_i of species i: Here the density W is given by the partial density ρ_i, which denotes the mass of species i per unit volume:

$$\rho_i = \frac{m_i}{V} = (m_i/m)(m/V) = w_i \rho \tag{2.15}$$

The flux J is given by the product of the partial density and the mass velocity u_i of species i:

$$J = \rho_i u_i = w_i \rho u_i \tag{2.16}$$

In contrast with the conservation equation for the total mass, this equation has a source term which describes the formation or consumption of species i in chemical reactions. This term is given by:

$$Q = MW_i (\partial c_i / \partial t)_{chem} = r_i \tag{2.17}$$

where MW_i denotes the molecular weight of species i, $(\partial c_i/\partial t)_{chem}$ the *chemical rate of production* of species i in chemical reactions, and r_i the chemical rate of production. Together with Eq. 2.13 this leads to:

$$\frac{\partial(\rho w_i)}{\partial t} + \frac{\partial(\rho w_i u_i)}{\partial z} = r_i \tag{2.18}$$

The mass velocity u_i of the species i is composed of the mean mass velocity u of the centre of mass of the mixture and a *diffusion velocity* V_i (relative to the centre of mass), which is caused by molecular transport due to concentration gradients of the species i:

$$u_i = u + V_i \tag{2.19}$$

Simple transformations (product law for differentiation) lead then to:

$$u_i \frac{\partial \rho}{\partial t} + \rho \frac{\partial w_i}{\partial t} + \rho u \frac{\partial w_i}{\partial z} + w_i \frac{\partial (\rho u)}{\partial z} + \frac{\partial j_i}{\partial z} = r_i \tag{2.20}$$

where the symbol j_i denotes the diffusion flux of species i (in the centre of mass system):

$$j_i = \rho w_i V_i = \rho_i V_i \tag{2.21}$$

Together with Eq. 2.13, this equation simplifies to the species mass conservation equation:

$$\rho \frac{\partial w_i}{\partial t} + \rho u \frac{\partial w_i}{\partial z} + \frac{\partial j_i}{\partial z} = r_i \tag{2.22}$$

Conservation of the enthalpy h of the mixture: In this case, the different terms in Eq. 2.13 are given by:

$$W = \sum_j \rho_j \, h_j = \sum_j \rho w_j \, h_j$$

$$J = \sum_j \rho_j \, u_j h_j + j_q = \sum_j \rho \, u_j w_j h_j + j_q \tag{2.23}$$

$$Q = 0$$

Here h_j denotes the specific enthalpy of species j and j_q a heat flux, which corresponds to the diffusion flux j_i introduced above and is caused by transport due to temperature gradients. The term $\sum_j \rho_j \, u_j h_j$ describes the change of enthalpy due to the flow of species (composed of the mean mass velocity u and the diffusion velocity V_j). Substitution into Eq. 2.13, using Eq. 2.19, yields:

$$\sum_j \frac{\partial}{\partial z}\left(\rho u w_j h_j\right) + \sum_j \frac{\partial}{\partial z}\left(\rho V_j w_j h_j\right) + \frac{\partial j_q}{\partial z} + \sum_j \frac{\partial}{\partial t}\left(\rho w_j h_j\right) = 0 \tag{2.24}$$

Performing some substitution and mathematical operations, the final equation for the conservation of the mixture enthalpy is obtained:

$$\rho u \sum_j w_j \frac{\partial h}{\partial z} + \rho \sum_j w_j \frac{\partial h}{\partial t} + \sum_j h_j \, r_j + \sum_j j_j \frac{\partial h_j}{\partial z} + \frac{\partial j_q}{\partial z} = 0 \tag{2.25}$$

The values for j_i and j_q (diffusion heat flux) still have to be specified with respect to the properties of the mixture (pressure, temperature, composition). Use of the conservation of momentum is not here necessary due to the assumption of constant pressure.

2.3.2 Heat and Mass Transport

Empirical observations have established that concentration gradients lead to mass transport called *diffusion* and temperature gradients lead to heat transport called *heat conduction.* These empirical observations were later explained by the theory of irreversible thermodynamics. For the sake of brevity only the empirical laws are discussed here. For the heat flux j_q, numerous measurements support the empirical *law of Fourier* in the form:

$$j_q = -\lambda \frac{\partial T}{\partial z} \tag{2.26}$$

where λ denotes the *heat conductivity of the mixture*. For the mass flux j_i one obtains an extended form of the law of Fick:

$$j_i = \frac{c^2}{\rho} MW_i \sum_j MW_j D_{ij} \frac{\partial x_j}{\partial z} - \frac{D_i^T}{T}\frac{\partial T}{\partial z} \tag{2.27}$$

Where c denotes the molar concentration in mol/m^3; D_{ij} are *multicomponent diffusion coefficients* and D_i^T the *thermal diffusion coefficient* of the species i based on the temperature gradient. Species transport caused by a temperature gradient (*thermal diffusion*) is also called *Soret effect.* For many practical applications the simplified formula is sufficiently accurate for the mass flux j_i.

$$j_i = -D_i^M \rho \frac{w_i}{x_i}\frac{\partial x_i}{\partial z} - \frac{D_i^T}{T}\frac{\partial T}{\partial z} \tag{2.28}$$

Here D_i^M denotes the diffusion coefficient for species i into the mixture of the other species. For binary mixtures and for trace species ($w_i \rightarrow 0$) this simplified formulation is equivalent to Eq. 2.27. This assumption of strong dilution is reasonable if the oxidizer is air, because nitrogen is in excess in this case.

2.3.3 The Description of a Laminar Premixed Flat Flame Front

As previously mentioned, for a complete description of laminar flat premixed flame fronts, temperature T, pressure p, velocity u and the partial densities $\rho_i (i = 1, \ldots, S$ for S species) or the overall density ρ and the S-1 linearly independent mass fractions $w_1, \ldots, w_{S-1}$ ($w_S = 1 - w_1 - \ldots - w_{S-1}$) have to be known as functions of the spatial coordinate z. The following equations are available to determine the variables listed:

- Pressure is assumed to be constant and equal to surrounding pressure
- Density ρ can be calculated from temperature, pressure and composition using Eq. 2.8
- Velocity u is obtained from the continuity equation (Eq. 2.14). Because the flame is assumed to be stationary (no temporal dependence), Eq. 2.14 reduces to

$$\frac{\partial(\rho u)}{\partial z} = 0 \tag{2.29}$$

- Using the given mass flux $(\rho u)_u$ of the unburnt gases, u can be calculated at each point in the flame.
- The mass fractions $w_i (i = 1, .., S)$ are determined by solving S-1 species conservation equations, combined with the constraint that the mass fractions sum to unity.
- Thermal diffusion, which is important for species with a small molar mass (H, H_2, He), is safely neglected here because the concentration of these species is rarely significant for this process to contribute. Then, introducing the diffusional mass flux $j_i = -D_i^M \rho (\partial w/\partial z)$ (simplified form of Eq. 2.28 for constant mean molecular weight $\overline{MW}$) into the species conservation Eq. 2.22 leads to:

$$\rho \frac{\partial w_i}{\partial t} = \frac{\partial}{\partial z}\left(D_i^M \rho \frac{\partial w_i}{\partial z}\right) - \rho u \frac{\partial w_i}{\partial z} - r_i \tag{2.30}$$

- The temperature can be calculated from the energy conservation equation. Inserting the heat flux j_q (Eq. 2.26) and using $c_{p,j} = dh_j$ (for an ideal gas); $c_p = \sum_j w_j \, c_{p,j}$ yields:

$$\rho c_p \frac{\partial T}{\partial t} = \frac{\partial}{\partial z}\left(\lambda \frac{\partial T}{\partial z}\right) - \left(\rho u c_p + \textstyle\sum_j j_j \, c_{p,j}\right)\frac{\partial T}{\partial z} - \textstyle\sum_j h_j \, r_j \tag{2.31}$$

Now all the equations required to solve the problem are given. After rearranging, they yield a partial differential equation system of the general form:

$$\frac{\partial Y}{\partial t} = A \frac{\partial^2 Y}{\partial z^2} + B \frac{\partial Y}{\partial z} + C \tag{2.32}$$

The terms in Eq. 2.31-2.32 are now discussed in detail. The term $\partial Y/\partial t$ denotes the temporal change of the variables Y at the spatial location z, the second derivatives describe the molecular transport (diffusion, heat conduction), the first derivatives describe the flow (in Eq. 2.31 $\sum_j j_j \, c_{p,j}$ is a correction, which accounts for transport of heat by diffusion of species), and the terms without derivatives describe the local changes due to chemical reaction. The influence of the different terms can be best seen if selected simplified systems are considered, where some of the terms are negligible. However, no further details will be provided for the sake of brevity. It is worthwhile spending a few words on freely propagating flames, being the reference mathematical description used in the present thesis to compute s_L. For a flat, freely propagating flame, the appropriate reference system is fixed to the propagating flame. Thus any observer following the flame would experience the unburnt mixture of fuel and oxidants approaching at the flame speed s_L. The continuity equation describes the conservation of momentum, ρu, over the flame zone and, since the density of the burnt (hot) gases is lower, continuity requires that the speed of the burnt gases is higher than that of the unburnt gases. Integration of Eq. 2.29 yields:

$$\rho_u u_u = \rho_u s_L = \rho_b u_b \tag{2.33}$$

The fundamental property of a premixed flame, the laminar flame speed s_L, can be found by solving the conservation equations above.

2.4 Homogeneous Reactors

Homogeneous reactors are also used in the present thesis. Although their governing equations can be derived similarly to those previously derived for a flat premixed flame, the fundamental equations used while performing such kind of simulations are hereby briefly recalled for the sake of completeness and brevity.

2.4.1 Governing Balance Equations

All the equations are derived for a generic system characterized by a number of inlets N_{in} and outlets N_{out}, in which a number of species N_s evolve. In the following equations, V indicates the control volume, where the sum over l indicates the number of inlets and k the number of outlets. If a source term is present, ω_i is the net reaction rate associated with the i^{th} species.

- **Balance of Mass:** The balance equation for the total mass is derived through summation of the total number of chemical species present in the reactor, where the last equality comes from the fact that total formation and consumption have to be zero.

$$\frac{\partial m}{\partial t} = \sum_i^{N_s} \frac{\partial m_i}{\partial t} = \sum_i^{N_s} \left(\sum_l^{N_{in}} \dot{m}_{i,l} - \sum_k^{N_{out}} \dot{m}_{k,l} + \omega_i \overline{MW_i} \right) = \sum_l^{N_{in}} \dot{m}_l - \sum_k^{N_{out}} \dot{m}_k \qquad (2.34)$$

- **Balance of Species Mass Fraction:** The balance equation for the mass fraction Y_i of species i is derived in a similar way, with two terms describing change due to in- and outflow and one due to production (consumption).

$$\frac{\partial Y_i}{\partial t} = \sum_l^{N_{in}} \frac{\dot{m}_l}{m} \left(Y_{i,l} - Y_i \right) + \frac{\omega_i W_i}{\rho} \qquad (2.35)$$

- **Balance of Energy:** The energy equation is presented in two forms, one using specific internal energy and one using specific enthalpy. The reason for this is that reactors with constant volume and reactors with constant pressure have different definitions of specific heat.

$$\frac{\partial U}{\partial t} = \dot{Q} - p \frac{dV}{dt} + \sum_l^{N_{in}} \dot{m}_l \sum_i^{N_s} Y_{i,l} h_{i,l} - \sum_k^{N_{out}} \dot{m}_k \sum_k^{N_s} Y_{i,k} h_{i,k} \qquad (2.36)$$

- **Balance of Energy in Terms of Specific Enthalpy:**

$$\rho c_p \frac{\partial T}{\partial t} = \sum_l^{N_{in}} \frac{\dot{m}_l}{V} \sum_i^{N_s} Y_{i,l} \left(h_{i,l} - h_i \right) - \sum_i^{N_s} \omega_i H_i + \frac{h_c A}{V} (T - T_w) + \sigma \varepsilon \frac{A}{V} (T^4 - T_w^4) \qquad (2.37)$$

- **Balance of Energy in Terms of Specific Internal Energy:**

$$\rho c_v \frac{\partial T}{\partial t} = \sum_l^{N_{in}} \frac{\dot{m}_l}{V} \sum_i^{N_s} Y_{i,l} \left(u_{i,l} - u_i \right) - \sum_i^{N_s} \omega_i U_i + \sum_l^{N_{in}} \frac{\dot{m}_l}{V} \frac{R_0 T_l}{\bar{W}_l} - \sum_k^{N_{out}} \frac{\dot{m}_l}{V} \frac{R_0 T_k}{\bar{W}_k} + \frac{h_c A}{V} (T - T_w) + \sigma \varepsilon \frac{A}{V} (T^4 - T_w^4) \qquad (2.38)$$

- **Balance of Momentum in One-dimensional Flow:**

$$-\frac{dp}{dx} = \rho u \frac{dv}{dx} \tag{2.39}$$

2.4.2 Constant Volume Reactor

The Constant Volume (CV) reactor consists of a closed rigid vessel in which the volume is kept constant during combustion, allowing the pressure to increase. Being a closed system, no mass flows into or out the system and since mass cannot be created the mass conservation equation reads:

$$\frac{\partial m}{\partial t} = 0 \tag{2.40}$$

Since $Y_{i,l} = Y_{i,i}$, the conservation equation for a species mass fraction becomes:

$$\frac{\partial Y_i}{\partial t} = \frac{\omega_i W_i}{\rho} \tag{2.41}$$

The energy conservation equation is expressed in terms of specific internal energy, Eq. 2.38, since the volume is constant. With the proper simplifications, such as $u_{i,l} = u_i$, yields:

$$\rho c_v \frac{\partial T}{\partial t} = \sigma \varepsilon \frac{A}{V}(T^4 - T_w^4) - \sum_i^{N_s} \omega_i U_i \tag{2.42}$$

Since the system is assumed to be stationary and homogeneous, the momentum is zero and no balance equation for momentum is solved.

2.4.3 Constant Pressure Reactor

The Constant Pressure (CP) reactor is used to represent a gas that is allowed to expand freely. Such reactor, for instance, can consist of a tube, closed at one end and with a movable piston at the other, assuring a constant pressure during combustion. As for the CV reactor, the CP reactor is assumed to be a closed system, hence there is no inflow or outflow and the balance equations become simple conservation equations (Eq. 2.40-2.41). In this case, the energy conservation equation is expressed in terms of specific enthalpy (Eq. 2.37) and since $h_{i,l} = h_i$ the energy equation becomes:

$$\rho c_p \frac{\partial T}{\partial t} = \sigma \varepsilon \frac{A}{V}(T^4 - T_w^4) - \sum_i^{N_s} \omega_i H_i \tag{2.43}$$

The system is stationary and homogeneous and the momentum is zero, so no balance equation for momentum is solved.

2.5 Basics of Chemical Kinetics

The thermodynamic laws allow the determination of the equilibrium state of a chemical reaction system. If one assumes that the chemical reactions are fast compared to the other processes like diffusion, heat conduction, and flow, thermodynamics alone allow the description of the system locally. In some case, however, chemical reactions occur on time scales comparable with that of the flow and of the molecular transport processes. Therefore, information is needed about the rate of chemical reactions, i.e. the *chemical kinetics*.

2.5.1 Rate Laws and Reaction Orders

The so-called rate law is discussed for a chemical reaction, which in its general case can be described by the equation:

$$A + B + C + \cdots \overset{k}{\rightarrow} D + E + F + \cdots \qquad (2.44)$$

where $A, B, C, \ldots$ denote the different species involved in the reaction. A rate law describes an empirical formulation of the *reaction rate*, i.e., the rate of formation or consumption of a species in a chemical reaction. Focusing on the consumption of species A, the reaction rate can be expresses according to:

$$\frac{d[A]}{dt} = -k \cdot [A]^a [B]^b [C]^c \ldots \qquad (2.45)$$

Here a,b,c, … are reaction orders with respect to the species A, B, C, … and k is the *rate coefficient* of the reaction. The sum of all exponents is the *overall reaction order*. Frequently some species are in excess. In this case their concentrations do not change noticeably. If, e.g., $[B]$, $[C]$, … remain nearly constant during the reaction, an effective rate coefficient can be generated from the rate coefficient and the nearly constant concentrations of the species in excess, and, using $k_{exp} = k \cdot [B]^b [C]^c \ldots$, a simplified version of Eq. 2.45 is obtained:

$$\frac{d[A]}{dt} = -k_{exp}\, [A]^a \qquad (2.46)$$

The temporal change of the concentration of species A can be calculated by integrating this differential equation, as it will be shown next for some typical cases. For *first-order* reactions ($a = 1$), the integration of Eq. 2.46 yields the first order time behaviour:

$$ln \frac{[A]_t}{[A]_0} = -k_{exp}(t - t_0) \qquad (2.47)$$

where $[A]_0$ and $[A]_t$ denote the concentration of species A at time t_0 and t, respectively.

Accordingly, one obtains for second-order ($a = 2$) and third-order reactions ($a = 3$) the expressions in Eq. 2.48 and Eq.2.49, respectively.

$$\frac{1}{[A]_t} - \frac{1}{[A]_0} = k_{exp}(t - t_0) \tag{2.48}$$

$$\frac{1}{{[A]_t}^2} - \frac{1}{{[A]_0}^2} = 2k_{exp}(t - t_0) \tag{2.49}$$

If the time behaviour is measured, the reaction order can be determined.

○ 2.5.2 Temperature Dependence of Rate Coefficients

It is characteristic of chemical reactions that their rate coefficients depend strongly in a non-linear way on temperature. According to Arrhenius (1889), this temperature dependence can be described by the simple formula (Arrhenius law) reported in Eq. 2.50.

$$k = A' \cdot exp\left(-\frac{E_a'}{RT}\right) \tag{2.50}$$

More recently, accurate measurements showed a temperature dependence of the *pre-exponential factor* A', which, however is usually small compared to the exponential dependence.

$$k = A'T^b \cdot exp\left(-\frac{E_a'}{RT}\right) \tag{2.51}$$

The activation energy E_a corresponds to an energy barrier to be overcome during the reaction. Its maximum value corresponds to the bond energies in the molecule (in dissociation reactions, e.g. the activation energy is approximately equal to the bond energy of the bond, which is split), but it can also be much smaller (or even zero), if new bonds are formed simultaneously with the breaking of the old bonds. For unimolecular reactions, the reciprocal value of A corresponds to a mean lifetime of an activated (reactive) molecule. In dissociation reactions, this lifetime is determined by the frequency of the vibration of the bond which is broken. For bimolecular reactions the pre-exponential factor A' corresponds to a product of collision rate and probability of reaction. This collision rate is an upper limit for the reaction rate. In trimolecular reactions, a third collision partner has to remove the energy of the reaction.

Chapter 3: Fuel Surrogates Modelling

⬡ 3.1 Auto-ignition Quality and Flame Propagation Characteristics

⬡ 3.1.1 Relevance of Comprehensive Gasoline Fuel Surrogates Formulation

As previously mentioned, $3D$-CFD simulations have become a common practice in the design workflow of modern ICE. In particular, a number of numerical models specifically engineered to predict flame propagation and knock occurrence in $RANS$ and Large Eddy Simulations (LES) frameworks [39-40] emerged. Since fuel composition and properties can deeply affect ICE performance and emissions [24], fuel properties have become an additional control parameter. Engine manufacturers are therefore tending towards a comprehensive development of fuel and engine in the design of new combustion systems [6]. Given the intrinsic dependence of flame propagation and knock on fuel properties [41,42,43,44,45], many detailed and semi-detailed chemical kinetics mechanisms [57,58,59,60,61,62,63] were recently developed to predict gasoline main oxidation pathways and reactivity under different combustion modes (e.g. auto-ignition, premixed flame propagation, etc.). These mechanisms are often used in $3D$-CFD engine simulations to provide fundamental chemistry-based input to numerical models either in the form of correlations, tables and libraries or, in recent years, directly solving chemistry at a cell-wise level during run time thanks to a direct coupling with the CFD model. For example, flamelet combustion models used to predict turbulent combustion processes in SI units rely on the estimation of s_L for the prediction of turbulent combustion rate and knock models rely on the prediction of the end-gas reactivity via τ_{ig} calculations. As previously mentioned, both s_L and τ_{ig} are fundamental properties of the fuel. Since practical fuels are mixtures of hundreds of hydrocarbon species, simplified surrogate fuels are used to represent them in computational models [16]. Surrogates are essentially blends of a small number of well-characterized compounds to represent refinery-grade fuels by emulating their thermo-physical and chemical kinetics processes [64]. In $3D$-CFD practice, a fuel surrogate is often a user input parameter used to compute chemistry-based s_L and τ_{ig} simulations in chemistry solvers, which are in turn used in combustion and knock numerical models, respectively. The importance of gasoline fuel surrogates has led many researchers to develop, during the years, methodologies of increasing complexity to match all the main chemical and physical characteristics with a unique fuel surrogate [52-65-66-67-68-69-70-71]. In order to match an increasing number of properties, the number of pure components chosen to formulate the blend has often increased. Surrogates with the higher degree of complexity are nowadays multicomponent blends able to match the main physical properties affecting gasoline spray evolution (such as density ρ and the distillation curve), the main chemical properties driving the combustion process (such as H/C, O/C and Lower Heating Value LHV) and the main combustion-relevant characteristics (such as Research Octane Number RON, Motor Octane Number MON, Sensitivity S, Anti-Knock Index AKI, etc.). Although being the state-of-the-art methodologies for engine CFD gasoline surrogate formulation, none of the previous studies includes a specific methodology to target s_L. This is further confirmed by the fact that recent studies [72,73] underestimate s_L for rich fuel-air mixtures at high pressure conditions (e.g. 20 and 25 bar) [74] when tested against s_L experimental dataset presented by Jerzembeck et al. in [75]. While Piehl et al. [74] attribute these discrepancies to the fact that these surrogates [72,73] were designed to emulate non-oxygenated RD387 gasoline [66], not adequately representing the measured EN228 gasoline [75], Many Sarathy et al [6] argue that s_L is more sensitive to gasoline composition and that non-availability of detailed composition prevents from drawing any conclusion. The data presented by Dirrenberger et al [76], in which addition of ethanol up to 15% to a commercial gasoline had negligible effect on laminar flame speed, supports the latter. In the end, this lack of accuracy in describing s_L strongly limits the use of such surrogates in $3D\text{-}CFD$ combustion and knock simulations, where high degree of accuracy is needed not only when estimating the reactivity of the end-gas but also in correctly representing the turbulent flame speed s_T, which is in turn dependent on s_L [59]. For this reason, it is not unusual in standard ICE $3D\text{-}CFD$ best practices to use more than a single gasoline fuel surrogate to mimic distinct combustion-relevant characteristics such as τ_{ig} [65,69] on one side (e.g. end-gas) and s_L [76,77,78] on the other (e.g. flame front). This workaround allows to perform combustion and knock simulations retaining a quantitative high degree of accuracy in flame propagation and end-gas reactivity but has intrinsic limitations. Firstly, using two different surrogates for τ_{ig} and s_L might lead to discontinuities in the properties of the burnt and unburnt gases, since the surrogate formulation needed to match the former are likely to be different from the latter. This is a non-negligible issue in $3D\text{-}CFD$ simulations, since the Stoichiometric Air-to-Fuel ratio (α_s) in the end-gas will be different from the corresponding one in the flame front. Such misalignment might cause non-negligible errors in CFD simulations. The same rationale holds when estimating cell-wise s_L values using libraries or correlations derived with a fuel surrogate whose properties are different from those of the fuel adopted by the combustion model. The high sensitivity of s_L to gasoline composition [6] and the need to simultaneously target gasoline flame propagation and auto-ignition characteristics motivates the following discussion. In particular, a novel methodology to formulate multicomponent gasoline fuel surrogates simultaneously matching, not only the main chemico-physical properties of interest but also auto-ignition and flame propagation characteristics is proposed. Moreover, in contrast to most of the previous studies, the present dissertation focuses on commercial oxygenated gasolines. In fact, due to $REDII$ [26], oxygenated compounds content is becoming more and more important. In the next paragraph, a detailed background on the key elements needed to introduce the main steps of the methodology are outlined and an overview of current commercial gasolines properties is portrayed. Afterwards, the reference surrogate palette composition is discussed. In the last part of the paragraph, the core of the methodology is outlined and the former is used to generate three surrogates of increasing complexity, namely a Toluene Reference Fuel (TRF) surrogate, an Ethanol Toluene Reference Fuel ($ETRF$) surrogate and a senary (SEN) multicomponent fuel surrogate. In the validation section, the three fuel surrogates are validated against Shock-Tube (ST) and Rapid Compression Machine (RCM) experiments [6] as well as laminar flame speed experiments [75-79]. Coherently with the targeted fuel surrogates, it is also important to point out that all the reference experimental datasets refer to oxygenated gasoline fuels.

⎔ 3.1.2 Background and Surrogate Palette Composition

$3D\text{-}CFD$ modelling of regular and abnormal combustion processes requires a detailed modelling of fuel chemistry. The need of fuel-related properties such as τ_{ig} and s_L have brought to the development of detailed chemical kinetics mechanism comprising hundreds of species and thousands of reactions. These mechanisms describe the main oxidation pathways of the main fuel constituents in high and low temperature regions. It is mandatory to use well-validated mechanism able to describe the reactivity of all the components used in the surrogate [65]. For this reason, in most of the previous works [55,71], chemical kinetics mechanisms were engineered or modified to better represent the reactivity and the oxidation pathways of the components of interest. While this approach guarantees the highest possible degree of accuracy, a non-trivial work must be carried out to adapt the mechanisms updating the sub-mechanisms for each pure compound. Furthermore, dedicated experiments are needed for validation. Ultimately, state-of-the-art mechanisms usually have a number of species and reactions which makes their use in $3D\text{-}CFD$ simulations computationally unfeasible for the industry standard. For instance, Mani Sarathy et al. [71] developed a gasoline surrogate kinetic model including 2315 species and 10079 reactions. Such mechanisms are difficult to apply to one-dimensional ($1D$) flame simulations [80] and the wide range of timescales result in computational stiffness, which makes them unsuitable for multidimensional reacting flow simulations [60]. As reported by Mehl et al. [72], the size of detailed mechanisms is prohibitive for CFD applications and a reduction to skeletal mechanisms is needed. Again, this process requires a step-by-step validation process based on dedicated experimental campaigns. Nonetheless, reduced mechanisms are optimized to match experiments using a particular fuel surrogate, therefore lacking generality. Conversely, the aim of the present thesis is to provide a simple methodology applicable to any validated mechanism for gasoline-like fuels. A drawback of the proposed approach is the limitation associated with the choice of the individual compounds to formulate the surrogate, since their chemical kinetics must be included and properly described in the mechanism. Two different well-validated semi-detailed mechanisms for gasoline, previously used and extensively validated in [81,82], are adopted to prove the solidity of the proposed methodology. The first mechanism, with 202 species and 996 reactions, was formulated by Andrae et al. [60,61,62], while the second, POLIMI_GASOLINE_156 reduced mechanism with 156 species and 3465 reactions [63], was proposed by CRECK Modeling Group (PoliMi). Both mechanisms were validated in terms of τ_{ig}, s_L and species mole fraction profiles. Generally speaking, a fuel model is obtained selecting an appropriate blend of pure compounds in close conjunction with the selected chemical kinetics mechanisms. While choosing the compounds, it must be kept in mind that it is unlikely to formulate a surrogate able to match all the properties of interest. Different components should be chosen depending on the targeted properties [6]. A literature review of commercial gasoline properties, available at the time of dissertation, is therefore presented. Most of the previous works [75,79] on the topic specifically target RD387 gasoline [69,70], which is deemed to be representative of an average commercial non-oxygenated American (US) gasoline. Although being one of the most complete dataset available in literature, providing a complete $EPIONA$ (Ethanol/Paraffins/Iso-paraffins/Olefins/Naphtenes/Aromatics) composition [52] through Detailed Hydrocarbon Analysis (DHA), its properties are not representative of a current oxygenated commercial gasoline in terms composition [70] and auto-ignition characteristics ($RON = 91$, $MON = 82.7$ [70]). Most importantly, s_L experiments are not available for RD387. To emphasize the differences, the main properties and partial compositions of four American (LEV III Prem, Tier 3 Prem, LEV II, Tier 2), two European (Euro 5, Euro 6) and a Chinese (China 6 Prem) commercial gasolines are reported in Table 3.1 thanks to the dataset provided in [83].

	LEV II	**LEV III Prem**	**Tier 2**	**Tier 3 Prem**	**Euro 5**	**Euro 6**	**China 6 Premium**
RON D2699	100.5	99.8	96.5	99.5	96.9	96.3	96.6
MON D2700	88.5	88.8	86.8	88	87.1	85.6	85.9
Aromatics [%v/v] D1319/5769	23.1	-	26	23.4	32.2	25.1	31.3
Olefins [%v/v] D1319/6550	4.8	-	8.4	6.5	5.1	10.1	12.5
Oxygenates [%v/v] D4815	10.88	10	0	9.71	5.07	9.87	8.17
Oxygenate Type	MTBE	Ethanol	None	Ethanol	Ethanol	Ethanol	MTBE

Table 3.1. Properties and partial Composition for American, European and Chinese commercial gasolines [83].

Only Tier 2 gasoline lacks of oxygenates. This further confirms the need of including oxygenates in the fuel surrogate to correctly represent commercial gasolines. While methyl-t-butyl ether ($MTBE$) is used in two gasolines, the majority contains ethanol. It is noteworthy that European grade gasolines, to the extent of the dataset presented, only contain ethanol. It is also important to notice the non-negligible difference, in terms of auto-ignition characteristics (RON, MON), comparing RD387 to commercial gasolines currently sold on the market. While the dataset reported in Table 3.1 constitutes a useful basis, none of such fuels can be targeted in the present thesis since their complete composition, in terms of $EPIONA$, is not reported. The $EPIONA$ composition of a gasoline, usually obtained using Gas Chromatography (GC) [84], is an extremely valuable information while formulating a fuel surrogate since the final properties of a fuel are quantitatively dependent on the hydrocarbon classes content. To the author best knowledge, only a limited number of previous works reported the complete composition of commercial gasolines apart from RD387 gasoline. In [16] a dataset is presented for a commercial Euro 5 non-oxygenated gasoline. In another work [77], the complete composition of Exxon 708629-60 non-oxygenated commercial gasoline is reported but no information is available on its chemico-physical properties and auto-ignition quality. In a recent work [85], the complete composition of CNPC#92 fuel, representative of a commercial Chinese gasoline, is reported. s_L measurements are available, but a limited amount of information is given on its physical properties and auto-ignition propensity. The dataset presented in [65,76] is one of the widest in literature at present, describing the properties and composition of an average commercial oxygenated European gasoline. In the work by Pera et al. [65], fuel surrogates emulating a $RON95$ unleaded European gasoline, certified according to the EN228 specification, were formulated. A wide experimental campaign was carried out analysing with GC numerous samples in the 2005-2009 period to obtain a statistically-relevant composition of an "average gasoline", denoted ULG95. This approach allows to take into account for uncertainties related to variations in composition for the same gasoline; a known issue reported in previous studies [16,65,86]. This dataset is therefore particularly useful, since a wide number of data is available. Properties and compositions of gasolines retrieved from this literature review are reported in Table 3.2 and Table 3.3, respectively. Due to the availability of detailed information and because of the statistical relevance of the dataset, ULG95 gasoline is chosen as target for the fuel surrogate methodology. Furthermore, the availability of s_L experimental measurements for an oxygenated commercial gasoline [75], certified according to EN228 specification, is a relevant advantage for validation purposes.

	ULG95 [65,76]	**EUR Grade [16]**	**RD387 [69,70]**	**Exxon 708629-60 [77]**	**CNPC#92 [85]**
ACA **[-]**	6.76	6.64	-	-	-
AHA **[-]**	12.48	12.11	-	-	-
AOA **[-]**	0.08	0.00	-	-	-
RON **[-]**	95.00	95.40	91.00	-	92.00
MON **[-]**	85.00	85.60	82.70	-	-
S **[-]**	10.00	9.80	8.30	-	-
AKI **[-]**	90.00	90.50	86.85	-	-
H/C **[-]**	1.801	-	1.869	-	1.83
O/C **[-]**	0.011	0.000	0.00	-	-
MW **[g/mol]**	94.30	-	-	-	96.35
$\rho\ at\ 298\ K$ **[kg/m^3]**	749.00	-	745.60	-	744.00
LHV **[kJ/mol]**	42801	43500	43152	-	-
T_b **[K]**	363.52	321.15	-	-	-

Table 3.2. Properties of commercial gasolines from [16,65,69,70,76,77,85].

	ULG95 [65,76]	**EUR Grade [16]**	**RD387 [69,70]**	**Exxon 708629-60 [77]**	**CNPC#92 [85]**
Paraffins [%v/v]	10.70	10.80	9.49	10.37	8.10
Iso-paraffins [%v/v]	39.80	43.40	42.26	40.20	27.46
Olefins [%v/v]	4.80	8.60	4.73	5.65	17.40
Naphthenes [%v/v]	8.80	2.90	16.00	9.39	5.32
Aromatics [%v/v]	31.20	33.60	26.41	34.39	37.02
Oxygenates [%v/v]	4.70	0.00	0.00	0.00	3.85

Table 3.3. Composition of commercial gasolines from [16,65,69,70,76,77,85].

Moreover, targeting ULG95 allows to generate a dedicated surrogate consistent with the European RON95 E5 gasoline, being "E" oxygenates content by volume, used in the experiments, detailed in Chapter 5. As a final remark, differences reported in Tables 3.2 and 3.3 further confirm the impossibility of defining a universal gasoline surrogate due to compositional differences from one country to another [65]. Once a suitable commercial gasoline is chosen, a palette of representative hydrocarbons for each class is needed to formulate a surrogate. An appropriate surrogate palette is critical to match the desired properties of the targeted fuel [87]. The number of hydrocarbons to be included is a degree of freedom and usually an increase in the number of components allows to match a higher number of properties. Two conflicting aspects must be considered. On one side, the possibility to match a higher number of properties would suggest to increase the number of representative components, and therefore the complexity of the surrogate. On the other hand, the need of well-validated chemical kinetics sub-mechanisms for each compound limits the complexity of surrogates commonly used in the industry. Ternary surrogates based on n-heptane, iso-octane and toluene, so-called Toluene Reference Fuels (TRF), are commonly adopted for $3D\text{-}CFD$ engine simulations due to the availability of mature chemical kinetics mechanisms [57,58,59,60]. As reported in [72], the choice of iso-octane, n-heptane and toluene is based mainly on historical reasons, since they have been widely used by the combustion community to represent the chemistry of iso-alkanes, n-alkanes and aromatics. The wide use of TRF surrogates and their capability of describing the main gasoline characteristics is due to the high content of paraffins, iso-paraffins and aromatics in commercial gasolines regardless of their origin, as visible in Table 3.3. Paraffins, although not being as quantitatively present as iso-paraffins and aromatics, deeply influence the combustion-related characteristics of gasoline due to their extremely low octane quality [6] and their high reactivity in low-temperature combustion [88]. While detailed chemical kinetics models [89,90] have been developed to describe the oxidation of the main n-alkanes present in gasoline, n-heptane was historically chosen as a representative of paraffins because of its octane number. N-heptane high concentration in gasoline fuel [74] further consolidated its position as best candidate to represent paraffins (e.g., n-heptane is the second most important compound in ULG95). As clearly visible in Table 3.3, iso-alkanes are the largest hydrocarbon class found in commercial gasolines due to their high octane number [6]. 2,2,4-trimethylpentane (commonly known as iso-octane) is the second most important branched paraffin (11.1 %mol) present in ULG95 and it resembles gasoline combustion to a good degree of accuracy [74]. Iso-octane chemical kinetics models have been extensively studied and validated [91,92,93]. Aromatics are the highest MW hydrocarbons in gasoline fuels, falling in the C_6 to C_9 carbon number range [6]; they are a major component in commercial gasolines, as confirmed by the dataset reported in Table 3.3. Aromatics are also the class characterised by the highest resistance to auto-ignition. As reported in [6], this is caused by the reactions of resonantly stabilized radicals with other radicals, explaining their low reactivity. Although aromatics are present in high concentration, their content is limited by regulations typically below 30-35 %vol due to their propensity to increase soot emissions. Toluene is the most predominant aromatic found in gasoline, followed by xylene isomers [6]. In particular, toluene is the main aromatic species (11.7 %mol) in ULG95 gasoline

[65]. Chemical kinetic models of toluene have been extensively validated against auto-ignition experiments [57,58,59,69,94,95,96]. Historically, oxygenated compounds such as methyl t-butyl ether ($MTBE$), ethyl t-butyl ether ($ETBE$), t-amyl methyl ether ($TAME$), diisopropyl ether ($DIPE$), methanol, ethanol and t-butanol were introduced to improve the octane rating of crude oil [65]. Ethanol is by far the most widespread oxygenated species used in commercial gasoline, as shown in Table 3.1, and it is the second for presence in ULG95 gasoline (30% mol). Ethanol combustion characteristics have been widely studied [52,97,98,99] and a wide number of kinetics models have been formulated [100,101,102,103]. A surrogate based on the pure components chosen so far is often named $ETRF$ (Ethanol $+TRF$). Several chemistry-based and $3D$-CFD modelling studies reported the benefits of using $ETRF$ surrogates in combustion and knock simulations [44,45,79]. The addition of further compounds to the surrogate palette must be carefully evaluated, introducing components with physical and chemical properties complementary with those previously added. In other words, surrogates belonging to hydrocarbon classes not yet represented in the palette showing combustion-relevant characteristics not properly modelled by an $ETRF$ surrogate must be identified. As reported in [87], gasoline composition has a significant impact on its combustion behaviour. Moreover, as suggested in [58], targeting properties such as $EPIONA$ allows an accurate prediction of ρ and LHV. Therefore, other two compounds, representing naphthenes and olefins, are added to the surrogate palette. Naphthenes, also known as cycloalkanes, may constitute a significant portion of the hydrocarbons in commercial gasolines, as visible in Table 3.3. Their concentration is, however, usually limited by their high sooting tendency [104,105,106,107], mainly due to sequential dehydrogenation at high temperature pyrolytic conditions [6]. Typical naphthenes found in gasolines are in the C_5 to C_8 range and include species such as cyclopentane, cyclohexane, methyl cyclopentane, methyl cyclohexane and dimethyl cyclohexane isomers [6]. Quantitatively, cycloalkanes in ULG95 are almost exclusively made of cyclopentane (8.5%mol) and cyclohexane (0.9%mol), although a large variance is experienced on cyclic paraffins statistics over different seasons [65]. These two compounds are those for which most of the kinetic mechanisms have been studied [74], due to their simplicity. Several chemical kinetics studies were validated based on experiments carried out for cyclopentane in different reactors [102,105,106,107,108], although some of the mechanisms need further improvements due to their unreliability and inaccuracy [101]. Since cyclopentane is the main representative and it has the highest octane rating in the class it is chosen as the best candidate to represent naphthenes in the surrogate palette. Olefins are usually a minor species in commercial gasolines due to their poor oxidative stability [6], although some commercial gasolines (e.g. CNPC#92 Chinese gasoline) might contain a concentration higher than the average. Most of the hydrocarbons belonging to this chemical family are found in the C_5-C_6 range [65,74]. The most important olefins in ULG95 are 2-methyl-2-butene (1.7%mol) and 1-pentene (0.9%mol). The presence of double covalent bonds in olefins molecular structure is the reason for their high octane numbers [6]. Since 1-pentene is characterized by lower octane numbers ($RON = 90.9$, $MON = 77.1$ [112]) compared to 2-methyl-2-butene ($RON = 97.3$, $MON = 84.7$ [113]), its addition to the surrogate palette counterbalances the high octane numbers of iso-octane, toluene and ethanol. Olefins have also been identified as a key component in determining the octane sensitivity of a fuel [74], being this a characteristics of this specific chemical class [6]. 1-pentene chemical kinetics mechanisms development has been addressed in previous studies [72,114,115]. The previous digression on the properties of the different hydrocarbon classes and the choice of suitable compounds, representative for each class, was carried out with the main aim of targeting the physico-chemical ignition characteristics of a commercial gasoline. A similar approach was presented in previous works [55,65,71,72,73,87]. Unlike the previous works, the aim of the present study is to formulate gasoline fuel surrogates able to represent also flame propagation characteristics of a commercial gasoline. To a certain extent, pure compounds included in the palette should be representative for the flame propagation characteristics of each class. In a previous work [50], measured s_L of 45 hydrocarbons in a constant volume vessel at elevated temperature and

pressure were reported. This study is useful to determine whether the previously chosen compounds are able to represent the flame propagation characteristics of each hydrocarbon classes, over a wide carbon number (e.g. C_5 to C_8 for cycloalkanes). In [50] hydrocarbons were tested at 3.04 bar and 450 K over $\phi = 0.5{:}\,1.3$ as reference condition. N-alkanes, iso-alkanes and cyclo-alkanes exhibit a relative independence of peak s_L on the carbon number in the range (C_5 to C_8), therefore iso-octane, n-heptane and cyclopentane can be considered as representative for their hydrocarbon classes. In terms of ranking, linear alkanes exhibit the highest s_L while branched alkanes the lowest. Cycloalkanes show intermediate values for s_L, thanks to the methyl substitution, which leads to a slight increase in speed compared to the branched alkanes [50]. In terms of quantitative results, the three classes exhibit very similar values in the lean to stoichiometric region and the highest difference is spotted in the rich region. Around equivalence ratio $\phi = 1.3$, the relative difference between the slowest (iso-alkanes) and fastest class (n-alkanes) is around 10%. In conclusion, although the difference in the molecule structure influences the flame propagating characteristics, the three classes considered have similar s_L at the sample condition analysed. In particular, n-heptane is faster than cyclopentane, which is faster than iso-octane. Conversely, s_L for alkenes is known to be higher than that of the corresponding alkanes. In [50] different alkenes in the C_2-C_5 were tested, showing a much higher s_L dependence on the carbon number. As a general trend, molecules with lower carbon number are faster burning. Although this evidence questions the possibility of representing s_L of alkenes with a single pure compound, it must be underlined that most of the alkenes in commercial gasolines belong to C_5 class [65]. Measurements [50] for 1-pentene, cyclopentene, 2-pentene, 2-methyl-2-butene and 2-methyl-1-butene locate the highest differences in the rich region. The highest difference between 1-pentene and 2-methyl-2-butene is approximately 17% for $\phi = 1.1$, with the former faster than the latter. At this point, 1-pentene is a reasonable candidate to represent alkenes propagating characteristics, being its chemistry more widely studied. Unlike the previous hydrocarbon classes, s_L of aromatics strongly depends on the decomposition pathways rather than on the molecular structure. In particular, s_L is strongly reduced upon sequential methyl addition [50]. In fact, as shown in [50], the fastest aromatic tested (benzene) is 35% faster than the slowest one (m-xylene) for $\phi = 1.1$. In this case, the choice of toluene as a representative for the aromatics is legitimated by the fact that it lies exactly between benzene and m-xylene in the experiments [50]. Moving to oxygenates, only three compounds are tested in [30]: Ethanol, Anisole and $MTBE$. As clearly visible in Table 3.1, most of current commercial gasolines are doped with either Ethanol or $MTBE$. This choice might have a non-negligible effect on the flame propagation characteristics due to the differences observed in [50], where Ethanol is approximately 20% faster than $MTBE$ around $\phi = 1.1$. It is therefore important to include in the surrogate palette the same oxygenated compound present in the reference gasoline. In the case of ULG95, ethanol is the main oxygenate and its choice is in line with the previous considerations. The final surrogate palette is therefore composed by the six hydrocarbons reported in Table 3.4, together with their reference properties.

Class	**Oxygenates**	**Paraffins**	**Iso-paraffins**	**Olefins**	**Naphtenes**	**Aromatics**
Compound	**Ethanol**	**n-Heptane**	**Iso-octane**	**1-Pentene**	**Cyclopentane**	**Toluene**
Formula	**C2H5OH**	**C7H16**	**C8H18**	**C5H10**	**C5H10**	**C6H5CH3**
$\boldsymbol{\rho}\ [\boldsymbol{kg/m^3}]$	785.0	684.0	692.0	641.0	751.0	867.0
$\boldsymbol{T_b}\ [\boldsymbol{K}]$	351.52	371.57	372.15	304.00	322.00	383.75
$\boldsymbol{LHV}\ [\boldsymbol{kJ/kg}]$	26800.0	44566.0	44427.0	45031.0	44636.0	40589.0
$\boldsymbol{MW}\ [\boldsymbol{g/mol}]$	46.07	100.2	114.23	70.135	70.135	92.14
$\boldsymbol{RON}$ [-]	108.0	0.0	100.0	90.9	101.6	120.0
$\boldsymbol{MON}$ [-]	90.0	0.0	100.0	77.1	84.9	103.5

Table 3.4. Properties of pure compounds constituting the surrogate palette.

⎔ 3.1.3 Fuel Surrogates Formulation Methodology

In this section, the fuel surrogate formulation methodology is discussed in detail. Although ULG95 gasoline is targeted for the scope of the present thesis, the methodology has general validity and it can be applied, in principle, to target any commercial gasoline. While undertaking a gasoline fuel surrogate formulation, particular care is needed to determine which key properties of the real fuel need to be targeted. While some properties are specifically related to specific CFD applications for which the surrogate is formulated (e.g. spray modelling, combustion modelling, soot modelling, etc.), others are usually considered fundamental for the fuel description due to their simultaneous influence on several processes. Many authors agree that targeting H/C is essential to correctly describe s_L [69,84], adiabatic flame temperature T_f [72,87], heat of combustion [65,72,87], α_s [65,87], ρ [65], MW [65] and boiling point T_b [65]. Therefore, as suggested by Pera et al. [62], H/C is hereafter directly targeted to match the previously underlined properties. O/C is also included as a target in order to extend the validity of the methodology to highly oxygenated fuels, for which O/C is mandatory to estimate α_s. RON and MON, therefore the auto-ignition characteristics. In [65] Pera et al. proposed a simple approach to formulate multicomponent fuel surrogates matching $H/C,\ O/C,\ RON$ and MON. Once these properties of the targeted gasoline are known, a set of equations is needed to estimate the surrogate ones. In particular, a reliable estimation of RON and MON is a non-trivial task considering that, as reported in many studies [65,116,117,118,119], a non-linear dependence of the Octane Numbers (ON) of a mixture based on the ON of the pure compounds exists, especially if ethanol is included in the surrogate palette. This well-known behaviour is due to synergistic and antagonistic effects between intermediate species generating in the oxidation pathways of the pure compounds [65]. The linear by volume combination of compounds ON may not be the most accurate model to represent the blend octane numbers [116]. Different correlations have been proposed to estimate ON of blends, including non-linear correlations based on a fitting procedure [116,118,119] and models based on a linear by volume weighting of the compounds multiplied by constants for each chemical family [117]. While non-linear blending models better describe real interactions between compounds arising during blending, their main limitation is the higher degree of complexity introduced while solving non-linear equations. With the aim of retaining a set of linear equations, the linear by mole fraction weighting approach proposed in [65] is used in the present study. Despite its very simple form, this approach was proven to be almost as accurate as the non-linear approaches proposed in [116,117]. The set of equations in Eq. 3.1-3.2-3.3-3.4 is therefore used in the present study, as suggested in [65,87].

$$H/C_{blend} = \frac{\sum_{i=1}^{n} x_i H_i}{\sum_{i=1}^{n} x_i C_i} \tag{3.1}$$

$$O/C_{blend} = \frac{\sum_{i=1}^{n} x_i O_i}{\sum_{i=1}^{n} x_i C_i} \tag{3.2}$$

$$RON_{blend} = \sum_{i=1}^{n} x_i RON_i \tag{3.3}$$

$$MON_{blend} = \sum_{i=1}^{n} x_i MON_i \tag{3.4}$$

where x_i, H_i, C_i are the mole fraction of the i^{th} component, the number of hydrogen and carbon atoms in species i and n is the number of compounds used in the blend. RON_i and MON_i are the properties of the i^{th} component. Finally, a mathematical formulation needs to be introduced in order to estimate s_L of a blend. In [78] Sileghem et al. investigated the possibility of estimating s_L of hydrocarbons mixtures using simple Mixing Rules (MR) based on s_L of pure compounds . In particular, three different MR were found to provide results in reasonable agreement with the experimental measurements: a MR based on pure compounds energy fraction [120], Le Chatelier's energy fraction-based MR [78] and Le Chatelier's mole fraction-based MR [78] based on Le Chatelier's flammability limit MR [121]. Using Le Chatelier's mole fraction-based MR, whose expression is reported in Eq. 3.5, Di Sarli et al. [122] were able to successfully predict s_L of hydrogen-methane premixed flames up to 10 bar and 400 K.

$$s_{L,blend}(\Phi) = \frac{1}{\sum_{i=1}^{n} \frac{x_i}{s_{L,i}(\Phi)}} \tag{3.5}$$

where x_i and $s_{L,i}$ are, respectively, the mole fraction and s_L of the i^{th} component and n is the number of compounds used in the blend. More complex MR have been subsequently developed with the aim of better representing s_L. As demonstrated by Pio et al. [123] and Sileghem et al. [124], flame temperature is the dominant factor on s_L and therefore more complex models, such as the one proposed by Hirasawa et al. [125], are able to obtain a higher degree of accuracy on s_L prediction. Nevertheless, such models are again based on non-linear expressions and a higher number of information is needed as input, such as T_f of individual compounds. In order to provide the simplest tool possible and in view of the good performance exhibited by Le Chatelier's mole-fraction based MR [75,78], this last is used to estimate hydrocarbon blends s_L in the present study. However, it must be underlined that the presented approach can be implemented with any MR if the appropriate solver is adopted. Once a MR is chosen, an appropriate experimental s_L dataset is needed as target. To the author's best knowledge, no experimental values are reported in literature for ULG95 gasoline. The dataset provided by Jerzembeck et al. [75] for a commercial oxygenated $RON95$ gasoline is therefore targeted in the present study. Such dataset includes s_L measurements at 373 K, four different pressure levels (10 bar, 15 bar, 20 bar, 25 bar) and $\phi = 0.7{:}\,0.1{:}\,1.2$, for a total number of 24 values. Such dataset was previously used as validation in other studies focused on fuel surrogate formulation and s_L modelling [59,72,73,81,82] due to the availability of high-pressure s_L measurements, which makes it the dataset closest to engine conditions. From now on, an experimental s_L targeted value, for a generic thermodynamic and mixture quality condition, is represented by $s^*_{L,target} = s^*_{L,target}(p^*, T^*_u, \phi^*, EGR^*)$. Due to the widespread use of TRF gasoline surrogates, the methodology will be firstly presented in its simplest form using a TRF surrogate. Starting from the approach proposed in [65], Eq. 3.1-3.2-3.3-3.4 can be considered in the form of a linear system to be solved targeting ULG95 gasoline properties: H/C_{ULG95}, O/C_{ULG95}, RON_{ULG95}, MON_{ULG95}. Obviously, the condition expressed in Eq. 6 must be introduced to ensure that total molar fraction equals unity.

$$\sum_{i=1}^{n} x_i = 1 \tag{3.6}$$

While considering a TRF surrogate, a linear system in its classic form can be easily solved targeting three selected properties, as reported in [65]. Since the constraint in Eq. 3.6 is mandatory, only two properties can actually be targeted. Due to the previous considerations, H/C_{ULG95} is necessarily included in the targeted properties. With a single property left to target, the original aim of matching simultaneously auto-ignition and flame propagating characteristics seems to be prohibitive. The proposed solution is to generate an overdetermined linear system by introducing two additional equations, respectively targeting RON_{ULG95} and $s^*_{L,target}(p^*, T^*_u, \phi^*, EGR^*)$ the linear system is reported in Eq. 3.7.

$$\begin{cases} x_{iso}+x_{nhept}+x_{tol}=1 \\ \dfrac{x_{iso}H_{iso}+x_{nhept}H_{nhept}+x_{tol}H_{tol}}{x_{iso}C_{iso}+x_{nhept}C_{nhept}+x_{tol}C_{tol}}=H/C_{ULG95} \\ x_{iso}RON_{iso}+x_{nhept}RON_{nhept}+x_{tol}RON_{tol}=RON_{ULG95} \\ \dfrac{1}{\frac{x_{iso}}{s^*_{L,iso}}+\frac{x_{nhept}}{s^*_{L,nhept}}+\frac{x_{tol}}{s^*_{L,tol}}}=s^*_{L,target} \end{cases} \tag{3.7}$$

It is possible to notice that MON was not explicitly targeted to avoid an excessive numerical stiffness when solving the equations. The system has four equations and three unknowns and it is therefore over-constrained. Eq. 3.7 can be reformulated to obtain the linear system in the explicit form $\bar{\bar{A}}\bar{x}=\bar{b}$, as in Eq. 3.8.

$$\begin{bmatrix} 1 & 1 & 1 \\ H_{iso}-C_{iso}\frac{H}{C}_{ULG95} & H_{nept}-C_{nept}\frac{H}{C}_{ULG95} & H_{tol}-C_{tol}\frac{H}{C}_{ULG95} \\ RON_{iso} & RON_{iso} & RON_{tol} \\ s^*_{L,nhept}s^*_{L,tol} & s^*_{L,iso}s^*_{L,tol} & s^*_{L,iso}s^*_{L,nhept} \end{bmatrix} \begin{bmatrix} x_{iso} \\ x_{nhept} \\ x_{tol} \end{bmatrix} = \begin{bmatrix} 1 \\ 0 \\ RON_{ULG95} \\ s^*_{L,target} \end{bmatrix} \tag{3.8}$$

where $s^*_{L,iso}$, $s^*_{L,nhept}$, $s^*_{L,tol}$ are iso-octane, n-heptane and toluene s_L values estimated via chemical kinetics calculations at the reference condition targeted. It is straightforward to notice that $s^*_{L,iso}$, $s^*_{L,nhept}$, $s^*_{L,tol}$ are therefore dependent on the chosen chemical kinetics mechanism. Considering that the final fuel surrogate will be used in conjunction with a chemical kinetics mechanism to perform chemistry-based calculations, the same mechanism must be used to estimate $s^*_{L,iso}$, $s^*_{L,nhept}$, $s^*_{L,tol}$ for the sake of consistency. In previous works by the authors, chemical kinetics calculations were used to estimate s_L at engine-relevant conditions, most of which fall well beyond the usual range of validation of the chemical kinetics mechanisms (e.g. 100 bar-1000 K). Due to the unavailability of experiments, the authors estimate s_L using multiple mechanisms to provide a statistical description of s_L. In this way, possible localized non-physical behaviours or issues related to numerical stiffness and instabilities are dampened. The same approach is used hereafter, estimating the s_L of pure compounds with both Andrae's [60,61,62] and PoliMi [63] mechanisms. Such choice does not spoil the validity of the proposed methodology, which can be used in conjunction with any chemical kinetics mechanism(s). The overdetermined linear system in Eq. 3.8 can be solved using a least-square technique, introducing the additional constraint of non-negativity on the unknowns for which the system is solved for. In mathematical terms, this can be expressed as follows:

$$min\left\|\bar{\bar{A}}\bar{x}-\bar{b}\right\|^2 \; with\, \bar{x}\geq 0 \tag{3.9}$$

Solving the system in Eq. 3.8 with the approach proposed in Eq. 3.9, the composition of a ternary fuel surrogate matching H/C, RON and a given $s^*_{L,target}$ is found. In particular, the system in Eq. 3.8 is solved multiple times, targeting 24 different $s^*_{L,target}\,(p^*, T^*_u, \phi^*, EGR^*)$. This procedure is used to extend the capability of the final surrogate to represent flame propagation characteristics on the entire experimental dataset reported in [75]. As a result, 24 TRF surrogate compositions are obtained. Each of these 24 solutions represents fuel surrogate composition ideally needed to match H/C_{ULG95}, RON_{ULG95} and a given $s^*_{L,target}\,(p^*, T^*_u, \phi^*, EGR^*)$, minimizing the deviations from the targeted values gathered in $\bar{b}$. Generally speaking, when a n-component blend is used to target m s_L experimental points, the methodology will produce m solutions in the n-dimensional components space. While a deviation from the aforementioned targets can be accepted, the total molar fraction unity condition must be, necessarily, fulfilled. Therefore, the m solutions $\bar{x}^m$ are normalized to meet such condition, as follows.

$$x_i^{m,norm} = \frac{|x_i^m|}{\sum_{i=1}^{n} x_i^m} \tag{3.10}$$

being $x_i^{m,norm}$ the final i$^{\text{th}}$ component molar fraction content of the n-component surrogate matching $s_{L,target}^m$. Following the rationale proposed in [126], hereafter outlined in detail, the final composition can be found arithmetically averaging the molar fraction content over the m points for each n^{th}component. As a matter of fact, the m $\bar{x}^{m,norm}$ surrogates will exhibit non-negligible differences in terms of composition. In fact, the first two targets are fixed for the whole dataset but a different $s_{L,target}^*\,(p^*, T_u^*, \phi^*, EGR^*)$ is targeted for the m^{th} point. As a last step, the $\bar{x}^{m,norm}$ surrogates need to be reduced to a unique fuel surrogate. In general, these surrogates can be represented as an ensemble of scattered points in R^n. Once again, a least square approach can be used to find a single surrogate minimizing the distance from the $\bar{x}^{m,norm}$ surrogates in R^n. If no weights are applied to the m points, by definition, the point minimizing the distance from each of them is the centroid of the distribution. Therefore, the final composition can be found arithmetically averaging the molar fraction content over the m points for each n^{th}component. In the case of a TRF surrogate yields:

$$x_{iso}^f = \frac{\sum_{i=1}^{m} x_{iso}^{i,norm}}{m} \qquad x_{nhept}^f = \frac{\sum_{i=1}^{m} x_{nhept}^{i,norm}}{m} \qquad x_{tol}^f = \frac{\sum_{i=1}^{m} x_{tol}^{i,norm}}{m} \tag{3.11}$$

A unique TRF surrogate with the final composition $\bar{x}_f = \left|x_{iso}^f \quad x_{nhept}^f \quad x_{tol}^f\right|$ is found. The methodology can be modified based on the specific needs to target different/additional properties or to add a higher number of pure compounds. For example, it can be easily extended to target oxygenated fuels by adding O/C among the targets and introducing ethanol in the base surrogate. Since one additional property is targeted, the resulting linear system, reported in Eq. 3.12, is still overdetermined. It must be underlined that MON is once again not targeted to avoid numerical stiffness while solving Eq. 3.9.

$$\begin{bmatrix} 1 & 1 & 1 & 1 \\ H_{iso} - C_{iso}\frac{H}{C}_{ULG95} & H_{nhept} - C_{nhept}\frac{H}{C}_{ULG95} & H_{tol} - C_{tol}\frac{H}{C}_{ULG95} & H_{eth} - C_{eth}\frac{H}{C}_{ULG95} \\ O_{iso} - C_{iso}\frac{O}{C}_{ULG95} & O_{nhept} - C_{nhept}\frac{O}{C}_{ULG95} & O_{tol} - C_{tol}\frac{O}{C}_{ULG95} & O_{eth} - C_{eth}\frac{O}{C}_{ULG95} \\ RON_{iso} & RON_{nhept} & RON_{tol} & RON_{eth} \\ s_{L,nhept}^* s_{L,tol}^* s_{L,eth}^* & s_{L,iso}^* s_{L,tol}^* s_{L,eth}^* & s_{L,iso}^* s_{L,nhept}^* s_{L,eth}^* & s_{L,iso}^* s_{L,nhept}^* s_{L,tol}^* \end{bmatrix} \begin{bmatrix} x_{iso} \\ x_{nhept} \\ x_{tol} \\ x_{eth} \end{bmatrix} = \begin{bmatrix} 1 \\ 0 \\ 0 \\ RON_{ULG95} \\ s_{L,target}^* \end{bmatrix} \tag{3.12}$$

Similarly, a SEN fuel surrogate can be formulated adding cyclopentane and 1-pentene to the base surrogate in order to add MON to the targeted properties. This allows an enhanced description of fuel reactivity in the Negative Temperature Coefficient region (NTC) when performing ignition delay calculations. The linear system can be written as outlined in Eq.3.13-3.14.

$$\begin{bmatrix} 1 & 1 & 1 & 1 & 1 & 1 \\ H_{iso} - C_{iso}\frac{H}{C}_{ULG95} & H_{nhept} - C_{nhept}\frac{H}{C}_{ULG95} & H_{tol} - C_{tol}\frac{H}{C}_{ULG95} & H_{eth} - C_{eth}\frac{H}{C}_{ULG95} & H_{1pen} - C_{1pen}\frac{H}{C}_{ULG95} & H_{cpen} - C_{pen}\frac{H}{C}_{ULG95} \\ O_{iso} - C_{iso}\frac{O}{C}_{ULG95} & O_{nhept} - C_{nhept}\frac{O}{C}_{ULG95} & O_{tol} - C_{tol}\frac{O}{C}_{ULG95} & O_{eth} - C_{eth}\frac{O}{C}_{ULG95} & O_{1pen} - C_{1pen}\frac{O}{C}_{ULG95} & O_{cpen} - C_{cpen}\frac{O}{C}_{ULG95} \\ RON_{iso} & RON_{nhept} & RON_{tol} & RON_{eth} & RON_{1pen} & RON_{cpen} \\ MON_{iso} & MON_{nhept} & MON_{tol} & MON_{eth} & MON_{1pen} & MON_{cpen} \\ A & B & C & D & E & F \end{bmatrix} \begin{bmatrix} x_{iso} \\ x_{nhept} \\ x_{tol} \\ x_{eth} \\ x_{1pen} \\ x_{cpen} \end{bmatrix} = \begin{bmatrix} 1 \\ 0 \\ 0 \\ RON_{ULG95} \\ MON_{ULG95} \\ s_{L,target}^* \end{bmatrix} \tag{3.13}$$

where:

$$A = s^*_{L,nhept}s^*_{L,tol}s^*_{L,eth}s^*_{L,1pen}s^*_{L,cpen}\ ;\ B = s^*_{L,iso}s^*_{L,tol}s^*_{L,eth}s^*_{L,1pen}s^*_{L,cpen}\ ;\ C = s^*_{L,iso}s^*_{L,nhept}s^*_{L,eth}s^*_{L,1pen}s^*_{L,cpen}$$
$$D = s^*_{L,iso}s^*_{L,nhept}s^*_{L,tol}s^*_{L,1pen}s^*_{L,cpen}\ ;\ E = s^*_{L,iso}s^*_{L,nhept}s^*_{L,tol}s^*_{L,eth}s^*_{L,cpen}\ ;\ F = s^*_{L,iso}s^*_{L,nhept}s^*_{L,tol}s^*_{L,eth}s^*_{L,1pen} \tag{3.14}$$

The resulting compositions for the $ETRF$ and SEN surrogates are computed, based on Eq. 3.12 and Eq. 3.13, respectively, using the same rationale described in [126] and previously outlined.

⬡ 3.1.4 Fuel Surrogates Comparison

In this section, results provided by the methodology are discussed in detail. To provide a general overview of the results, the three surrogate compositions are reported in Table 3.5 and compared with that of ULG95. Similarly, the properties for the surrogates and the ULG95 are reported in Table 3.6 for the sake of comparison.

[%mol]	E (Oxygenates)	P (Paraffins)	I (Iso-Paraffins)	O (Olefins)	N (Naphtenes)	A (Aromatics)
$ULG95$	5.9	10.7	35.1	5.7	10.9	31.7
TRF	-	13.750777	40.980106	-	-	45.269117
$ETRF$	8.255273	13.048068	40.424232	-	-	38.272426
SEN	6.376249	10.452431	24.290356	9.505895	16.517242	32.857827

Table 3.5. Compositions of the targeted fuel [65,76] and surrogates.

	ULG95	TRF	ETRF	SEN
$H/C^{*TRF,ETRF,SEN}$ [-]	1.801	1.781	1.848	1.821
$O/C^{*ETRF,SEN}$ [-]	0.011	0.000	0.012	0.010
α_s	14.254	14.414	14.258	14.257
MW $[g/mol]$	94.3	102.30	98.32	89.68
ρ at 298 K $[kg/m^3]$	749	752.77	748.45	748.02
LHV $[kJ/kg]$	42801	42881	42387	42642
T_b $[K]$	363.52	377.32	374.81	359.82
ACA [-]	6.76	7.410	6.991	6.404
AHA [-]	12.48	13.198	12.921	11.658
AOA [-]	0.08	0.000	0.083	0.064
$RON^{*TRF,ETRF,SEN}$ [-]	95	95.30	95.27	95.37
MON^{*SEN} [-]	85	87.83	87.47	85.39
S [-]	10	7.47	7.80	9.98
AKI [-]	90	91.57	91.37	90.38

Table 3.6. Properties of the targeted fuel [65,76] and surrogates.

Comparing the compositions in Fig. 3.1, it is straightforward to notice that increasing the number of components improves the representation of the reference ULG95 $EPIONA$ spectrum. As expected, TRF and $ETRF$ surrogates are not able to reproduce the hydrocarbon class distribution of the targeted gasoline while SEN surrogate exhibits a good agreement with the experimental composition.

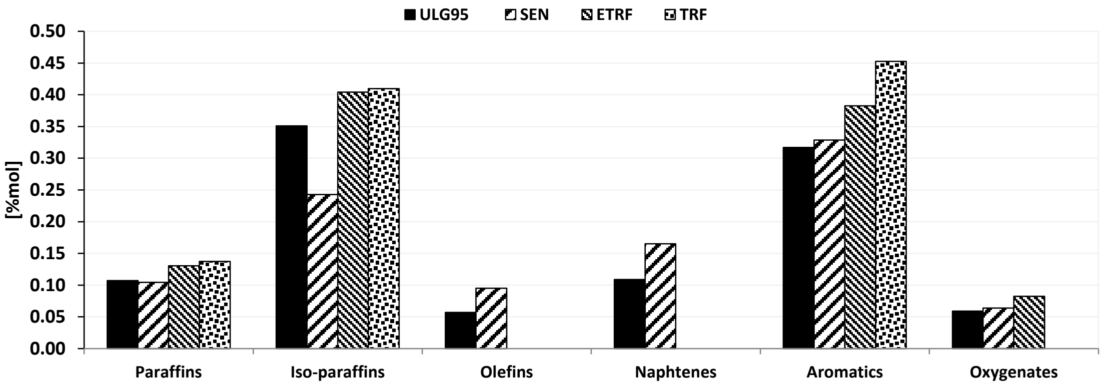

Figure 3.1. $EPIONA$ composition of the targeted fuel and surrogates.

Such observation is well summarized in Fig. 3.2, where the relative error for targeted and untargeted properties is reported for the three surrogates. A double vertical axis layout is used to better represent the results on a single graph. Black solid bars and red lines refer to the left and the right y-axis, respectively. The benefits deriving from an increasing complexity of the fuel surrogate are clearly noticeable. As shown in Fig. 3.2, increasing the number of components, not only enhances the accuracy, but also allows to simultaneously target more properties with a higher degree of accuracy.

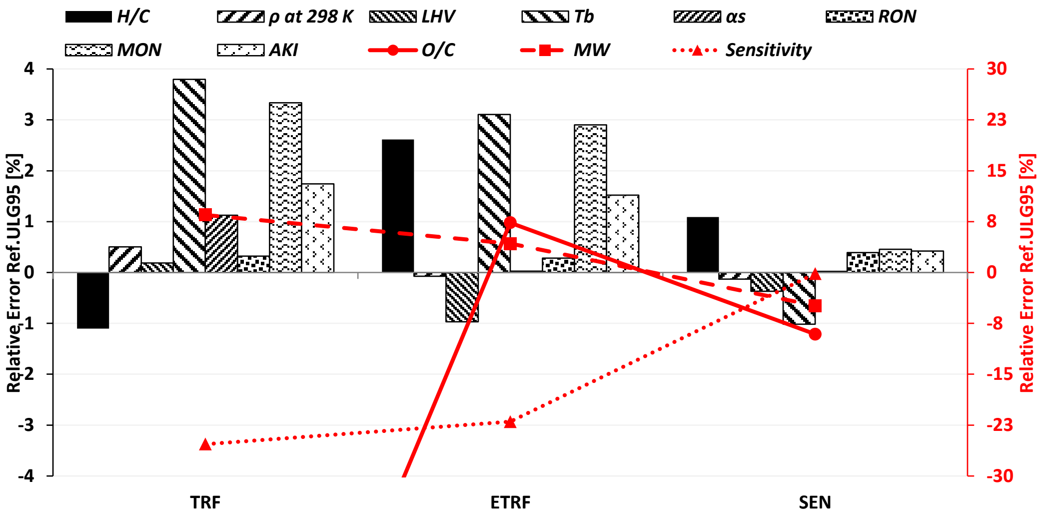

Figure 3.2. TRF, $ETRF$ and SEN properties relative error using ULG95 as reference.

Analysing the results in details, it is possible to state that H/C is satisfactorily matched by all three surrogates. Furthermore, oxygenates are crucial to quantitatively represent nominal ULG95 α_s. In fact, both $ETRF$ and SEN surrogates closely match the target. This aspect is of primary importance since too high deviations from the nominal α_s value might lead to non-negligible errors in the estimation of ϕ, which is in turn a key property used to infer tabulated-based and correlation-based quantities in widely adopted $3D$-CFD modelling approaches. It can be concluded that O/C constitutes a key parameter to properly mimic the chemical properties of a gasoline fuel. For the sake of completeness, it must be underlined that ULG95 α_s value was estimated based on the experimental gross composition. Thanks to the adopted strategy, a reasonable agreement with experimental ρ, MW, LHV and T_b values is obtained, although such properties were not explicitly targeted. This confirms other studies, reporting the possibility of indirectly matching a wide set of properties targeting H/C [65,72,87]. While a fairly good agreement with the experimental values is obtained for ρ and LHV for all surrogates, an increase in surrogate complexity yields a higher accuracy especially for MW and T_b, estimated based on the final compositions using the approach suggested in [65,127]. As a further comment, the very good agreement with the experimental ρ, MW and T_b for SEN suggest that this surrogate might be a good starting point to target additional spray-relevant characteristics such as saturation pressure and distillation curve. Moving to auto-ignition, all the three surrogates properly match the target RON, while only SEN surrogate is able to simultaneously match MON. At a first glance, this result might be erroneously associated to the lack of accuracy on MON for TRF and $ETRF$ surrogates. The addition of MON condition to Eq. 3.8-3.11 would negligibly impact on the estimation of MON, but also decrease the accuracy on the remaining properties due to the increased stiffness deriving from a further degree of overdetermination. The lack of accuracy is due to the impossibility of matching S without olefins and naphtenes. The addition of representative compounds allows to perfectly match S and AKI. As clearly visible in Fig. 3.2, SEN surrogate exhibits a relative error on S lower than unity compared to the other surrogates which both underestimate S by -23% approximately. So far, all targeted properties have been analysed apart from s_L. As previously outlined, Le Chatelier's MR is used to find a suitable composition to match pointwise $s^*_{L,target}\,(p^*, T^*_u, \phi^*, EGR^*)$. In Fig. 3.3, the compositional variation of the 24 solutions, targeting Jerzembeck's dataset [75], is reported component by component for the TRF surrogate.

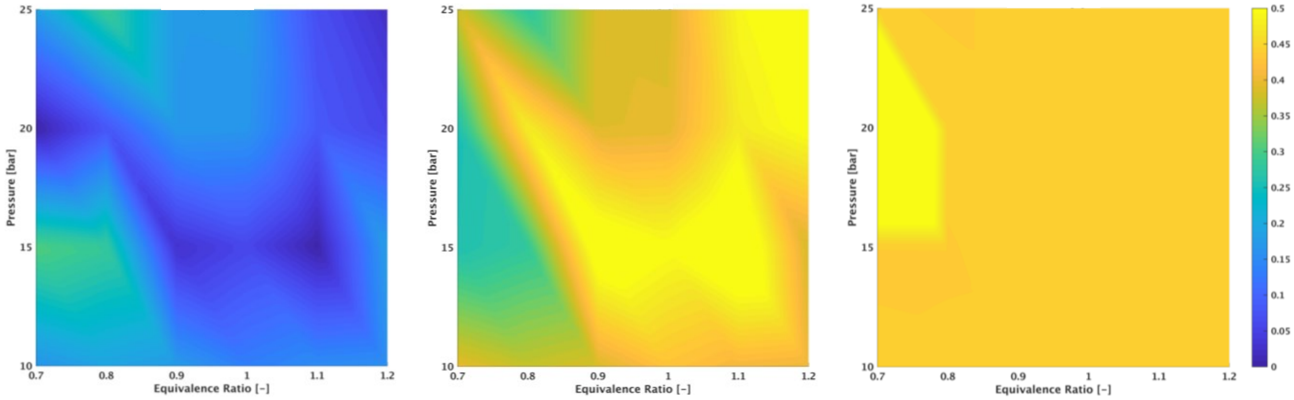

(a) (b) (c)

Figure 3.3. TRF surrogate n-heptane (a), iso-octane (b) and toluene (c) molar fraction [$\%mol$] matching targeted chemical/auto-ignition characteristics (H/C, RON) and pointwise experimental [75] $s^*_{L,target}\,(p^*, T^*_u, \phi^*, EGR^*)$.

Although the compositional variation reported in Fig. 3.3, is portrayed as an interpolated surface, it must be kept in mind that the original map is based on a scatter of points varying in p and ϕ. From one point to another, composition is adjusted, solving Eq. 3.8, with the aim of retaining an acceptable degree of accuracy on the fixed targets (H/C, RON) and simultaneously adapting the blend to match $s^*_{L,target}$. It is noteworthy how n-heptane and iso-octane exhibit a wider span in terms of absolute content over the analysed conditions. Conversely, toluene content is almost constant. This can be explained considering that iso-octane and n-heptane have similar H/C values. Having toluene a quiet different hydrogen and carbon content, it is the key pure compound in a TRF surrogate that allows to match the targeted H/C_{ULG95}. Once toluene content is fixed, n-heptane and iso-octane are varied to match RON_{ULG95} and $s^*_{L,target}$. Being iso-octane RON very close to RON_{ULG95}, it is not surprising that it shows higher concentrations compared to n-heptane. In very lean conditions, it is possible to notice an increased use of toluene compared to iso-octane. Such strategy is followed by the solver to match the experimental $s^*_{L,target}$, which experiences a steep decrease. Toluene concentration is therefore increased due to its lower s_L, in turn increasing the RON of the blend. In order to counterbalance this effect, iso-octane concentration is decreased. The rationale used by the solver while solving Eq. 3.12 is, as shown in Fig. 3.4, similar. The introduction of O/C_{ULG95} as an additional target, pushes the solver to use ethanol in limited but almost

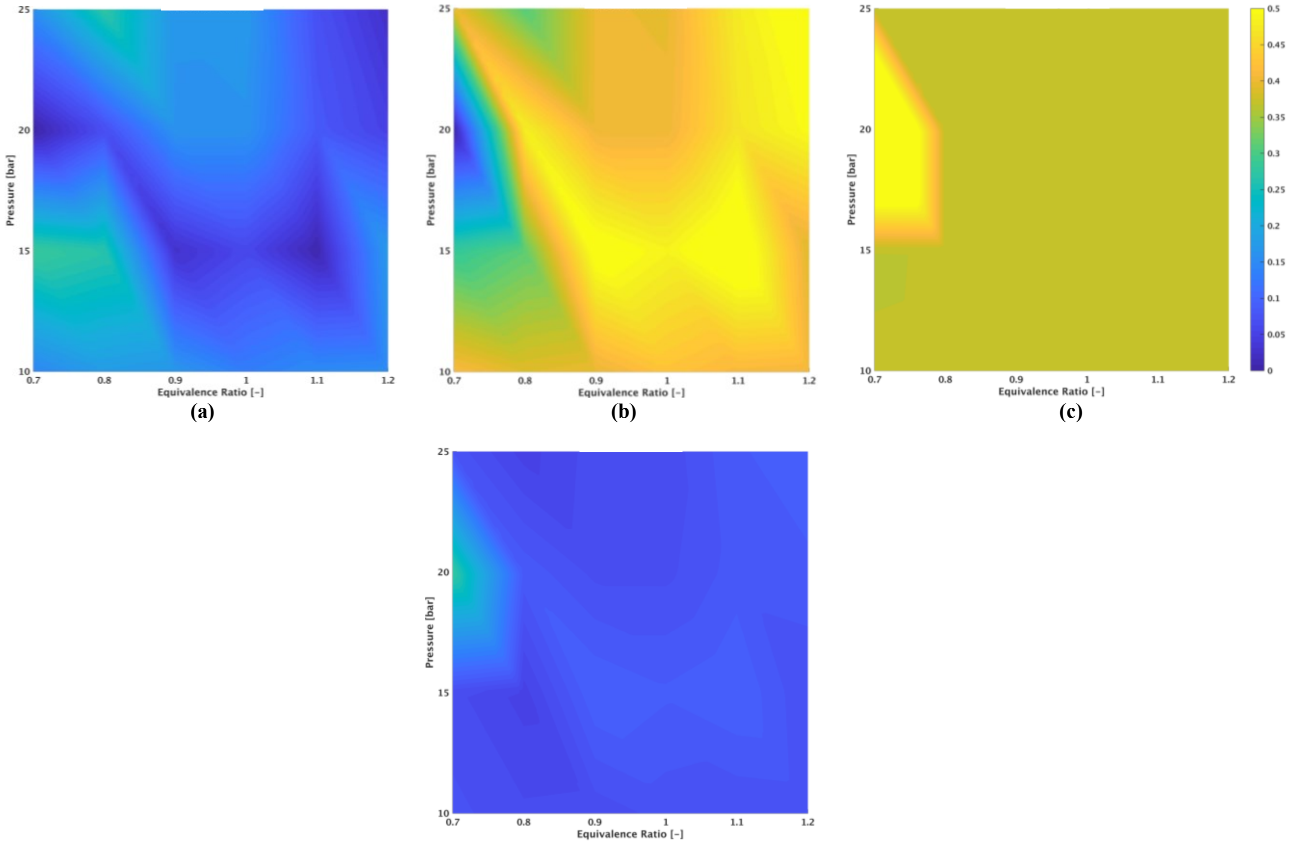

(a) (b) (c)

(d)

Figure 3.4. $ETRF$ surrogate n-heptane (a), iso-octane (b), toluene (c) and ethanol (d) molar fraction $[\%mol]$ matching targeted chemical/auto-ignition characteristics (H/C, RON) and pointwise experimental [75] $s^*_{L,target}$ $(p^*, T^*_u, \phi^*, EGR^*)$

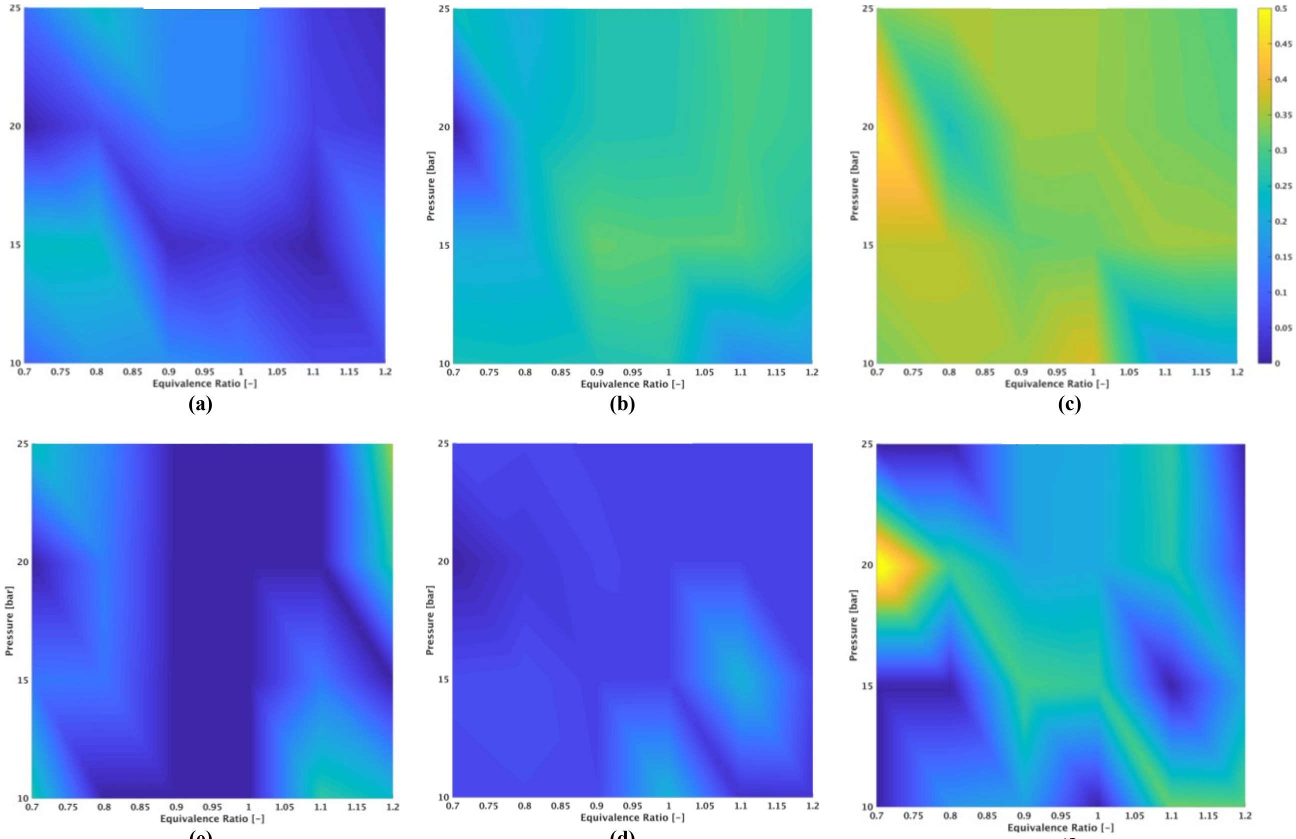

(a) (b) (c)

(e) (d) (f)

Figure 3.5 SEN surrogate n-Heptane (a), Iso-octane (b), Toluene (c), Ethanol (d), 1-Pentene (e) and Cyclopentane (f) molar fraction $[\%mol]$ matching targeted chemical/auto-ignition characteristics (H/C, RON) and pointwise experimental [75] $s^*_{L,target}$ $(p^*, T^*_u, \phi^*, EGR^*)$

constant concentrations, being the only oxygenated compound. Since ethanol has a much higher RON than RON_{ULG95}, toluene (compound with the highest RON) is used with the very same logic previously presented but in slightly lower concentrations. More interestingly, the solver strategy drastically changes while solving Eq.3.13 for SEN surrogate. Maps for SEN surrogate are reported in Fig. 3.5. In this case, the introduction of high sensitivity compounds such as cyclopentane and 1-pentene makes S targeting feasible, adding MON_{ULG95} to the targeted quantities. The key compound, in this sense, is cyclopentane which is characterized by high RON and S. Conversely, in cases where blend RON would be too high using cyclopentane, 1-pentene is used due to its high S and lower RON. This explains the complementary use of cyclopentane and 1-pentene. This strategy does not affect the final H/C since compounds share the same H/C. The introduction of high RON compounds explains the decreased homogeneity of toluene concentrations over the considered conditions. Coherently with $ETRF$ surrogate, ethanol content is almost homogeneous to guarantee O/C_{ULG95} targeting, apart from localized increases needed to act on blend s_L. It is also noticeable how iso-octane concentration is smoothly varied on the map and it is present in lower concentrations compared to TRF and $ETRF$ surrogates. This behaviour is explained by the reduced need of iso-octane to match RON_{ULG95}, which in turn can be exploited to better match point-wise $s^*_{L,target}$. The above considerations are better clarified in Fig. 3.6, in which the point-wise surrogate pattern adopted by the solver are reported in a synthetic form. In particular, dots are coloured differently for each pure compound and their size is proportional to their local use. It is straightforward to notice the enhanced flexibility obtained by the introduction of an increasing number of compounds. In fact, quiet interestingly, SEN surrogate not only locally changes the number of compounds used but also converges towards different patterns based on the local condition.

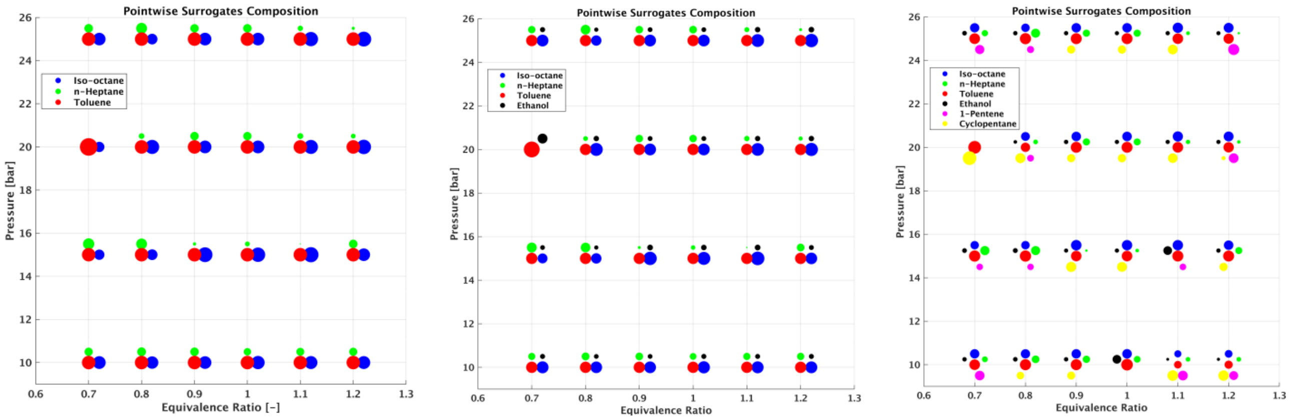

(a) (b) (c)

Figure 3.6 TRF (a), $ETRF$ (b), SEN (c) pointwise surrogate composition. Dots size is proportional to their concentration.

The authors would like to emphasize that the proposed approach is used to quantitatively estimate individual compositions matching the local targeted conditions, while the need for a unique final composition requires the application of a further least-square approach [126]. For this reason, in the next paragraphs, the final TRF, $ETRF$, SEN surrogates are compared with s_L and τ_{ig} experimental data to validate the methodology using DARSv2019.1 chemistry solver.

⬡ 3.1.5 Laminar Flame Speed Validation

In order to validate the methodology, three validation steps are presented. Firstly, the possibility of matching s_L using a synthetic approach is discussed. Secondly, the ability of the final surrogates to effectively match the targeted values is demonstrated. As a last step, the ability of the surrogates to effectively represent the propagation characteristics of a $RON95$ oxygenated gasoline is proven performing a blind test on another s_L experimental dataset. Concerning the first validation step, individual Le Chatelier's MR-based predictions through the solution of the linear systems are reported, with cross-shaped dots, in Fig. 3.7 a-d, Fig. 3.7 e-h and Fig. 3.7 i-l for TRF, $ETRF$ and SEN surrogates respectively.

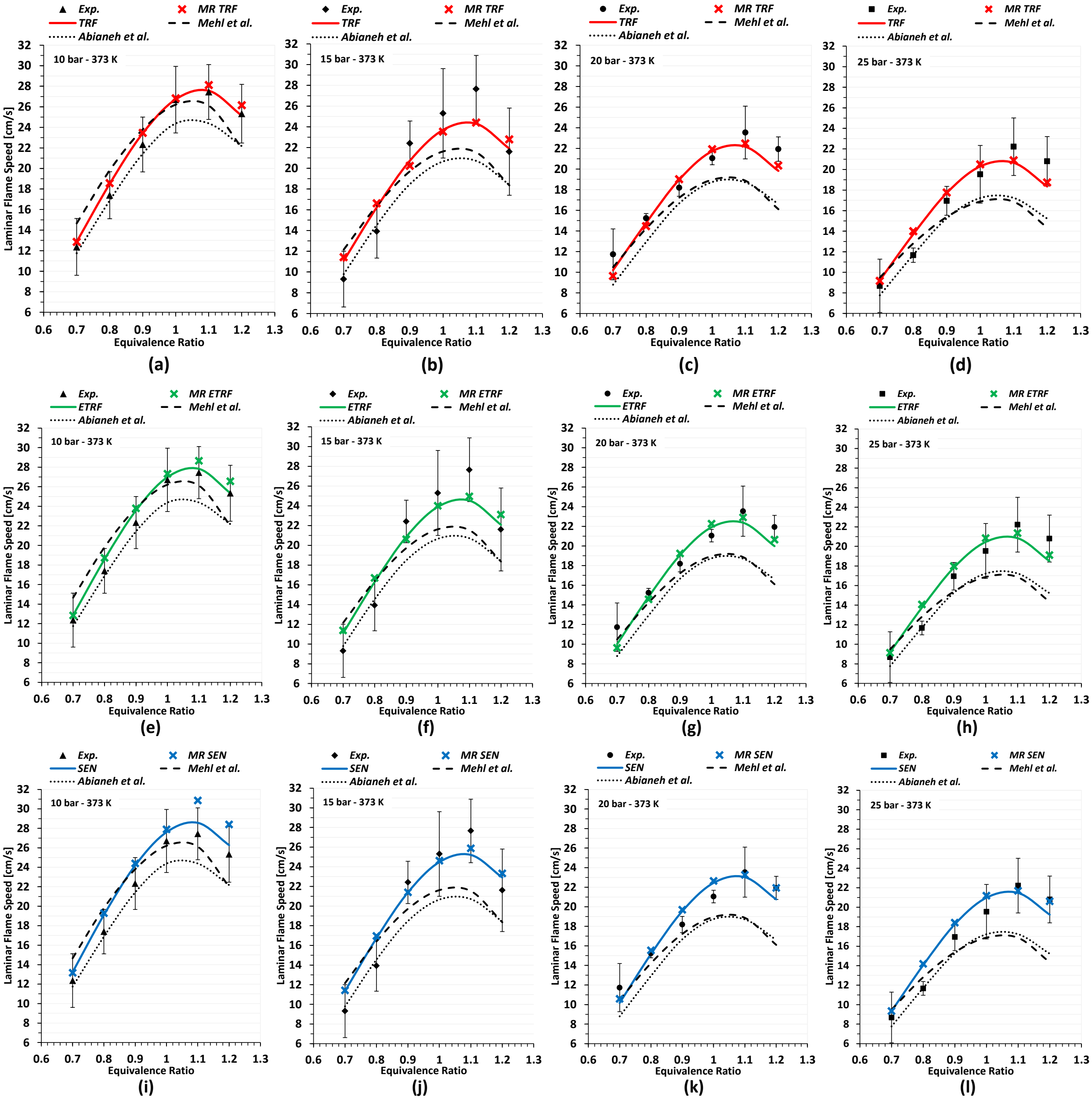

(a) (b) (c) (d)

(e) (f) (g) (h)

(i) (j) (k) (l)

Figure 3.7 TRF (a-d), $ETRF$ (e-h) and SEN (i-l) s_L predicted by Le Chatelier's MR (coloured dots) and chemistry-based simulations results (coloured solid lines) against experimental data from [75] (black dots) and chemistry-based simulations results reported in [72,73] (dashed lines).

As visible, the point-wise compositions accurately match the targeted conditions for all three surrogates. As expected, TRF, $ETRF$ and SEN estimated s_L exhibit small deviations, on equal target $s^*_{L,target}$, due to differences in the base surrogate palettes. Generally speaking, the increase in surrogate complexity allows the solver to improve the prediction of $s^*_{L,target}$ for rich mixtures. As for the second validation step, $1D$ freely propagating simulations results using the final resulting surrogates reported in Table 3.5 and the chosen mechanisms [57,58,59,60] are reported in the same Fig. 3.7 a-l using continuous solid lines. As clearly visible, results are in very good agreement with the individual MR-based estimation. Moreover, the SEN surrogate allows to slightly better match the experiments in the rich region, as visible in

Fig. 3.7 (i-l). For the sake of completeness, results obtained in previous studies [72,73] are added as dotted lines. The exhibited s_L underestimation in the rich mixture region might be related to the missing evaluation of compositional effects on propagation characteristics, explicitly pointed out as a strong limitation in [6]. It is therefore possible to conclude that the proposed methodology is able to improve the formulation of fuel surrogates adding propagation characteristics among the target. Finally, TRF, $ETRF$ and SEN flame propagation characteristics are tested on the experimental dataset presented in [79] by Di Lorenzo et al. In this study, the authors tested a European oxygenated gasoline named B71 188 ESSH EURO 5 and an ETRF surrogate, hereafter named ETRF-B71, specifically conceived to represent the flame propagation characteristics of the actual fuel. Since B71 188 ESSH EURO 5 and ULG95 share very similar properties, as reported in Table 3.7, the experimental dataset [79] constitutes a solid database to perform a blind test and further assess the validity of the proposed methodology.

	RON	***MON***	**ρ [kg/m^3]**	**Oxygenates [%v/v]**	**Aromatics [%v/v]**	**Olefins [%v/v]**
ULG95	95	85	749	4.7	31.2	4.8
B71 188 ESSH EURO 5	96.6	86.2	753	5.0	33.7	6.2

Table 3.7. Properties and partial composition for the reference commercial gasolines in [79] and for the present study.

Mixture quality sweeps are provided for $\phi = 0.8 \div 1.4$ and EGR =0%, 10%, 20%. EGR sweep is particularly interesting to evaluate the capability of fuel models to quantitatively mimic real fuel sensitivity to increasing dilution rates. $1D$ freely propagating simulations results are summarized in Fig. 3.8.

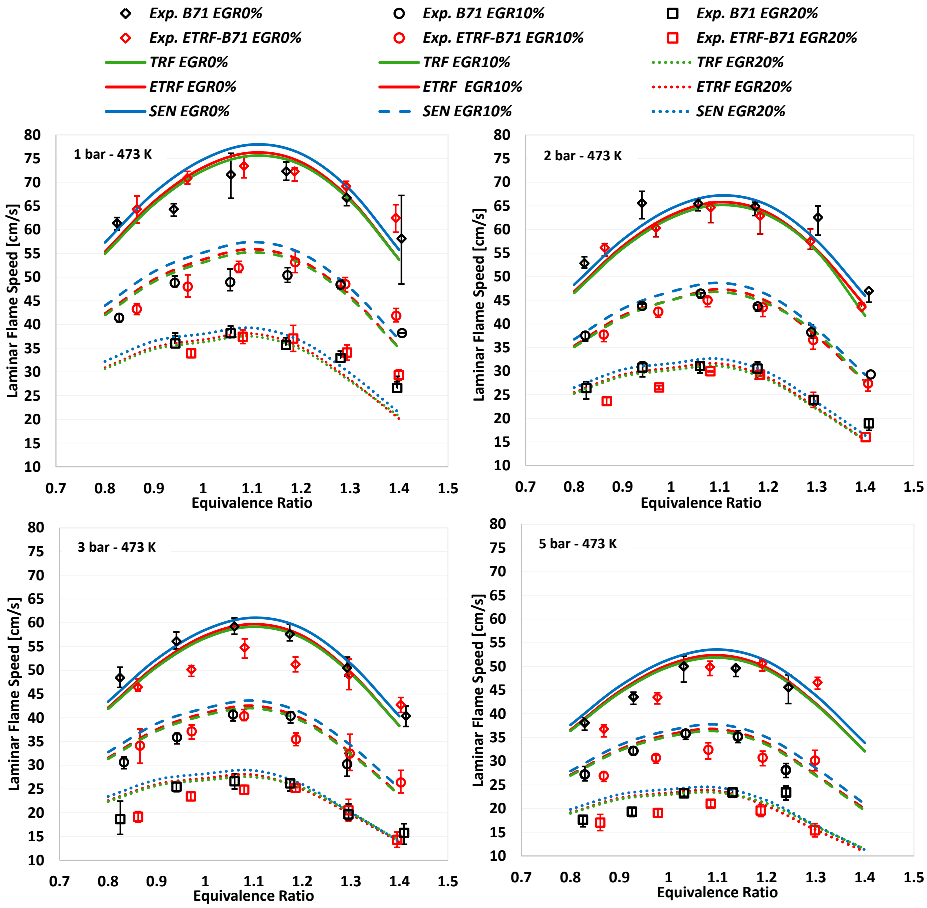

Figure 3.8 Comparison between chemistry-based s_L predicted by 1D simulations performed using the generated TRF (green lines), $ETRF$ (red lines) and SEN (blue lines) surrogates and measured s_L from [79] for B71 188 ESSH EURO 5 commercial gasoline and its surrogate ETRF-B71 proposed in [79].

To enhance readability, B71 188 ESSH EURO 5 is hereby referred to as B71. Generally speaking, all the three formulated surrogates are able to quantitatively predict the propagation characteristics of $RON95$ E5 commercial gasoline investigated in [79]. Apart from a slight s_L overestimation at the lowest pressure level (e.g. 1 bar), the proposed surrogates well predict B71 propagation characteristics in terms of both peak velocity in undiluted conditions (e.g. 3 bar-$EGR0\%$ dataset) and dilution effect on velocity decrease. This further validation step significantly increases the solidity of the proposed approach since, conversely from Jerzembeck's [75], the target s_L does not share any information with the surrogate formulation process.

⬡ 3.1.6 Ignition Delay Validation

To fully validate the methodology a further step is needed. In particular, attention is now shifted to evaluate the capability of the surrogates to match the auto-ignition behaviour of a $RON95$ gasoline characterized by a sensitivity around $S = 10$. As reported by Pera et al. [65], no ignition delay experiments specifically carried out for a fully consistent European gasoline are available in literature. However, a recent study [52] explored the oxidation behaviour of two oxygenated gasolines and the variation of fuel reactivity with molecular composition. The certified gasolines were supplied by Coryton Advanced Fuels and Haltermann Solutions. Their partial compositions and properties are reported in Table 3.8 and compared with ULG95.

	Haltermann	**Coryton**	**ULG95**
RON	91	97.5	95
MON	83.4	86.6	85
S	7.6	10.9	10
H/C	1.97	1.776	1.801
E (Oxygenates) [%mol]	16.8	8.2	4.7
P (Paraffins) [%mol]	12.2	10.1	10.7
I (Iso-paraffins) [%mol]	26.1	31.9	39.8
O (Olefins) [%mol]	6.3	11.2	4.8
N (Naphthenes) [%mol]	15.2	5.0	8.8
A (Aromatics) [%mol]	22.7	33.6	31.2

Table 3.8. Properties and compositions for Haltermann and Coryton gasolines tested in [52] and ULG95 gasoline [65,76] targeted in the present study.

As visible, the two gasolines not only have different RON but also different S. In particular, ULG95 exhibits properties similar to Coryton gasoline, despite a slightly lower RON. Fuels reactivity was tested in [52] via Shock-Tube (ST) and Rapid Compression Machine (RCM) measurements over a wide range of T_u = 650-1250 K, p = 10-40 bar and ϕ = 10-40 bar. Since surrogates were generated using a simple MR to estimate RON/MON, this dataset constitutes the key to quantitatively prove that the reactivity of the proposed surrogates is consistent with the one of the targeted fuel. Furthermore, low temperature range measurements give the possibility to evaluate the specific behaviour of SEN surrogate in the NTC region and generally at low temperatures, in view of the introduction of olefins and napthenes and the related higher S. While measurements were performed in ST and RCM, ignition delay calculations are performed in this work using Constant Volume (CV) reactors only due to the unavailability of geometrical parameters and boundary conditions characterizing the RCM used in [52].

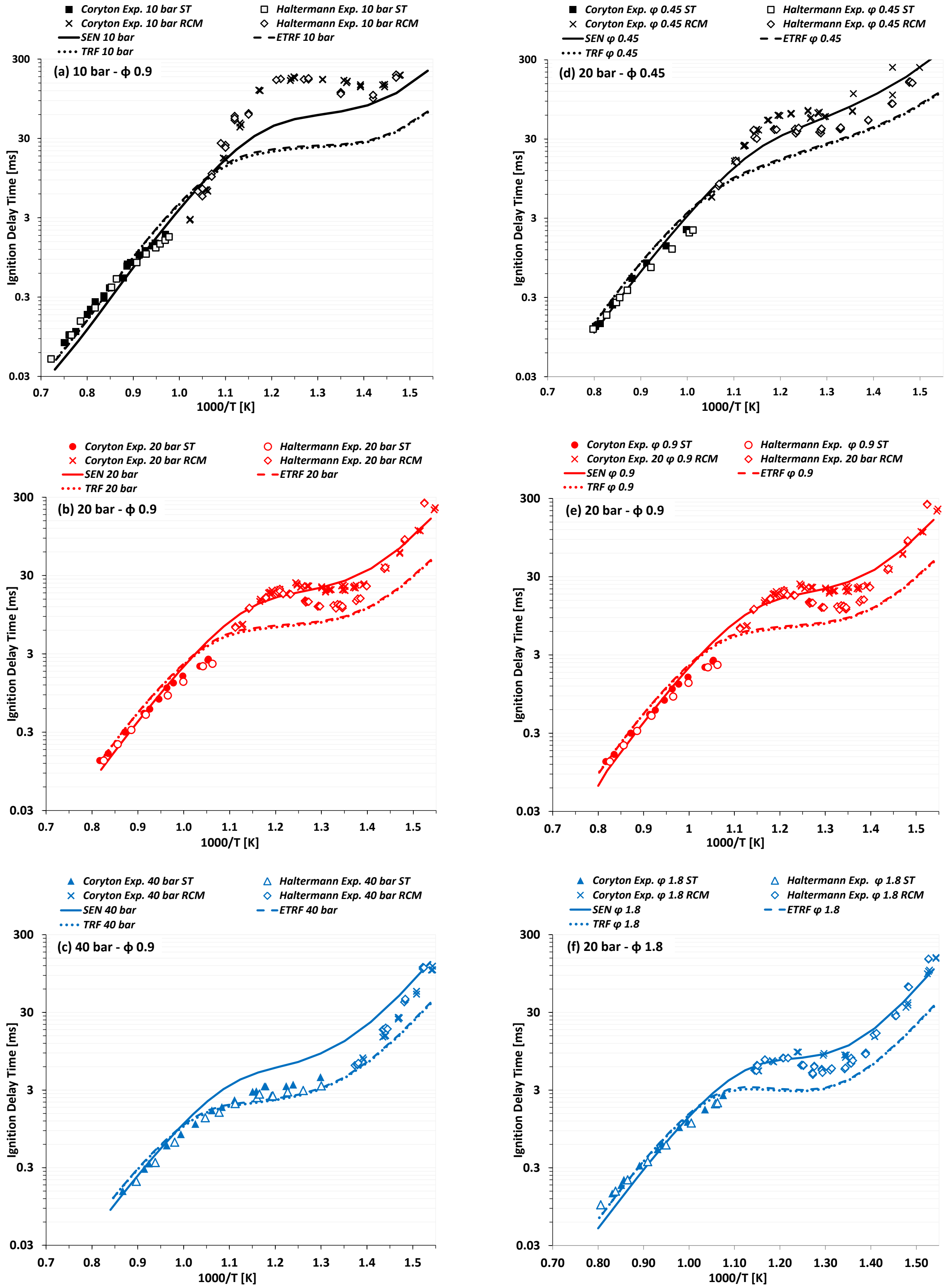

Figure 3.9 CV simulations results carried out with TRF, $ETRF$, SEN surrogates and PoliMi mechanism (dotted lines) compared with ST and RCM experimental data for (a) 10 bar-ϕ 0.9 (b) 20 bar-ϕ 0.9 (c) 40 bar-ϕ 0.9 (d) 20 bar-ϕ 0.45 (e) 20 bar-ϕ 0.9 (f) 20 bar-ϕ 1.8 conditions. Experimental data from [52] are reported with dots for Coryton and Haltermann gasolines.

The use of CV reactors is consistent with the thermodynamic conditions occurring behind the reflected shock generated in ST experiments [52]. Simulations are carried out for three pressure levels $p = 10$ bar, 20 bar, 40 bar and for lean ($\phi = 0.45$), quasi-stoichiometric ($\phi = 0.9$) and rich ($\phi = 1.8$) conditions. $T_u + 400$K is adopted as thresholding condition to estimate the ignition delay. Such criterion is widely used in the industry to infer auto-ignition occurrence. Hydroxyl radical peak concentration was also monitored to track and double-check mixture reactivity. Experimental and simulated values are reported in Fig. 3.9 (a)-(b)-(c) to compare reactivity with increasing pressure at reference $\phi = 0.9$. Focusing firstly on the experimental data, both Haltermann and Coryton gasolines experience an increasing reactivity as pressure increases. At high temperatures ($T_u > 900K$) both fuels exhibit very similar reactivity across the range of conditions [52], with Haltermann fuel being slightly more reactive due to its lower RON. In this temperature range, simulations results are in very good agreement for all three surrogates. Such observation proves that all formulated surrogates show RONs in line with those predicted by the proposed methodology. Since high temperature regions tend to hide the reactivity dependence on RON/MON and composition, the most interesting region to validate the proposed approach is the intermediate temperature range (~700-850 K). In fact, as clearly visible in Fig. 3.9 (a)-(b)-(c), the two tested fuels are characterized by a different reactivity and behaviour in the NTC region. As expected, Coryton gasoline has a lower reactivity, consistently with its higher RON. Most interestingly, Haltermann gasoline exhibits a more pronounced NTC behaviour compared to Coryton gasoline [52], due to its its higher olefinic and naphtenic content, resulting in lower S. Interestingly, the three simulated surrogates predict now largely different reactivities. In particular, TRF and $ETRF$ surrogates share a tendency to overestimate the reactivity at lower pressure levels although perfectly matching τ_{ig} at 40 bar. Conversely, SEN surrogate exhibits a lower reactivity, perfectly matching Coryton reactivity at 20 bar, in agreement with their similar S. Despite minor reactivity misalignments, the proposed SEN surrogate better describes the reactivity dependence on pressure in the NTC region. Moreover, it better matches the reactivity of both tested gasolines in the low temperature region ($T_u < 700K$). In Fig. 3.9 (d)-(e)-(f), a similar comparison is carried out for three different mixture qualities. Consistent considerations can be made for the different temperature regions: all three surrogates are quantitatively able to represent the auto ignition quality of the fuels in the high temperature range.

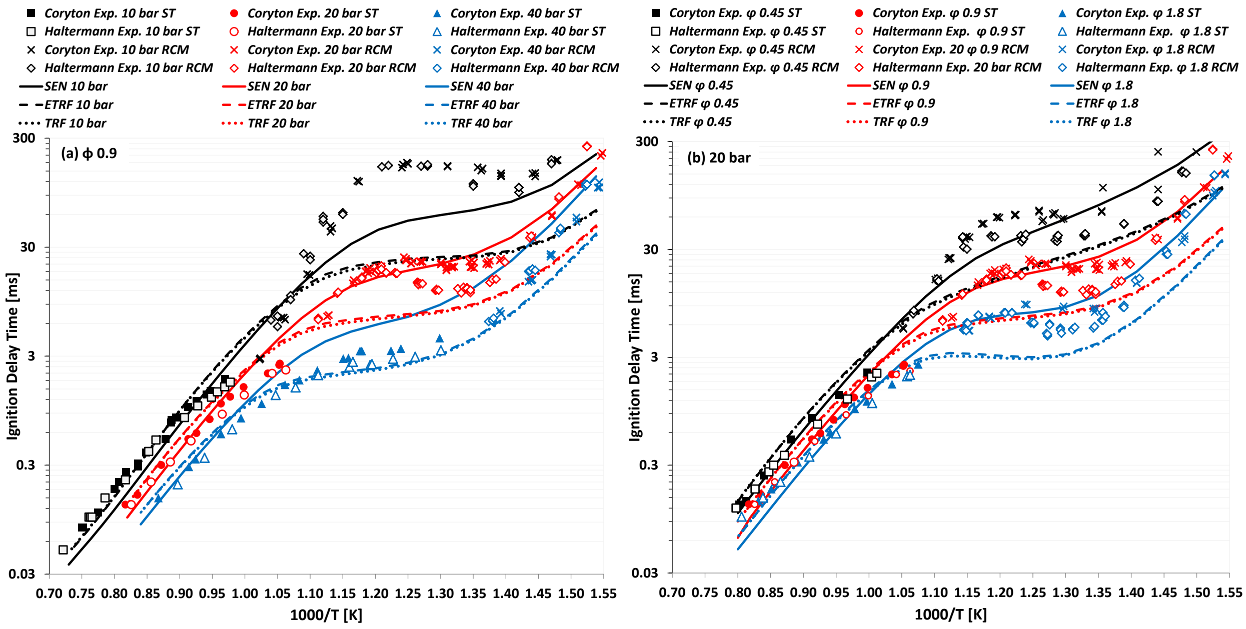

Figure 3.10 CV simulations results carried out with TRF, $ETRF$, SEN surrogates and PoliMi mechanism (dotted lines) compared with ST and RCM experimental data for (a) 10 bar-20 bar-40 bar at ϕ 0.9 and (b) ϕ 0.45- ϕ 0.9- ϕ 1.8 at 20 bar. Experimental data from [52] are reported with dots for Coryton and Haltermann gasolines.

Moving to the intermediate T_u region, the SEN surrogate better matches the fuel reactivity dependence on mixture quality. In particular, it closely resembles Coryton fuel auto-ignition characteristics, due to the similarity of S. Such outcome is of particular interest for engine knock simulations, considering that end-gas region under incipient Knock Limited Spark Advance ($KLSA$) conditions usually exhibits temperature values in the T_u = 800-900 K range. In the low T_u region, SEN surrogate is able to quantitatively match the behaviour of the Coryton gasoline. In order to estimate the potential errors introduced by the proposed fuel models, all results are reported on two separate graphs, in Fig.3.10, summarizing pressure and mixture quality effect. As visible, while all three surrogates are able to correctly match fuel reactivity in the high T_u region, non-negligible deviations arise in the intermediate T_u range if surrogates lack of olefinic and naphtenic content. Both TRF and $ETRF$ surrogates exhibit a mixture reactivity at 10 bar equal to the experimental ones at 20 bar. Furthermore, both TRF and $ETRF$ surrogates overestimate gasoline reactivity over the whole mixture quality range. SEN surrogate shows superior performance to model gasoline reactivity over the investigated p, T_u, ϕ range. This suggests SEN surrogate as the most promising surrogate to represent end-gas reactivity in knock simulations. Based the obtained results, a unique fuel surrogate formulated with the proposed approach can be therefore used for combustion and knock simulations in $3D\text{-}CFD$ simulations.

3.2 Sooting Tendency in Combustion Systems

3.2.1 Importance of Modelling Sooting Tendency

PM emissions is becoming an ever increasing concern for engine manufacturers due to the strong limits imposed by worldwide regulations, especially for Gasoline Direct Injection engines. While pushing the boundaries to find new technological innovations to design more efficient and cleaner engines, fuel impact on engine-out soot emissions has also gained increasing attention by researchers in the engine community. As demonstrated in previous studies, fuel composition plays a key role in determining the extent to which soot is formed during the combustion process. In the attempt of finding new strategies to reduce engine-out emissions and gain a deeper understanding on GDI soot formation root causes, advanced emission models, such as the Method of Moments [46,47] and the Sectional Method [46,47,48,49] have been developed to predict soot formation in ICE and have been applied to GDI engine simulations [128,129]. Soot emission predictions are known to be a non-trivial challenge due to the complexities associated with modelling fuel chemistry and fuel composition [51]. In fact, soot emissions are known to be deeply influenced by engine architecture, operating point and combustion strategy [130,131], as well as by fuel chemical composition and physical properties. On one side, this led to the development of detailed chemical kinetics mechanisms [59,132,133,134] able to predict PAH formation in both premixed and diffusive environments, which are known to be responsible for soot formation by nucleation [47]. On the other hand, in view of the key role played by fuel chemistry, several studies proposed in literature investigated the impact of fuel properties on engine-out emissions, with the aim of providing correlations to estimate fuels physical and chemical properties impact [53,135,136,137,138, 139,140,141,142,143]. The aforementioned studies differ in terms of approach but agree that fuel composition and properties are essential parameters when evaluating soot formation in combustion processes. This is further emphasized by the presence of specific local emission regulations worldwide that require the use of specific certification fuels which must be considered in the engine design [83]. This constitutes a challenging task for Automotive OEMs. As previously pointed out in paragraph 3.1, petroleum-derived fuels are essentially chemically complex mixtures of compounds belonging to different hydrocarbon classes [73] which makes computational studies of their fundamental combustion properties intractable [144]. Therefore surrogates, as the ones formulated in paragraph 3.1.4, are generally used to emulate fuel behaviour [65] and to represent them in computational models [16]. In this scenario, CFD engineers responsible for engine design optimization are requested to evaluate soot emissions produced by the engine when fuelled with commercial gasoline sold in different regions worldwide [83]. Regardless the chosen soot emission modelling approach, either based on tabulated approach or detailed chemistry calculations, there is a need of formulating different fuel surrogates able to mimic sooting tendency (ST) of different commercial gasolines sold worldwide. This is confirmed by McEnally et al. [145], which demonstrated that gasoline sooting behaviour can vary considerably within the range of acceptable compositions and that such variations can be accurately predicted with empirical models and computational simulations. A wide number of studies present in literature experimentally characterized the ST of jet and diesel fuels, proposing surrogates able to mimic their behaviour [144,146,147, 148,149,150]. Conversely, a limited number of studies focused on commercial gasolines and their surrogates [51,145,152]. The lack of comprehensive experimental dataset characterizing the ST of different commercial gasolines hinders the definition of surrogates able to represent them in the CFD framework. As pointed out in [145], accurate gasoline surrogates and validated mechanisms are necessary to enable CFD simulations that can be used to design SI engines optimized for low particulate emissions. The aim of the present paragraph is to provide a relatively simple yet effective methodology able to: 1) estimate the ST of commercial gasolines based on the composition and a set information readily retrieved from fuel suppliers data 2) provide surrogates representing ST and combustion-relevant characteristics of the targeted fuels. In paragraph 3.1.2, Threshold Soot Index (TSI) is investigated as a potential indicator to characterise the compositional effects on soot formation. A TSI-based approach is then introduced to estimate the ST of different European, American and Chinese commercial gasolines from [83]. In paragraph 3.2.4, a modified version of the methodology discussed in paragraph 3.1.3 is presented and exploited to formulate $ETRF$ (ethanol/toluene/n-heptane/iso-octane) surrogates targeting the aforementioned fuels. The choice of including ethanol in the surrogate palette is made to take into account for the influence of oxygenates content on soot formation, widely documented in different studies [153,154,155,156,157,158]. To conclude, a $3D$-CFD engine case is presented in paragraph 3.2.5 to validate the methodology using the Sectional Method model [46,47,48,49] coupled with a constant pressure-based tabulated approach for soot constants. It is noteworthy that the engine case considered is the single-cylinder optically accessible research unit that will be used as final validation, in Chapter 5, of the methodologies discussed in the present thesis. In this paragraph, only the basic details of the CFD methodology used will be presented. A comprehensive discussion on the CFD methodology used is presented in Chapter 5.

3.2.2 Threshold Soot Index as Sooting Tendency Indicator

Methodologies aiming to correlate smoke levels to fuel composition were historically investigated on aircraft engines since soot is reported to affect engine performance and decrease combustor liner lifetime due to the increased heat loading deriving from radiation flux [150]. Smoke Point (SP), defined as the maximum height in millimetres of a smoke-free laminar non-premixed flame [152] with ASTM D1322 standard [159], has been widely used to quantitatively estimate pure compounds ST. In other words, SP is the height of a flame at the point of incipient smoking, occurring when there is too much fuel for the oxygen available [160]. In this sense, at the SP the production of soot is exactly offset by its oxidation [161] and a further increase in fuel amount causes the appearance of the so-called “sooting wings” on the flame sides. ST is then proportional to the inverse of the smoke point [162]. SP-based measurements are affected by well-known drawbacks such as its unsuitability to test gaseous fuels [163] and results dependency on apparatus design [164]. This ultimately led to inconsistencies in the various soot threshold measurements made on identical fuels in different laboratories and under different burning conditions [150]. With the aim of obtaining apparatus-independent soot measurements, Calcote and Manos [165] proposed TSI as universal measure of fuel sooting tendency, defined as in Eq. 3.15:

$$TSI = a\left(\frac{MW}{SP}\right) + b \tag{3.15}$$

where a and b are apparatus-dependent constants, MW and SP are respectively the molecular weight and smoke point of the fuel tested. The introduction of the MW allows to take into account for differences in α_{st} among the compounds. The range of TSI values is artificially assigned from 0 to 100 selecting two representative species as the least and most sooting [162]. Constants a and b are determined by selecting compounds in common with other available datasets, then adjusting with least-squares fitting to minimize the difference of TSI values of individual components from different sources [162]. This procedure is analogous to the one used to determine octane and cetane ratings for fuels in internal combustion engines [144]. As a matter of fact, TSI is valuable for being the first numerical scale for sooting tendencies of pure hydrocarbons which is device independent and inherently determined by a compound molecular structure [144]. The datasets provided by Calcote and Manos [165] and Olson et al. [166] constitutes the most complete TSI collection, comprising approximately 100 hydrocarbons. The other main advantage deriving by the use of TSI is the possibility to estimate a blend ST as a pure compounds TSI linear sum weighted by their molar fractions x_i as shown in Eq. 3.16.

$$TSI_{blend} = \sum_{i}^{n} x_i TSI_i \tag{3.16}$$

where TSI_i is the TSI of the i^{th} pure compound and n is the number of pure compounds used in the blend. The linear correlation in Eq. 3.16 was proposed and validated for diffusive flames by Gill et al. in [150,167]. It must be noted that Gill et al. [150,167] also proposed a MR valid for premixed laminar flames, which is not hereby used due to the very limited number of TSI values available for pure compounds. Yang et al. [149] proved that TSI model correlates very well with fuel hydrocarbon composition over a wide range of fuel samples and yet a very good correlation was found between TSI and actual combustor soot formation over a broad matrix of fuel origins, combustor operating conditions and soot formation parameters. Despite the scaling procedures used by Calcote and Manos [165] and by Olson et al. [166] to minimize differences between sources, TSI data might vary considerably for certain compounds. Moreover, measurements of heavily sooting compounds might be effected by a relevant error due to the very low smoke points which in turn can result in large TSI variations [151]. For the aforementioned reasons, McEnally and Pfefferle [145] proposed the use of the Yield Soot Index (YSI) which is based on Laser Induced Incandescence (LII) intensities, commonly recognized to be proportional to soot volume fraction. Although YSI is proven to have a better accuracy, YSI values have not been measured for many n-alkanes or iso-alkanes which constitute a major part of commercial gasolines [151]. Moreover, YSIs measured for different compounds in [144] correlated well with their corresponding TSIs [151,166] over a large sooting range covering n-alkanes, iso-alkanes, cycloalkanes, single-ring and multi-ring aromatics. This further suggests that using different soot indices will not affect the soot propensity ranking when analysing different gasolines. Therefore, TSI is used as reference index in the present work. Although focusing in particular on surrogates able to mimic commercial gasolines sooting tendency, the proposed methodology is conceived to have general validity and to be potentially applied to other hydrocarbon mixtures such as diesel, marine and jet fuels. Due to the very different hydrocarbon range characterizing each of the previous fuels, different compounds should be used to form the base surrogate palette since ST is proven to be strictly linked to the carbon number [151]. In fact, as carbon number increases and hydrogen to carbon ratio H/C decreases, it is expected that T_f, representing the highest temperature that a combustion process can produce for a specific mixture regardless of the combustion device, raises [168]. As a direct consequence, particles passing through the flames of larger hydrocarbons are exposed to higher temperatures and are therefore more intensely oxidised [148]. For the aforementioned reasons, a correlation is needed to directly estimate TSI based on the molecular structure, in order to compensate for the possible data unavailability for certain compounds. Yan et al. [162] developed a structural group contributions-based methodology able to estimate pure compounds TSI without the need of experimental procedures. As previous studies in literature on the Quantitative Structure-Property Relationships ($QSPR$), the idea of structural group contribution was adopted in [162] to develop a correlation for ST. In particular, Joback's method [169] is adopted in the present study to correlate molecular structure with TSI based on 41 atoms/groups. The polynomial regression model in Eq. 3.17 is exploited in [162] to obtain a correlation using a least-squares algorithm.

$$TSI = a\left(\sum_k (N_k sp_k)\right)^{-1} + b + c\left(\sum_k (N_k sp_k)\right) + \left(\sum_k (N_k sp_k)\right)^2 + e\left(\sum_k (N_k sp_k)\right)^3 + f\left(\sum_k (N_k sp_k)\right)^4 \tag{3.17}$$

where sp_k is the contribution from the k^{th} group identified in the Joback's method [169]. Coefficients a, b, c, d, e, f constitutes the output of the fitting procedure proposed in [162]. A strong correlation (R^2 = 0.989) was found by Yan et al. [162] between the experimental and estimated TSIs, using Eq. 3.17 for different compounds. This confirms the existence of a strong correlation between fuel molecular structure and ST. The correlation in Eq. 3.17 can be used to estimate the TSI of pure compounds present in the surrogate palette for which data are not present in literature.

Blend No.	***n-Heptane* [%v/v]**	***Iso-octane* [%v/v]**	***Toluene* [%v/v]**	***TSI* [-]**	***RON* [-]**
1	0.000	0.000	1.000	44.0	120.00
2	0.167	0.167	0.667	32.1	101.35
3	0.000	0.500	0.500	31.1	112.17
4	0.500	0.000	0.500	27.9	69.55
5	0.333	0.333	0.333	22.7	77.87
6	0.167	0.667	0.167	14.6	87.76
7	0.667	0.167	0.167	10.9	40.64
8	0.000	1.000	0.000	6.7	100.00
9	0.500	0.500	0.000	3.4	47.02
10	1.000	0.000	0.000	2.3	0.00

Table 3.9..TRF blends tested in [160] according to ASTM D1322 standard.

In order to further test the possibility of relying only on Eq. 3.17 rather than on experimental dataset, this approach is tested against the experimental TSI dataset provided in [160] in which the ten different TRF blends, reported in Table 3.9, were tested according to ASTM D1322 standard. It is noteworthy that blends no 1, 8, 9 and 10 are respectively pure toluene, pure iso-octane, a Primary Reference Fuel (PRF) and pure n-heptane. The measured TSIs are reported in Table 3.9 for each blend. Using the methodology proposed in [162] n-heptane, iso-octane and toluene TSIs are estimated using Eq. 3.17. The blends TSI is estimated using the linear mixing rule reported in Eq. 3.16. The comparison between experimental and calculated data is reported in Fig. 3.11. As visible, a very strong correlation exists between the two datasets. The structural group contribution-based methodology proposed in [162] is therefore considered reliable and can be used to effectively estimate TSI of pure compounds and blends without the need of experimental measurements. It must be underlined that both the reference experimental dataset [160] and the correlation used [162] are deemed to be valid for diffusive-like combustion processes. Although fuel composition plays an important role on ST, the extent to which a given fuel system produces soot is also strongly dependent on the type of combustion system (e.g. flame structure) controlling the process and the temperature of the system, as pointed out by Glassman in [170]. While the aim of the present study is to provide a general purpose methodology, the main goal is to estimate and target ST of commercial gasolines to model their propensity to form soot in GDI engines. This technology is known to promote the occurrence of local diffusive-based combustion phenomena deriving from pool fires, retaining a globally premixed-based dominant combustion mode. Since a constant pressure reactor-based tabulated approach is used as preferential approach for GDI soot modelling in the present study, a further validation step is undertaken to investigate whether the TSI-based approach is valid under premixed conditions. This also allows to further widen the validity of the proposed approach, investigating its capability of representing fuels ST independent on the intrinsic nature of the analysed combustion system. In order to do this, a CP reactor-based simulation campaign is carried out, with DARSv2019.1, investigating the ST of the ten blends reported in Table 3.9 at a reference condition $(p = 10\, bar, T_u = 800\, K, EGR = 0\%)$ under a broad range of equivalence ratio values $\phi = 1.0 \div 4.0$. The choice of using CP reactors is done in order to be consistent with the approach used afterwards to generate dedicated soot libraries, which is CP-based. This reference condition is chosen to be representative of a typical GDI cold start catalyst heating operating point which is commonly recognized to be responsible for almost the entire amount of soot emissions in driving cycles [171]. While temperature variation effect on ST is taken into account due to the temperature history taking place in the reactors, which spans from the initial temperature ($T_u = 800$ K) to absolute temperatures T higher than 2000 K, pressure variation and dilution effect are not investigated due to their minor impact on soot formation. The ϕ sweep from stoichiometric to extremely rich conditions allows to investigate the effect on ST of a transition from a mixture quality representative of the average condition experienced by flames in the combustion chamber to ones representative of local rich spots arising from spray-wall interactions. This further validation step has two distinct goals. Firstly, a confirmation that ST ranking observed in the experiments for the investigated blends is retained in chemistry-based simulations. Secondly, a

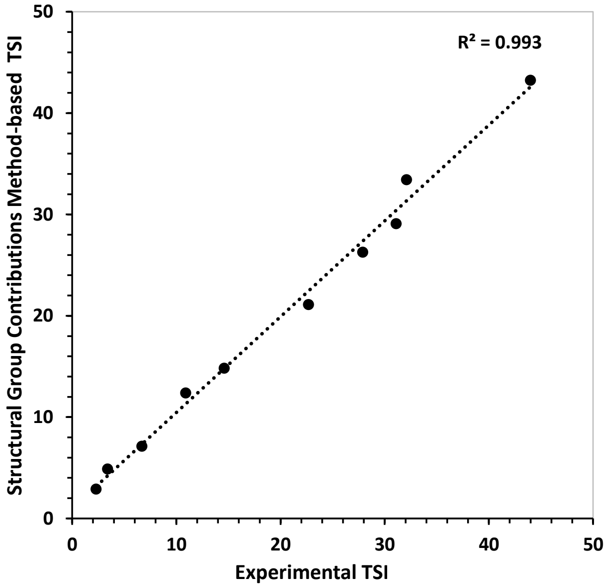

Figure 3.11. TRF blends tested in [160] according to ASTM D1322 standard.

quantitative scaling correspondence between experimentally measured TSIs and amount of soot produced in the numerical domain for a given blend is investigated. In other words, this analysis focuses on determining whether blend characterized by a TSI value twice as high as another one, produces twice the soot amount in a premixed numerical reactor or not. Exploiting the availability of experimental data for different blends, it is possible to neglect possible errors deriving from the use of Eq. 3.16-3.17 investigating the capability of TSI to effectively represent blends different ST in CFD simulations. In order to quantitatively estimate soot formation in $0D$ simulations, a soot model and a validated chemical kinetics mechanism provided with a validated PAH formation sub-mechanism are needed. In order to find a compromise between computational efficiency and accuracy, the Method of Moments [172] is used as reference soot model in constant pressure reactor simulations. The model describes the evolution and characteristics of the $PSDF$ generated in a combustion system under sooting conditions introducing a number of transport equations for the moments, whose generic form is reported for the r^{th} moment in Eq. 3.18:

$$M_r = \sum_{i=1}^{\infty} i^r N_i \tag{3.18}$$

where N_i is the number density of soot particles of size class i, with a mass $m_i = i\, m_1$, being m_1 the mass difference between two adjacent soot size classes, which is normally set to two carbon atoms. Hereafter, only the first two moments M_0 and M_1 are used in reactor-based calculations, since previous studies [46,47] demonstrated the suitability of this approach to accurately describe most of the soot properties of interest in a combustion system, namely PN (M_0) and total soot volume or soot mass (M_1). Their definition is reported in Eq. 3.19-3.20.

$$M_0 = \sum_{i=1}^{\infty} N_i \tag{3.19}$$

$$M_1 = \sum_{i=1}^{\infty} i N_i = f_v \frac{\rho_s}{m_1} \tag{3.20}$$

where f_v is soot volume fraction and ρ_s is soot density. Higher order moments control $PSDF$ characteristics and are not therefore considered for the present analysis which is focused on ST estimation only. Despite its relatively low computational cost, the model takes into account for the five main processes influencing soot formation and evolution in combustion systems: particle inception, condensation, coagulation, surface growth and oxidation. Being PAH and soot formation interdependent in combustion processes [173], an accurate estimation of PAH formation rate is essential for soot modelling. In fact, they are known to combine to form incipient soot particles, which then grow and aggregate into large structures [174]. PAH also contribute to soot growth process condensing directly onto the surface of soot particles and consuming other smaller chemical species during growth, which would otherwise react and bind to soot particles [173]. Since the choice of the reaction mechanism has a key role in soot formation models, a suitable reaction scheme must be identified. In [174] Blanquart et al. proposed a chemical kinetics mechanism for the high temperature combustion of a wide range of hydrocarbon fuels from methane to iso-octane. In this kinetic model [174], particular care is devoted to the development of accurate sub-models for the formation of soot precursors for realistic fuel surrogates in both premixed and diffusive combustion. Moreover, this mechanism describes in detail all the formation pathways relevant to the main soot precursors usually considered to estimate the nucleation rate in soot calculations, such as acetylene, benzene, naphthalene, phenanthrene and, most importantly, pyrene. At the same time, the selection of a fuel surrogate including compounds representing the hydrocarbon classes characterizing the fuel sooting tendency (aromatics and oxygenates) is mandatory. Therefore, the chemical kinetics mechanism proposed by Cai et al. [134], which was developed starting from the mechanism proposed by Blanquart et al. [174], is used to take into account the influence of oxygenates in the fuel surrogate on the PAH formation at engine-relevant conditions. Since an ethanol model is integrated into this combustion mechanism, the chemical kinetic scheme proposed in [134] is deemed to be suitable for gasoline-ethanol blend combustion. Moreover, this mechanism describes in detail the oxidation of various C_0-C_8 hydrocarbon species, which is a key aspect to quantitatively evaluate the concentration of small hydrocarbons contributing to soot formation, such as acetylene C_2H_2. The proposed mechanism is therefore used in the present study due to the detailed description of ethanol oxidation pathways and contribution to PAH formation. As a last step, a metric is needed to evaluate blends ST in $0D$ calculations. In this context, the maximum soot mass fraction Y_{soot}^{max} is the most obvious parameter. On the other hand, a ranking based on this approach might lead to misleading conclusions since Y_{soot}^{max} might depend on the time frame used in the simulations, which is indeed arbitrary. This observation is particularly true considering that the analysed blends have quite different RON, as reported in Table 3.9. Blends RON in Table 3.9 are estimated using the linear MR weighted on compounds mole fractions suggested in [65] and previously reported in Eq. 3.3. A time frame of one second is used in $0D$ simulations for each reactor. While this promotes a convergence of soot quantities in time, results are still time-dependent and therefore not strictly related to the TSI concept. In fact, establishing a ranking based on soot mass fraction value at a certain moment in time is still an arbitrary approach. This issue is hereby solved introducing a parameter which is representative of the average ST, STR_{av}, from the time of ignition τ_{ig} to the simulation final time τ_f, defined as follows.

$$ST_{av} = \frac{\int_{t_{ig}}^{t_f} Y_{soot}(t)\,dt}{t_f - t_{ig}} \tag{3.21}$$

where $Y_{soot}(t)$ is the instantaneous soot mass fraction in the reactor. As a further advantage, ST_{av} has the physical meaning of average Y_{soot} produced during combustion, in the simulation time τ_f. It is noteworthy that ST_{av} is calculated only during combustion, otherwise a more reactive (e.g. lower t_{ig}) but less sooting compound might result, on average, more sooting than less reactive but more sooting compounds (e.g. toluene). The aim of the present analysis is to investigate the existence of a proportional scaling between measured TSIs and ST in the numerical framework. Results in $0D$ simulations are therefore compared normalizing on the most sooting compound in the experiments (e.g. Blend no 1 - toluene) introducing the normalized average ST for the i^{th} blend, defined in Eq.3.22.

$$NST_{av,i} = \frac{\left(\frac{\int_{t_{ig,i}}^{t_f} Y_{soot,i}(t)\,dt}{t_f - t_{ig,i}}\right)}{\left(\frac{\int_{t_{ig,1}}^{t_f} Y_{soot,1}(t)\,dt}{t_f - t_{ig,1}}\right)} \tag{3.22}$$

It is noteworthy that τ_{ig} might have slightly different values based on the threshold used to determine ignition event occurrence. Consistently with the simulations carried out in paragraph 3.6.1, $T_u + 400$ K ignition criterion [176] is used. Having defined a proper metric to compare experimental and calculated values, $0D$ simulations are carried out on the test condition previously identified for the following mixture qualities $\phi = 1.0, 1.15, 1.3, 1.4, 1.5, 1.75, 2.0,$ $2.25, 2.5, 2.75, 3.0, 3.5, 4.0$. The local refinement from stoichiometric to $\phi = 1.5$ is used to better investigate the sooting threshold sensitivity to blend composition, which was previously investigated in literature via experiments on burners [167] and SI engines [177]. A sample output of the constant pressure simulations is reported in Fig. 3.12, in terms of T

and Y_{soot} evolution, for a slightly rich ($\phi = 1.3$) and very rich ($\phi = 3.0$) configurations. As expected, the maximum temperature reached in the reactors is lower at $\phi = 3.0$, since T_f exhibits a maximum for slightly rich mixtures. Consistently with observations in [168], pure toluene exhibits the highest T_f due to its lower H/C ratio.

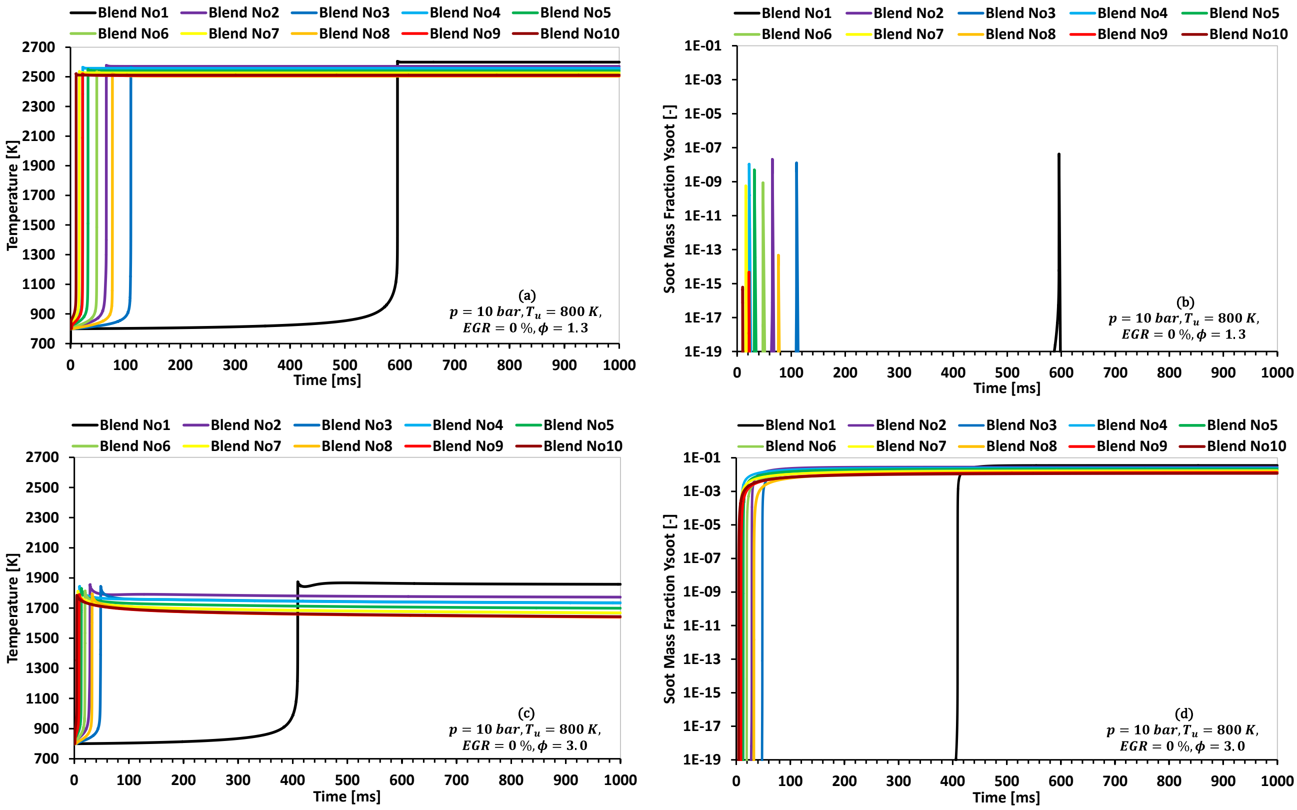

Figure 3.12. Constant pressure reactor simulations results: temperature (a,c) and soot mass fraction (b,d) profiles for $\phi = 1.3$ and $\phi = 3.0$ respectively. Each coloured solid line represent the blends analysed in [160].

In terms of reactivity, fuel mixture enrichment promotes a decrease of τ_{ig} for all the blends analysed. Furthermore, it is important to notice that τ_{ig} ranking is consistent with the estimated RON in Table 3.9. In particular, n-heptane is confirmed to be the most reacting and toluene the least reacting. Blends containing n-heptane are among the most reactive and their reactivity is confirmed to be proportional to n-heptane content. Iso-octane reactivity falls in between n-heptane and toluene ones, in line with the expectations. The relative trend in terms of reactivity remains unchanged moving from $\phi = 1.3$ to $\phi = 3.0$. Analysing soot results it is straightforward to notice how soot formation occurs slightly after the ignition event. Both in $\phi = 1.3$ and $\phi = 3.0$ reactors ST ranking, qualitatively based on Y_{soot}^{max} appears to be consistent with the experimental TSI ranking from [160]. Interestingly, a change in Y_{soot} evolution is observed moving from a slightly rich to extremely rich reactors. While in the former distinct formation and oxidation stages are clearly found, the latter exhibit an asymptotic behaviour in Y_{soot}. This is consistent with the observations in diffusive flames under very rich conditions, where the highly anoxic conditions promote soot accumulation mode [170] which along with a reduced oxidative attack on soot precursors, due to much lower peak temperatures shown in Fig. 2(c), explain the trend in Fig. 2(d). This ultimately leads to much higher Y_{soot} levels in extremely rich conditions. In particular, it is important to notice that extremely rich conditions dampen the difference in terms of soot produced among the different blends considered. This effect is further emphasized analysing ST_{av} dependency on ϕ, as reported in Fig. 3.13. In order to isolate toluene effect on ST_{av}, blends containing toluene are represented by coloured lines. Conversely, black coloured-data represent blends or pure compounds not containing aromatics. Similarly, dashed lines are used to distinguish pure compounds from blends, represented by solid lines. In the first place, it is immediate to notice that aromatics content is responsible for a sensibly higher ST_{av} in stoichiometric to slightly rich mixtures. Although aromatic-based blends retain a higher ST_{av}, ST difference is strongly dampened in extremely rich mixtures where ST_{av} variation is within one order of magnitude regardless of the considered blend.

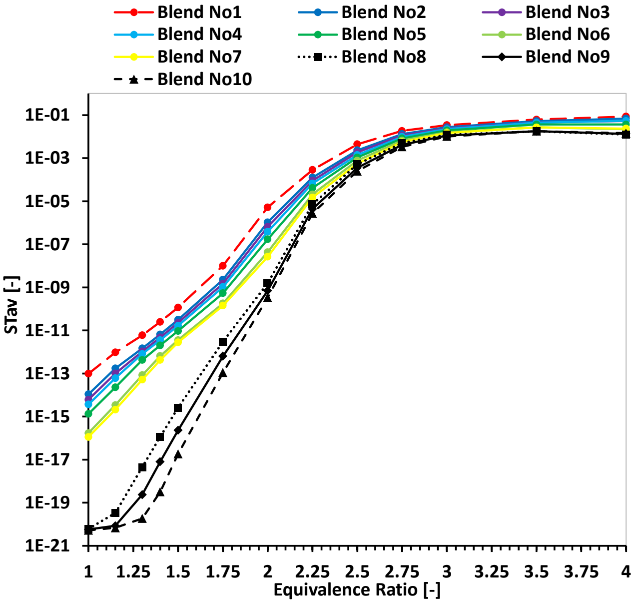

Figure 3.13. ST_{av} dependency on ϕ in constant pressure reactor simulations for the blends experimentally tested in [160].

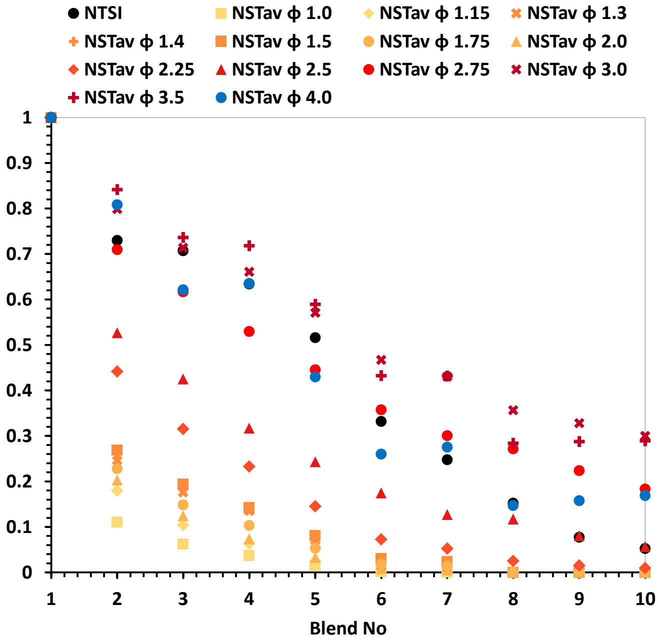

Figure 3.14. NST_{av} dependency on ϕ in constant pressure reactor simulations for the blends experimentally tested in [160] represented by coloured dots. Normalized TSI values are reported with black circles for the experimental measurements reported in [160].

This would suggest that aromatic content strongly affects ST especially in stoichiometric to slightly rich mixtures. Moreover, in agreement with the experimental evidence on a PFI engine reported by Hageman et al. [177], a three order of magnitude increase is present increasing the mixture richness from stoichiometric conditions to $\phi = 1.5$. The previous considerations on compositional effects on ST apply also in this case. Generally speaking, the results in Fig. 3.13 clearly show that ST ranking obtained in the experiments is retained in CP reactor calculations. As a further step,

NST_{av} index is compared with experimental TSI values normalized over the most sooting of the blends tested in [160]. For this purpose, $NTSI_i$ is calculated based on the i^{th} compound TSI_i value as:

$$NTSI_i = \frac{TSI_i}{TSI_1} \tag{3.23}$$

where TSI_1 is the experimentally measured TSI for blend one in Table 3.9. The normalized numerical ST, represented by $NST_{av,i}$, is therefore compared with the experimental normalized ST, represented by $NTSI_i$, in Fig. 3.14. This allows to investigate the existence of a ST scalability between the numerical and experimental frameworks for different mixture quality conditions. The experimentally measured TSI values normalized over the first blend one is reported with black circles and represents the ST scalability among the blends. For instance, it is possible to notice that blend no 5 is characterized by a ST which is halved compared to blend no 1. The coloured dots, representing the numerical sooting propensity NST_{av}, exhibit a colour of increasing intensity moving from stoichiometric to rich conditions. In particular, the results obtained in the richest of the conditions investigated ($\phi = 4.0$) are reported in blue circles. In agreement with the previous observations, numerical ST scalability is correct, but not strongly, correlated with $NTSI$. For example, it is straightforward to notice that blend no 2 is less sooting compared to blend no 1 in the numerical framework. Moving towards richer mixtures NST_{av} trend progressively gets closer to $NTSI$. For reactors characterized by $\phi \geq 2.75$, indicated by circular red dots, a very good agreement is found in terms of ST scalability compared with the experimental reference. For instance, $NTSI$ and NST_{av} for blend no 2 exhibit a very similar value. In practical terms, if blend no 2 is found to be 30% less sooting than blend no 1 in the experiments, based on the TSI metric, the very same gap between the blends is observed when those are tested in constant pressure reactors. In order to further support the existence of a correlation between $NTSI$ and NST_{av} data are reported in Fig. 3.15 (a)-(b) for $\phi \geq 1.0$ and $\phi \geq 3.0$.

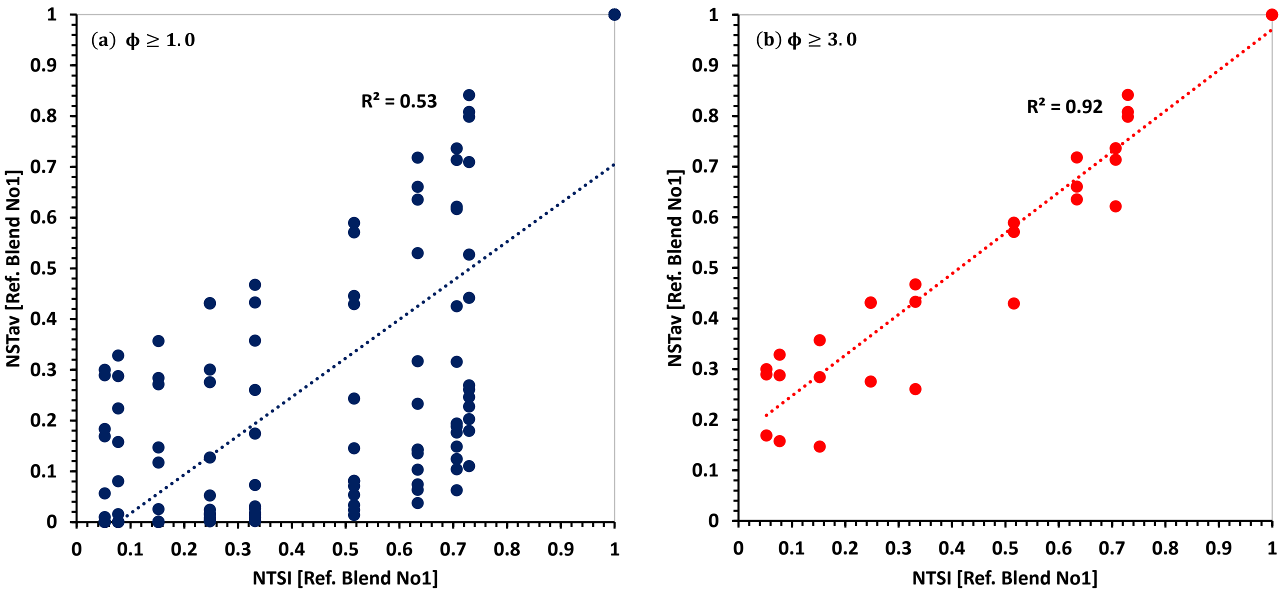

Figure 3.15. $NTSI$-NST_{av} correlation for (a) ≥ 1.0 and (b) ϕ ≥ 3.0.

It is straightforward to notice that a strong correlation and quantitative scalability is present for reactors with $\phi \geq 3.0$ threshold. Considering that soot formation in GDI engines is dominated by liquid film formation pools leading to very rich pockets consumed by the flame while approaching combustion chamber walls, it is reasonable to believe that the proposed approach would allow to distinguish among blends ST both qualitatively and quantitatively when performing

GDI soot $3D\text{-}CFD$ simulations. It can be concluded that diffusive TSI-based blends ST estimation starting from hydrocarbon classes composition is able to quantitatively distinguish to which extent different blends will promote soot formation in a dominantly premixed combustion system. The proposed approach can therefore be used, in principle, to quantitatively estimate commercial gasolines ST, based on the hydrocarbon classes spectrum in terms of $EPIONA$, once representative compounds for each class are chosen and their TSI is estimated using Eq. 3.17.

⬡ 3.2.3 Quantitative Estimation of Commercial Gasolines Sooting Tendency

Due to the impact of oxygenated compounds on ST, the commercial oxygenated gasolines dataset from [83], reported in Table 3.1, is considered. This dataset is of particular interest since it reports not only partial gasolines composition but also RON and MON. On the other hand, the lack of n-paraffins, iso-paraffins and cycloparaffins content constitutes an issue. However, the properties (Table 3.2) and complete compositions (Table 3.3) of other commercial gasolines can be used to make some preliminary considerations. Focusing on gasolines composition, at first, it is possible to notice that, despite the compositional differences due to implications related to being sold in different regions worldwide, paraffinic content is very similar. Furthermore, iso-paraffins/n-paraffins ratio is also very similar. It must be underlined that significant compositional variations might be present when analysing compounds in summer and winter [65]. For this reason, previous studies focused on the formulation of statistically-relevant gasolines averaging the composition based on a sampling campaign [65,76,69,70]. With this in mind, average paraffinic content and iso-paraffins/n-paraffins can be calculated based on the dataset in Table 3.3. Based on the assumption that such values might be representative for the dataset in Table 3.1, a complete composition is rebuilt for each of the gasoline in [83], apart from LEVIII Prem gasoline, whose partial composition is not available. Rebuilt compositions, represented by striped bars, are compared with the complete dataset, reported in Table 3.3 and represented by filled bars, in Fig. 3.16. All gasolines from Table 3.2-3.3 have been used apart from CNPC#92 due to uncertainties on the composition reported in [85].

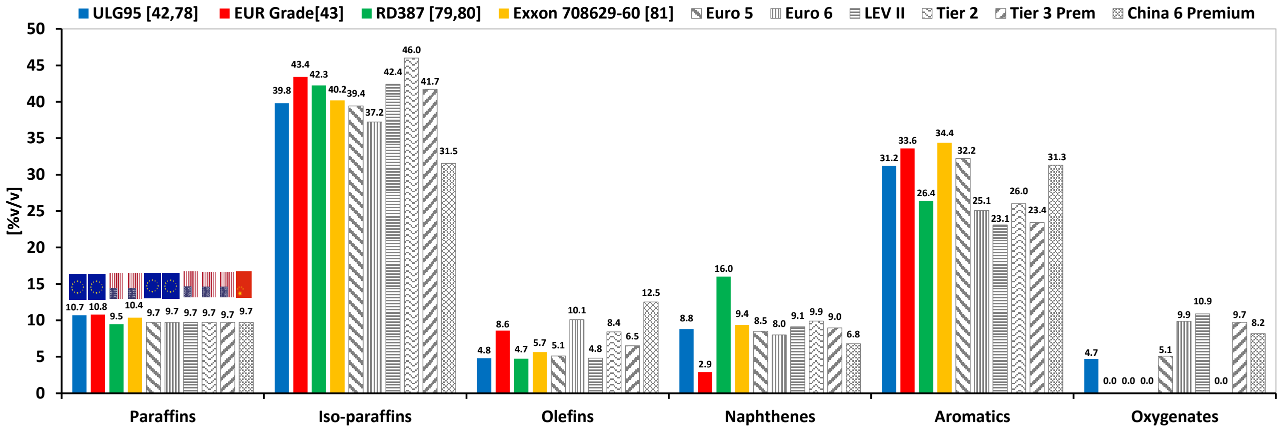

Figure 3.16. $EPIONA$ composition of commercial gasolines from [16,65,69,70,76,77] compared with rebuilt composition based on the partial dataset from [83] for European, American and Chinese commercial gasolines.

It must be noted that all rebuilt gasolines contain oxygenates apart from Tier 2 american gasoline. For the sake of consistency, the same surrogate palette introduced in paragraph 3.1.2 is used and reference compounds TSI is estimated using the Structural Groups Contributions-based methodology previously validated. In particular, Eq. 3.17 is used to estimate TSI for the rest of the pure compounds chosen, whose experimental TSI values are difficult to find in literature. The resulting values are reported in Table 3.10 for the sake of completeness.

Class	**Oxygenates**	**Paraffins**	**Iso-paraffins**	**Olefins**	**Naphthenes**	**Aromatics**
Compound	Ethanol	n-Heptane	Iso-octane	1-Pentene	Cyclopentane	Toluene
Estimated TSI [-]	-19.01	2.89	7.12	10.10	11.53	43.23

Table 3.10. Estimated TSI for the pure compounds representative of the main hydrocarbon classes.

It is important to underline that ST ranking of the pure compounds constituting the surrogate palette correctly replicates the ST ranking reported in literature for the hydrocarbon classes [148,178]:

$$Aromatics > Naphthenes > Olefins > Iso-paraffins > n-Paraffins > Alcohols$$

It is also important to notice that the negative TSI value is consistent with the default TSI scale, which usually does not include oxygenates. While evaluating ethanol impact on a blend ST, a negative value also allows to emphasize the enhanced oxidative effect, which otherwise (with a very small but positive value) would be seen as a decrease in ST mainly due to the lower content of highly sooting compounds. Since MR reported in Eq. 3.16 was found to predict with a satisfactory accuracy TSI of different TRF-based blends, the same is used in the present study to estimate TSI of the commercial gasolines in Table 3.1. This allows to have a quantitative estimation of the ST, using the TSI, to be used as target in the surrogate formulation methodology. In order to widen the analysis, the commercial gasolines in Table 3.2-3.3 are also considered. The estimated TSI is reported for each gasoline in Table 3.11.

Estimated TSI [-]									
ULG95	**EUR Grade**	**RD387**	**Exxon 708629-60**	**Euro 5**	**Euro 6**	**LEV II**	**Tier 2**	**Tier 3 Prem**	**China 6 Premium**
17.71	22.17	19.35	22.29	17.87	12.28	10.91	19.10	11.71	15.52

Table 3.11..Estimated TSI for the commercial gasolines from [16,65,69,70,76,77] and [83].

The proposed approach yields very different values for the targeted gasolines. The gasolines characterised by the highest estimated TSI are EUR Grade, RD387, Exxon 708629-60 and Tier 2. This is consistent with the absence of oxygenated compounds, as visible in Fig. 3.16, which are known to reduce the ST of fuels in combustion systems [179]. The effect of oxygenates on ST is even more evident considering the TSI of the three different gasolines formulated accordingly with EN228 specification, namely: ULG95, EUR Grade and Euro 5. In the first instance, EUR Grade has a higher TSI due to the absence of oxygenates despite similar paraffinic, iso-paraffinic and aromatics content. Further analysing EUR grade composition, which is attributable to a winter grade gasoline [65], it is possible to notice a sensibly higher olefinic content and lower naphthenic content. While aromatics are known to be the most soot promoting class, olefins and naphthenes strongly affect ST [148,160]. In particular, it is recognized that naphtenes are generally more sooting than olefins [165,178]. In this sense, the lower naphthenic content counterbalances the highest olefinic content. The higher TSI is therefore also due to the slightly higher aromatic content compared to ULG95 and Euro 5. Coherently, the slightly higher TSI exhibited by Euro 5 compared to ULG95 is due to the slightly higher aromatics content, despite exhibiting a higher oxygenates content. In fact, paraffins and iso-paraffins content is similar and the higher olefinic content in Euro 5 weights approximately as much as the higher naphthenic content in ULG95. The similar TSI of RD387 and Tier 2 gasolines demonstrates the comparable impact on ST of naphtenes and olefins. Furthermore, it demonstrates their impact on the quantitative TSI value, which is quite high for both gasolines despite the low aromatics content. Further analysing the results reported in Table 3.11, LEVII gasoline has the lowest estimated TSI consistently with its high oxygenates and low aromatics content. The methodology is also able to take into account for regional compositional differences on ST. This is demonstrated by the relatively high TSI of China 6 Premium gasoline, which is attributed to its high olefinic content. The proposed approach also takes into account for the reference regulation on ST, as visible comparing Euro 5 and Euro 6. As a final remark, paraffins and iso-paraffins impact can be considered negligible as demonstrated by n-heptane and iso-octane TSI in Table 3.1. While constituting an interesting tool to forecast compositional effects on ST, the final estimated TSI values obtained for the considered commercial gasolines must be compared with experimental data to validate the capability of numerically estimating commercial fuels tendency to promote soot formation. Jameel et al.[152] studied different Fuels for Advanced Combustion Engines ($FACE$) gasolines, namely $FACE$ A, C, F, G, I and J, formulating two-component surrogates able to mimic the main chemico-physical combustion relevant properties of the targeted gasolines. TSI and SP measurements also demonstrated that surrogates were able to reproduce gasolines ST. This dataset constitutes a solid validation dataset, providing TSI measurements for gasolines over a wide C/H range. For this reason, the estimated TSI values (Table 3.11) are compared with the experimental TSI values measured for $FACE$ gasolines [152] in Fig. 3.17.

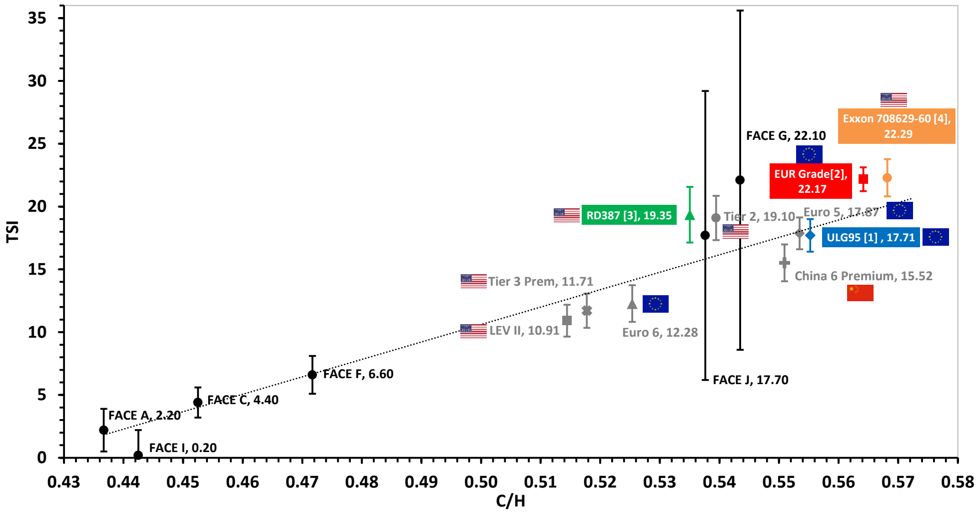

Figure 3.17. Commercial gasolines from [42,43,78,79,80,81] (filled coloured dots) and [83] (filled grey-coloured dots) compared with $FACE$ gasolines from [152] (filled black-coloured dots) in terms of C/H-TSI.

It is clearly visible that the estimated TSIs are quantitatively in line with those measured in [152] for different C/H values. Furthermore, the proposed approach is able to correctly predict ST increase as C/H increases, indicated by the dotted regression line in Fig. 3.17. Since the methodology used to estimate commercial gasolines ST based on $EPIONA$ composition provides results in good agreement with experimental measurements, such TSI dataset can be targeted while generating fuel surrogates for the considered commercial gasolines.

⬡ 3.2.4 Threshold Soot Index-based Fuel Surrogate Formulation Methodology

While having general validity, the methodology hereafter outlined is used to target the commercial gasolines previously analysed. As already pointed out in paragraph 3.1, important chemico-physical and combustion-relevant properties considered fundamental for the fuel description must be taken into account. Again, H/C is as an essential parameter to correctly describe T_f [72,87], Lower Heating Value (LHV) [65,72,87], α_{st} [65,87], density ρ [65,72], MW [65] and T_b [65]. As already shown in Fig. 3.17, a strong correlation is generally present between H/C and ST. In practical terms, it is immediate to notice that commercial gasolines might have similar H/C and different TSIs. As already pointed out,

H/C influences T_f, which in turn affects the effectiveness of the oxidation processes. Moreover, a precise targeting of H/C is crucial to obtain a surrogate with a α_{st} consistent with the real fuel. Any deviation from the reference value inevitably leads to an error in ϕ calculation, which is a fundamental parameter to characterize critical sooting thresholds, as demonstrated in Fig. 3.13-3.14. Targeting H/C also allows to indirectly match most of the previously cited properties [65]. Since most of the analysed fuel contains oxygenates, O/C is also considered among the targeted properties due to its influence on AFR_{st} and auto-ignition characteristics (RON, MON). These last are particularly important in the present study, since a constant pressure tabulated approach is used to store soot-related constants needed by the Sectional Method model to correctly evaluate particle inception, condensation, surface growth and oxidation in $3D\text{-}CFD$ calculations [47,48]. Since auto-ignition characteristics influence τ_{ig} and consequently temperature and heat release rate (HRR) evolution in the reactors, which in turn affect soot chemistry, RON and MON must be included among the targeted properties. This further explains the interest for the dataset reported in [83], which provides RON and MON values for each gasoline. Consistently with the approach outlined in paragraph 3.1.3, the linear system obtained considering Eq. 3.1-3.2-3.3-3.4-3.6 can be used to target the listed properties. While H/C influences ST, TSI measurements on $FACE$ gasolines [152] clearly show that gasolines with similar H/C might have different ST. This further explains the need to introduce, estimate and specifically target TSI in order to accurately match ST. An additional equation is therefore introduced to target the previously estimated TSIs. Being TSI_{gas}, the estimated TSI of a targeted fuel, Eq. 3.24 is added to the linear system.

$$TSI_{gas} = \sum_i^n x_i TSI_i \tag{3.24}$$

While composing the fuel surrogate palette to be used in the fuel surrogate formulation process, it must be considered that resulting surrogates will be used in conjunction with the $ETRF$ gasoline fuel surrogate chemical kinetics mechanism previously identified to generate fuel specific CP-based soot libraries to be used for the validation on the engine case. Due to the complex chemistry interactions between the oxidation pathways and the PAH mechanism and the lack of validation for olefinic and naphthenic compounds, it is chosen to limit the surrogate palette to n-heptane, iso-octane, toluene and ethanol only. Despite being conservative, this approach allows to avoid the introduction of uncertainties related to PAH mechanism prediction when olefins and naphthenes are introduced in the surrogate. Moreover, since all targeted gasolines are characterized by not dramatically high S values, the addition of olefins and naphtenes in the surrogate palette is not strictly needed. Moreover, consistently with Eq. 3.12, MON is not included in the targeted properties to avoid too high numerical stiffness. The linear system constituted by Eq. 3.1-3.2-3.3-3.6-3.24 can be written using matrix notation as reported in Eq. 3.25.

$$\begin{bmatrix} 1 & 1 & 1 & 1 \\ H_{iso} - C_{iso}\frac{H}{C}_{gas} & H_{nhept} - C_{nhept}\frac{H}{C}_{gas} & H_{tol} - C_{tol}\frac{H}{C}_{gas} & H_{eth} - C_{eth}\frac{H}{C}_{gas} \\ O_{iso} - C_{iso}\frac{O}{C}_{gas} & O_{nhept} - C_{nhept}\frac{O}{C}_{gas} & O_{tol} - C_{tol}\frac{O}{C}_{gas} & O_{eth} - C_{eth}\frac{O}{C}_{gas} \\ RON_{iso} & RON_{nhept} & RON_{tol} & RON_{eth} \\ TSI_{iso} & TSI_{nhept} & TSI_{tol} & TSI_{eth} \end{bmatrix} \begin{bmatrix} x_{iso} \\ x_{nhept} \\ x_{tol} \\ x_{eth} \end{bmatrix} = \begin{bmatrix} 1 \\ 0 \\ 0 \\ RON_{gas} \\ TSI_{gas} \end{bmatrix} \tag{3.25}$$

The least-square technique introduced in paragraph 3.1.3 is used to solve the linear system. The methodology is used to target and formulate $ETRF$ surrogates for each of the commercial gasolines reported in Fig. 3.17. A comparison between the targeted fuels and the resulting surrogates is portrayed, in terms of compositions in Fig. 3.18. The main surrogates properties are reported in Table 3.12 for the sake of completeness. All the formulated surrogates contain ethanol except for Tier 2 gasoline surrogate, being Tier 2 the only non-oxygenated gasoline. Generally speaking, it is

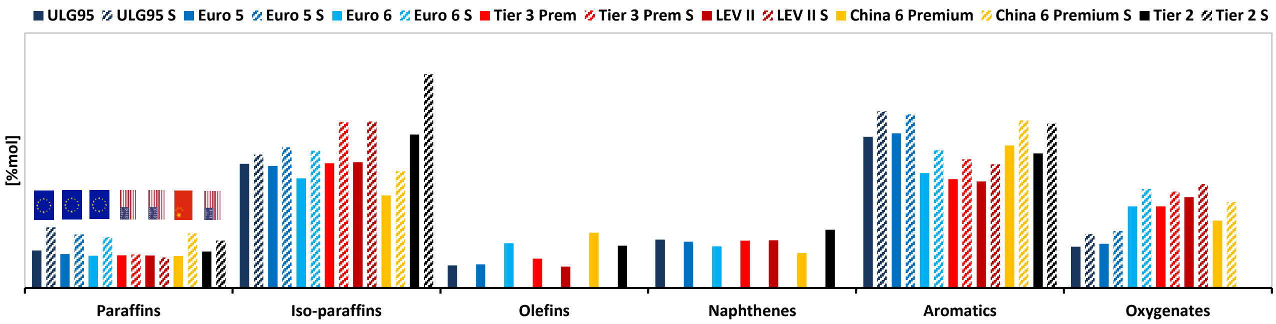

Figure 3.18. Commercial gasolines composition from [83] (solid coloured bars) compared with the surrogates compositions obtained solving Eq.3.25.

	ULG 95 S	Euro 5 S	Tier 3 Prem S	LEV II S	Euro 6 S	Tier 2 S	China 6 Premium S
H/C [-]	1.802	1.810	1.932	1.946	1.903	1.855	1.816
O/C [-]	0.019	0.020	0.036	0.040	0.038	0.000	0.032
AFR_{st} [-]	14.03	14.03	13.87	13.83	13.80	14.52	13.79
RON [-]	95.03	96.62	99.96	100.55	96.41	96.59	96.60
MON [-]	85.88	87.46	90.87	91.34	86.85	90.21	86.46
S [-]	9.15	9.16	9.09	9.21	9.55	6.37	10.14
TSI [-]	18.19	17.82	11.81	10.96	12.23	20.59	15.53

Table 3.12. Properties of the $ETRF$ surrogates formulated targeting the chemico-physical, auto-ignition and estimated sooting characteristics of the commercial gasolines from [83].

possible to notice that the proposed methodology is able to formulate surrogates whose quantitative contribution ranking in each hydrocarbon class is in good agreement with the one exhibited by the targeted gasolines. Comparing surrogates properties, in Table 3.12 with those of the targeted gasolines, in Table 3.2, it is possible to notice how the formulated surrogates are theoretically able to mimic to a good extent the targeted auto-ignition characteristics. In particular, while RON is matched to a satisfactory agreement it is necessary to underline the lower degree of accuracy obtained targeting MON. The lower S exhibited by the surrogates are partially due to the least-square approach technique used to solve the linear system and in majority due to the choice of neglecting any olefins or naphthenes the surrogate palette. In any case, the olefins and naphthenes are excluded on purpose due to the uncertainties related to the unavailability of a chemical kinetics mechanisms able to take into account the influence of their oxidation pathways on PAH chemistry. Although the proposed approach capability of matching auto-ignition characteristics has been extensively elucidated in paragraph 3.1.6, a further validation step is undertaken for a selection of surrogates. In [180] Badra et al. proposed a set of correlations between ignition delay time and ON at specific test conditions deemed to be representative of RON and MON test conditions. The formulated $ETRF$ surrogates are tested in CV reactor simulations carried out on a RON-like sample condition identified in [180], in particular: 20 bar, 835 K. Since such correlations were derived from a set of chemistry-based simulations for different TRF blends using homogeneous constant volume reactors, the same approach is used in DARSv2019.1 chemistry solver to quantitatively estimate the reactivity of the formulated surrogates. Coherently with the previous approach the chemical kinetics mechanism previously identified [134] is used to perform the simulations and $T_u + 400\ K$ ignition criterion [176] is used to determine τ_{ig}. Simulations are carried out for the surrogates targeting commercial gasolines in [83], since these last are used to generate CP-based soot libraries tested on the engine case afterwards. In order to validate the reactivity of the formulated surrogates, points for each gasoline are added in Fig. 3.19 based on the τ_{ig} resulting from chemistry-based simulations and the ON estimated with Eq. 3.3-3.4 for each surrogate. If surrogates markers lie on the lines representing the correlations from [180], their reactivity quantitatively matches the targeted RON and MON. A very good agreement is found for ULG95, Euro 5, Euro 6 and China 6 Premium surrogates for both ON. Despite exhibiting a lower reactivity, consistently with the commercial gasolines ON values, LEVII and Tier 3 surrogates slightly overestimate the reactivity of the targeted gasolines. In fact, based on their τ_{ig} values on the test condition, the correlation from [180] would predict RON and

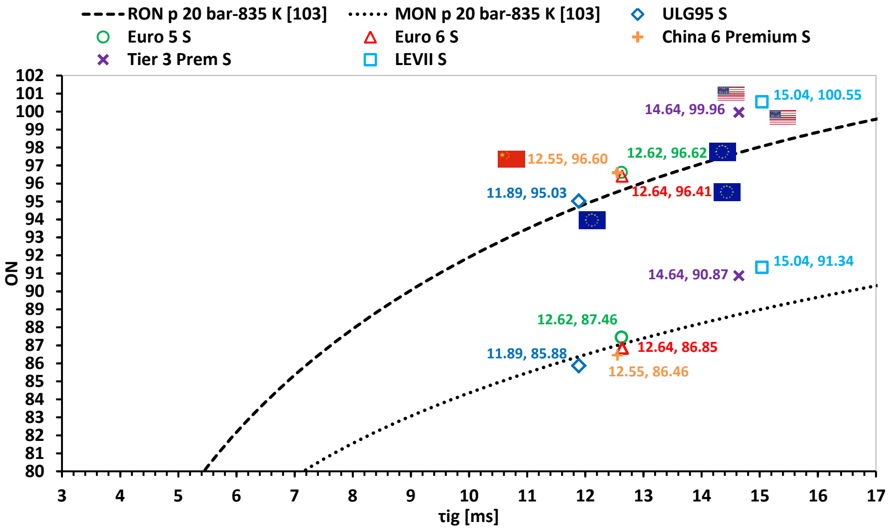

Figure 3.19. Surrogates auto-ignition characteristics validation based on the τ_{ig}-ON correlation derived in [180] for a selection of gasolines from [16,65,69,70,76,77,83].

MON values around 99 and 89 respectively. The formulated surrogates are therefore able to quantitatively represent, to a satisfactory degree of accuracy, the auto-ignition characteristics of the targeted gasoline. It is also interesting to notice that surrogate targeting ULG95 gasoline ST exhibits a very good agreement with data from [180], consistently with the previous $ETRF$ one generated in paragraph 3.1 targeting s_L, which slightly differs in terms of composition. Results suggest that the proposed methodology is able to blend surrogates based effectively on the targeted quantities chosen. Furthermore, although more advanced models [117,118,119] would guarantee a higher degree of accuracy, the simple approach proposed in [65] can be used to target ON retaining a set of linear equations. Analysing surrogates ability to match ST, it is straightforward to notice, in Fig. 3.20, that the obtained surrogates are characterized by TSI values in good agreement with the targeted ones.

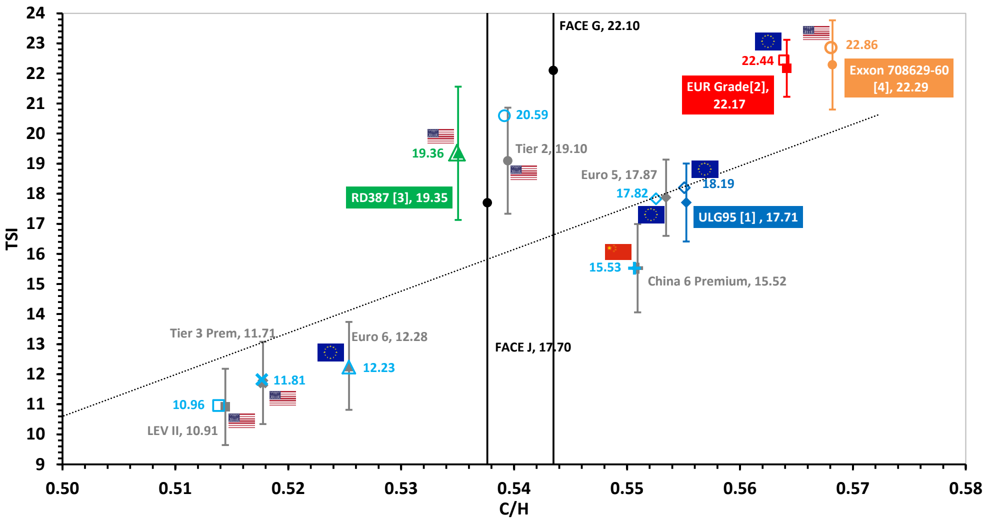

Figure 3.20. Commercial gasolines from [16,65,69,70,76,77] (filled coloured dots) and [83] (filled grey-coloured dots) compared with their surrogates, represented by unfilled dots respectively randomly coloured and light blue coloured, in terms of C/H-TSI.

In particular, the generated surrogates not only closely mimic the estimated TSI values but also the C/H and therefore α_{st}. It is possible to conclude that the proposed methodology is able to formulate $ETRF$ surrogates able to match the main chemico-physical properties, auto-ignition characteristics and the estimated ST. Despite surrogates TSI values correctly depict ST ranking and match the gasolines estimated TSI to a good extent, a further validation step is needed to demonstrate that the same scaling is obtained, in terms of soot characteristic quantities, in $3D\text{-}CFD$ simulations.

⬡ 3.2.5 Engine Case Validation for US, EU, CN Surrogates

In the present paragraph, a further effort is spent to further validate the methodology. In fact, although matching with a good degree of accuracy the targeted TSIs, surrogates ability to match gasolines ST is of practical interest especially if a similar scalability in terms of ST is observed in $3D\text{-}CFD$ soot calculations. Moreover, such validation procedure aims to isolate the compositional effects on ST considering a reference stratification at spark timing. In fact, since evaporation characteristics and saturation properties targeting is not addressed in the present work, the formulated surrogates are only used to generate soot libraries containing Sectional Method model constants which are essential to correctly estimate most of the relevant processes involved in soot formation. In this section, the mathematical formulation of the model is not discussed and the reader is invited to refer to Chapter 5 for further details. Since combustion process in GDI engines is known to be mostly but not exclusively premixed, a CP-based reactors simulation campaign is carried out to create dedicated soot libraries able to provide estimation on the ensemble (p, T_u, ϕ, EGR) conditions encountered by the flame front propagating in the combustion chamber, using DARSv2019.1. It must be underlined that soot coefficients are stored in the library not only as a function of a specific $(p^*, T_u^*, \Phi^*, EGR^*)$ but also based on the value of a progress variable c, defined as in Eq. 3.26.

$$c(t) = \frac{h_{298}(t) - h_{298}^{in}}{h_{298}^{eq} - h_{298}^{in}} \tag{3.26}$$

where h_{298} is the enthalpy of formation, calculated from the current composition $h_{298}(t)$, the initial composition h_{298}^{in} and the equilibrium composition h_{298}^{eq}. This allows to track the combustion process development in the reactor to provide an estimation of the chemistry-based soot formation processes based on a cell-wise combustion development status. Libraries are generated for an ensemble of $ETRF$ gasoline surrogates in Table 3.12, namely: Euro 5, Tier 3 Prem, Euro 6, Tier 2 and China 6 Premium. Retaining the same library stepping and the CFD model setup, this comparison allows to effectively evaluate surrogates compositional effect on soot formation over the engine cycle. The CFD model used for this purpose replicates a single cylinder optically accessible research GDI engine available at the Istituto Motori of the National Research Council ($IM\text{-}CNR$) of Italy. This engine has been widely studied by the author and colleagues in publications focusing on knock [41,42,43,181,182], s_L modelling [82], alternative fuels [183] and soot emission modelling [184,185]. A detailed description of the engine and of the CFD model is given in Chapter 5 and the basic details for the purpose of the present analysis are briefly recalled hereafter. The engine features a commercial cylinder head of an engine with four valves per cylinder, wall-guided direct injection and centrally located spark plug. Engine specifications and details on the investigated WOT operating condition are briefly reported in Table 3.13. As visible in Table 3.13, the chosen operating condition is characterised by an early injection strategy with a single injection pulse. Being the focus of the present analysis a relative comparison of the compositional effects on ST on equal fuel-air mixture stratification at spark timing, the CFD model, extensively presented and discussed in Chapter 5, is used as a virtual test bench to run combustion calculations with the Sectional Method model [46,47,48,49] coupled with dedicated soot libraries generated with the formulated surrogates.

Displacement	Stroke	Bore	Compression Ratio	Number of Valves	Engine Speed
399 cm^3	81.3 *mm*	79 *mm*	10:1	4	2000 *rpm*
IVO	**IVC**	**EVO**	**EVC**	**SOI**	**Spark Timing**
363 CAD $bTDC$	144 CAD $bTDC$	153 CAD $bTDC$	360 CAD $aTDC$	340 CAD $bTDC$	15 CAD $bTDC$

Table 3.13. Engine specifications and operating condition parameters.

In order to provide the reader with basic information on the chosen modelling approach, the $3D$-CFD engine model is created using a customized version of STAR-CDv2019.1. Taking advantage of the geometrical symmetries, a half-chamber model is adopted including both intake and exhaust ports and simulations are carried out in the $RANS$ framework. Since in Chapter 5 a detailed discussion of CFD results is provided, only results fundamental for the sake of clarity in the present discussion are provided. The advanced single injection strategy leads to the formation of liquid film pools on the combustion chamber walls, especially on the piston crown. Despite the increase time for mixing obtained with an advanced SOI, rich mixture pockets persists on the piston crown at spark timing. Furthermore, a partial rebound of the fuel droplets leads to a slightly rich mixture in the end-gas region near the exhaust valve. This leads to an evident mixture inhomogeneity in the combustion chamber at spark onset, as visible in Fig. 3.21.

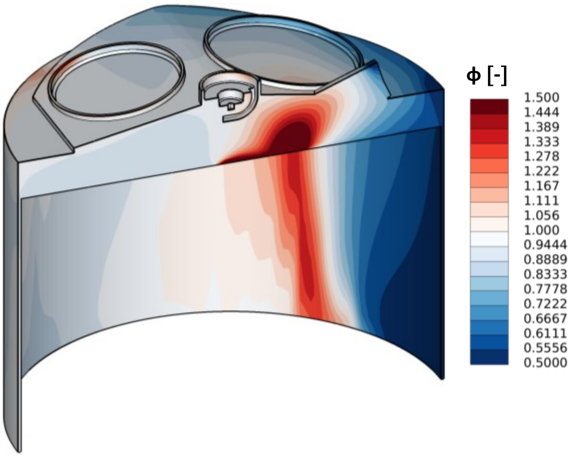

Figure 3.21. Stratification at spark timing represented by scalar ϕ field.

$ECFM$-$3Z$ combustion model [39], customized with a methodology to accurately estimate s_L at engine-relevant conditions [81,82] and presented in Chapter 4, is used. A simple flame kernel deposition model [186], based on Flame Surface Density (FSD), is chosen to model spark ignition. Sectional Method model is used to predict soot formation using 40 sections in order to widen the range of soot particles modelled in the simulation and default constants are adopted for particle inception, condensation, surface growth and oxidation. A combustion simulation is carried out from spark onset for each of the generated soot libraries. Being the Sectional Method a passive model, a unique combustion model tuning is used for all cases. A comparison between the experimental and simulated average in-cylinder pressure traces and cumulative apparent heat release rate is portrayed in Fig. 3.22(a)-(b). Since temperature is a key parameter involved in soot formation, the average in-cylinder absolute temperature obtained during combustion simulation is added in Fig. 3.22(a). While correctly matching the early stages of flame kernel development, the CFD model slightly overestimates the Crank Angle Degree (CAD) at which 10% of fuel mass fraction is burnt $MFB10$, as visible in Fig.3.22(b). A slightly higher turbulent combustion rate allows the model to correctly match $MFB50$, despite slightly overestimating in-cylinder peak pressure. Considering $MFB10$-$MFB90$, the CFD model is able to match to a satisfactory agreement overall combustion duration. Since main combustion indicators and combustion phasing predicted by CFD is in good agreement with the experiments, Sectional Method model PM emission prediction can be

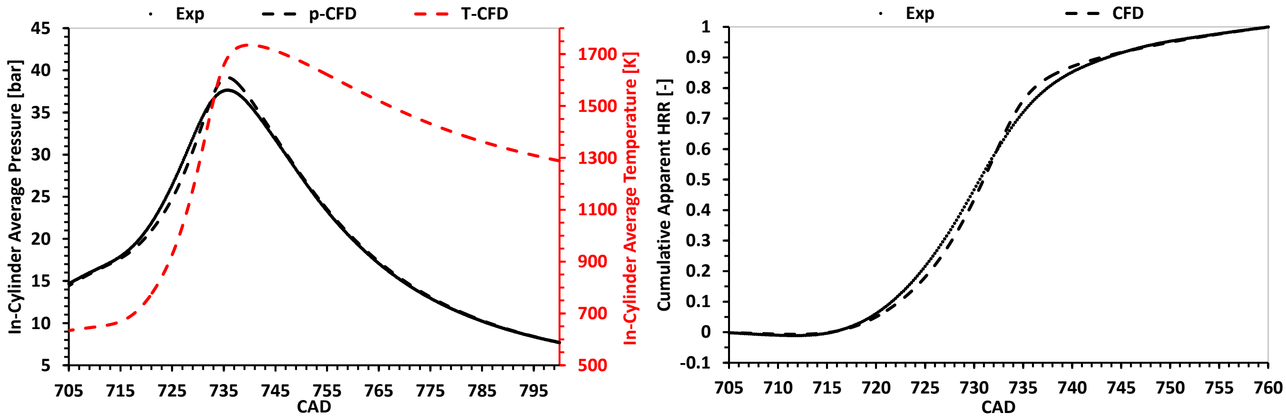

(a) (b)

Figure 3.22. (a) In-cylinder average pressure trace obtained from experiments (dotted black line) and CFD (dashed black line). In-cylinder average temperature obtained from CFD (dashed red line). (b) Cumulative apparent heat release rate obtained from experiments (dotted black line) and CFD (dashed black line) calculated starting from measured and calculated pressure traces.

analysed into detail. The aim of the analysis is, primarily, to verify that ST ranking obtained estimating TSI based on $EPIONA$ composition of the considered gasolines is retained in CFD prediction. Secondly, and most importantly, a further investigation is carried out to understand if PM predicted by CFD simulations scales proportionally with TSI, in a similar fashion to what was previously demonstrated for TRF surrogates in chemistry-based reactor simulations. Consistently with previous studies in literature, soot characteristic quantities are compared at EVO [48,49,120]. The evolution of in-cylinder PM over the engine cycle is reported in Fig. 3.23(a) for the different fuels modelled. In order to improve readability and easily identify the region of origins, a specific colour code is used. Non-oxygenated gasolines are represented in black and oxygenated ones are represented by coloured lines where red represents American gasolines, blue European ones and orange Chinese ones. Tier 2 American gasoline is the only one in the dataset not containing oxygenates. PN evolution during the cycle is also reported in Fig. 3.23(b).

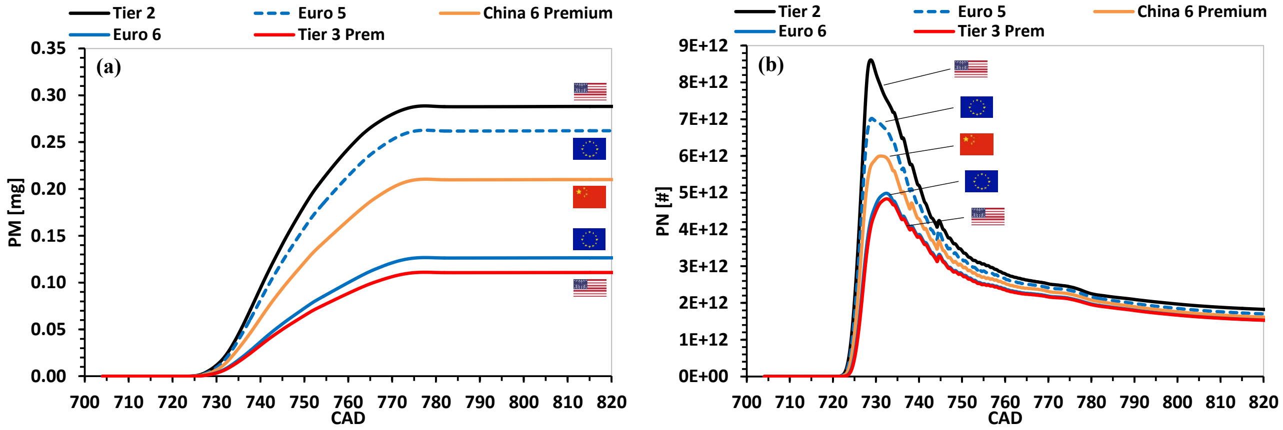

(a) (b)

Figure 3.23. In-cylinder (a) PM , (b) PN evolution for a selection of fuel surrogates reported in Table 3.12.

It is straightforward to notice how surrogate composition strongly impacts PM formation on even stratification and thermodynamic history of the combustion process. In the first place, PM formation in the simulations perfectly matches, in terms of ST ranking, the one outlined by TSI estimation based on $EPIONA$ composition reported in Table 3.11 As expected, Tier 2 is the most sooting gasoline and Tier 3 Prem E10 is the less sooting one. Although PM has been chosen as reference index to evaluate ST, in order to be consistent with Y_{soot} previously used, PN exhibits the same ranking obtained with PM. This indicates that surrogates characterized by higher ST, not only have a higher nucleation mode, but also have a higher accumulation mode associated to condensation, coagulation and surface growth processes. This statement is further supported by the $PSDF$ evaluated at EVO for the considered surrogates reported in Fig. 3.24(a)-(b) on logarithmic and linear scales, respectively.

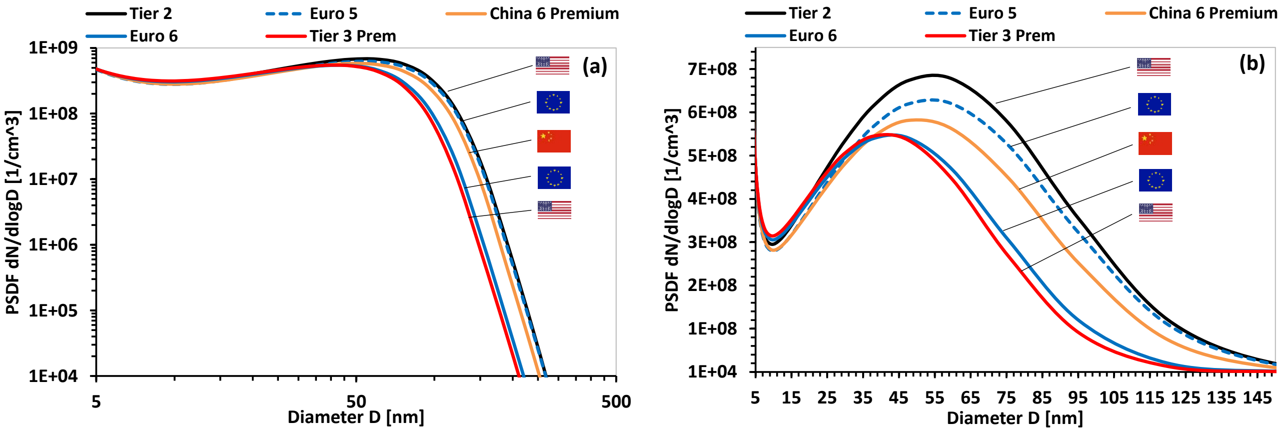

(a) (b)

Figure 3.24. $PSDF$ predicted by CFD simulations at EVO for the targeted gasolines reported on (a) logarithmic and (b) linear scales.

In Fig. 3.24(a) is possible to appreciate the orders of magnitude present between more and less sooting gasolines in terms of high diameter particles ($d \geq 150\,nm$). Thanks to the linear scales plots in Fig. 3.24(b) it is also possible to appreciate the different diameters for which $PSDF$ exhibit peak concentration $d_{PSDF,max}$: Tier 3 Prem and Euro 6 ($d_{PSDF,max} \approx 43\,nm$), China 6 Premium ($d_{PSDF,max} \approx 52\,nm$), Euro 5 and Tier 3 Prem ($d_{PSDF,max} \approx 57\,nm$). Considering now PM produced by each gasoline and normalizing data using the most sooting one (Tier 2) as reference, a normalized CFD-related PM-based index $NPM\text{-}CFD$ is introduced to quantitatively evaluate the correlation with $NTSI$ previously introduced. In equations, for the generic i^{th} simulated gasoline:

$$NPM\text{-}CFD_i = \frac{PM_i^{EVO}}{PM_{Tier\ 2}^{EVO}} \tag{3.27}$$

In practical terms, $NPM\text{-}CFD$ is the $3D\text{-}CFD$ version of NST_{av} used in CP reactors simulations. As visible in Fig. 3.25(a), $NTSI$ appears to be well correlated with $NPM\text{-}CFD$ since the ST ranking obtained in $3D\text{-}CFD$ is consistent with the $EPIONA$-based TSI estimation. This first result demonstrates that ST, estimated with a limited number of information on gasoline composition, is representative of the fuel surrogates behaviour in a CFD engine case. Following a similar rationale to the one used in the previous paragraph, it is particularly interesting to understand if the amount of PM formed in the CFD case is quantitatively linked to TSI values. For this purpose, $NTSI$ and $NPM\text{-}CFD$ trends, calculated using Tier 2 gasoline as reference, are compared in Fig. 3.25(b). $NTSI$ calculated based on $ETRF$ surrogates TSI values is also added for the sake of completeness. It is straightforward to notice that the quantitative decrease in PM formed in CFD very well matches the quantitative decrease in estimated TSI values for Euro 5 and China 6. The quantitative PM decrease observed in CFD switching from Tier 2 gasoline $ETRF$ surrogates to Euro 6 and Tier 3 Prem ones is overestimated approximately by 30% compared to the quantitative ST decrease estimated based on TSI. Generally speaking, the quantitative ST decrease obtained in CFD is in good agreement with the corresponding decrease estimated based on TSI. The aforementioned trend is confirmed by in-cylinder $3D\text{-}CFD$ local soot visualizations, at the peak sooting condition over the cycle (740 CAD), reported in Fig. 3.26. Local soot formation pockets originating on the piston crown can be appreciated in the dedicated view proposed in Fig. 3.27.

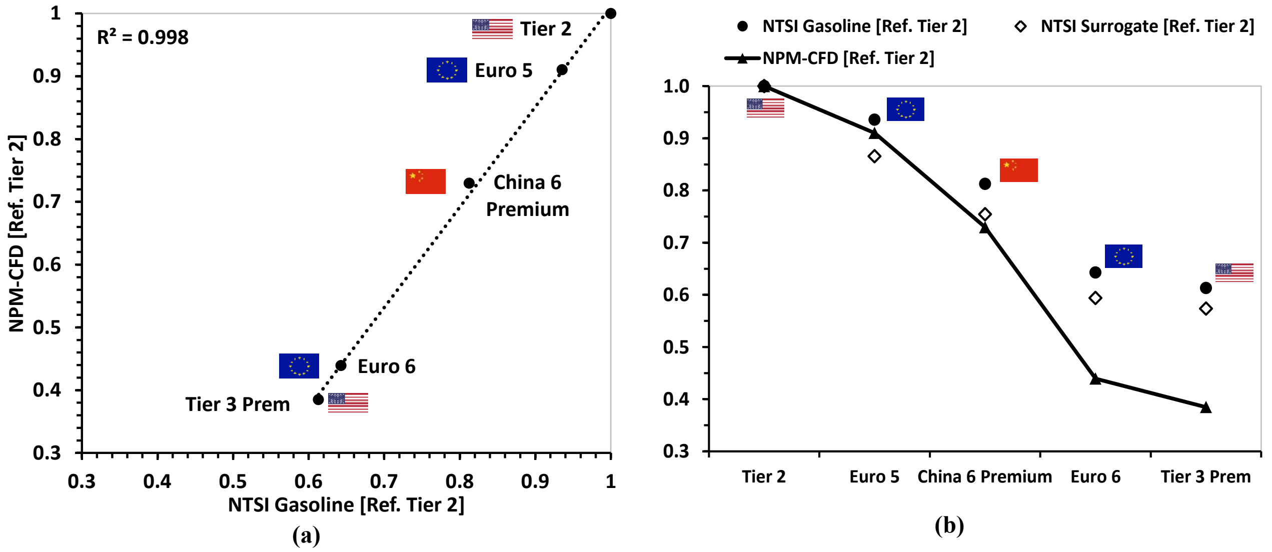

Figure 3.25. (a) $NTSI/NPM\text{-}CFD$ correlation obtained for a selection of gasolines from [83] (b) $NTSI$ (gasolines-based: filled circles), $NTSI$ (surrogates-based: unfilled diamonds) and $NPM\text{-}CFD$ (black solid line with filled triangles) scaling comparison for the analysed gasolines using Tier 2 values as reference.

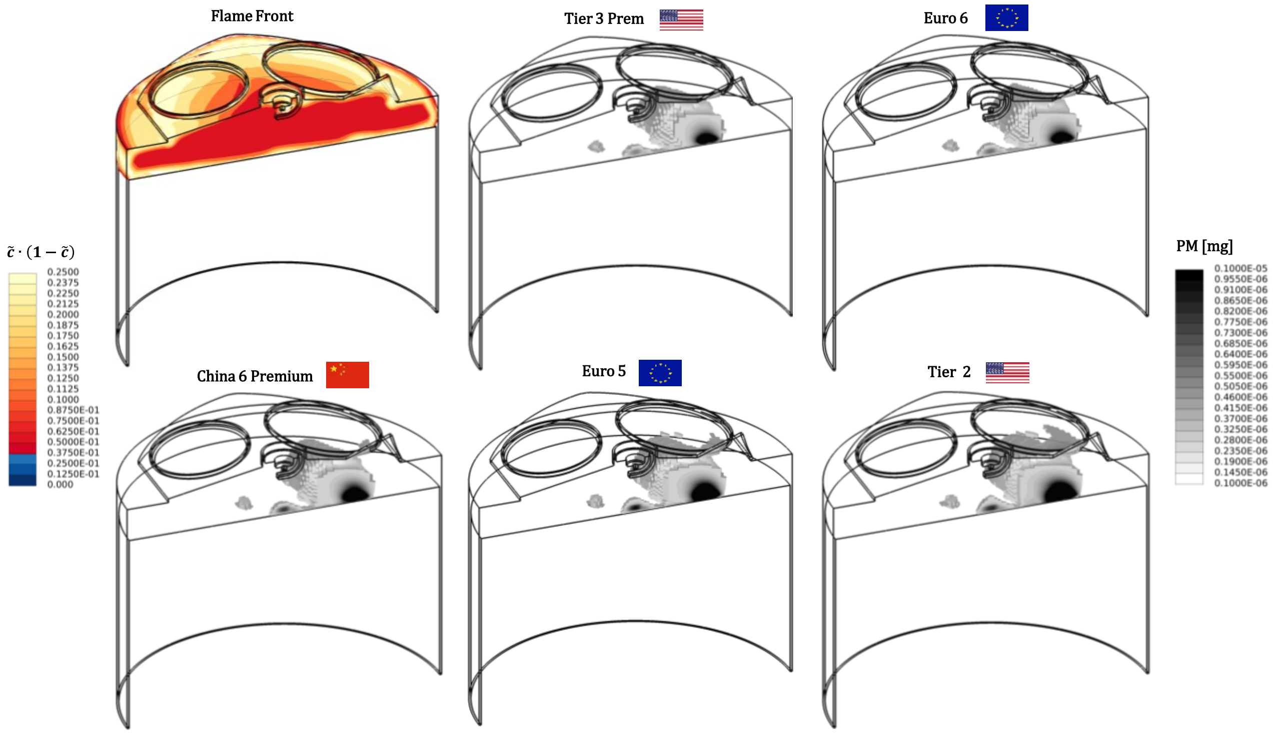

Figure 3.26. $3D\text{-}CFD$ results at 740 CAD: Flame front isosurfaces for different local progress variable values and PM subset for the investigated gasolines.

As a further comment, soot formation locally takes place, as expected, in correspondence of rich mixture pockets. The outlined results are in agreement with those provided by McEnally et al. [145], who previously demonstrated that the range of possible compositions of viable gasolines can change the intrinsic chemical tendency to form soot by over a factor of 2. It is therefore possible to conclude that the proposed approach is able to represent to a satisfactory degree of accuracy the impact of gasoline composition on PM formation in quantitative terms. It must be further underlined that the aforementioned analysis was carried out on even stratification at spark timing to isolate such contributions. Even more pronounced quantitative differences are therefore expected if the compositional effects on spray evolution are

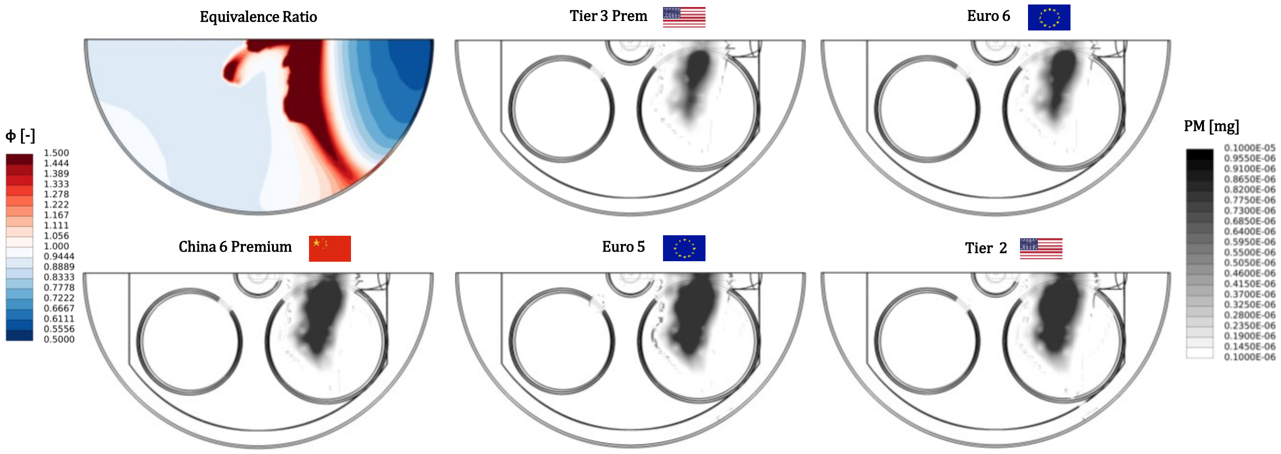

Figure 3.27. $3D$-CFD results at 740 CAD on the piston crown: Flame front isosurfaces for different local progress variable values and PM subset for the investigated gasolines.

included in CFD simulations. In fact, as shown in [83], the considered gasolines are characterised by different evaporation characteristics and this implicitly means that some fuels are likely more prone than others to form liquid film pools. Locally richer mixture could potentially further emphasize the differences in terms of $PSDF$, considering that, as clearly shown in Fig. 3.24(b), surrogates already exhibit quiet different accumulation modes on even stratification. Targeting distillation characteristics is the natural evolution of the proposed methodology since the ability of matching such property and ST would allow a direct CFD comparison with experimental soot measurements on the engine, similar to those reported in [83]. As a further comment, this results demonstrates that diffusive-based TSI values can be used to estimate ST in predominantly premixed turbulent combustion processes. Another interesting aspect is that these results were obtained in an application characterised by turbulent flow motions. As pointed out in [150], laboratory soot measurements of fuel ST are almost exclusively made in atmospheric pressure laminar flames using pure chemical compounds and the effects of turbulence, pressure and multicomponent fuel blending on fuel ST are virtually unknown. Usually, the assumption that fuel composition effects dominate over these other effects is made [150]. The outcome of CFD calculations clearly demonstrate the validity of these assumptions and that soot characteristic quantities scale accordingly with the TSI-based estimated ST also in turbulent combustion processes. Moreover, the methodology proved to take into account for the different hydrocarbon classes impact on ST, including oxygenates. The proposed fuel surrogate formulation methodology targeting ST, constitutes a practical tool for CFD engineers and researchers who needs to take into account for real fuels composition impact on soot formation in CFD framework. Despite being widely validated on commercial gasolines, the methodology could be used to target diesel, marine and jet fuels adjusting the surrogate palette to match the average carbon number of each hydrocarbon class of real fuels. As a final remark, the soot library generated with ULG95 gasoline surrogate formulated with this methodology is used to enhance Sectional Method predictions in the calculations presented in Chapter 5.

3.3 Alternative Fuels

3.3.1 Background and Motivation

According to $REDII$ [23], at least 10% of the energy used in transportation must be bio-based by 2020. The same directive force fuel suppliers to a minimum market share equal to 6.8% of low-emissions and renewable fuels, including advanced biofuels, by 2030. Ethanol is a renewable source of energy with lower production costs compared to other alcohols, such as n-butanol or methanol. As a consequence, it is the main biofuel used in current production engines [187,188]. Several experimental studies investigated the effect of pure bio-alcohols fuels on combustion characteristics in modern Direct-Injection Spark-Ignition engines ($DISI$). Irimescu et al. [130] compared stoichiometric butanol and ethanol mixtures in terms of combustion indicators and emissions in an optically accessible DISI research engine operated at full-load. In order to analyze the impact of the injection strategy, three different SOI were investigated. Despite ethanol exhibited advantages in terms of HC and CO emissions, a non-negligible decrease of performance was found for deviations from the optimal injection phasing. Different studies [189,190,191] discouraged the use of pure ethanol with a standard engine hardware, as highly corrosive, thus detrimental for the injection system components. Conversely, other studies [192] reported that minor modifications to both hardware and Electronic Control Unit (ECU) are needed up to ethanol contents equal to 30% by volume. Therefore, many researchers focused the attention on gasoline-ethanol blends as a feasible compromise to meet the upcoming regulations retaining the overall architecture of modern $DISI$ units. Several experimental studies were carried out on standard SI engines, with various architectures and injection systems, at different operating points (OP). Different gasoline-ethanol blends in terms of ethanol content were investigated. As a general trend, each experimental dataset confirmed the benefits in terms of CO and unburned hydrocarbons (UHC) reduction increasing the ethanol content in the blend [191,193,194,195,196,197,198,199]. Despite gasoline-ethanol blends constitute a promising solution to lower the environmental impact of ICEs, it is clear that further efforts in terms of control strategy optimization are mandatory in order to extend their benefits over a wider range of OPs. For instance, Sarathy et al. [6] pointed out that the addition of oxygenates produces a decrease in the mass-based LHV of the blend, as fuel oxygen atoms do not contribute to heat production; therefore the reduction of the LHV is proportional to the mass percentage of oxygen. In order to optimize engine control strategy for gasoline-ethanol blends, $3D\text{-}CFD$ combustion simulations can be used. In the present paragraph, the fuel surrogate formulation methodology presented in Paragraph 3.1 is used to formulate $ETRF$ surrogates suitable for representing gasoline-ethanol blends up to 85% of ethanol volume content. Such surrogates are used in Chapter 4 to derive dedicated s_L correlations for the considered blends. In the following paragraph, the methodology used to formulate gasoline-ethanol blends surrogates is briefly described and the resulting properties are compared with a wide experimental dataset derived from a literature survey. This allows to further validate the methodology introduced in this chapter and to demonstrate the practical benefits deriving from its use.

3.2.2 Gasoline-ethanol Blends Surrogates

When referring to a generic gasoline-ethanol blend, the integer number following the capital letter "E" indicates the ethanol content by volume [200]. Once a gasoline-ethanol blend is considered, its ethanol content is uniquely defined (e.g. for $E5$ it is 5vol%), while a suitable fuel surrogate is required for describing the properties of the base gasoline. Since ethanol is blended at a later stage in exact proportion based on the targeted blend, a TRF fuel surrogate is needed. For this purpose, the methodology discussed in Paragraph 3.1 is used to formulate a $E0$ gasoline fuel surrogate targeting

ULG95 for the sake of consistency or, generally speaking, a $RON95$-$MON85$ commercial European gasoline. At this stage, a family of gasoline-ethanol blends surrogates can be generated, as ethanol content in volume is imposed by definition and TRF components are scaled accordingly. The compositions and properties of the resulting $ETRF$ surrogates are reported for increasing ethanol content in Table 3.14-3.15, respectively.

	$E0$	$E5$	$E10$	$E20$	$E85$	$E100$
Iso-octane	40.94	36.49	32.56	25.92	2.90	0.00
n-Heptane	13.91	12.40	11.07	8.81	0.98	0.00
Toluene	45.15	40.24	35.91	28.59	3.20	0.00
Ethanol	0.00	10.87	20.47	36.67	92.92	100.00

Table 3.14. Formulated gasoline-ethanol blend surrogate compositions.

	$Ethanol$ [%vol]	ACA [-]	AHA [-]	AOA [-]	RON* [-]	MON [-]	H/C* [-]	O/C [-]	α_s [-]	LHV [MJ/kg]	ρ at 298 K [kg/m^3]	T_b [K]
$E0$	0	7.409	13.207	0.000	95.12	87.67	1.782	0.000	14.416	42.714	752.57	377.31
$E5$	5	6.822	12.424	0.109	96.52	87.92	1.821	0.016	14.133	40.984	754.19	374.50
$E10$	10	6.302	11.732	0.205	97.75	88.14	1.862	0.032	13.850	39.456	755.81	372.03
$E20$	20	5.426	10.564	0.367	99.84	88.52	1.947	0.068	13.289	36.878	759.06	367.85
$E85$	85	2.383	6.510	0.929	107.09	89.83	2.732	0.390	9.755	27.927	780.14	353.35
$E100$	100	2.000	6.000	1.000	108.0	90.00	3.000	0.500	8.967	26.800	785.00	351.52

Table 3.15. Formulated gasoline-ethanol blend surrogate properties. Targeted properties when generating base gasoline TRF surrogate are marked with "*".

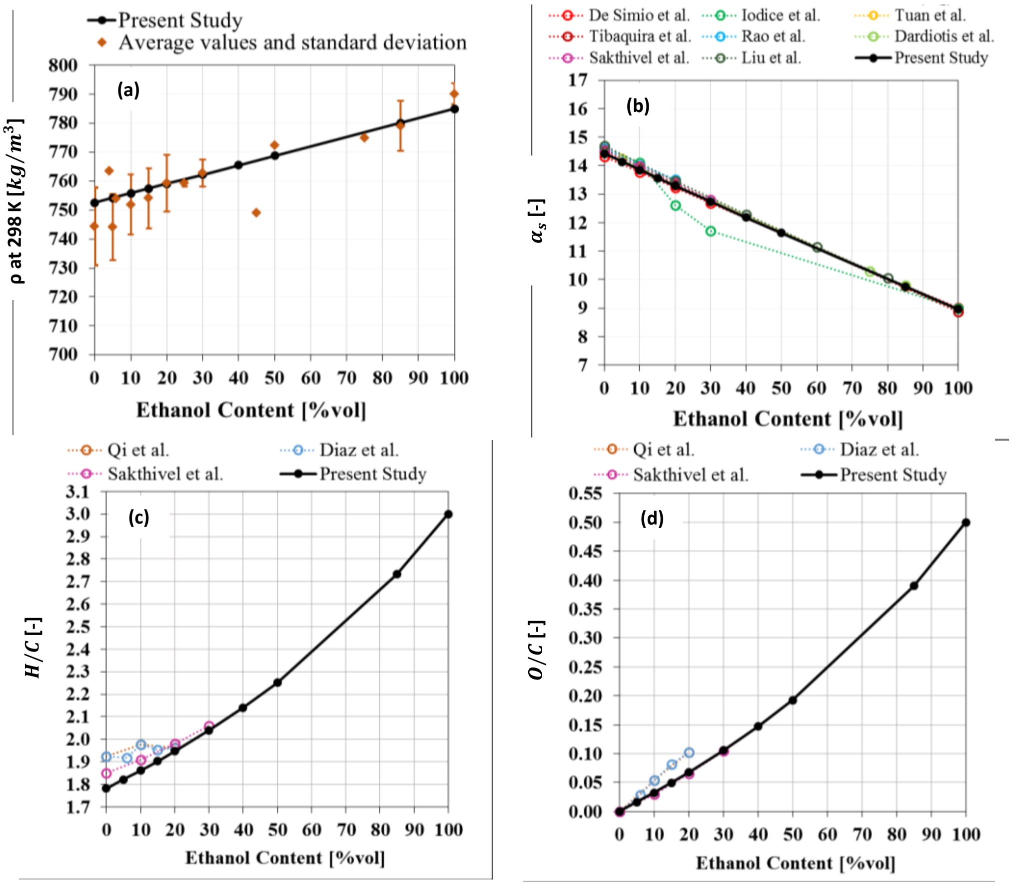

Figure 3.28. (a) Density at ambient conditions: present work compared to the average value and its variance (reported as error bar) for each ethanol %vol, (b) Stoichiometric air-to-fuel ratio, (c) H/C ratio and (d) O/C ratio. Dotted lines report values from literature, while solid ones represent properties calculated with the proposed methodology.

To further validate the proposed methodology and the formulated surrogates, in Fig. 3.28-3.29 the properties reported in Table 3.15 are compared with the ones provided by a wide dataset available in literature [189,190,191,192,193,194, 195,196,197,199,201,202,203,204,205,206,207,208,209,210,211,212]. It must be underlined that most of the aforementioned studies are based on experimental measurements of several gasoline-ethanol blends using base gasolines with different properties. In Fig. 3.29(a), the liquid density of the surrogates at ambient conditions is compared with the experimental dataset. The generated surrogate family shows an increasing trend for increasing ethanol contents, in agreement with the experiments. It is interesting to note that the higher is the ethanol content, the lower is the data dispersion, which is due to the different base gasolines ($E0$) used to generate the blends. For increased ethanol content, the fuel mixture properties depicted in Fig. 3.28(a)-(b)-(c)-(d) present a less remarked data scatter. The reason of this behaviour is barely due to decreased influence of the base gasoline properties as the ethanol content of the mixture increases. Similarly, α_s reported in Fig. 3.28(b) are closely matched by the generated surrogates, which is important to have coherent equivalence ratios between actual fuels and surrogates. Any misalignment leads to non-negligible deviations in terms of s_L prediction. The H/C and O/C ratios are in good agreement as well, as visible in Figures 3.28(c)-(d). As for real gasoline-ethanol blend, data dispersion for the H/C ratio is higher for poorly oxygenated blends, similarly to liquid density data from literature depicted in Fig. 3.28(a). Conversely, an opposite trend is found for the O/C ratio, which exhibits higher dispersion for higher ethanol contents. This behavior can be explained considering the slight differences in the ethanol content, compared to the nominal values, in the commercial blends. Moving to the auto-ignition tendency of the surrogates, a wide RON dataset of gasoline-ethanol blends is available for validation. The dataset includes several engine-based experiments (dotted lines) and a few data coming from previous studies (solid lines) [210,211,212], aiming at formulating multicomponent surrogates able to predict gasoline-ethanol blend auto-ignition tendency. Such a goal is not straightforward, as ethanol acts synergistically with isooctane and toluene and antagonistically with n-heptane, in terms of octane numbers [210]. This motivates the non-linear increase of RON with increasing ethanol content, as shown in Fig. 3.29(a). Generated surrogates are able to reproduce this non-linear behaviour consistently. Although [59,118,119] proposed a valid and detailed approach for targeting octane numbers non-linear behaviour when ethanol is added to hydrocarbon mixtures, Pera et al. [65] demonstrated that a linear mole-weighted mixing rule is able to provide very close estimations of RON and MON compared to the non-linear approaches proposed in [59,116,117,119]. This comparison carried out by Pera et al [65], highlighted a negligible deviation of the linear rule within 35%vol content, which is the standard aromatic content for commercial gasoline. As for the literature data dealing with the octane numbers, the higher data dispersion for poorly oxygenated blends is due to different gasolines for the blend formulations. The non-linear increase of MON with ethanol is qualitatively captured as well. In this case, a quantitative misalignment is noticed, due to the overestimation of the gasoline MON, which is an intrinsic limitation of the ternary approach to formulate a gasoline surrogate. A better estimation of the MON could be obtained formulating the gasoline surrogate with a higher number of components. Fig. 3.29(c) shows LHV, which decreases increasing the ethanol content. $1D$ outcomes match satisfactorily the experimental data. Finally, an estimation of the blend boiling point can be obtained via the simple approach proposed in [127]. Fig. 3.29(d) reveals that the proposed methodology is qualitatively able to match the decreasing trend of T_b as a function of the ethanol content, but the absolute value is generally over-predicted. In particular, for ethanol content higher than 40 vol%, the hydrocarbon and ethanol mixture exhibit an azeotropic behavior [213]. Ignoring this effect leads to an higher reckoned mixture T_b. In the present work, this facet is neglected since T_b is not among the targeted properties. However, due to the importance of fuel evaporation induced mixture cooling, a better estimate of the boiling point is highly desirable, and it will be one of the key topics for further development of the methodology.

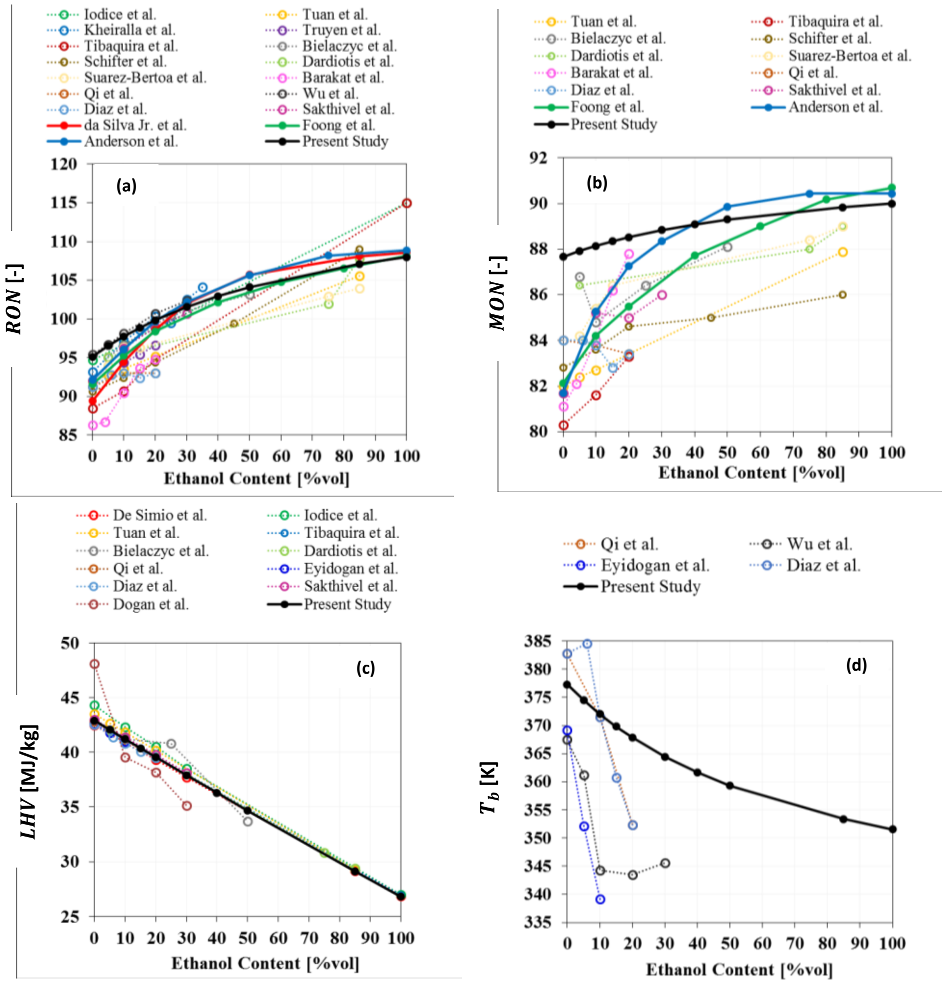

Figure 3.29. (a) Research Octane Number, (b) Motor Octane Number, (c) Lower Heating Value at ambient conditions, (d) Boiling point. Dotted lines report values from literature, while solid ones represent properties calculated with the proposed methodology.

Chapter 4: Laminar Flame Speed Modelling

4.1 Laminar Flame Speed in Combustion Modelling

4.1.1 Relevance in Flamelet Combustion Models

One of the most widely exploited concepts in engine combustion simulation is the flamelet hypothesis, which assumes a time-scale separation between the turbulent eddy turn-over time and the combustion time-scale [214]. Given the shorter duration of the latter, turbulent mixing is the global rate-controlling process and the flame front preserves its laminar-like inner structure, with turbulence acting as a surface-amplifier for reactant interface. This assumption allowed researchers to develop combustion models based on the flamelet concept, where s_L of a given air-fuel mixture is a model input and the turbulence effect on the flame surface is modelled. In the $ECFM$ [39] combustion model family the Flame Surface Density Σ (FSD) concept is adopted, whose transport equation is reported in Eq. 4.1

$$\frac{\partial\Sigma}{\partial t} + \nabla\cdot(\tilde{u}\Sigma) = \nabla\cdot(D_t\nabla\Sigma) + C_1\frac{\varepsilon}{k}\Sigma - C_2 s_L\frac{\Sigma^2}{1-\tilde{c}} \tag{4.1}$$

Using FSD the model takes into account for the geometrical amplification of the reaction surface area per volume unit operated by turbulence. The turbulent burn rate (ω) is given by:

$$\omega = \rho_u Y_F \Sigma s_L \tag{4.2}$$

where Y_F fuel mass fraction and ρ_u the unburnt mixture density. All the invoked quantities but s_L are calculated through transport equations, while s_L is defined based on available correlations such as the Methghalchi and Keck's [215] or the Gülder's [216] formulation. Another popular flamelet model is the G-equation (or Level Set) model [40], where the mean flame brush position is associated to the iso-level of a passive transported G-scalar (Eq. 4.3) and its variance G' (Eq. 4.4).

$$\frac{\partial}{\partial t}\rho G + \frac{\partial}{\partial x_i}\rho u_i G = \rho s_T|\nabla G|\, with\, s_T = f(s_L) \tag{4.3}$$

$$\frac{\partial}{\partial t}\rho G' + \frac{\partial}{\partial x_i}\rho u_i G' - \rho s_T\frac{\nabla G'\cdot\nabla G}{|\nabla G|} = 2\frac{\mu_t}{\sigma_t}\left[\frac{\partial G}{\partial x_i}\frac{\partial G}{\partial x_i}\right] - c_s\rho\frac{\varepsilon}{k}G' \tag{4.4}$$

where $c_s = 2$ and s_T is the turbulent flame speed. In this model, the turbulent burn rate is modelled through empirical correlations, accounting for the laminar velocity s_L amplification experimentally measured under turbulent conditions. Such amplification can be represented as first-order dependent on the local turbulence intensity u' only [217], although refined formulations considering non-dimensional groups are proposed in [218,219] to consider the conflicting nature of burn rate promotion and of flame quenching given by ever-increasing turbulence levels. Focusing on the role of s_L, this is the only input variable used for burn rate reconstruction, therefore its accurate definition emerges as a crucial aspect. The two mentioned combustion models have widespread application in the engine community and both rely on the definition of a mixture s_L to express the burn rate dependence on local thermodynamic parameters, without the direct solution of any chemical reaction. As previously mentioned, s_L is, by definition [50], a mixture property depending on p, T_u, ϕ and EGR which is quantitatively expressed hereafter in terms of residuals mass fraction Y_{res}. As anticipated, the most common approach is to calculate s_L using polynomials defined as fitting functions of available experimental data. They usually take the form of power-laws (Eq. 4.5), such as in [215] for which coefficients for the flame speed at ambient conditions $s_{L,0}$ are proposed for iso-octane, propane, methanol and for a commercial gasoline (RMFD-303), while temperature and pressure exponents (α and β, respectively) are a function of ϕ only and are restricted to the range $\phi = 0.8 - 1.5$.

$$s_L = s_{L,0}\left(\frac{T_u}{T_0}\right)^{\alpha}\left(\frac{p}{p_0}\right)^{\beta}(1 - f_{res}\cdot Y_{res}) \tag{4.5}$$

A similar formulation, albeit with different coefficients, is found in other widely adopted correlations, such as the one proposed by Gülder [216] or by Rhodes and Keck [220]. While the former suggests s_L values for RMFD-303 in the range $\phi = 0.7 - 1.6$ from 1 to 8 bar, the latter is valid for pressures below 12 atm in the same range ϕ range.

4.1.2 Issues at Engine Conditions

None of the above correlations is deemed to be valid at engine-typical conditions, where pressure and temperature simultaneously increase and large ϕ variations are potentially experienced by the flame. Focusing on the experimental determination of s_L, a huge though poorly coherent literature survey is possible. The framework is made even more complex by relevant pioneering studies of spherically expanding flames where the effect of flame stretch was neglected, as exhaustively reported by Gillespie et al. in [221]. This is part of the reason of the very sparse dataset of s_L present in literature for the same fuels. The recent development of techniques for flame speed measurement error minimization such as [222] allows to improve the data interpretation when comparing different experiments. Experimental studies in literature focused on s_L measurements for pure compounds [223,224,225,228], alcohols [226,227], gasoline [76,77] and blends [76,231,232]. All these studies were carried out at ambient conditions or at low pressures and temperatures. Although being not fully representative of engine-like conditions the most interesting measurements are reported in the studies by Jerzembeck et al. [75] and Di Lorenzo et al. [79], previously used as target and validation datasets in Chapter 3. As shown in Chapter 3, chemical kinetics mechanisms [60,61,62,63] are able to accurately describe s_L at these conditions, if a an accurate fuel surrogate is used, since mechanisms are usually validated up to 50 bar [60,61,62,63]. Vancoillie et al. first attempted in [230] to rely on results from validated chemical mechanisms well outside the validation range to cover engine-typical pressure and temperature ranges, and s_L and flame thickness (δ_L) correlations were proposed to be used in engine combustion models. A common limitation of all the examined studies is that all the mentioned mechanisms were validated against experiments representative, to a limited extent, of the actual conditions experienced by SI engine flames, at least at high to full load conditions. In order to overcome this limitation (i.e. relying on low p-T_u experiments only), a simulation study based on chemical mechanisms is conducted at engine-typical gas states, although mechanisms are only validated at different test conditions, as previously outlined. However, model-based simulation of s_L at engine conditions is considered to be more adherent to flame chemistry than simply relying on polynomial extrapolations. A chemistry-based approach is therefore proposed to estimate s_L at engine-like conditions based on $1D$ freely propagating simulations, used to provide correlations able to mimic dependency on local (p, T_u, ϕ, EGR) conditions experienced by flames in numerical simulations. The main reasons for this approach are:

- Retained CPU-efficiency: the final outcome of this study is an algebraic correlation similar to [215,216,220] though based on chemistry simulations, hence no computational overload is demanded to the CFD solver. The proposed correlation finds immediate application in the most widespread combustion models.
- Reduced chemical kinetics effort: the identification of engine-relevant (p,T_u) states is used to restrict the number of s_L simulations only to conditions at which flames actually exist in engines. Conversely, if look-up tables (instead of correlations) were used, the number of needed states for multi-linear interpolation would be much higher.
- Improved chemistry accuracy: the proposed polynomials for s_L are based upon validated chemical mechanisms [60,61,62,63]. Despite their application outside the validation range, the predicted s_L results are still based on complex chemistry outcomes rather than on physics-unrelated polynomial extrapolations, as with [215,216,220].
- Insight into relevant pathways/reactions for s_L at engine conditions: the proposed method can be used to study the role of individual chemical reactions on overall flame speed, with particular emphasis on those involving unstable chemical species.

⬡ 4.2 Typical Engine Conditions

An exploration study is at first carried out regarding the p-T_u history experienced in SI units operated under full-load and part-load conditions. Hereafter, p and T_u are considered, while the effect of mixture composition (i.e. ϕ and Y_{res}) will be addressed in the next paragraph. The unburnt temperature T_u (i.e. the temperature of the non-reacting air-fuel mixture) is not affected by combustion through chemical reactions, although the effect of developing combustion is present through gas compression: fresh mixture is heated because of cylinder pressure increase, well before flame front reactions. This explains the simultaneous increase of both p and T_u. An analysis of several SI engines operated at different OPs is carried out to verify whether typical ranges of thermodynamic conditions can be identified. As for T_u, this is calculated by the CFD solver through the energy equation in terms of unburnt enthalpy h_u, finally converted into T_u through the mixture specific heat. Following the mentioned link between p and T_u, this last can be alternatively calculated based on the polytrophic compression-expansion law (Eq. 4.6), where the γ exponent (i.e. the ratio of isobaric over isochoric mixture specific heat) should consider the heat loss through the metal walls and it usually ranges in-between 1.30-1.33.

$$T_{u,i} = T_{u,i-1} \left(\frac{p_i}{p_{i-1}}\right)^{\frac{\gamma-1}{\gamma}} \tag{4.6}$$

This second method is pursued and the best results are obtained using $\gamma = 1.32$ for all the engines/OPs. The error with respect to the exact T_u value given by the dedicated h_u equation is approximately 10 K, which is considered as acceptable. The results are reported in Fig. 4.1, in terms of (p, T_u) history, from combustion onset to peak pressure for different engine architectures, loads and speeds. The main characteristics of each engine/OP are reported in Table 4.1. As visible, despite the ranges of architectures (bore/stroke, number of cylinders) and OPs (load, speed, average ϕ) draw a wide matrix, all the (p,T_u) traces lie in a rather restricted band for full-load conditions. A wider scatter is observable for part-load conditions due to similar temperature levels but much lower pressure values. Based on this observation, engine-typical conditions for pressure and temperature can be identified to be representative for full-load and part-load operations on a generic SI engine. Such conditions constitute a discrete matrix of reference thermodynamic conditions, Engine Conditions (EC), for which chemistry-based s_L $1D$ freely propagating simulations are carried out.

Engine Name	Engine Speed	Engine Architecture/Displacement	Average ϕ	SOC [CAD bTDC]
Engine A	7000 rpm	V8 / 5000 cm^3	1.3	15
Engine B	1500 rpm	4-Line / 1800 cm^3	1.0	-5
Engine B	5000 rpm	4-Line / 1800 cm^3	1.0	10
Engine C	2000 rpm	4-Line / 2000 cm^3	0.9	0
Engine C	3200 rpm	4-Line / 2000 cm^3	0.9	3
Engine C	6000 rpm	4-Line / 2000 cm^3	0.9	6
Engine D	2000 rpm	V6 / 3800 cm^3	1.1	0
Engine D	5200 rpm	V6 / 3800 cm^3	1.1	12
Engine E	5000 rpm	V8 / 3900 cm^3	1.1	10
Engine E	7000 rpm	V8 / 3900 cm^3	1.15	15
Engine F	6500 rpm	V8 / 3900 cm^3	1.3	13
Engine G	5200 rpm	4-Line / 2000 cm^3	1.05	8
Engine G	6000 rpm	4-Line / 2000 cm^3	1.1	12
Engine H	2000 rpm	4-Line / 1600 cm^3	1.05	16
Engine H	1500 rpm	4-Line / 1600 cm^3	1.05	16
Research Engine OP1	2000 rpm	Single Cylinder	1.0	30
Research Engine OP2	2000 rpm	Single Cylinder	1.0	15
Research Engine OP3	2000 rpm	Single Cylinder	1.0	30
Research Engine WOT	2000 rpm	Single Cylinder	1.0	15

Table 4.1. List of SI engines and operating conditions investigated under full-load and part-load operation.

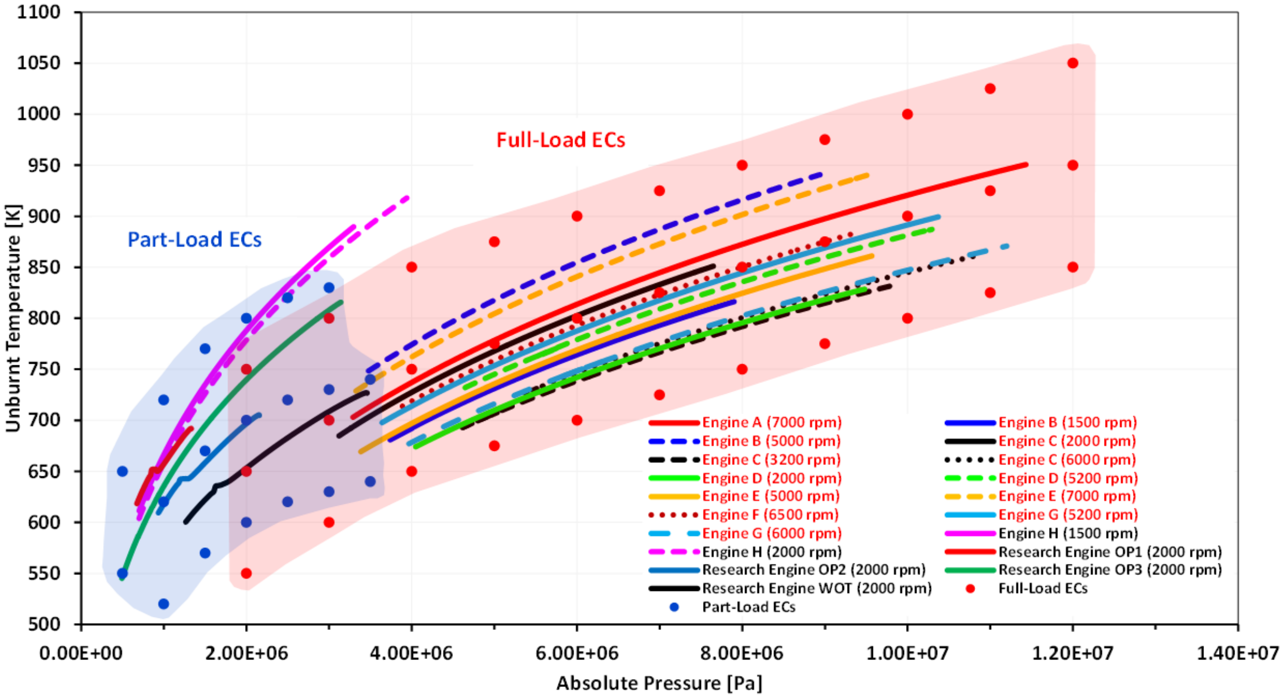

Figure 4.1. p,T_u traces for all the operating conditions considered from spark time to peak pressure. Red dots: Full-load engine conditions. Blue dots: Part-load engine conditions.

In order to further extend the validity of the proposed correlations, a possible temperature variation (range ±100 K) is assumed for each pressure level (e.g. to account for higher/lower charge cooling levels). This justifies the T_u uncertainty deriving from the use of Eq. 4.6. Moreover, it is noteworthy that selected points can be further identified in three different T_u levels, for a given pressure, here referred to as Low (LOW), Medium (MED) and High ($HIGH$). Therefore, reference ECs for part-load and full-load OPs are represented with blue and red dots, respectively, in Fig. 4.1. Once a dataset of s_L is simulated for conditions fully covering the thermodynamic range experienced by the flame for different SI engines/OPs, it is used to define s_L correlations valid for generic part-load and full-load SI combustion. The relevant computational benefit given by the proposed approach is that s_L calculation is restricted to conditions actually experienced by the flame in actual engines, thus concentrating the simulation effort where this is needed and avoiding calculating s_L for unrealistic states (e.g. (10 bar,1000 K) or (100 bar, 400 K). With particular reference to the part-load selected ECs, it is noteworthy that points were chosen to create a dedicated correlation for the research engine investigated in the present work to ensure maximum accuracy. A general purpose part-load correlation was formulated but not reported in the present thesis for the sake of brevity. Consequently, s_L correlations derived from simulations are valid in the red-shaded and blue-shaded areas reported in Fig. 4.1. The choice of formulating dedicated correlations for part-load and full-load conditions is not ideal but allows a higher degree of accuracy during the fitting procedure, compared to the one obtained using a single correlation covering the entire (p,T_u) map.

⬡ 4.3 Laminar Flame Speed Correlation Methodology

In the following paragraph, the methodology used to derive chemistry-based s_L correlations is described in detailed. Such methodology has general validity and can be used to model any kind of fuel on desired thermodynamic and mixture quality states. For this reason, the methodology is presented in its general form and results given by the correlation on part-load and full-load conditions for commercial gasoline are presented in the following paragraphs.

⬡ 4.3.1 Fitting Methodology

Focusing on the evolution of the modelled physical phenomena, it is straightforward to notice that flames will experience not only variations in terms of local p and T_u but also a variety of ϕ and Y_{res} dependent on the local mixture quality. Ranges for ϕ and Y_{res} might depend on the specific engine and OP considered. In the present work, upper and lower limits for each variable were chosen based on $3D$-CFD analysis of the engine cases previously presented in Table 4.1. In particular, s_L is calculated from $\phi = 0.4$ to $\phi = 2.0$ (step $\phi = 0.1$, 17 points) and for residuals mass fraction $\mathrm{Y_{res}}$ in the range 0%-20% (step $\mathrm{Y_{res}} = 5\%$, 5 points). As for residuals composition, combustion products concentrations for the specific ϕ value are used. Simulations are carried out for each EC identified in Fig. 4.1. Simulations are carried out using a $1D$ unstretched flame model (i.e. freely propagating) available in DARSv2019.1, in which the steady-state conditions in terms of species concentrations is calculated on a spatial grid consisting of 150 to 300 points, non-uniformly distributed and dynamically moved along the flame profile based on local temperature and species concentration gradients. Once a steady-state profile is obtained for all the intermediate species, the resulting s_L value used in the present study is the opposite velocity of the free air/residuals stream feeding the flame. In the present work, multiple chemical kinetics mechanisms are used to perform such kind of simulations. As previously mentioned this choice is undertaken in order to dampen possible unfeasible predictions given by a single mechanism due to an excessive numerical stiffness in specific conditions. This rationale is further supported by the evidence that chemical kinetics mechanisms available in literature are not validated at such high (p,T_u) values. In other words, this approach allows to estimate average chemistry-based s_L values relying on the prediction of multiple mechanisms. In the present work, Andrae's [60,61,62] and PoliMi [63] well-validated mechanisms for gasoline are used for s_L prediction. An additional mechanism, proposed by Cai et al. [59], is also used to estimate s_L conditions in order to increase the number of evaluations in conditions extremely out of mechanisms validation range. Such procedure is not necessary at part-load conditions, which are definitely closer to mechanisms validation range. In these conditions, mechanisms are found to give very similar predictions, allowing a decrease of the overall computational cost. Sticking to the specific case presented in Chapter 5, correlations are presented in this work for a European $RON95$ $E5$ gasoline, which has been used to fuel the research engine in the experiments used as reference in Chapter 5. Therefore, the $ETRF$ fuel surrogate formulated in Chapter 3.1, targeting ULG95 gasoline, has been used to perform $1D$ freely propagating simulations with the adopted mechanisms. Since multiple mechanisms are used, for each single (p, T_u, ϕ, EGR) condition, different s_L values are available from chemical kinetics calculations. Based on the previously explained rationale, the target s_L for the fitting procedure is defined as the algebraic mean of the s_L values obtained with the mechanisms considered. An ad-hoc fitting polynomial is calculated to efficiently use the discrete dataset of calculated s_L. The procedure follows the approach proposed in [233], where an assumption is made that s_L dependence on p, T_u and ϕ can be expressed by a commonly adopted power-law relationship such as that in Eq. 4.5, once accurate forms for $s_{L,0}$, α and β are given. The effect of residuals will be discussed separately. In the proposed approach, s_L simulations serve as virtual experiments of flame speed; $s_{L,0}$, α and β have then to be fitted on simulation results. A fifth order logarithmic polynomial form is used as functional fitting form, as shown in Eq. 4.6.

$$s_L = \left[\sum_{i=0}^{5} a_i \cdot log(\phi)^i\right] \cdot \left(\frac{T}{T_0}\right)^{\sum_{i=0}^{5} b_i \cdot log(\phi)^i} \cdot \left(\frac{p}{p_0}\right)^{\sum_{i=0}^{5} c_i \cdot log(\phi)^i} \tag{4.7}$$

This relationship is still based upon the power-law formalism of Eq. 4.5, although the definition of $s_{L,0}$, α and β follows a 5^{th} order logarithmic function of ϕ through the coefficients a_i, b_i and c_i respectively. The a_i coefficients describe ϕ dependence of s_L at reference conditions, and they are grouped in the $\bar{A}$ vector, which is determined by a least square minimization of the system in Eq. 4.8. Reference conditions p_0, T_0 can be, deliberately, chosen for the fitting procedure.

$$\begin{bmatrix} s_{L,0}(\Phi_1) \\ s_{L,0}(\Phi_2) \\ \vdots \\ s_{L,0}(\Phi_n) \end{bmatrix} = \begin{bmatrix} 1 & ln(\Phi_1) & [ln(\Phi_1)]^2 & \cdots & [ln(\Phi_1)]^5 \\ 1 & ln(\Phi_2) & [ln(\Phi_2)]^2 & \cdots & [ln(\Phi_2)]^5 \\ \vdots & \vdots & \vdots & \ddots & \vdots \\ 1 & ln(\Phi_n) & [ln(\Phi_n)]^2 & \cdots & [ln(\Phi_n)]^5 \end{bmatrix} \cdot \underbrace{\begin{bmatrix} a_1 \\ a_2 \\ \vdots \\ a_n \end{bmatrix}}_{\bar{A}} \tag{4.8}$$

Similarly, chemistry-based correlations for s_L variation with temperature and pressure (hereafter $s_{L,pT}$) are expressed by the six b_i and the six c_i coefficients, grouped in the $\bar{B}$ vector and similarly determined by a least square minimization of the system (Eq. 4.9). The $\bar{\bar{L}}_{Tp}$ is composed by $\bar{\bar{L}}_T$ and $\bar{\bar{L}}_p$ matrices (Eq. 4.9 and 4.10), illustrated as separate for the sake of clarity.

$$\begin{bmatrix} ln\left(\frac{s_{L,pT}(\Phi_1)}{s_{L,0}(\Phi_1)}\right) \\ ln\left(\frac{s_{L,pT}(\Phi_2)}{s_{L,0}(\Phi_2)}\right) \\ \vdots \\ ln\left(\frac{s_{L,pT}(\Phi_n)}{s_{L,0}(\Phi_n)}\right) \end{bmatrix} = \underbrace{\left[\bar{\bar{L}}_T \; \bar{\bar{L}}_p\right]}_{\bar{\bar{L}}_{Tp}} \cdot \underbrace{\begin{bmatrix} b_1 \\ b_2 \\ \vdots \\ b_n \\ c_1 \\ c_2 \\ \vdots \\ c_n \end{bmatrix}}_{\bar{B}} \tag{4.9}$$

$$\bar{\bar{L}}_T = \begin{bmatrix} ln\left(\frac{T}{T_0}\right) & ln\left(\frac{T}{T_0}\right) \cdot ln(\phi_1) & ln\left(\frac{T}{T_0}\right) \cdot [ln(\phi_1)]^2 & \cdots & ln\left(\frac{T}{T_0}\right) \cdot [ln(\phi_1)]^5 \\ ln\left(\frac{T}{T_0}\right) & ln\left(\frac{T}{T_0}\right) \cdot ln(\phi_2) & ln\left(\frac{T}{T_0}\right) \cdot [ln(\phi_2)]^2 & \cdots & ln\left(\frac{T}{T_0}\right) \cdot [ln(\phi_2)]^5 \\ \vdots & \vdots & \vdots & \ddots & \vdots \\ ln\left(\frac{T}{T_0}\right) & ln\left(\frac{T}{T_0}\right) \cdot ln(\phi_n) & ln\left(\frac{T}{T_0}\right) \cdot [ln(\phi_n)]^2 & \cdots & ln\left(\frac{T}{T_0}\right) \cdot [ln(\phi_n)]^5 \end{bmatrix} \tag{4.10}$$

$$\bar{L}_p = \begin{bmatrix} ln\left(\frac{p}{p_0}\right) & ln\left(\frac{p}{p_0}\right)\cdot ln(\phi_1) & ln\left(\frac{p}{p_0}\right)\cdot [ln(\phi_1)]^2 & \cdots & ln\left(\frac{p}{p_0}\right)\cdot [ln(\phi_1)]^5 \\ ln\left(\frac{p}{p_0}\right) & ln\left(\frac{p}{p_0}\right)\cdot ln(\phi_2) & ln\left(\frac{p}{p_0}\right)\cdot [ln(\phi_2)]^2 & \cdots & ln\left(\frac{p}{p_0}\right)\cdot [ln(\phi_2)]^5 \\ \vdots & \vdots & \vdots & \ddots & \vdots \\ ln\left(\frac{p}{p_0}\right) & ln\left(\frac{p}{p_0}\right)\cdot ln(\phi_n) & ln\left(\frac{p}{p_0}\right)\cdot [ln(\phi_n)]^2 & \cdots & ln\left(\frac{p}{p_0}\right)\cdot [ln(\phi_n)]^5 \end{bmatrix} \tag{4.11}$$

The outlined procedure determines the set of eighteen simulation-based coefficients providing a closure to the polynomial in Eq. 4.7. Finally, s_L reduction due to residuals is accounted for by a linear decrease rate, similarly to what proposed in [215], as a function of the diluent mass fraction Y_{res} as in Eq. 4.5. In [215] $f_{res} = 2.1$, while here f_{res} factor is expressed through Eq. 4.12 and 4.13 as the relative s_L loss as a function of Y_{res}.

$$s_{L,res} = s_{L,pT} \cdot (1 - f_{res} \cdot Y_{res}) \tag{4.12}$$

$$f_{res} = \frac{1}{Y_{res}} \cdot \left(1 - \frac{s_{L,res}}{s_{L,pT}}\right) \tag{4.13}$$

Fuel-specific f_{res} is calculated by the analysis of the simulated flame speeds for increasing EGR rates. A linear decreasing behaviour was observed for a wide variety of fuels throughout the entire range of simulated Y_{res}. A fuel-specific f_{res} coefficient is then defined based on flame simulations. The final correlation for s_L is therefore modified as in Eq. 4.14.

$$s_{L,res} = \left[\sum_{i=0}^{5} a_i \cdot log(\phi)^i\right] \cdot \left(\frac{T}{T_0}\right)^{\sum_{i=0}^{5} b_i \cdot log(\phi)^i} \cdot \left(\frac{p}{p_0}\right)^{\sum_{i=0}^{5} c_i \cdot log(\phi)^i} \cdot (1 - f_{res} \cdot Y_{res}) \tag{4.14}$$

Using the presented methodology, a fuel-specific polynomial form for s_L speed at engine-like conditions is proposed and can be generated for any kind of fuel if an appropriate fuel model (i.e. a well-validate chemical kinetics mechanism and a fuel surrogate able to represent its combustion-relevant characteristics) is available. As a further remark, the outlined methodology is used to fit chemistry-based s_L simulated dataset on a limited part of the entire ϕ domain considered in $1D$ simulations. In particular, this procedure is used to fit data in the ϕ = 0.7-1.4 range. This approach is used to maximize fitting accuracy in order to represent with high fidelity s_L around stoichiometry, which is usually the range of major interest for CFD simulations. This also allows to correctly represent s_L peak which is usually predicted around ϕ = 1.1 for a wide variety of hydrocarbons. A dedicated fitting methodology is therefore presented in the next paragraph to fit simulated data for lean and rich mixtures. This aspect is particularly important since, as already shown in Paragraph 3.2.5 and outlined more in detail in Chapter 5, GDI technology is likely to produce very lean and rich mixture pockets, especially at part-load condition. Furthermore, flames at part-load OPs usually experience T_u levels similar to those found at full-load OPs but at much lower pressure levels. A dedicated Temperature-Pressure Scaling (TPS) methodology is therefore formulated to take into account for the separate contributions of p and T_u on s_L for ultra-lean and ultra-rich mixtures. Since temperature scaling effect is more pronounced at part-load conditions, simulated gasoline s_L dataset at part-load ECs is exploited to better explain the proposed methodology

4.3.2 Fitting Extensions and Temperature-Pressure Scaling Methodology

In the present paragraph, a methodology is presented, firstly, to take into account for pressure scaling effect and, secondly, to consider temperature effect as well. Finally, a comprehensive formulation is considered to simultaneously combine pressure and temperature effects in a unique scaling factor. As a first step, pressure effect for rich mixtures is investigated. Focusing on the rich mixture side, s_L results from ϕ = 1.4 to ϕ = 2.0 are normalized based on their value at ϕ = 1.4, as in Eq. 4.15. In a similar manner, a similar definition can be introduced for lean mixtures in Eq. 4.16.

$$s_L^{n,rich}(\phi) = \frac{s_L(\phi)}{s_{L,\phi=1.4}} \tag{4.15}$$

$$s_L^{n,lean}(\phi) = \frac{s_L(\phi)}{s_{L,\phi=0.7}} \tag{4.16}$$

Therefore, the normalized s_L for rich mixtures, $s_L^{n,rich}$, is studied for all the calculated ECs, ranging below 100% (s_L value for ϕ = 1.4). A fitting function is proposed considering that the slope of $s_L^{n,rich}$ for all the ECs is similar regardless the specific (p,T_u): this states that the rich-side slope of $s_L^{n,rich}$ (ϕ) shows a reduced sensitivity to the EC. Therefore, the chemistry-based polynomial correlation in Eq. 4.16 is introduced an acts, via $|\phi - 1.4|/\phi_{max} - 1.4$ term, as an efficiency function to account for an observed pressure-scaling dependency of $s_L^{n,rich}$ for ϕ higher than the reference value 1.4, i.e. it is null for ϕ = 1.4 and equal to 1.0 for ϕ = 2.0. For this reason, Eq. 4.16 provides a Pressure Scaling Factor (PSF) used to evaluate pressure effect on s_L scaling while increasing ϕ and varying pressure level from p_{ref} value, which is arbitrarily chosen. In the specific case of the part-load correlation used in the present work for $3D$-CFD simulations $p_{ref} = 20\ bar$.

$$PSF^{rich}(\phi) = \frac{r_3|\phi-1.4|^2+r_2|\phi-1.4|^2+r_1|\phi-1.4|+r_0}{r_0} \cdot \left[1 + m' \frac{p_{[bar]}-p_{ref}}{p_{ref}} \cdot \frac{|\phi-1.4|}{|\phi_{max}-1.4|}\right] \tag{4.17}$$

where ϕ_{max} is the richest mixture considered in freely propagating simulations and r_3, r_2, r_1, r_0 are fitting coefficients. An analogous expression, reported in Eq. 4.18, is used to take into account for pressure effect in lean mixtures introducing the so-called Pressure Scaling Factor (PSF). In this case, s_L scaling is investigated for mixtures leaner than a threshold value equal to ϕ = 0.7.

$$PSF^{lean}(\phi) = \frac{l_3|\phi-0.7|^2+l_2|\phi-0.7|^2+l_1|\phi-0.7|+l_0}{l_0} \cdot \left[1 + m" \frac{p_{[bar]}-p_{ref}}{p_{ref}} \cdot \frac{|\phi-0.7|}{|\phi_{min}-1.4|}\right] \tag{4.18}$$

where ϕ_{min} is the leanest mixture considered in freely propagating simulations and l_3, l_2, l_1, l_0 are fitting coefficients. The extrapolation to leaner mixtures indicates for all fuels a lower flammability limit at approximately ϕ = 0.4, in agreement with indications found in [234]. Now that dedicated expressions are available to model s_L dependence on pressure, it is mandatory to investigate temperature effect. In order to further support the need for a more detailed investigation, simulated s_L values (normalized over ϕ = 0.7 reference value) are reported, for a subset of part-load ECs, in Fig. 4.2 to understand the relative effect of pressure and temperature. In Fig. 4.2, ECs with the same pressure level are classified by colour while low, medium and high temperature level, for a given pressure level, are identified by different symbol shapes. In particular, circles are for low temperature level, triangles for medium temperature level and squares for high temperature level. It is straightforward to notice how the points, for a given ϕ, are rather gathered by shape than by colour, though a colour gradient is still observable. This means that temperature has a major influence on s_L values. A further evidence is given by the reduced difference, in terms of normalized s_L values, among ECs with similar temperature levels and different pressure levels. This further support the need for an additional methodology able to separately consider temperature effect while reconstructing s_L values for lean and rich extensions. Since points represented in Fig. 4.2 are gathered accordingly to temperature level a fitting procedure for the three different levels is required in order to model temperature effects. In order to find a dependence of normalized s_L values on temperature level and ϕ, calculated s_L values are reported in Fig. 4.3 as a function of ϕ and a normalized temperature, where T_{ref} = *550 K* is adopted as reference temperature for the present analysis at part-load conditions.

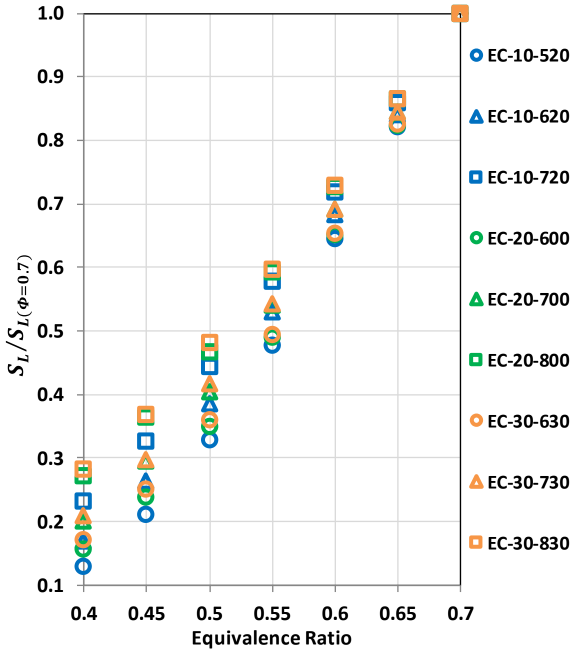

Figure 4.2 Normalized s_L values for $\phi < 0.7$ obtained from the chemical kinetics simulations for three selected ECs considered. Dot colours represent the pressure level while dot shapes represent the three temperature levels considered (low, medium and high).

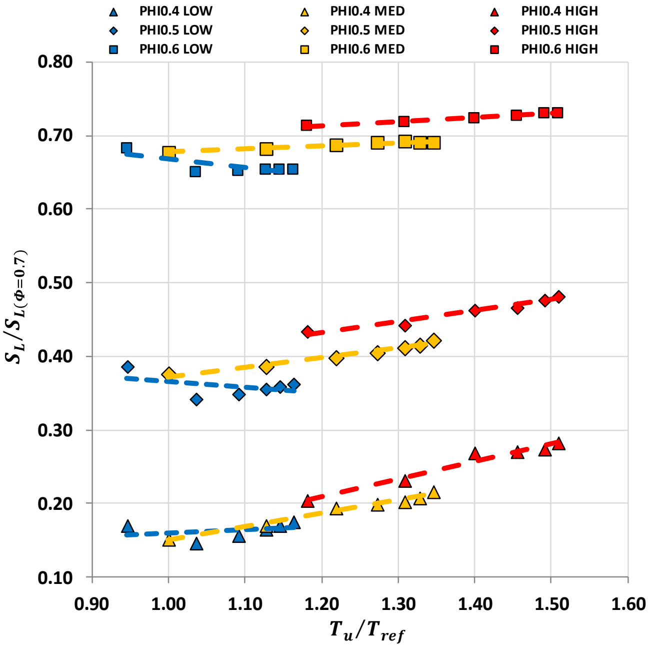

Figure 4.3 Dependence of normalized s_L values on equivalence ratio and normalized temperature (T_{ref} = 550 K) for $\phi < 0.7$. Dot shapes represent the equivalence ratios while colours represent the three temperature levels considered (low, medium and high).

Considering the trends shown in Figure 4.3, it is possible to conclude that normalized s_L dependence on temperature, for a given ϕ, is well represented by a linear function. Thus, a linear interpolation is considered for each temperature level and equivalence ratio value, totalling a number of nine different linear interpolations described by 18 coefficients (slope coefficient m and y-axis intercept coefficient q for each condition). At this point, a relationship to model the linear interpolation coefficients as a function of ϕ is considered. In fact, it is possible to notice how the dependence of m and q on ϕ can be efficiently described using a polynomial fitting, as represented in Fig. 4.4. Though the qualitative trends of the two coefficients as a function of ϕ could be satisfactorily described by a linear interpolation, a second order polynomial fitting is used in order to minimize the interpolation error avoiding at the same time the excessive use of fitting coefficients related to a higher order polynomial fitting.

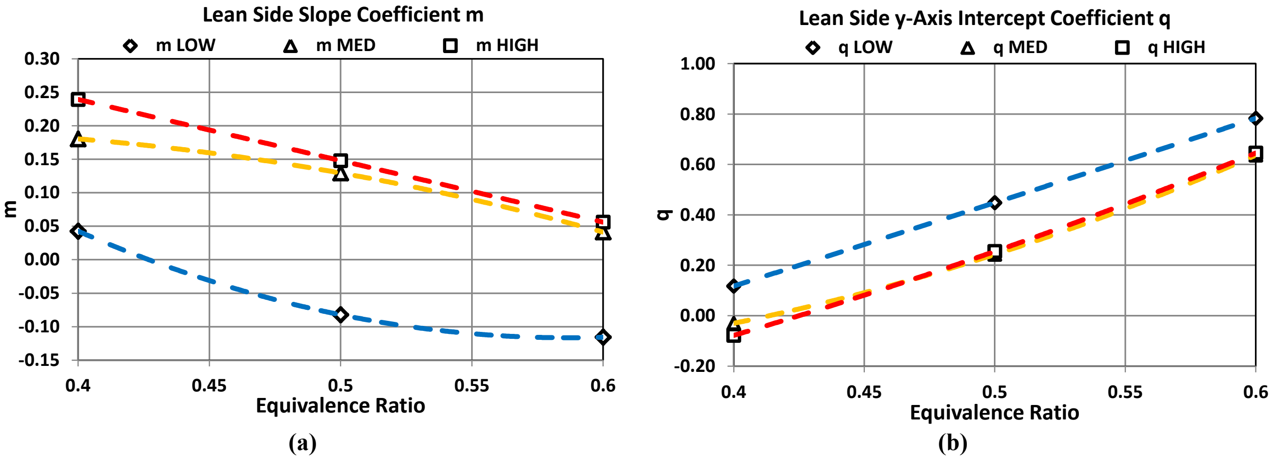

Figure 4.4 Lean mixtures slope coefficient m (a) and y-axis intercept coefficient q (b) dependence on equivalence ratio for the three temperature levels.

Second order interpolation is therefore the best trade-off between accuracy and efficiency. While a first order interpolation resulted to be enough accurate to describe coefficient q dependence on equivalence ratio, the results produced by a linear interpolation of the slope coefficient m produced a deviation of the predicted s_L from the calculated one. A set of 18 fitting coefficients is then derived to fit the slope coefficient m and the y-axis intercept coefficient q using a second order polynomial formulation; the coefficients are themselves used to fit by a linear interpolation the calculated s_L depending on ϕ and T_u for the three temperature levels. For instance, the slope coefficient of the low temperature fitting is reported in Eq. 5 for the sake of brevity.

$$m_{LOW}^{lean}(\phi) = lml_2 \cdot \phi^2 + lml_1 \cdot \phi + lml_0 \tag{4.19}$$

where lml_2, lml_1 and lml_0 are fitting coefficients. In the end, a Temperature Scaling Factor (TSF) representing the temperature scaling effect on the normalized s_L can be calculated for a given ϕ and for the low, medium and high temperature levels as reported in Eq. 4.20, Eq. 4.21, Eq. 4.22 respectively

$$TSF_{LOW}^{lean}(\phi, T_u) = m_{LOW}^{lean}(\phi) \cdot \frac{T_u}{T_{ref}} + q_{LOW}^{lean}(\phi) \tag{4.20}$$

$$TSF_{MED}^{lean}(\phi, T_u) = m_{MED}^{lean}(\phi) \cdot \frac{T_u}{T_{ref}} + q_{MED}^{lean}(\phi) \tag{4.21}$$

$$TSF_{HIGH}^{lean}(\phi, T_u) = m_{HIGH}^{lean}(\phi) \cdot \frac{T_u}{T_{ref}} + q_{HIGH}^{lean}(\phi) \tag{4.22}$$

The combination of TSF and PSF coefficients leads to the final fitting correlation in the form of a weighted average of the introduced scaling coefficients as shown in Eq. 4.23 for the low temperature fitting.

$$s_L^{n,lean}(\phi, T_u) = (PSF^{lean}(\phi) \cdot p_W + TSF_{LOW}^{lean}(\phi, T_u) \cdot T_W)/(p_W + T_W) \tag{4.23}$$

where p_W and T_W are weights respectively associated to pressure and temperature determined via a maximization of the determination coefficient R^2 in order minimize the deviation of the predicted s_L values from the target values. For the sake of consistency, the same weights are introduced both for lean and rich extension; for the present case the values ensuring the maximum accuracy are $p_W = 1$ and $T_W = 5$ though, in principle, the use of different coefficients for the two extensions could be justified by the different sensitivity of lean and rich mixtures to pressure and temperature. A comparison between Pressure Scaling (PS) and combined Temperature-Pressure Scaling (TPS) approaches is shown in Fig. 4.5.

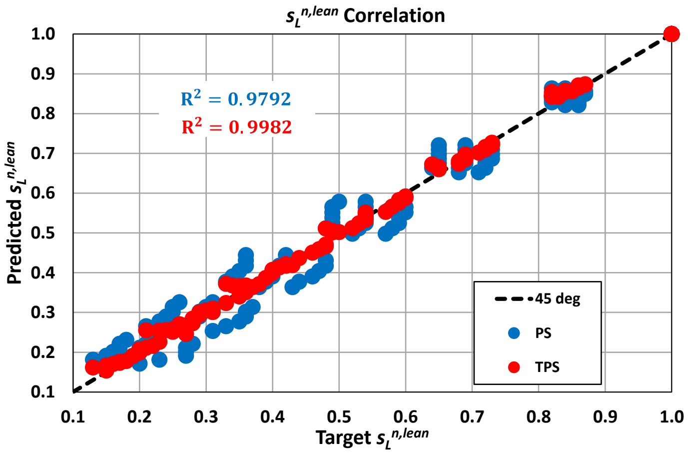

Figure 4.5 Correlation between s_L values obtained using pressure scaling (PS) and combined temperature-pressure scaling (TPS) for $\phi < 0.7$.

Observing the results, it can be stated that the higher complexity of the TPS approach, introduced to account for temperature dependence, is justified by a non-negligible increase in accuracy especially moving towards very lean mixtures. In fact, though variation in terms of absolute value may seem negligible, the relative error introduced by small variations of s_L are considerably high due to the low values typically encountered in ultra-lean conditions.

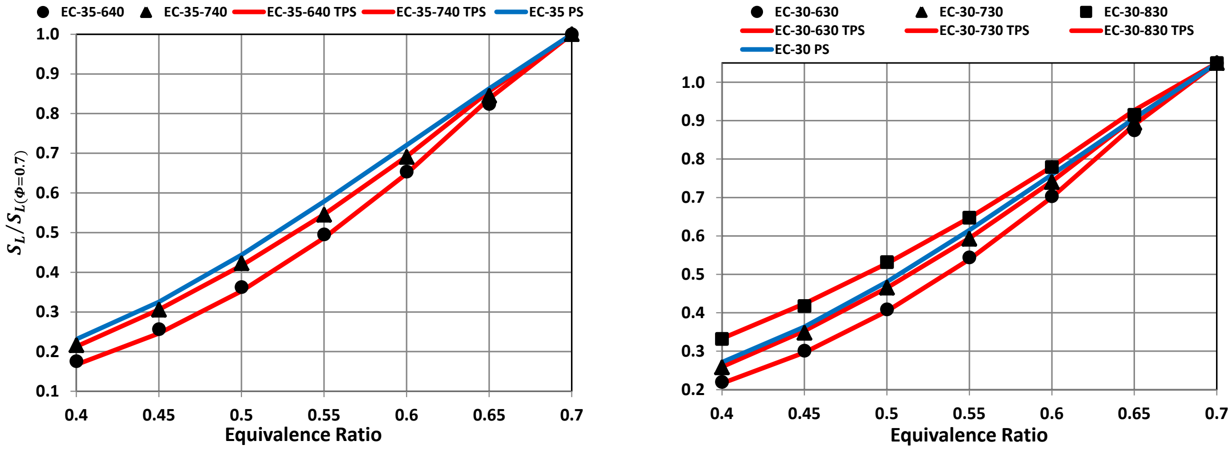

(a) (b)

Figure 4.6 Normalized s_L values predicted by pressure scaling (PS) and temperature-pressure scaling approach (TPS) for Φ<0.7 for (a) 35 bar and (b) 30 bar. Black-dashed data represent chemistry-based calculated values while blue and red lines represent calculated $s_L^{n,lean}$ with PS and TPS.

A further confirmation of the enhancement in terms of s_L prediction, achieved with the more complex TPS approach, is given by normalized s_L trends presented in Fig.4.6(a)-(b) for two selected ECs. The same methodology is used to the derive correlations valid for the rich mixture-side extensions starting from chemical kinetics results shown in Fig. 4.7, normalized based on the value at $\phi = 1.4$ for each EC considered accordingly to Eq. 4.14.

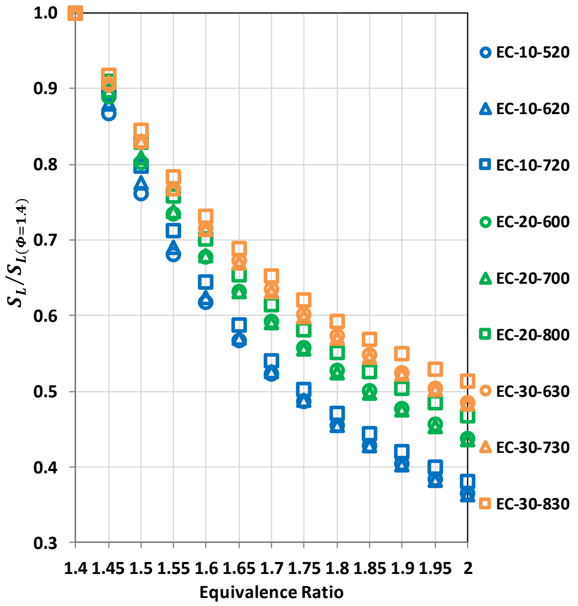

Figure 4.7 Normalized s_L values for $\phi > 1.4$ obtained from chemical kinetics simulations for three selected ECs considered. Normalized s_L values for $\phi > 1.4$. Colors represent the pressure level while dot shapes represent the temperature level (low, medium and high).

Compared to the results presented for the lean-side, rich-side ones are rather gathered by colour and not by shape as the former ones, meaning that pressure is the parameter of major influence although the effect of temperature is still present. In Fig. 4.8, normalized s_L values are reported as a function of ϕ and the temperature normalized over $T_{ref} = 550\ K$. Again, calculated s_L values are classified in three different temperature levels and the previously outlined procedure is followed. Coherently with the previous discussion, temperature dependence can be satisfactorily represented using a linear interpolation, for different ϕ levels.

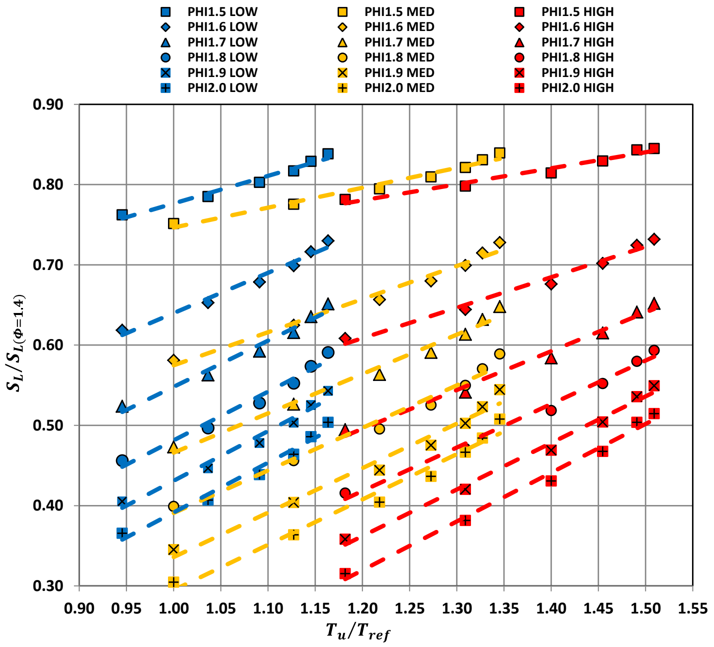

Figure 4.8 Dependence of normalized s_L values on ϕ and normalized temperature (T_{ref} = 550 K) for $\phi > 1.4$. Dot shapes represent the ϕ value while colors represent the temperature level considered (low, medium and high).

Following an analogous rationale, a relationship to model the linear interpolation coefficients dependence on ϕ is introduced by means of polynomial fitting. In this case, a fourth order polynomial fitting, reported in Fig. 4.9, is required to retain a high level of accuracy due to the higher number of conditions present on the rich mixture-side.

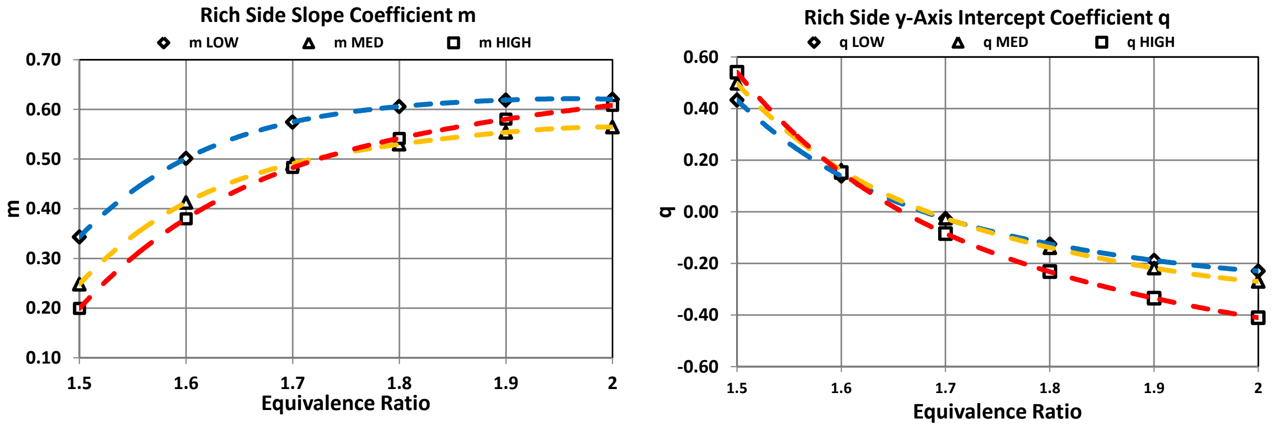

(a) **(b)**

Figure 4.9 Lean Mixtures Slope coefficient *m* (a) and y-Axis Intercept coefficient *q* (b) dependence on equivalence ratio for the three temperature levels.

In the end, a set of 30 fitting coefficients is derived to fit the slope coefficient m and the y-axis intercept coefficient q, using a fourth order polynomial formulation which is reported, for the sake of brevity, in Eq.4.24 for the slope coefficient of the high temperature fitting:

$$m_{HIGH}^{rich}(\phi) = rmh_4 \cdot \phi^4 + rmh_3 \cdot \phi^3 + rmh_2 \cdot \phi^2 + rmh_1 \cdot \phi + rmh_0 \tag{4.24}$$

where $rmh_4, rmh_3, rmh_2, rmh_1$ and rmh_0 are fitting coefficients. A TSF for the rich mixture side can be calculated for a given ϕ and for the low, medium and high temperature levels considered as shown respectively in Eq. 4.25-4.26-4.27.

$$TSF_{LOW}^{rich}(\phi, T_u) = m_{LOW}^{rich}(\phi) \cdot \frac{T_u}{T_{ref}} + q_{LOW}^{rich}(\phi) \tag{4.25}$$

$$TSF_{MED}^{rich}(\phi, T_u) = m_{MED}^{rich}(\phi) \cdot \frac{T_u}{T_{ref}} + q_{MED}^{rich}(\phi) \tag{4.26}$$

$$TSF_{HIGH}^{rich}(\phi, T_u) = m_{HIGH}^{rich}(\phi) \cdot \frac{T_u}{T_{ref}} + q_{HIGH}^{rich}(\phi) \tag{4.27}$$

The final fitting correlation for rich mixtures, reported in Eq. 4.28, is obtained considering TSF and PSF,as previously done for lean mixtures.

$$s_L^{n,rich}(\phi, T_u) = \left(PSF^{rich}(\phi) \cdot p_W + TSF_{HIGH}^{rich}(\phi, T_u) \cdot T_W\right)/(p_W + T_W) \tag{4.28}$$

where p_W and T_W are, in the case of the dedicated correlation derived for the present study, the same weights previously used for the lean-side extension since their values have been determined in order to maximize both lean and rich side coefficients of determination. These last are presented in Fig. 4.10 to directly compare the effect of accounting for PS only or for the combined effect of pressure and temperature.

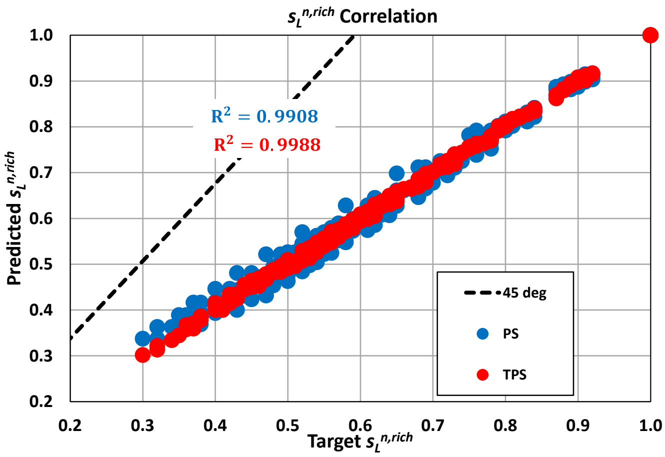

Figure 4.10 Correlation between s_L values obtained using pressure scaling (PS) and combined temperature-pressure (TPS) scaling for $\phi > 1.4$.

Compared to the lean side extension case, the gap between the approaches is reduced; still TPS guarantees an enhancement of the fitting accuracy. The reduced benefit of the new methodology could be reasonably due to the reduced influence of temperature on the rich side, clearly detected in Fig. 4.7. A comparison on s_L prediction for the rich side extension is presented in Fig. 4.11 for 5 bar pressure level, to demonstrate that, despite being less effective, temperature still plays a role in s_L scaling.

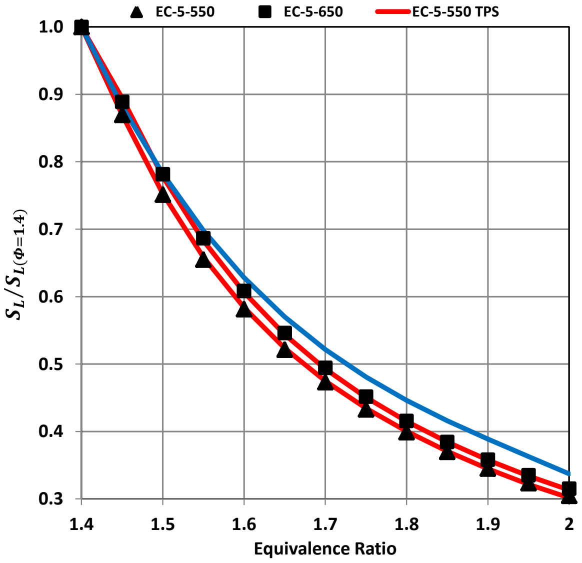

Figure 4.11 Normalized s_L values predicted by pressure scaling (PS) and temperature-pressure scaling approach (TPS) for $\phi > 1.4$ and 5 bar pressure condition. Black-dashed data represent the calculated values while blue and red lines are calculated with PS and TPS methodologies, respectively.

While in the present paragraph the proposed methodology has been extensively outlined, the next paragraph will focus on the fitting accuracy for both full-load and part-load correlations derived for commercial gasoline. Furthermore, correlations prediction is compared, for selected ECs, with results provided by correlations commonly used in $3D$-CFD combustion simulations [215,216].

⎔ 4.3.3 Fitting Results

The proposed methodology is used in the present study to predict commercial gasoline s_L at engine-like conditions. While fitting extensions results are presented in Paragraph 4.3.2 focusing on the part-load correlation, used afterwards in the present work, fitting accuracy is here analysed around stoichiometry for both full-load and part-load correlations to further highlight the suitability of the proposed approach for describing chemistry-based s_L on the entire engine OPs with simple polynomial correlations. In order to investigate the accuracy of the correlations, the relative error with respect to the chemistry-based calculated values is reported in the form of map in Fig. 4.12(a)-(b) for full-load and part-load correlations, respectively.

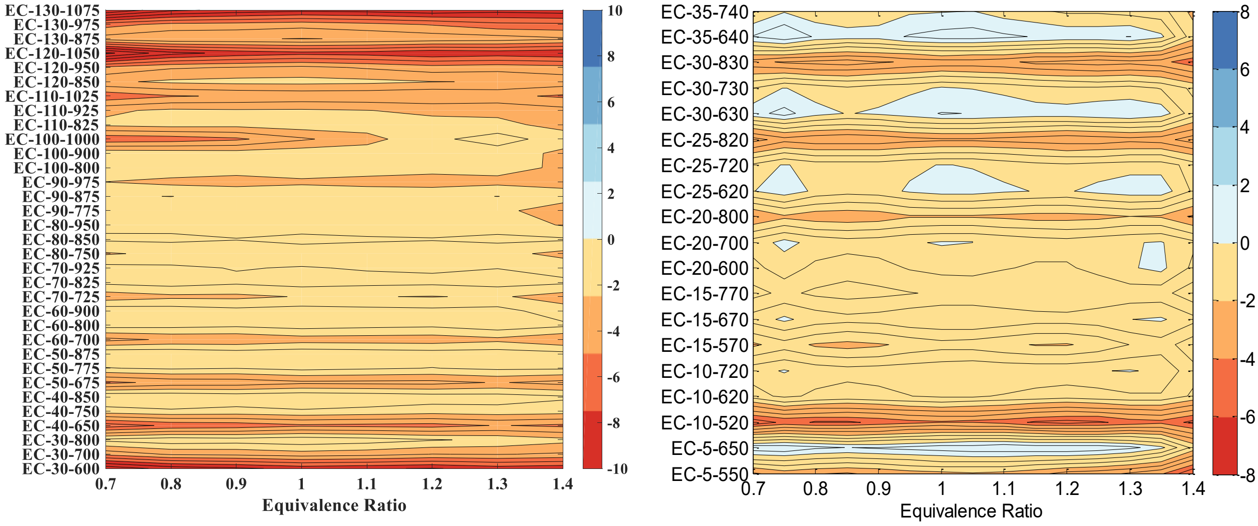

(a) **(b)**

Figure 4.12 Relative fitting error of polynomials of Eq. 4.13 against calculated s_L data for gasoline (a) full-load and (b) part-load correlations. The target value for the fitting procedure is the average value of the results obtained with the chemical kinetics mechanisms previously.

As visible in Fig. 4.12, both correlations introduce an average error well within 5% compared to the reference chemistry-based s_L values. The maximum error is found for the full-load correlation and is estimated to be around 10%. This is due to the higher number of ECs targeted with this correlations. As shown in Fig. 4.12(b) a reduction in the number of targeted conditions yields reduced errors in reproducing calculated s_L values. In order to further confirm the ability of the derived correlations to accurately represent the chemistry-based s_L datasets obtained via $1D$ simulations, a comparison is reported in Fig. 4.13 for a selected number of full-load ECs, where the final polynomial fitting form represented by Eq. 4.14, with dedicated extensions for lean (Eq. 4.23) and rich mixtures (Eq. 4.28), is compared with chemical kinetics simulations obtained with the reference mechanisms. As a first comment, it is immediately noticeable how the proposed correlation is able to accurately represent the average of the predictions obtained with the considered mechanisms for full-load ECs, hereafter named respectively: ANDRAE [60,61,62], POLIMI [63] and RWTH [59]. For the sake of brevity, results are hereafter reported for a limited number of ECs but the selected ones span over a wide range of pressure and temperature. It is therefore possible to conclude that the derived correlation is able to correctly represent s_L simulated dataset. In the second place, it is also interesting to compare chemistry-based calculations results with the prediction obtained extrapolating common s_L correlations well-beyond their validation range [215,216], named M&K RMFD-303 and R&K RMFD-303. A third empirical correlation, derived from Metghalchi and Keck's one [215], is considered. This correlation, named Modified M&K RMFD-303, is a modified version of M&K RMFD-303 correlation with dedicated extensions for very lean and rich conditions. This last correlation is particularly interesting as it is the correlation used by default in STAR-CDv2019.1 code, used in the present work. A marked difference is found between correlations, not only in terms of s_L absolute peak but also in terms of peak position in terms of ϕ. Comparing correlations and simulated values, it is straightforward to notice how chemistry-based predictions are in good agreement despite the use of different mechanisms. This is a clear evidence of the higher reliability of a chemistry-based approach.

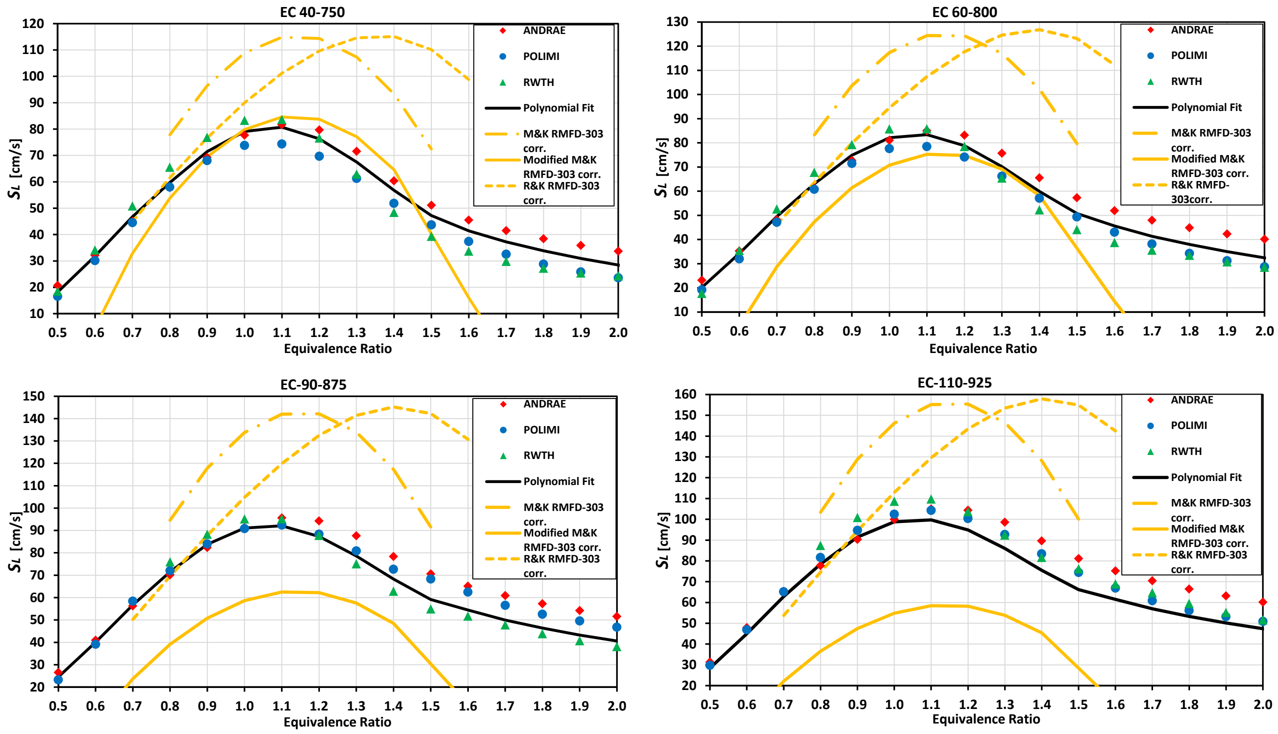

Figure 4.13 Calculated s_L data with the considered mechanisms [59,60,61,62,63] (coloured dots) compared with full-load correlation proposed in the present work (solid black line). A correlation available in literature [125] and its modified version implemented by default in the CFD solver are also reported (orange solid and dashed lines).

Further commenting the results, it is important to mention that STAR-CD default correlation provides similar result to the derived correlations at low pressures and temperatures, while moving to higher values an increased gap is spotted. Moving to part-load conditions, the same analysis can be done for selected number of conditions, characterised by low pressures and pressures, considering Fig. 4.14.

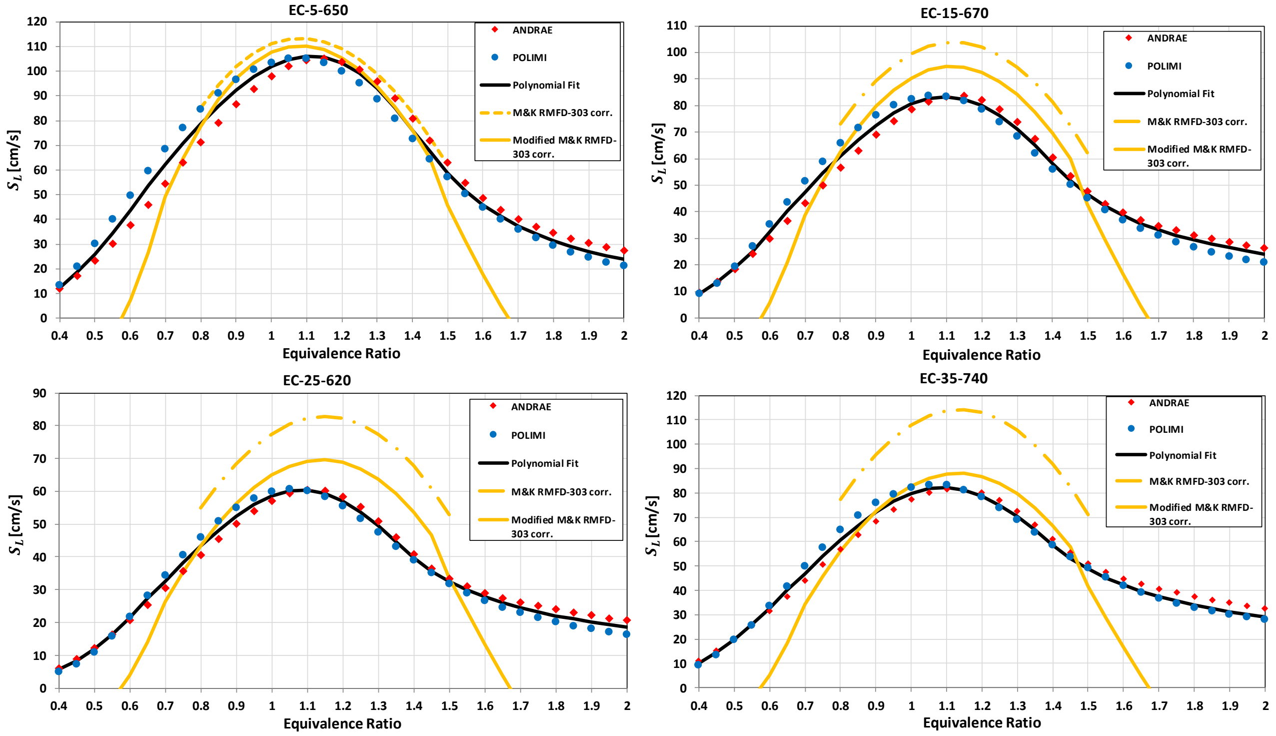

Figure 4.14 Calculated s_L data with the considered mechanisms [60,61,62,63] (coloured dots) compared with part-load correlation proposed in the present work (solid black line). A correlation available in literature [125] and its modified version implemented by default in the CFD solver are also reported (orange solid and dashed lines).

As a first comment, results from the mechanisms proposed by Cai et al. [59] (RWTH) are not present anymore since chemical kinetics simulations provided very similar results to the ones obtained with PoliMi mechanism [63]. Secondly, it is immediate to notice how empirical correlations still provide quiet different s_L values, despite much lower values of pressure and temperature. Conversely, chemical kinetics mechanisms predictions are in good agreement, despite some, negligible, deviations are still present. This due to the fact that mechanisms are used in their validation range and constitute a clear evidence of the reliability of a chemistry-based approach for s_L prediction. As a final remark, it is important to notice the marked difference between the proposed part-load correlation and empirical correlations in very lean and rich conditions which are likely to be present in GDI units. This last aspect further emphasizes the limitation of empirical correlations which neglect very lean and rich conditions. In order to further investigate this aspect and to provide a further validation of the methodology, the proposed part-load correlation is tested, in the next paragraph, on the research engine used as reference in the present work.

⬡ 4.4 Engine Case Validation

As previously mentioned in Chapter 3, research engine and CFD model details are discussed in Chapter 5 together with the experimental techniques used to obtain measurements used as validation in the present paragraph. For this analysis, the single-cylinder optically accessible research engine is operated at a throttled conditions (0.7 bar pressure in the intake manifold) and SOC occurs at 30 CAD bTDC. The aim of the $3D$-CFD analysis here presented is to further validate the benefits deriving from the chemistry-based s_L correlation, previously derived, compared to the widely used M&K RMFD-303 [6] and a modified version implemented in STAR-CD (Modified M&K RMFD-303). Three different $3D$-CFD simulation sets are therefore analysed using the same CFD setup except for the correlation used to evaluate s_L based on the cell-wise p, T_u, ϕ and EGR. $3D$-CFD results were obtained without any case-to-case tuning, therefore differences arising between the cases in terms of combustion phasing are only due to the s_L correlation used case by case. Average in-cylinder pressure trace, apparent and cumulative HRR are reported for the three cases in Fig. 4.15.

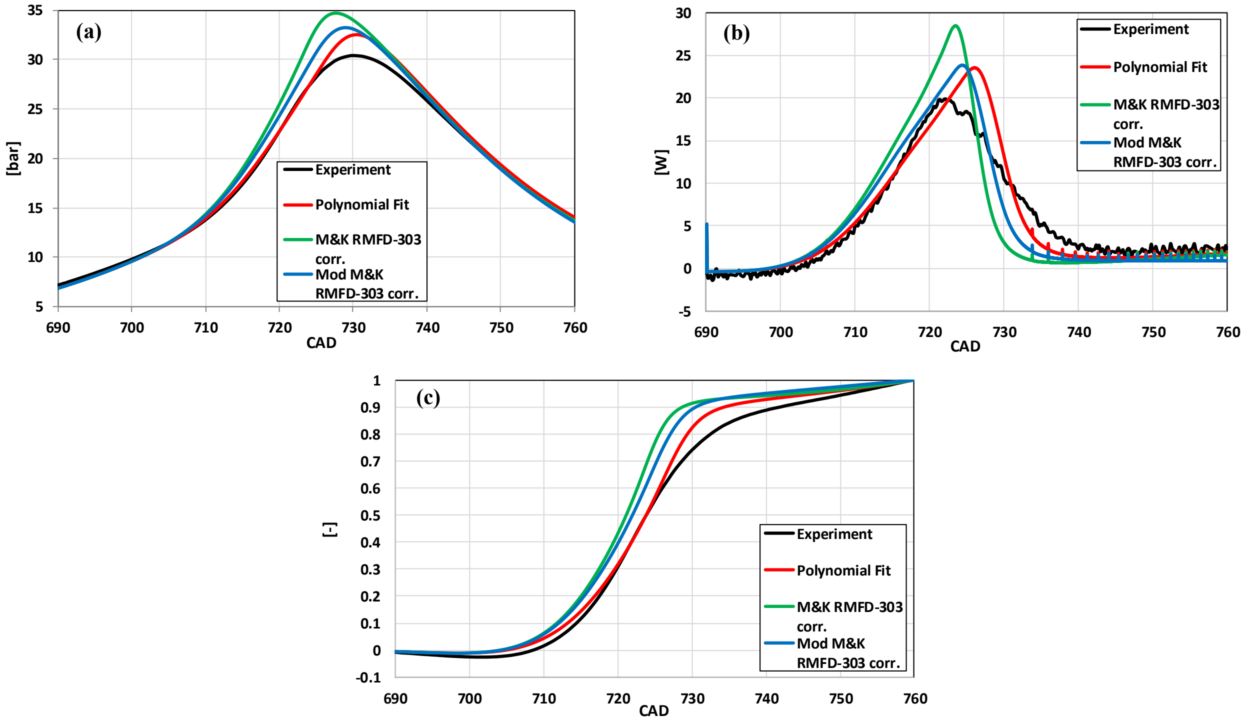

Figure 4.15 $3D$-CFD mean in-cylinder pressure (a), apparent heat release rate (b) and cumulative heat release rate (c) curves against experimental data during the combustion process.

Analyzing Fig. 4.15, it is possible to notice that pressure trace related to the proposed polynomial fitting is in slightly better agreement with the experimental data in terms of peak pressure prediction. In-cylinder pressure is correctly captured throughout the combustion process, being the slopes in agreement both in the early flame development stage and in the completion of combustion. Considering the pressure traces obtained with the standard correlation (M&K RMFD-303 corr.) and with the modified one (Mod M&K RMFD-303 corr.) the agreement worsens both in terms of peak pressure prediction and phasing. Misalignments are found both in the early development and in the last portion of the combustion process. A further confirmation of the improved accuracy using the polynomial fit is given by the apparent heat release rate and the cumulative apparent heat release rate reported in Fig. 4.15(a)-(b). In particular, it is noteworthy the very close alignment to the experimental data for the central part of the combustion process. The differences arising from approximately 730 CAD are mainly due to the quenching model which was purposely not calibrated. A detailed calibration of the quenching model would probably lead to an improvement of the combustion completion stage prediction. To quantitatively compare the effect of the proposed s_L correlation on the combustion development the main mass fraction burnt indicators are reported in Fig. 4.16.

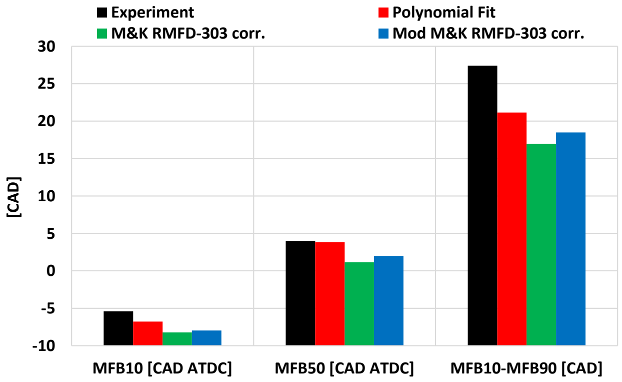

Figure 4.16 Main combustion indicators based on the effective mass fraction burnt for the experimental and the $3D$-CFD cases.

A very good agreement with the experimental $MFB50$ for the case performed with the proposed correlation is found, especially if compared with Metghalchi and Keck's correlations results, retaining still a good alignment for $MFB10$ and the combustion duration $MFB10$-$MFB90$. A comparison between the experimental and measured flame areas as function of CAD after spark onset is reported in Fig. 4.17(a).

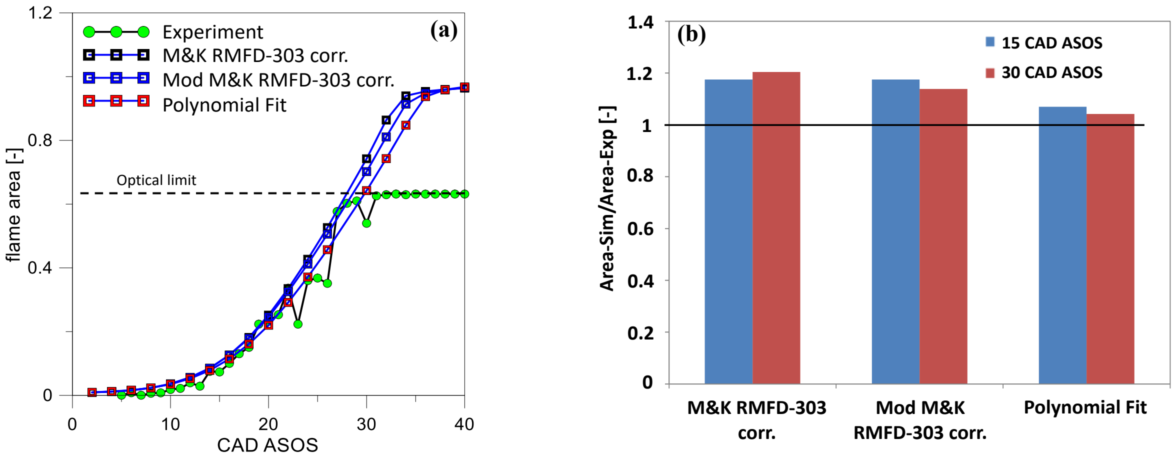

Figure 4.17 (a) Comparison between the experimental and calculated flame area as function of CAD after spark onset. Experimental optical limit is highlighted by the dashed black line (b) Ratio between simulated and experimental (averaged over 100 consecutive cycles) flame area at 15 and 30 CAD $ASOS$.

Similarly to the in-cylinder pressure trace, results using the proposed s_L correlation are in good agreement with the experimental data up to the optical limit, i.e. approximately 30 CAD After Start Of Spark ($ASOS$). Similar considerations can be drawn by observing Fig. 4.17(b), where the ratio between simulated and experimental flame areas at 15 and 30 CAD $ASOS$. For both CADs, the polynomial fit is better correlated with the experimental measurements. The comparison among different s_L correlations confirms the validity of the proposed chemistry-based correlation methodology previously presented, being this the only correlation able to match the experimental combustion process development, especially in the early combustion phase after spark onset. In order to motivate the impact of the proposed correlation on the results, ϕ and s_L fields for the three correlations are reported at spark time (690 CAD) in Figure 4.18. Firstly, it is noteworthy that improper mixing leads to the formation of a rich mixture at the exhaust side, leaving a lean mixture region under the intake valves. Such ϕ distribution has of course a non–negligible impact on the preferential direction for flame development after spark onset, as further demonstrated by s_L field, characterized by higher values under the exhaust valves for all the tested correlations. The area of lower s_L predicted by the polynomial fitting at the spark electrodes motivates the reduced in-cylinder pressure curve slope shown in Figure 4.15(a).

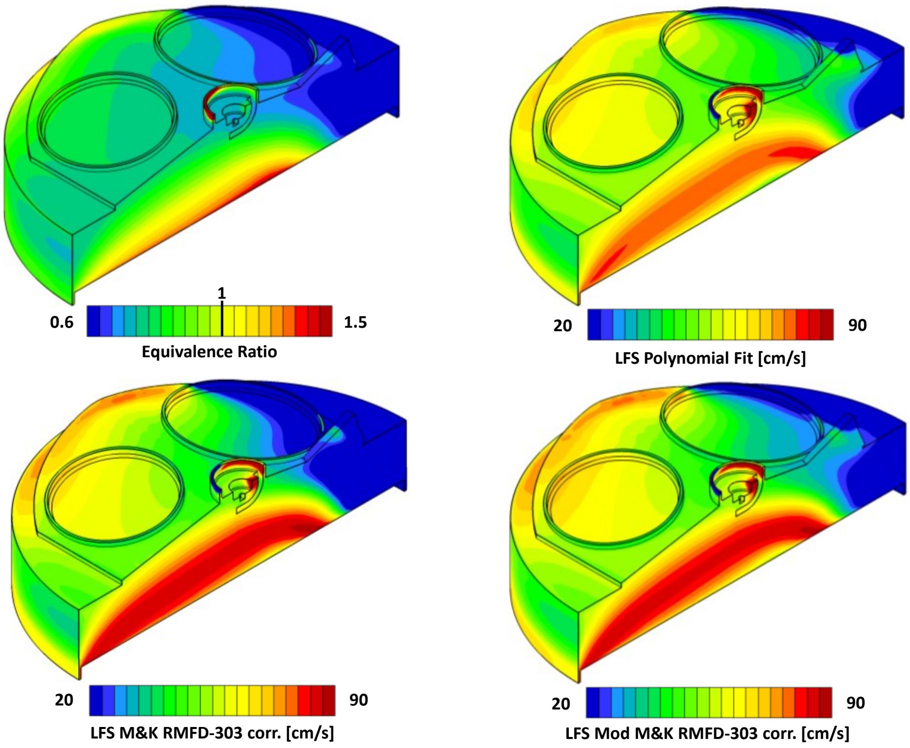

Figure 4.18 Calculated ϕ field and s_L scalar fields for the considere correlations at spark onset.

Based on the results discussed in this paragraph, it can be concluded that the proposed methodology to formulate chemistry-based s_L correlations is effectively able to enhance combustion prediction with a simple polynomial fitting form which greatly increases CPU efficiency compared to tabulated approaches. In fact, such kind of correlations rely on a set of coefficients, as the ones reported in Table 4.2 (a)-(b)-(c) for the commercial gasoline part-load correlation tested, which are easy to implement in any CFD solver and are used in a simple polynomial fitting form. Furthermore, such correlations can be generated for any kind of fuel, if suitable fuel surrogates and chemical kinetics mechanisms are available. This constitutes a powerful tool when it comes to alternative fuels combustion modelling, for which experimental-based s_L correlations are scarcely present in literature. For instance, gasoline-ethanol correlations sample results are briefly introduced in the following paragraph, exploiting the surrogates presented in Paragraph 3.3.3, to highlight the practical interest of the proposed chemistry-based methodology.

Polynomial Fitting Coefficients				Pressure Scaling Rich-side Extension Fitting Coefficients		Pressure Scaling Lean-side Extension Fitting Coefficients	
	a	***b***	***c***	r_3	-2.131027E+00	l_3	8.070175E+00
1	8.060000E+01	2.269200E+00	-2.768000E-01	r_2	3.363216E+00	l_2	-8.596491E-01
2	5.630000E+01	-2.652000E-01	4.000000E-03	r_1	-2.197159E+00	l_1	-3.131830E+00
3	-2.429000E+02	4.137300E+00	-6.614000E-01	r_0	9.989170E-01	l_0	1.000100E+00
4	-5.034000E+02	7.465000E+00	-1.013800E+00	**m'**	2.915208E-01	**m''**	1.994465E-01
5	5.100000E+01	-4.144000E-01	2.504800E+00	p_{ref} **[Pa]**	2.00E+06	p_{ref} **[Pa]**	2.00E+06
6	1.057300E+03	-2.467510E+01	8.561900E+00	T_{ref} **[K]**	550	T_{ref} **[K]**	550

Table 4.2 (a) Part-load fitting coefficients for gasoline s_L respectively valid in the range: $\mathbf{0.7 \leq \phi \leq 1.4}$, $\mathbf{\phi > 1.4}$ and $\mathbf{\phi < 0.7}$ with pressure scaling coefficients.

Temperature Scaling Rich-side Extension Fitting Coefficients						
	m LOW (rml)	**q LOW (rql)**	**m MED (rmm)**	**q MED (rqm)**	**m HIGH (rmh)**	**q HIGH (rqh)**
4	-7.412563E+00	1.040950E+01	-9.550146E+00	1.431624E+01	-4.951563E+00	9.397567E+00
3	5.593678E+01	-7.873684E+01	7.087918E+01	-1.068905E+02	3.841605E+01	-7.277776E+01
2	-1.587863E+02	2.243769E+02	-1.977421E+02	3.004508E+02	-1.121875E+02	2.125131E+02
1	2.010408E+02	-2.860356E+02	2.460067E+02	-3.775439E+02	1.464410E+02	-2.780766E+02
0	-9.520917E+01	1.376771E+02	-1.147117E+02	1.790791E+02	-7.162713E+01	1.375515E+02

Table 4.2 (b) Part-load temperature scaling coefficients for gasoline s_L valid for the rich-side extension ($\mathbf{\phi > 1.4}$).

Temperature Scaling Lean-side Extension Fitting Coefficients						
	m LOW (lml)	**q LOW (lql)**	**m MED (lmm)**	**q MED (lqm)**	**m HIGH (lmh)**	**q HIGH (lqh)**
2	4.571549E+00	1.997300E-01	-1.863679E+00	6.046105E+00	-2.573200E-02	2.866504E+00
1	-5.363573E+00	3.128426E+00	1.167977E+00	-2.712542E+00	-8.901132E-01	7.495661E-01
0	1.456678E+00	-1.165846E+00	1.146310E-02	8.754485E-02	5.994921E-01	-8.364781E-01

Table 4.2 (c) Part-load temperature scaling coefficients for gasoline s_L valid for the lean-side extension ($\mathbf{\phi < 0.7}$).

⬡ 4.5 Gasoline-Ethanol Blends Laminar Flame Speed Correlations

The methodology used to generate commercial gasoline s_L correlations used in the present study can be further extended to model any type of fuel of interest. As previously mentioned, alternative fuels are becoming increasingly important for ICE future developments and the lack of correlations for customized fuel blends hinders their virtual development via $3D\text{-}CFD$ simulations. In this paragraph, the potential of the proposed methodology is unleashed, analysing the results obtained by correlations generated for the gasoline-ethanol blends surrogates presented in Paragraph 3.3.2, for selected full-load ECs. Dedicated s_L correlations are formulated based on $1D$ freely propagating simulations carried out in DARSv2019.1 for each of the fuel surrogates ($E0$, $E5$, $E10$, $E20$, $E85$). The methodology previously presented is then used to fit simulations outcome with the 5th order logarithmic polynomial fit and dedicated extensions for lean and rich mixtures. Chemistry-based simulations results and correlations are reported in Fig. 4.19 for selected ECs. In the first place, derived correlations are able to replicate simulations results with a high degree of accuracy for all the blends considered. Since gasoline-ethanol blends s_L experimental data in literature are limited in number and performed at conditions far from those encountered in engines, only a qualitative comparison is possible. Dirrenberger et al. [76] reported no remarkable difference between $E0$ and $E15$ gasoline in experiments carried out on a burner at ambient pressure and 358 K. Similarly, Meng et al. [235] tested $E0$, $E5$, $E10$ and $E20$ gasolines and observed very similar results in terms of s_L. The same trend is found in chemistry-based calculations carried out in the present work and is accurately described by the correlations which exhibit a very reduced increase in s_L as ethanol content

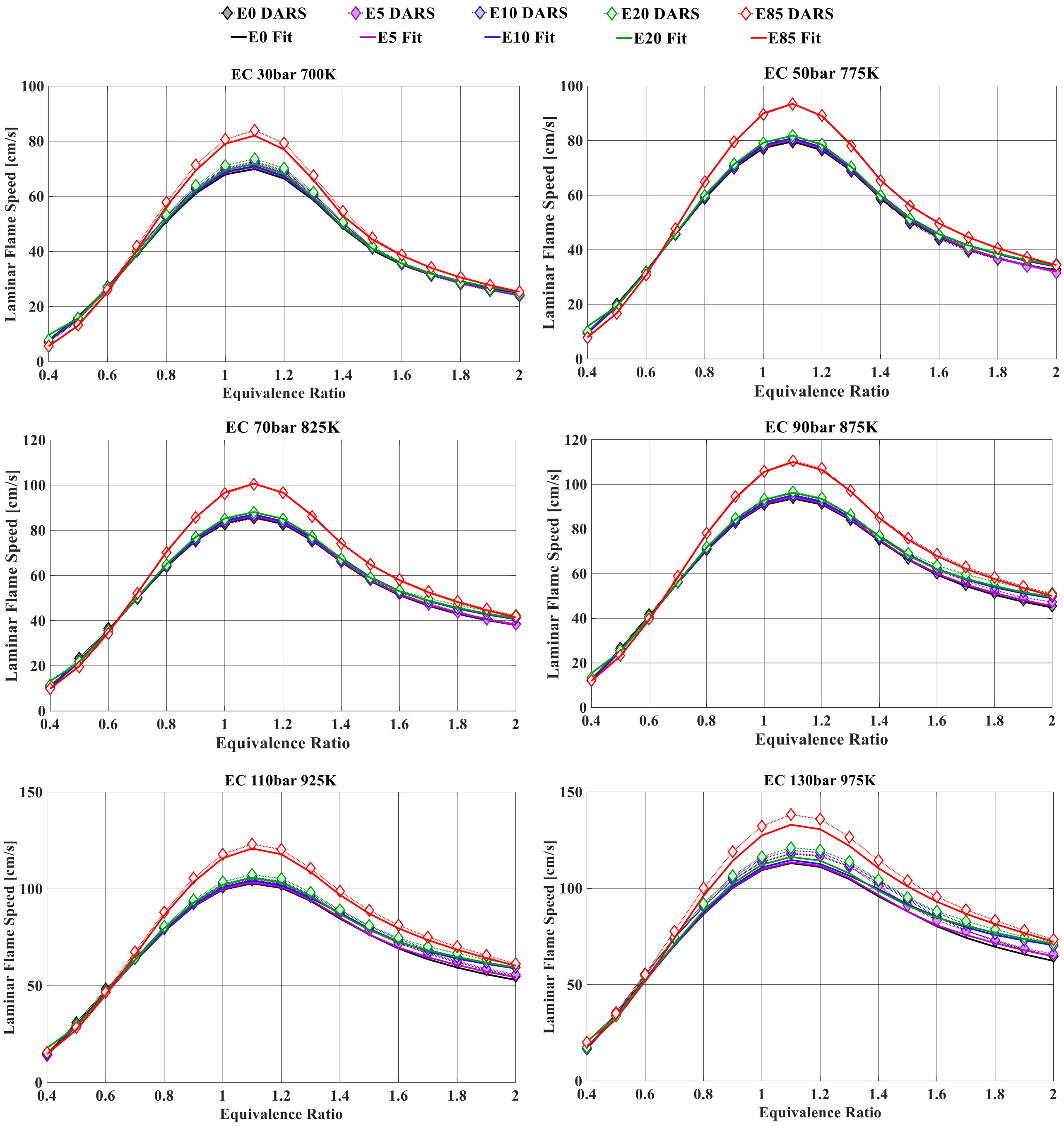

Figure 4.19 s_L for $E0$, $E5$, $E10$, $E20$, and $E85$, at different conditions. "DARS" refers to DARS $1D$ simulation results, while "Fit" stands for the s_L values predicted by correlations.

increases. Conversely, $E85$ shows a non-negligible increase of s_L at stoichiometric and rich conditions, while lower values are found on the lean side. Such behaviour may be explained considering the high O/C of the mixture resulting from the combination of the rich-in-oxygen blend with a lean (i.e. rich-in-oxygen) mixture. Similarly, the higher s_L in rich mixtures might be explained by the decomposition of ethanol which leads to the formation of monoatomic oxygen, able to trigger the formation of O_2 via reverse third-body reactions. These preliminary yet interesting results demonstrate the ability of the proposed methodology to effectively model s_L dependence on fuel composition and to integrate this information in $3D$-CFD simulations with a cost-effective approach based on simple polynomial correlations and dedicated fitting coefficients. As a final remark, it must be considered that the final result is obtained by the overall modelling approach presented for fuel surrogates and s_L.

Chapter 5: GDI Soot Modelling

⬡ 5.1 Notes on Soot

⬡ 5.1.1 Road Transport Contribution to Soot Emissions

In this paragraph, a summary of the results presented by the JRC of the European Commission science and knowledge service in 2017 [28] is reported to further emphasize the reason leading to a research activity focused on GDI soot emissions modelling. Many European cities suffer from poor air quality and still exceed the European standards prescribed by the Air Quality Directive (AQD) and the guidelines recommended by the WHO. This is the case for Fine Particulate Matter (PM_{10}) with concentrations exceeding the EU limit value and WHO guidelines in large parts of Europe. Although just 6% exceeded the EU $PM_{2.5}$ limit (annual average of 25 $\mu g/m^3$) in 2015, about 75% of them exceeded the WHO guideline (annual average of 10 $\mu g/m^3$). $PM_{2.5}$ is responsible of adverse health effects and premature deaths, with current estimate suggesting an average life loss of about 8 to 10 months in the most polluted European regions. Data presented hereafter focus on $PM_{2.5}$. In Fig. 5.1(a), annual mean $PM_{2.5}$ concentration detected by active stations in EU countries is reported in the form of map. As visible, only a few cities manage to keep concentrations below the suggested value of 10 $\mu g/m^3$.

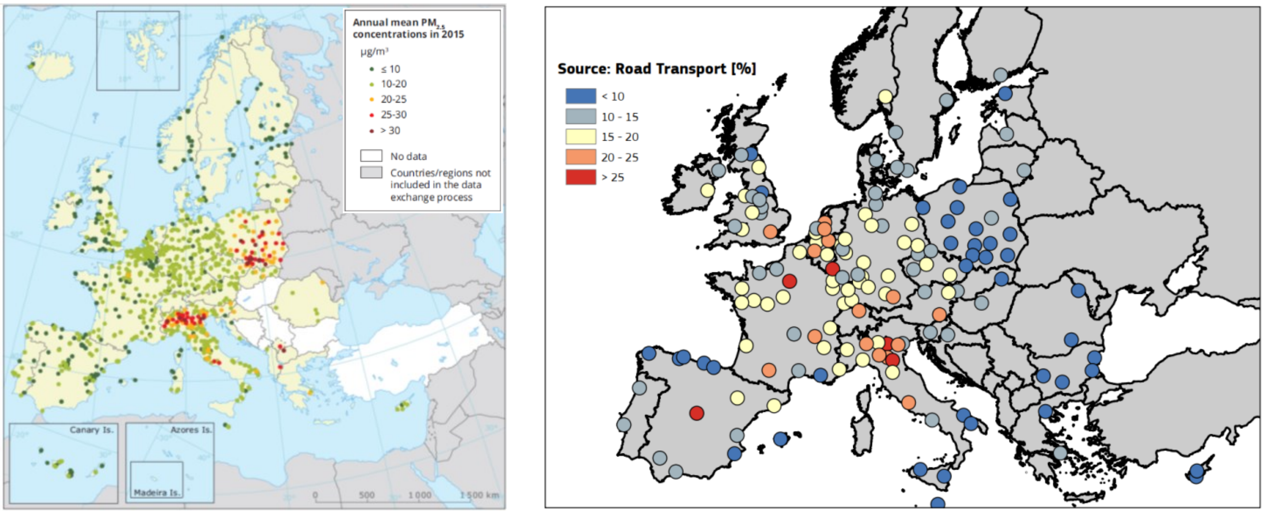

(a) **(b)**

Figure 5.1 (a) Ref. [1]: The red and dark dots indicate stations reporting concentrations above the EU annual target value for $PM_{2.5}$. The dark green dots indicate stations reporting values below the WHO AQD for $PM_{2.5}$. Only stations with >75% of valid data have been included in the map (b) Ref. [1]: Contribution of the transport sector to the $PM_{2.5}$ urban background concentration. Each dot represent one urban area.

Pollutant emissions originate from different human activities (e.g. residential heating, transport, etc.) as well as from natural sources (e.g. dust, sea-salt, fires, etc.). The sectorial apportionment of $PM_{2.5}$ reported in [1] distinguishes and quantifies the contributions from anthropogenic activity sectors and from natural sources. The transport sector, by definition, includes exhaust and evaporative emissions from light and heavy-duty vehicles and motorcycles as well as non-exhaust PM emissions due to road abrasion of tyres and brake wear. The average contribution from road transport, in Fig. 5.1(b), in the 150 urban areas is 14%. This data increases up to 39% considering only the largest urban areas. It is important to note that the numbers concern the transport contribution to urban background concentrations. At traffic stations, the contributions is likely to be proportionally larger. Focusing on the main urban areas in the northern part of Italy, a strong correlation exists between annual mean $PM_{2.5}$ concentration and local road transport contribution. This last data is of particular concern due to the hazardous effect of high $PM_{2.5}$ concentration to human health [26]. As a further confirmation of the relationship between size of the considered city and $PM_{2.5}$ concentration, a comparison of $PM_{2.5}$ levels registered in Milano and Modena in 2015 is reported in Fig. 5.2.

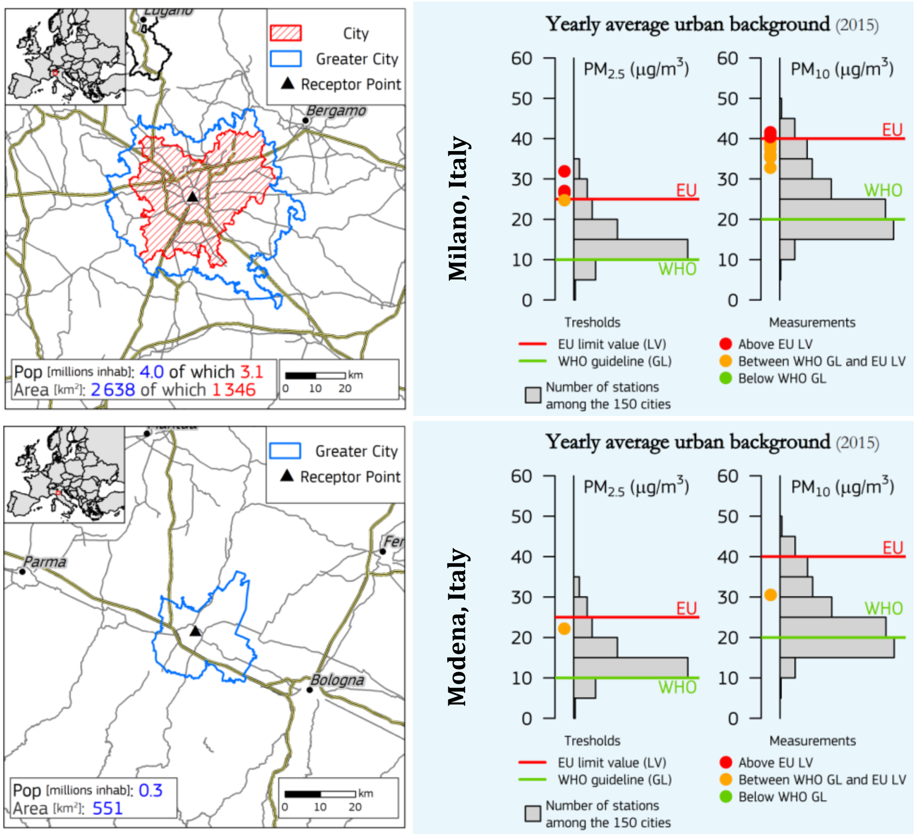

Figure 5.2 Ref [1]: Information on measured $PM_{2.5}$ concentration levels and on their compliance with the standards in the EU AQD and the WHO Air Quality Guideline. The histogram in each fiche provides an overview of the reported PM concentration in the 150 cities, while the colour coded dots indicate the values measured at all background monitoring stations located in the greater city area (green: below WHO guidelines; red: above AQD limit values; orange: in between).

The previous data clearly demonstrates how road transport contribution plays a key role in overall $PM_{2.5}$ concentration emissions. For this reason, the EU introduced the EURO6 regulations. In particular, from the EURO6c stage, entered into force on September 2017, GDI units must meet the 4.5 mg/km and 6.0×10^{11} #/km, for PM and PN respectively [36].

5.1.2 Soot in GDI Engines

Generally speaking soot consists of spherical particles of carbon with a diameter varying from 1 nm to hundreds of nm [170]. Despite being essentially composed of carbon, soot contains other elements such as hydrogen and oxygen which are equally present even in small quantities. Soot often contains also a soluble organic fraction whose components include UHC, oxygenated derivatives (ketones, esters, aldehydes, lactones, ethers, organic acids) and PAHs together with their respective nitrates, oxygenates, etc. Mineral derivatives (SO_2, sulfates, etc..) and metal derivatives may be present as well. Combustion-generated particles are found to grow from nearly spherical primary particles into fractal-like agglomerates [236]. This change in morphology with growth has profound implications on a wide range of particle properties, including density, transport and potential health effects. The question of soot structure and growth has received extensive attention, primarily in the form of light scattering and Transmission Electron Microscopy (TEM).This technology proves a useful diagnostic for aggregate morphology, providing a direct measure of primary particle size and a complementary determination of fractal dimension [236]. An example of TEM images of collected GDI soot particles are reported from [237] and shown in Fig. 5.3. These particles were collected during an experimental campaign [237] in which a GDI was tested over the old New European Driving Cycle ($NEDC$). Based on Fig. 5.3, two clearly distinct particle types are typically found at the exhaust.

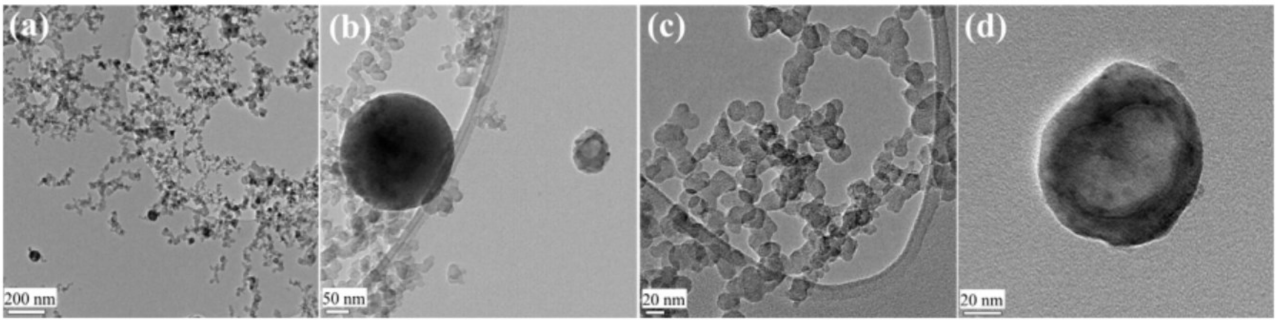

Figure 5.3 Ref: [237] TEM images of collected exhaust particles during the $NEDC$ cycle with various magnifications.

In the first category, nearly spherical particles as in Fig. 5.3(a)-(b)-(d), often containing internal structure of lighter and darker areas, are found. The size of those particles varies from 10 nm to 200 nm and are composed of at least oxygen, zinc, phosphorous and calcium where metals are compounds of engine oil but not of fuel. In fact, particles characterized by darker colours are essentially made of lubricating oil compounds. The second particle type is, as previously mentioned, agglomerated soot mostly consisting of elemental carbon. Also in this case several soot particles might include darker parts. It should be noted that also very small nearly spherical soot-like particles might be present. Based on TEM technique, also the inner structure of soot particles can be further investigated. As sketched in Fig. 5.4, the sub-structure of a soot particle is made up of a large number of *Crystallites*, consisting of 5-10 layers of carbon sheets called *Plates*.

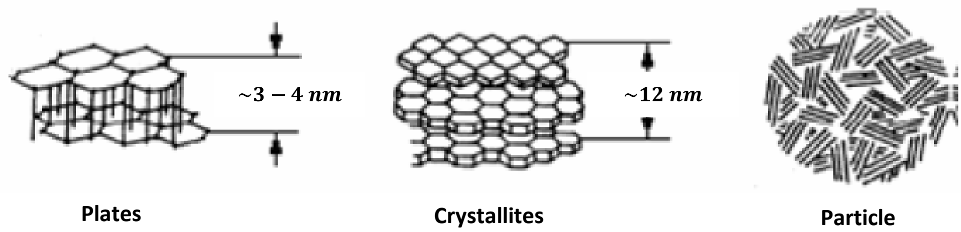

Figure 5.4 Sub-structure of a soot particle.

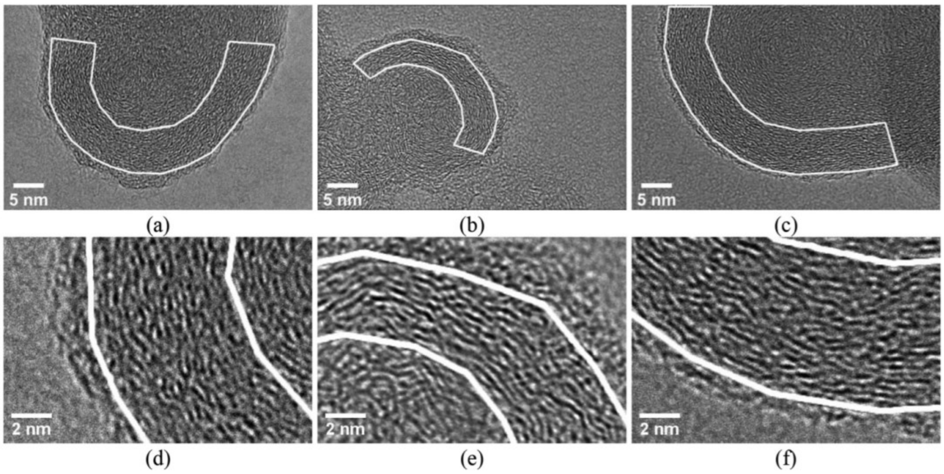

Figure 5.5 Ref: [238] TEM images of GDI soot (a), Diesel soot (b) and carbon black (c) primary particles. Further, enlarged sections are reported for GDI soot (d), Diesel soot (e) and carbon black (f).

The carbon atoms in these sheets form hexagonal patterns containing, typically, up to 100 carbon atoms. The spherical particles then cling to each other forming large chain-like structures (Fig. 5.3) called *Agglomerates*. The soot particles thereby assume a fractal shape and can be ascribed a corresponding fractal dimension. Regardless the differing physical conditions under which combustion is taking place, soot looks like surprisingly similar to the description above and can be assumed to form roughly along the same lines [170]. A further confirmation of this can be found in Fig. 5.5 , from [238], where TEM images of GDI soot, Diesel soot and carbon black primary particles are compared. Despite primary particles inner structure appears to be quiet independent of the combustion system under analysis, $PSDF$ is strongly affected by the combustion process characteristics. In fact, GDI engines are commonly recognized to produce, potentially, bimodal-like $PSDF$ while Diesel engines usually produce unimodal $PSDF$. As a final remark, as shown in Fig. 5.6 from [237], $PSDF$ in GDI engines strongly depends on the engine load (i.e. acceleration, deceleration and steady speed condition).

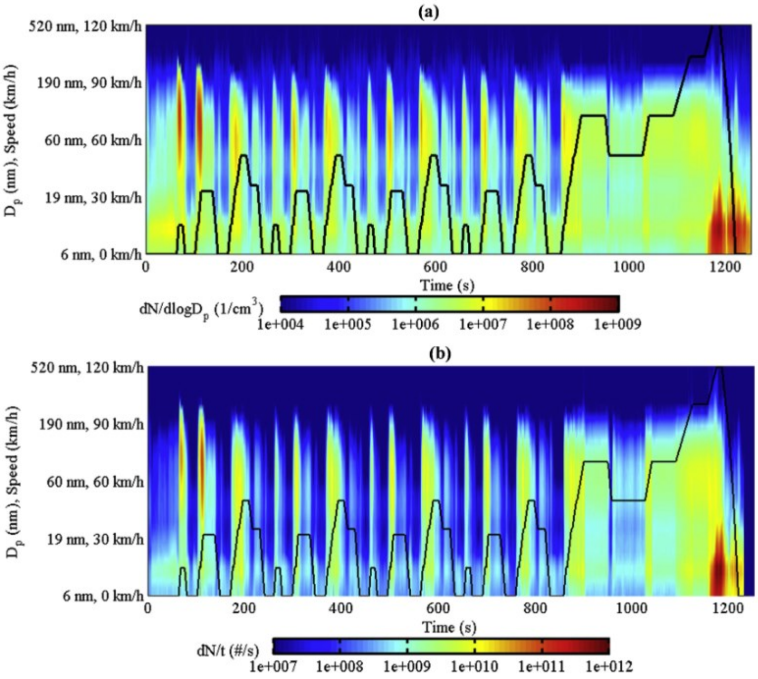

Figure 5.6 Ref: [237] Mean particle size distributions measured by the $EEPS$ during the $NEDC$ (8 repetitions) cycle in terms of (a) dilution ratio corrected particle concentrations ($dN/dlogDp$) and (b) particle emissions per second (dN/dt). Black line shows the wheel speed profile.

5.1.3 Aerosol Statistics Lognormal Distributions and dN/dlogDp

As visible in Fig. 5.6, measured $PSDF$ is reported in terms of $dN/dlogDp$. In this paragraph, notes on aerosol statistics are introduced in order to provide the basic notions [239] used afterwards to compare measured and calculated $PSDF$ consistently. Standard statistics based on normal distributions are frequently not suitable for most airborne particle (aerosol) size distributions. Despite no real theoretical reason, lognormal distributions tend to be the best fit for single source aerosols. Therefore, when statistical analysis is applied to aerosol size distributions, it is routinely based on lognormal distributions. Data are typically plotted on a lognormal axis. In the simples technique, particles data are plotted as a function of the concentration (dN) for each particle size bin. The mode concentration of the size distribution is often estimated by the concentration in the peak bin. In aerosol sizing instruments, the number of size bins is finite. Interestingly, as discussed afterwards, this is the case also for the Sectional Method model. This simple concentration vs. log particle diameter approach works well only when using one type of instrument or when comparing instruments with identical resolution. For example, on equal particle number in each bin, an instrument with a double resolution compared to a second one will yield half the concentration. However, this is just an illusion arising from the difference in resolution and is due to the fact that bin width is halved. The method used in statistics to avoid this problem is to plot data using normalized concentration ($dN/dlogD_p$), where dN (or ΔN) is the number of particles in the range (total concentration) and $dlogD_p$ (or $\Delta logD_p$) is the difference in the log of the channel width. $dlogD_p$ is calculated by subtracting the log of the lower bin boundary from the log of the upper boundary for each channel (normalizing for bin width). The concentration is divided by the bin width, giving a normalized concentration value that is independent of the bin width, as shown in Eq. 5.1.

$$\frac{dN}{dlogD_p} = \frac{dN}{logD_{p,u} - logD_{p,l}} \tag{5.1}$$

where D_p, $D_{p,u}$, $D_{p,l}$ are respectively the midpoint, upper and lower channel particle diameters. With normalized concentrations, values at the mode will be similar even on instruments with very different resolution. In the present chapter, Eq. 5.1 is exploited to compare measured and CFD data consistently.

⬡ 5.2 Fundamentals of Soot Modelling

⬡ 5.2.1 Introduction to Soot Modelling

Soot is formed in different combustion systems, at surfaces adjacent to combustion or via liquid-phase pyrolysis. However, in the present work, only soot formed by vapour-phase reactions in flames is considered. As previously mentioned, carbonaceous-based soot particles can be described in combustion processes by a Particle Size Distribution Function ($PSDF$). This means that the total soot mass is distributed on a large size scale, typically varying from particles containing less than 100 carbon atoms to particles containing millions of carbon atoms. It is commonly recognized that most practical properties of soot are known if the shape of $PSDF$ is known. There are two major problems which arise when attempting to model soot and its formation in combustion. First of all, the physical and chemical processes governing the formation of soot need to be established. Great controversies among researchers are still present on which processes are effectively involved in soot formation and in which way they contribute to soot formation [240,241,242,243]. For the present discussion, soot formation processes taken into account are the same presented in [244,245]. Particle inception, or Nucleation, is the process responsible for the formation of the smallest particles from gas phase species, commonly known as PAH. Condensation is a process by which gas phase soot precursors coagulate onto already existing soot particles. Once a solid phase is formed, particles can collide generating larger soot particles via Coagulation, which is a key physical process. In this chain, surface reaction-based processes, namely Surface Growth and Oxidation, may take place at any stage leading, respectively, to mass addition or mass abstraction from already existing soot particles. Generally speaking, there are two fundamental phenomena which explain the different soot formation processes: collisions-based and surface reaction processes. The first governs Particle inception, Condensation and Coagulation while the second, governed by chemical principles, describes Surface Growth and Oxidation. Now, a suitable mathematical framework is needed to quantitatively describe soot formation in flames. The main issue is due to soot diversity, meaning that a large size spectrum of soot particles that can be, ideally, divided in a multitude of different size classes [47]. The size of a soot particle highly affects its properties; therefore the different size classes have to be reflected in the mathematical description, while still retaining feasible CPU-times. Considering that infinite possible particle sizes constitute $PSDF$, an infinite number of equations would be required to solve the problem. Therefore, a proper mathematical tool is needed. In the present work, the Sectional Method model is chosen as reference mathematical formulation to appropriately describe and solve $PSDF$. While in the next paragraph the fundamentals of soot modelling are presented, the Sectional Method model is briefly presented in Paragraph 5.3, for the sake of brevity. The reader should refer to these specific publications [46,47,48,49], for additional information, where the model equations are derived and discussed more in detail.

⬡ 5.2.2 Gas-phase Chemistry and PAH Formation

An accurate gas-phase chemistry model is essential for an accurate quantitative description of soot characteristic quantities, namely PM, PN and $PSDF$. In fact, as previously mentioned, gas phase species are responsible for soot precursors formation and constitute the main building blocks for further growth and oxidation of soot. For this reason, exploration studies have been carried out, via DARS $1D$ Burner Stabilized Flames (BSF) simulations, to evaluate selected chemical kinetics mechanisms ability to quantitatively describe soot-related gas-phase species formation in laminar premixed flames. However, such kind of analysis would require an additional separate discussion which could potentially result in an amount of material worth of another PhD dissertation. Therefore, results in Paragraph 5.4 are presented for the sake of completeness and to provide an overview of an essential activity for soot modelling, which is however too demanding to be extensively discussed in the present work. Although promising, results in Paragraph 5.4 are seen as a possible pathway for future developments, the final choice of a chemical kinetics mechanism for soot chemistry is folded to the overall need of the present dissertation. Elements of soot gas-phase chemistry are hereafter presented to provide the reader with the basic notions to understand the discussion following in Paragraph 5.4. The general opinion is that chemical precursors to soot are Polycyclic Aromatic Hydrocarbons (PAH) [240]. PAH are large molecules made up of aromatic rings, forming flat hexagonal structures made up of carbon atoms. The gas phase chemistry incorporates the mechanisms to take into account for the formation up to 4-ring PAH. An example of typical aromatic species considered among the main PAH species is provided in Fig. 5.7.

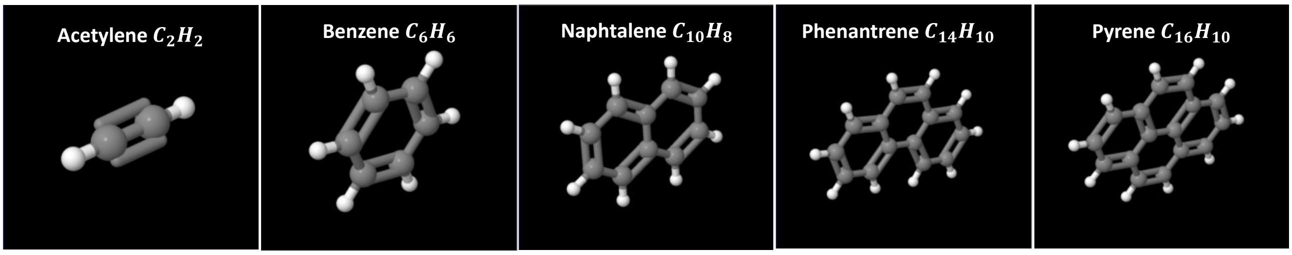

Figure 5.7 Main aromatic species considered among the soot precursors (PAH) in chemical kinetics models.

Earlier soot models included polymerisation model for PAH [244,245], allowing indefinitely more benzene rings to grow onto the PAH. One then gets a wide variety of sizes of PAH molecules. Studies using such models have shown that PAH distribution is strongly focused on the smallest PAH [246], with concentrations of larger PAH very rapidly decreasing. The distribution of PAH can therefore be approximated with one PAH molecule concentration. This approximation has negligible effects on overall soot formation. In the Sectional Method formulation used in the present study, pyrene is considered as reference soot precursor.

⬡ 5.2.3 Physical Models

In the free molecular regime, particles in a substance move around randomly; this is called Brownian motion. Particles will collide from time to time due to this motion. Sometimes the colliding particles will adhere to each other, thus forming new larger particles. This general phenomenon is the basic principle behind soot forming processes particle inception, condensation and coagulation. The characteristic distinguishing the aforementioned processes is the type of colliding bodies considered. Particle inception is, by definition, the coagulation of two PAH thus creating the first and smallest soot particles. Condensation is the coagulation of PAH onto soot pre-existing particles of different sizes. Finally, Coagulation is the process by which solid soot particles collide between each other forming a single particle whose size is the size of the two colliding particles taken together. The two particles are held together by van der Waals forces as opposed to chemical forces. Coagulation, in the general sense of the process by which two bodies collide, can be described by the Smoluchowski equation presented in Eq.

$$\dot{N}_i = \frac{1}{2}\sum_{j=1}^{i-1}\left(\beta_{j,i-j}N_jN_{i-j}\right) - \sum_{j=1}^{\infty}\left(\beta_{i,j}N_iN_j\right) \tag{5.2}$$

Where N_i is the number of particles of size i and $\dot{N}_i$ the time rate of change of N_i. $\beta_{i,j}$ is the collision frequency factor. The equation gives the change in number of particles of size i as a function of time. The first sum covers all collisions between smaller particles giving new particles of size i, the second sum reflects collisions between particles of size i with all other particles thus diminishing the number of particles of size i. The 1/2 factor in the first sum compensates for the fact that summation will run over each particle size twice. The collision frequency factor $\beta_{i,j}$ depends mainly on temperature and the size of the colliding particles. Different expressions for $\beta_{i,j}$ hold for different physical regimes. Usually a separation is made in three different regimes, depending on gas mean free path and particle size. In most cases, processes operate in the free molecular regime, when pressure is relatively low and particles relatively small. In this regime soot particles behave much like free molecules. On the other end of the scale, is the continuum regime where soot particles more or less float through the fluid made up of gas phase molecules. There is a borderless crossing between these regimes, which is called the transition regime. The different collision factors $\beta_{i,j}$, applicable in separate regimes, will be described in detail under each appropriate process. The different coagulating processes affect first of all soot particle number density, with the exception of particle inception which has a great influence on soot formation as a whole.

Particle Inception and Condensation

The border between large PAH and soot is not an obvious one to draw, in this work the step from gas phase to solid phase is taken when two PAH collide to form a $3D$ structure held together by Van der Waals-forces. This is called particle inception, and constitutes the formation of the smallest soot particles. For particle inception the Smoluchowski equation (Eq. 5.2) simplifies to the expression in Eq. 5.3:

$$\dot{N}_{i=2PAH,pi} = \beta_{i_{PAH},i_{PAH},}N_{PAH}^2 \tag{5.3}$$

where N_{PAH} denotes the concentration or number density of PAH molecules. Eq. 5.3 is given by running the Smoluchovski equation (Eq. 5.2) over a PAH “distribution” containing only one size, considering that in the present work a single PAH is considered (i.e. pyrene). For particle inception, the relevant coagulation regime is the free molecular, because of the small size of PAHs. In the free molecular regime the frequency factor is given by Eq. 5.4.

$$\beta_{i,j}^{fm} = \varepsilon_{i,j}\sqrt{\frac{8\pi k_bT}{\mu_{i,j}}}\left(r_i + r_j\right)^2 \tag{5.4}$$

where k_b is Boltzmann's constant, $\mu_{i,j}$ the reduced mass, r_i the radius of particles of size i and $\varepsilon_{i,j}$ is the size dependent coagulation enhancement factor due to attractive forces between particles. Eq. 5.4 can be rewritten as in Eq. 5.5.

$$\beta_{i,j}^{fm} = K_{fm}\left(i^{1/3} + j^{1/3}\right)^2 \left(\frac{1}{i} + \frac{1}{j}\right)^{1/2} \tag{5.5}$$

where:

$$K_{fm} = \varepsilon_{i,j} \left(\frac{3m_1}{4\pi\rho_s}\right)^{1/6} \left(\frac{6k_bT}{\rho_s}\right)^{1/2} \tag{5.6}$$

based on the fact that $V_i = i \cdot m_1/\rho_s$, m_1 being the mass of one size unit, typically two C-atoms and V_i being the volume of a particle of size i. In the case of particle inception Eq. 5.6 simplifies as follows in Eq.5.7.

$$\beta_{i_{PAH},i_{PAH}} = K_{fm}4\sqrt{2} \cdot i_{PAH}^{1/6} \tag{5.7}$$

PAH also collide and coagulate with soot particles. This process is condensation and is also covered by the Smoluchovski equation (Eq. 5.2), obtaining:

$$\dot{N}_i = \beta_{i_{PAH},i-i_{PAH}} N_{PAH} N_{i-i_{PAH}} - \beta_{i_{PAH},i} N_{PAH} N_i \tag{5.8}$$

Here no simple expression for the collision frequency exists, since PAH collide with soot particles of all sizes. However, if one assumes that PAH are much smaller than soot particles, the collision frequency can be expressed as follows:

$$\beta_{i,j}^{fm} = K_{fm} i^{2/3} j^{1/2} \; with \; i \gg j \tag{5.9}$$

Coagulation

The coagulation of two soot particles can be described by the Smoluchovski equation, with no simplifications as in particle inception and condensation. Unlike particle inception and condensation processes, coagulation process cannot normally be approximated with expressions containing only free molecular regime. Apart from an expression for coagulation in the free molecular regime, the continuum regime and the transition regime also have to be covered. The Smoluchowski equation (Eq. 5.2) holds under all these regimes, however the collision frequency differs. The Knudsen number, defined as reported in Eq, 5.10, is used as reference non-dimensional number to evaluate which is the reference regime for the specific collision process.

$$Kn = \frac{2\lambda_{gas}}{D_p} \tag{5.10}$$

where λ_{gas} is the gas mean free path and D_p is particle diameter. Based on the following thresholds, the reference regime is identified:

- $Kn \gg 1$: Free molecular regime
- $Kn \ll 1$: Continuum regime
- $0.1 < Kn < 10$: Transition regime

The expression for the frequency collision factor in the free molecular regime can be found in Eq. 5.5. In the continuum regime, the expression for the collision frequency is:

$$\beta_{i,j}^{c} = K_c\left(i^{1/3} + j^{1/3}\right)^2 \left(\frac{C_i}{i^{1/3}} + \frac{C_j}{j^{1/3}}\right)^{1/2} \tag{5.11}$$

$$K_c = \frac{2k_BT}{3\eta}\,, C_i = 1 + 1.257Kn_i \tag{5.12}$$

where η is the gas viscosity and C_i the Cunningham slip correction factor for particles with Knudsen number Kn_i. The semi-empirical Fuchs formula [242] is often used to express the coagulation in the transition regime. A reasonable approximation of $\beta_{i,j}^{tr}$ in the transition regime can be given by the harmonic mean between the free molecular $\beta_{i,j}^{fm}$ and continuum $\beta_{i,j}^{c}$.

5.2.4 Chemical Models

The other group of processes involved in soot formation are surface reactions. These constitute all the chemical reactions taking place at the surface of the soot particles, between gas phase species and sites on the soot surface. Surface reactions either result in carbon mass being added to the soot particle surface, this is called surface growth. The opposite, the removing of mass from the soot surface, is called oxidation. Surface reactions rate are directly dependent on gas phase chemistry, and also affect gas phase species concentrations. This processes, to a large extent, control total soot mass, and often have marginal effect on total number density of soot particles. The exception to this is oxidation, which potentially consumes particles until they vanish, thus affecting number density. As a general rule of thumb, soot consists to 1% by weight of hydrogen. In the present model, soot is considered to consist solely of carbon and the hydrogen content is neglected. The concept of active sites facilitates the calculation of surface reactions. For each aromatic ring on the surface, there is possibility for reactions. This is called an active site. The number of active sites is calculated and can be treated in analogy to gas phase species.

(1.a) $C_{soot,i}H + H \overset{k_{1a}}{\longleftrightarrow} C_{soot,i}^{*} + H_2$

(1.b) $C_{soot,i}H + OH \overset{k_{1b}}{\longleftrightarrow} C_{soot,i}^{*} + H_2O$

(2) $C_{soot,i}^{*} + H \overset{k_{1a}}{\longrightarrow} C_{soot,i}H$

(3.a) $C_{soot,i}^{*} + C_2H_2 \overset{k_{3a}}{\longleftrightarrow} C_{soot,i}^{*}C_2H_2$

(3.b) $C_{soot,i}^{*}C_2H_2 \overset{k_{3b}}{\longrightarrow} C_{soot,i+1}H + H$

(4.a) $C_{soot,i}^{*} + O_2 \overset{k_{4a}}{\longrightarrow} C_{soot,i-1}^{*} + 2CO$

(4.b) $C_{soot,i}^{*}C_2H_2 + O_2 \overset{k_{4b}}{\longrightarrow} C_{soot,i}^{*} + 2CHO$

(5) $C_{soot,i}H + OH \overset{k_5}{\rightarrow} C_{soot,i-1}^{*}$

Table 5.1 Reactions in the $HACARC$ mechanism for heterogeneous surface growth and oxidation.

At the active sites a number of reactions can take place according to Table 5.1. In the first step, an H-radical is abstracted from the soot surface (1.a&b) forming an active radical site on the soot surface. Addition of C_2H_2 at the active radical site follows (3.a). The formation of a new benzene-ring at the surface is completed in the ring closing reaction (3.b). There is in reactions (1.a), (1.b) and (3.a) the possibility for having a backwards reaction, as indicated by the double directed arrows in Table 5.1. The ring opening reaction (3.b) is elsewhere also referred to as fragmentation, and in some cases treated as a separate source term. The counterintuitive fact that only two carbon atoms are added to form a new benzene structure (or 6-ring), can be explained from the fact that soot surface is, generally speaking, very large. This means that, on average, the most usual surface structure is one where already 4 of the carbon atoms needed are present. Reactions (4) and (5) describe oxidation of soot. The reaction rate of reaction (3.1) for particles of size class i can thus be expressed as in Eq. 5.13.

$$r_{3a,i} = k_{3a,f}[C_2H_2][C^*_{soot,i}] \tag{5.13}$$

where $r_{3a,i}$ is time rate of reaction and $k_{3a,f}$ is the Arrhenius coefficient. The active radical soot sites are assumed to be in steady state, leading to algebraic equations for the concentration of active radical sites. Based on Table 5.1, the concentration of active radical sites is:

$$[C^*_{soot,i}] = A[C_{soot,i}] \tag{5.14}$$

$$A = \left(\frac{k_{1a,f}[H]+k_{1b,f}[OH]+k_5[OH]}{k_{1a,b}[H_2]+k_{1b,b}[H_2]+k_2[H]+k_{3a,f}[C_2H_2]f_{3,a}+k_4[O_2]}\right) \tag{5.15}$$

$$f_{3,a} = \left(\frac{k_{3b,f}}{k_{3b,f}+k_{3a,b}+k_{4,b}[O_2]}\right) \tag{5.16}$$

The concentration of active sites can be calculated as follows in Eq. 5.17.

$$[C_{soot,i}] = \alpha \frac{\chi_{soot}}{N_A} S_i N_i \tag{5.17}$$

where α is the fraction of possible sites which are actually active, χ_{soot} the number of sites per unit area, S_i the surface area. The fraction of active sites α has to be estimated. This quantity has been found to decrease with temperature but in the present work it is assumed to be constant. Since the number of possible active sites depend on number of benzene-rings on the soot surface such that $\chi_{soot}S_1 = 1$ the following expression holds:

$$\chi_{soot}S_i = \chi_{soot}S_1 i^{2/3} = i^{2/3} \tag{5.18}$$

if the assumption of spherical particles is introduced. In the present model, it is possible to set a fractal dimension of soot particles in the surface reactions modelling. Fractal dimension gives the possibility to set the shape of soot particles, so that mean shape of particles can be given any form between spherical particles and chain-shaped particles. As particles with higher fractal dimension have a higher area to volume ratio, a higher fractal dimension means increased surface reactions. This means that Eq. 5.18 is modified to the expression in Eq. 5.19.

$$\chi_{soot}S_i = \chi_{soot}S_1 i^{\theta/3} = i^{\theta/3} \tag{5.19}$$

where C signifies fractal dimension such that $\theta = 2$ means spherical particles, $\theta = 3$ means soot particles form chains of the smallest soot particles. With this definition a fractal dimension of 2.25 is normally used. This fractal dimension has experimentally been found to be a good approximation under most sooting conditions [240].

⬡ 5.3 The Sectional Method

In the previous paragraph, the basic mathematical formulations used to model physical and chemical phenomena taking part into soot formation have been presented. In the present paragraph, the concepts previously outlined are developed to provide an insight into Sectional Method model formulation. For the sake of brevity, this dissertation will not cover the entire mathematical formulation needed to derive the final set of equations but will provide the basic set of notions needed to understand the choices that led to the customized version of the model tested in the following paragraphs. The reader should consider the following reference publications for further details on the model implementation as used in the present work [46,47,48]. Firstly, the reason that led to the choice of this model while approaching GDI soot modelling needs to be discussed. Soot modelling is commonly recognized to be one of the most difficult subjects in $3D$-CFD in-cylinder simulations due to the complex interplay and interdependency of processes contributing to soot formation in combustion systems. As extensively mentioned previously, the main concern related to soot emissions is not strictly related to PM in general but also to PM_{10} and $PM_{2.5}$, especially in the urban areas. Focusing on the problem from OEMs standpoint, the biggest concern is limiting PN concentration at the exhaust. For this reason, empirical and semi-empirical soot models based on simple correlations providing an estimation of engine-out PM are simply not useful anymore. In this scenario, an advanced soot model able to reliably predict engine-out $PSDF$ at the exhaust is needed. The Method of Moments and the Sectional Method models are still considered among the most advanced soot models at the time of writing and have been successfully used to predict soot formation not only in laminar flames or burners [46,47] but also in Diesel engine cases [48,49]. The historical link with Diesel engine simulation is simply due to historical reasons, since originally gasoline PFI engines had no issues with engine-out PM. To the extent of the author's best knowledge, only a few studies in literature [128,129] focused on GDI soot modelling. These studies focused on a single OP and a comprehensive methodology for GDI soot modelling was not provided. Moreover, a poor experimental-CFD correlation was found and the only previous study that used the Sectional Method for GDI soot modelling found acceptable results only relying on a case to case tuning of the soot model constants [129]. As a further remark, no previous study focused on a methodology able to match engine-out $PSDF$. The final aim of the present work is to provide a methodology, based on the Sectional Method, to be used to quantitatively predict GDI soot without a dedicated soot model tuning. The Sectional Method constitutes an enhancement of the Method of Moments, as it provides information on the $PSDF$, without any assumption on the distribution, and fewer approximations are needed for the source terms. In the end, the Sectional Method is another way to mathematically express and predict the $PSDF$. In the Sectional Method, the vastness of the $PSDF$ is tackled by dividing it into a discrete number of finite sections [47]. In other words, the model relies on a volume-based discretization of the particles population constituting the $PSDF$, further introducing the assumption that particles in each section are perfectly spherical. This last hypothesis is introduced as it greatly simplifies the mathematical formulation, therefore decreasing its computational cost. In Fig. 5.8(a), an arbitrary $PSDF$ is shown.

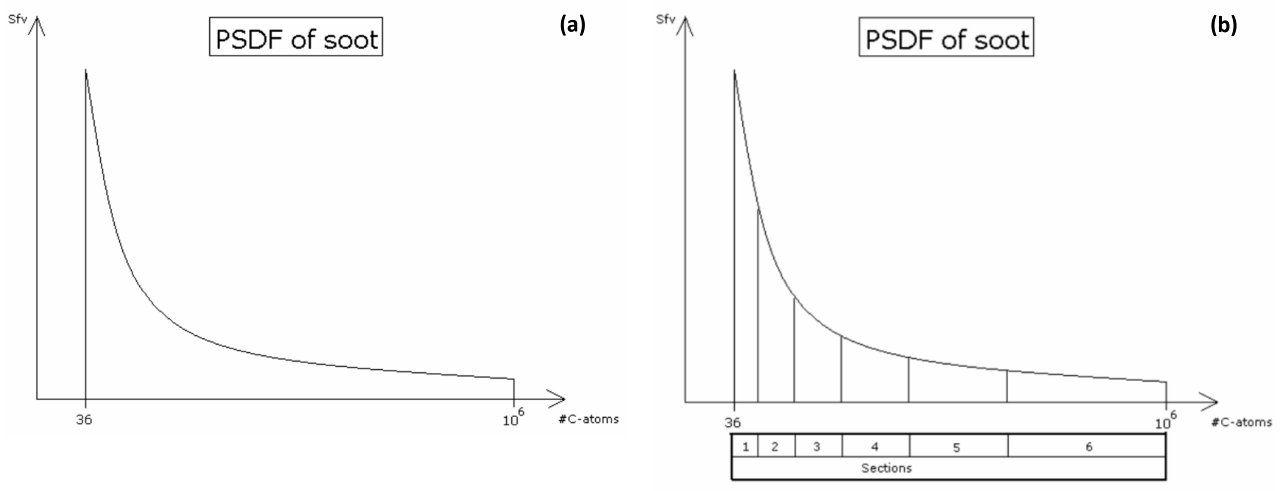

Figure 5.8 (a) An arbitrary $PSDF$ of soot (b) The $PSDF$ divided into sections.

The x-axis size scale is the volume of soot particle, v. The information present in the $PSDF$ within each section is condensed into one single scalar, which is Soot Volume Fraction (Q or sfv), reported on the y-axis. This choice is intentional since soot volume is the main entity treated in the model and the scalar for which soot source terms and balance equations are formulated. As visible in Fig. 5.8(b), a number of discrete sections is identified to discretize the $PSDF$. The space between the smallest soot particle (with volume v_{MIN}) and the largest soot particle (with volume v_{MAX}) is normally divided into sections of growing size, starting from the smallest soot particle. The reason for this is the size of the size scale. In fact, if the size scale in Fig. 5.8(a) was to be divided into 20 equally large sections, the first section would cover particles ranging in size from 36 to 50000 carbon atoms. Representing these with a single scalar would be a severe approximation. This means that a higher resolution is given to smaller particles. This choice makes sense, since for a given absolute size change, the relative difference is greater in the sections representing smaller soot particles. The volume-based discretization in sections hereafter provided is the mathematical formulation as implemented in STAR-CD solver, which is in particular based on the hypothesis that the maximum volume of the i^{th} section $v_{i,max}$ is twice as big as the minimum volume in the same section, $v_{i,min}$, as reported in Eq. 5.21. Therefore, the generic i^{th} section is identified by a lower, $v_{i,min}$, and upper, $v_{i,max}$, volume boundaries which are calculated as reported in Eq. 5.20-5.21. Based on these boundaries, the i^{th} section is populated by spherical soot particles of volume $v_{i,m}$, defined as reported in Eq. 5.22.

$$v_{i,min} = 1.5 v_{PAH} 2^{i-1} \tag{5.20}$$

$$v_{i,max} = 2 v_{i,min} \tag{5.21}$$

$$v_{i,m} = \frac{v_{i,min} + v_{i,max}}{2} \tag{5.22}$$

The model also assumes that the smallest soot particle considered has a volume equal to two pyrene molecules ($v_{PAH} = 0.4 \cdot 10^{-27}\text{m}^3$). As already mentioned, the model relies on the assumption that pyrene is the representative PAH species and that nucleation, occurring in the sole first section, takes place when two pyrene molecules collide successfully. When the section boundaries are clearly identified, the integral of the soot volume fraction density $q_i(v)$ over the i^{th} section yields the soot volume fraction Q_i. By definition, soot volume fraction is calculated as i^{th} section soot particle volume normalized by the total volume obtained summing both gas and solid phase volumes. Assuming that soot particle volume is negligible compared to the gas volume, Q_i can be calculated from Eq. 5.23, where the quantity reported as $\tilde{Y}_{s,i}$ is the soot mass fraction in the i^{th} section.

$$Q_i = \frac{\bar{\rho}}{\rho_s}\tilde{Y}_{s,i} \tag{5.23}$$

All soot related quantities are obtained by solving a number of transport equations, reported in Eq. 5.24, equal to the number of sections used for the volumetric discretization.

$$\frac{\partial\bar{\rho}\tilde{Y}_{s,i}}{\partial t} + \nabla\cdot\left(\bar{\rho}\tilde{u}\tilde{Y}_{s,i}\right) = +\nabla\cdot\left(\bar{\rho}D_{t,s}\nabla\tilde{Y}_{s,i}\right) + \rho_s\tilde{\Omega}_{s,i} \quad for\ i = 1{:}\,i_{max} \tag{5.24}$$

being $\bar{\rho}$ gas phase density, ρ_s soot density, $\tilde{u}$ the gas velocity, $D_{t,s}$ the soot turbulent diffusion coefficient, i_{max} the highest section number considered and $\Omega_{s,i}$ the soot source term for the i^{th} section. The total soot source term is then computed, based on a cell-wise thermodynamic and mixture quality states, as follows, in Eq. 5.25.

$$\tilde{\Omega}_{s,i} = \tilde{\Omega}_{pi,i} + \tilde{\Omega}_{cond,i} + \tilde{\Omega}_{coag,i} + \tilde{\Omega}_{sg,i} + \tilde{\Omega}_{ox,i} \quad with\,\Omega_{pi,i}|_{i\neq 1} = 0 \tag{5.25}$$

where $\tilde{\Omega}_{pi,i}$ is the particle inception source term, $\tilde{\Omega}_{cond,i}$ is the condensation source term, $\tilde{\Omega}_{coag,i}$ is the coagulation source term, $\tilde{\Omega}_{sg,i}$ is the surface growth source term and $\tilde{\Omega}_{ox,i}$ is the oxidation source term. Dedicated expressions can be derived for each source term, as shown in detail in [48]. The final expressions, as implemented in STAR-CD, are reported hereafter and discussed where needed. Based on a steady-state assumption between soot precursors formation rate in the gas phase $\widetilde{RPAH}$ and their consumption by nucleation and condensation processes, dedicated source terms for nucleation (Eq. 5.26) and condensation (Eq. 5.27) can be derived.

$$\tilde{\Omega}_{pi,1} = \frac{2\nu_{PAH}\widetilde{RPAH}^2}{\left[2C_{pi}A(\tilde{Y}_{s,i})^2\sqrt{\tilde{T}}+2\widetilde{RPAH}+2A(\tilde{Y}_{s,i})C_{pi}\sqrt{\tilde{T}}\sqrt{\frac{2\widetilde{RPAH}}{C_{pi}\sqrt{\tilde{T}}}+A(\tilde{Y}_{s,i})^2}\right]} \tag{5.26}$$

$$\tilde{\Omega}_{cond,i} = \frac{\nu_{PAH}C_{cond,i}f\left(\frac{\bar{\rho}\tilde{Y}_{s,i}}{\rho_s}\right)\widetilde{RPAH}}{0.5\sum_{i=1}^{i_{max}}C_{cond,i}f\left(\frac{\bar{\rho}\tilde{Y}_{s,i}}{\rho_s}\right)+\sqrt{\frac{2C_{pi}\widetilde{RPAH}}{\sqrt{\tilde{T}}}+\left(0.5\sum_{i=1}^{i_{max}}C_{cond,i}f\left(\frac{\bar{\rho}\tilde{Y}_{s,i}}{\rho_s}\right)\right)^2}} \tag{5.27}$$

It is interesting to notice how the frequency collision factors for nucleation, k_{pi}, and condensation, k_{cond}, are not explicitly reported in Eq. 5.26-5.27 and are highlighted in Eq. 5.28-5.29, respectively.

$$k_{pi} = C_{pi}\tilde{T} = 2.5\left(\frac{3}{4\pi}\right)^{1/6}\sqrt{\frac{6k_b}{\rho_s}}\sqrt{\frac{2}{\nu_{PAH}}}4(\nu_{PAH})^{2/3}\sqrt{\tilde{T}} \tag{5.28}$$

$$k_{cond} = \sum_{i=1}^{i_{MAX}} 1.3\left(\frac{3}{4\pi}\right)^{1/6}\sqrt{\frac{6k_b}{\rho_s}}\sqrt{\frac{1}{\nu_{i,m}}+\frac{1}{\nu_{PAH}}}\left(\nu_{i,m}^{1/3}+\nu_{PAH}^{1/3}\right)^2 f\left(\frac{\bar{\rho}\tilde{Y}_{s,i}}{\rho_s}\right)\sqrt{\tilde{T}} \tag{5.29}$$

where i_{MAX} is the total number of sections. In order to report the complete set of source terms for all the physical phenomena, the generic source term for coagulation is reported, in synthetic form, in Eq. 5.30.

$$\tilde{\Omega}_{coag,i} = \sum_{k=1}^{j-1}\left(\beta_{k,k} n_k n_k 2v_{m,k}\right) - \beta_{j,j} n_j n_j 2v_{m,j} + \sum_{k=1}^{j-1}\sum_{y=k+1}^{j}\left(\beta_{k,y} n_k n_y 2v_{m,k}\right) - \sum_{k=j+1}^{i_{MAX}-1}\left(\beta_{j,k} n_j n_k 2v_{m,j}\right) \quad (5.30)$$

where, generally speaking, n_k is soot number density for the k^{th} section and $\beta_{k,y}$ the frequency collision factor between particles of k^{th} and y^{th} sections. It is noteworthy, that being a purely physical-based phenomena not directly dependent on chemical processes, coagulation source term is the only one not dependent on chemistry-based coefficients. Moving to surface reactions processes, the source terms for surface growth and oxidation are reported in Eq. 5.31-5.32 for a generic i^{th} section, respectively. Such expressions are obtained introducing the hypothesis of spherical particles ($\theta = 2$).

$$\tilde{\Omega}_{sg,i} = \alpha\left(\nu_{C_2}\right)^{\frac{3-\theta}{\theta}}\left(\tilde{k}_d - \tilde{k}_{rev}\right)\begin{bmatrix} 2\left(\frac{3}{3+\theta} q_{i-1}\left(\nu_{i-1,max}{}^{\frac{3-\theta}{\theta}} - \nu_{i-1,min}{}^{\frac{3-\theta}{\theta}}\right) + \frac{3}{\theta} q_{i-1}^{\mu}\left(\nu_{i-1,max}{}^{\frac{\theta}{3}} - \nu_{i-1,min}{}^{\frac{\theta}{3}}\right)\right) \\ -\left(\frac{3}{3+\theta} q_{i}\left(\nu_{i,max}{}^{\frac{3-\theta}{\theta}} - \nu_{i,min}{}^{\frac{3-\theta}{\theta}}\right) + \frac{3}{\theta} q_{i}^{\mu}\left(\nu_{i-1,max}{}^{\frac{\theta}{3}} - \nu_{i-1,min}{}^{\frac{\theta}{3}}\right)\right) \end{bmatrix}$$
$$for\ i = 2, \dots, i_{MAX} - 1 \quad (5.31)$$

$$\tilde{\Omega}_{ox,i} = \alpha\left(\nu_{C_2}\right)^{\frac{3-\theta}{\theta}}\left(\tilde{k}_{O_2} + \tilde{k}_{OH}\right)\begin{bmatrix} \left(\frac{3}{3+\theta} q_{i+1}\left(\nu_{i+1,max}{}^{\frac{3-\theta}{\theta}} - \nu_{i+1,min}{}^{\frac{3-\theta}{\theta}}\right) + \frac{3}{\theta} q_{i+1}^{\mu}\left(\nu_{i+1,max}{}^{\frac{\theta}{3}} - \nu_{i+1,min}{}^{\frac{\theta}{3}}\right)\right) \\ -2\left(\frac{3}{3+\theta} q_{i}\left(\nu_{i,max}{}^{\frac{3-\theta}{\theta}} - \nu_{i,min}{}^{\frac{3-\theta}{\theta}}\right) + \frac{3}{\theta} q_{i}^{\mu}\left(\nu_{i,max}{}^{\frac{\theta}{3}} - \nu_{i,min}{}^{\frac{\theta}{3}}\right)\right) \end{bmatrix}$$
$$for\ i = 2, \dots, i_{MAX} - 1 \quad (5.32)$$

As visible, Eq. 5.31-5.32 are valid for sections ranging from the second to $i_{MAX} - 1$ sections. Dedicated expressions are, in fact, used for the first and the last (i_{MAX}) sections but are not here reported for the sake of brevity. Considering Eq. 5.31, surface growth source term $\tilde{\Omega}_{sg,i}$ depends on the difference between $\tilde{k}_d$ and $\tilde{k}_{rev}$, respectively the forward and backward reaction rate constants for the $HACARC$ mechanism, outlined in Table 5.1. Conversely, in Eq. 5.32, it is possible to notice how oxidation source term $\tilde{\Omega}_{ox,i}$ is proportional to the summation of $\tilde{k}_{O_2}$ and $\tilde{k}_{OH}$, the reaction rate constants for oxidation via O_2 and OH, respectively, whose reactions are reported in Table 5.1. The set of Eq. 5.26-5.27-5.30-5.31-5.32 constitutes a closure to Eq. 5.24-5.25. In order to fully close the mathematical formulation, $\widetilde{RPAH}, \tilde{k}_d, \tilde{k}_{rev}, \tilde{k}_{O_2}, \tilde{k}_{OH}$ coefficents have to be evaluated at a cell-wise level based local on thermodynamic and mixture quality states ($p^*, T_u^*, \phi^*, EGR^*$) and progress variable value $\tilde{c}^*$. As a final comment, it is important to underline that the Sectional Method is decoupled from the combustion model, $ECFM$-$3Z$ in the present work, since the characteristic timescale of soot chemistry is assumed to be higher than the characteristic turbulence timescale, as shown in Eq. 5.33. Based on the flamelet assumption, fuel oxidation timescale is assumed to be much lower than turbulence timescale, as reported in Eq. 5.34, and it is therefore possible to effectively decouple soot and combustion models.

$$Da_s = \frac{\tau_{turbulence}}{\tau_{soot\ chemistry}} < 1 \quad (5.33)$$

$$Da_{comb} = \frac{\tau_{turbulence}}{\tau_{fuel\ oxidation}} \gg 1 \quad (5.34)$$

where Da_s and Da_{comb} are the Damköhler numbers for soot and combustion, respectively.

⬡ 5.4 Soot Chemistry

⬡ 5.4.1 Exploratory Studies on 1D Burner Stabilized Flames

Based on the previous paragraph, it is essential to accurately estimate $\widetilde{RPAH}, \tilde{k}_d, \tilde{k}_{rev}, \tilde{k}_{O_2}, \tilde{k}_{OH}$ coefficients at engine-like conditions to provide the Sectional Method with quantitative data related to all the chemistry-based phenomena which are interdependent with the aforementioned phenomena involved in soot formation. These information are provided in the form of libraries where the coefficients are stored based on local on thermodynamic and mixture quality states $(p^*, T_u^*, \phi^*, EGR^*)$ and progress variable value $\tilde{c}^*$. In order to further stress the reader's attention on the key role of chemistry-based libraries, the links between soot theory, the Sectional Method and the chemistry solver are graphically outlined in in Fig. 5.9.

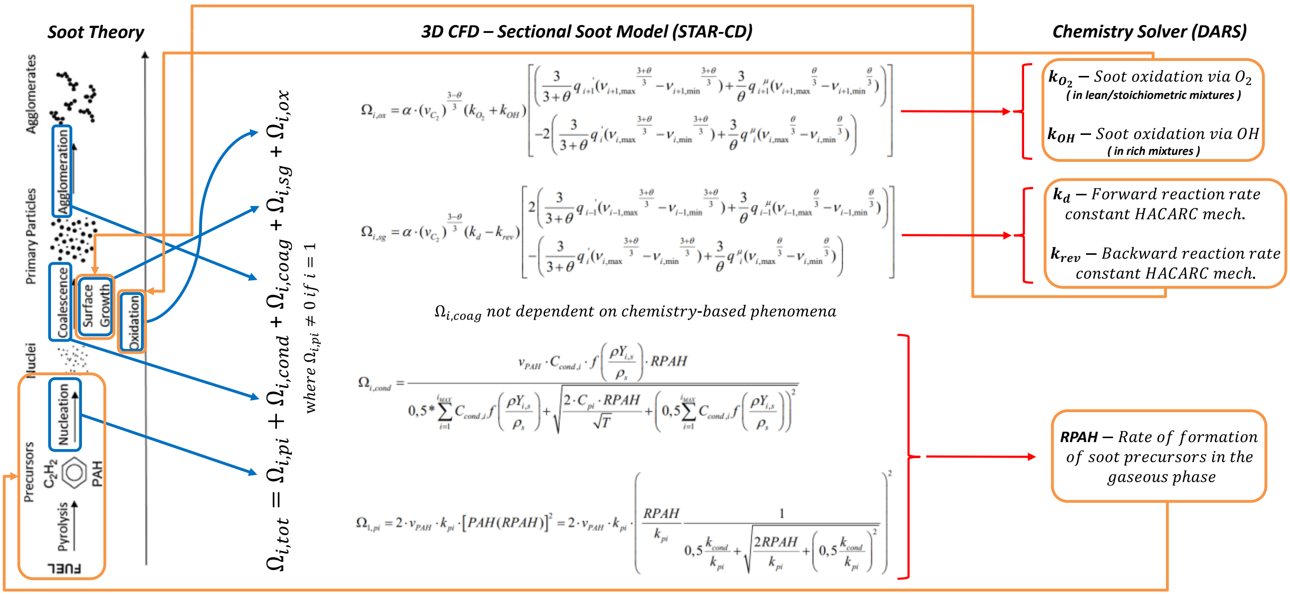

Figure 5.9 Schematic representation of the links between soot theory, the Sectional Method model as implemented in the CFD solver (STAR-CD) and the chemistry solver used in the present work (DARS).

Previous studies focusing on soot simulation using the Sectional Method, exploited diffusive flamelet libraries to model Diesel combustion [48,49] and Plug Flow Reactor (PFR) [129] ones to model GDI combustion. In the present work, a novel modelling approach is proposed to introduce chemistry-based information in $3D$-CFD simulations in the form of libraries. In fact, GDI combustion although being characterized by local diffusive phenomena is mainly premixed. This hinders the use of a diffusive flamelet-based approach while generating soot libraries. In the present work, the use of a CP-based tabulated approach is proposed to model relevant soot chemistry coefficients at engine-like conditions. For this reason, previous work on fuel surrogates specifically focused on the quantitative validation of reactivity via ignition delay calculations. This is an essential step since surrogates reactivity influences both temperature and HRR profiles in the reactor. A further big step, in this sense, has been the introduction of a dedicated methodology able to target a real fuel ST, as shown in Paragraph 3.2. The other main actor in this kind of simulations is the chemical kinetics mechanism chosen to model PAH chemistry. In this paragraph, an exploratory study aiming to evaluate suitable mechanisms is undertaken based on the availability of an experimental dataset found in literature [247]. As previously mentioned, the results reported in the present paragraph have to be considered as an exploration study for a number of reason discussed hereafter. First of all, the analysis focused on two mechanisms only and such dataset can not be considered wide enough to draw significant conclusions. A wider number of candidates should be considered, preferably focusing on mechanism provided by different sources. In fact, this would also allow to globally evaluate the solidity of fuel oxidation pathways description. Secondly, such kind of studies are usually carried out considering a multitude of experimental datasets covering pure compounds, blends and different test conditions. In the present analysis, two mechanisms are considered. The first, used as reference, is a quite old mechanism proposed by Blanquart et al. [132]. This mechanism has been commonly recognized as state-of-the-art mechanism in terms of PAH modelling for many years in the scientific community and has been extensively validated over a wide number of conditions. The second mechanism is the so-called PAN chemical kinetics mechanism proposed in [248] to estimate soot precursors formation in GDI applications. The PAN mechanism is modified here on purpose to include all the chemical species and reactions needed to estimate the aforementioned coefficients, as required by the Sectional Method. In particular, as reported in [49] pyrenyl radical A3R5$^-$ ($C_{16}H_9$) is required to estimate $RPAH$. The original PAN mechanism accounts for 85species and 439 reactions and features dedicated sub-mechanism for isooctane, n-heptane and toluene oxidation pathways together with a dedicated PAH sub-mechanism for soot precursors. The PAH sub-mechanism is modified accordingly to introduce pyrenyl radical ($C_{16}H_9$) and its main formation/consumption pathways. In Fig.5.10, the main modifications introduced in the original PAH mechanism are reported.

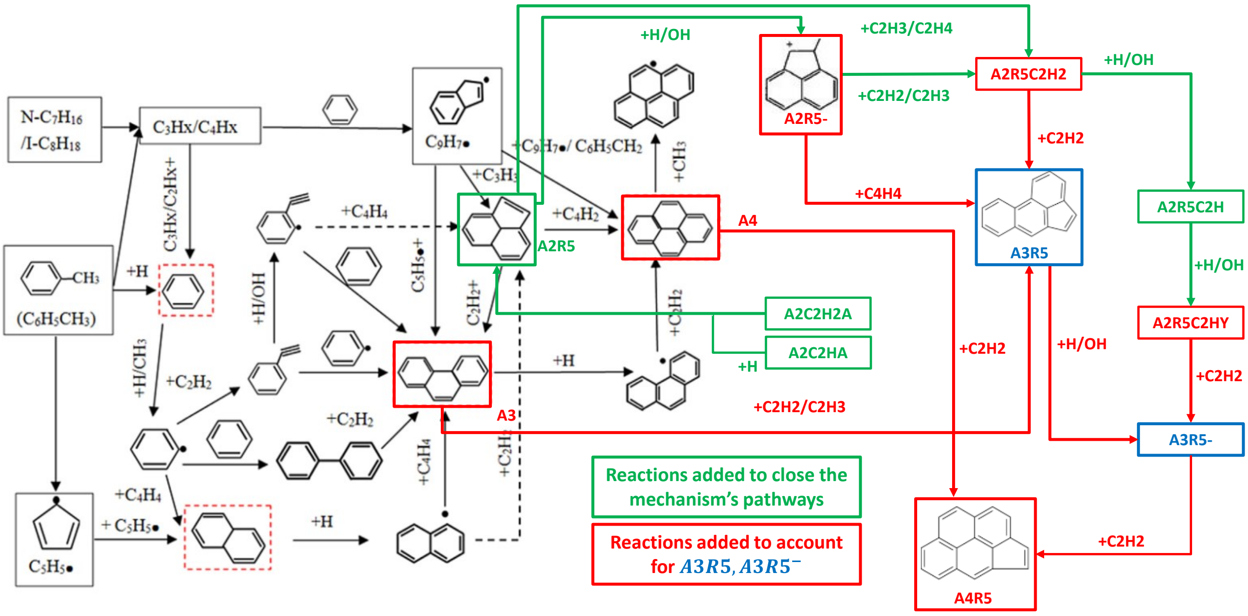

Figure 5.10. Modified PAH mechanism to account for A3R5 and A3R5$^-$. Original PAN mechanism PAH pathways (solid black line) and additional PAH pathways (solid colored lines) constituting the new PAN-HY mechanism.

In particular, species and reactions introduced to account for A3R5 and A3R5$^-$ are reported in red, while those represented in green are introduced to close the pathways related to the secondary species involved in A3R5 and A3R5$^-$formation and consumption. The final mechanism, herein referred to as PAN-HY, accounts for 95 species and 489 reactions. In order to validate the modified mechanism, the previously mentioned stabilized burner premixed flame experimental dataset presented in [247] is used as a reference to perform 1D simulations using DARSv2019.1 chemistry solver. In the experiments, the micro-structure of laminar premixed, atmospheric pressure, fuel-rich flames of n-heptane/oxygen/argon were studied at two reference equivalence ratios. In the present study, the so-called "Flame A" dataset is considered for validation purposes and the related details are summarized in Table 5.2.

	Cold flow initial velocity [cm/s]	**Burner surface temperature [K]**	**ϕ [-]**	**Fuel (*n-Heptane*) [%mol]**	**Oxidizer (O_2) [%mol]**	**Inert Gas (*Ar*) [%mol]**
Flame A	5.25	700	1.97	5.33	29.70	64.97

Table 5.2. Flame A dataset: flame characteristics and pre-combustion compositions.

A comparison between the interpolated and measured flame temperature profiles is reported in Fig. 5.11(a). For the sake of completeness, a comparison between the computed flame velocity and the measured velocity at the burner's surface is reported in Fig. 5.11(a). It must be noted that an uncertainty of ± 0.2 mm is reported in terms of measurements positional accuracy. An additional error of ± 80 K, due to the use of thermocouples for local temperature measurements, must also be considered. Moreover, the sampling probes used to measure species concentration might lead to flame perturbations. As highlighted in [249], such perturbations might cause a mismatch between measured and predicted species concentration. Therefore, the experimental temperature profile is imposed in numerical simulations. To overcome this problem, the experimental mole fraction profiles are shifted $+0.5$ mm upstream relative to the unperturbed flame temperature profile as suggested in [250]. This is a minor modification to the experimental dataset compared to the solutions presented in other studies such as [132], where the experimental temperature profile is adjusted to match fuel and oxidizer consumption. As visible in Fig. 5.11(b), calculated mole fraction evolution of main combustion products is in fairly good agreement with experimental data, despite the minor shift introduced with respect to the original dataset.

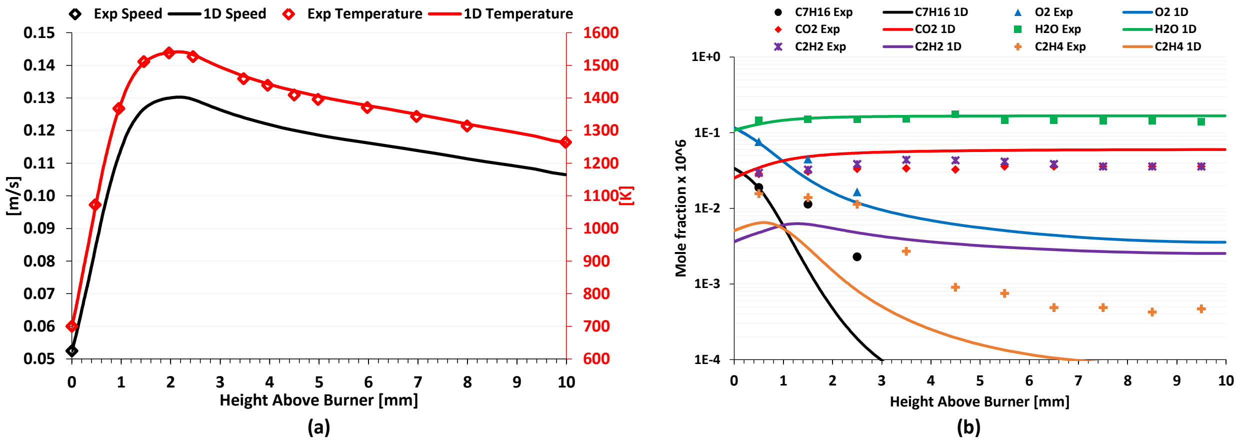

Figure 5.11. (a) Comparison between: experimental (dots)/interpolated (solid line) flame temperature profiles in red, experimental gas velocity measured at the burner's surface and calculated flame speed profile in black. (b) Comparison between measured (dots) and calculated species mole fraction (solid line).

With the present setup, n-heptane consumption is slightly overestimated and better results could potentially be achieved using the approach suggested in [132]. Focusing on the small hydrocarbon species, which usually constitute the main building blocks for PAH species formation, it is possible to notice how the proposed PAN-HY mechanism is able to predict the evolution of Acetylene (C_2H_2) and Ethylene (C_2H_4) mole fraction profiles although both are quantitatively underestimated. Since a good agreement was found between calculated and measured profiles for the main combustion products, a quantitative comparison between calculated and measured main PAH species profiles was carried out to investigate PAN-HY mechanism ability to predict soot precursors formation in premixed flames, as reported in Fig. 5.12. Although a wide variety of PAH species were measured in [247], only the key PAH species are here analysed. Namely: Benzene ($A1$), Naphthalene ($A2$), Phenanthrene ($A3$) and Pyrene ($A4$). Monitoring these species is particularly important since most bigger soot precursors start growing from incipient Benzene molecules which grow by addition of carbon atoms based on the HACARC mechanism previously outlined.

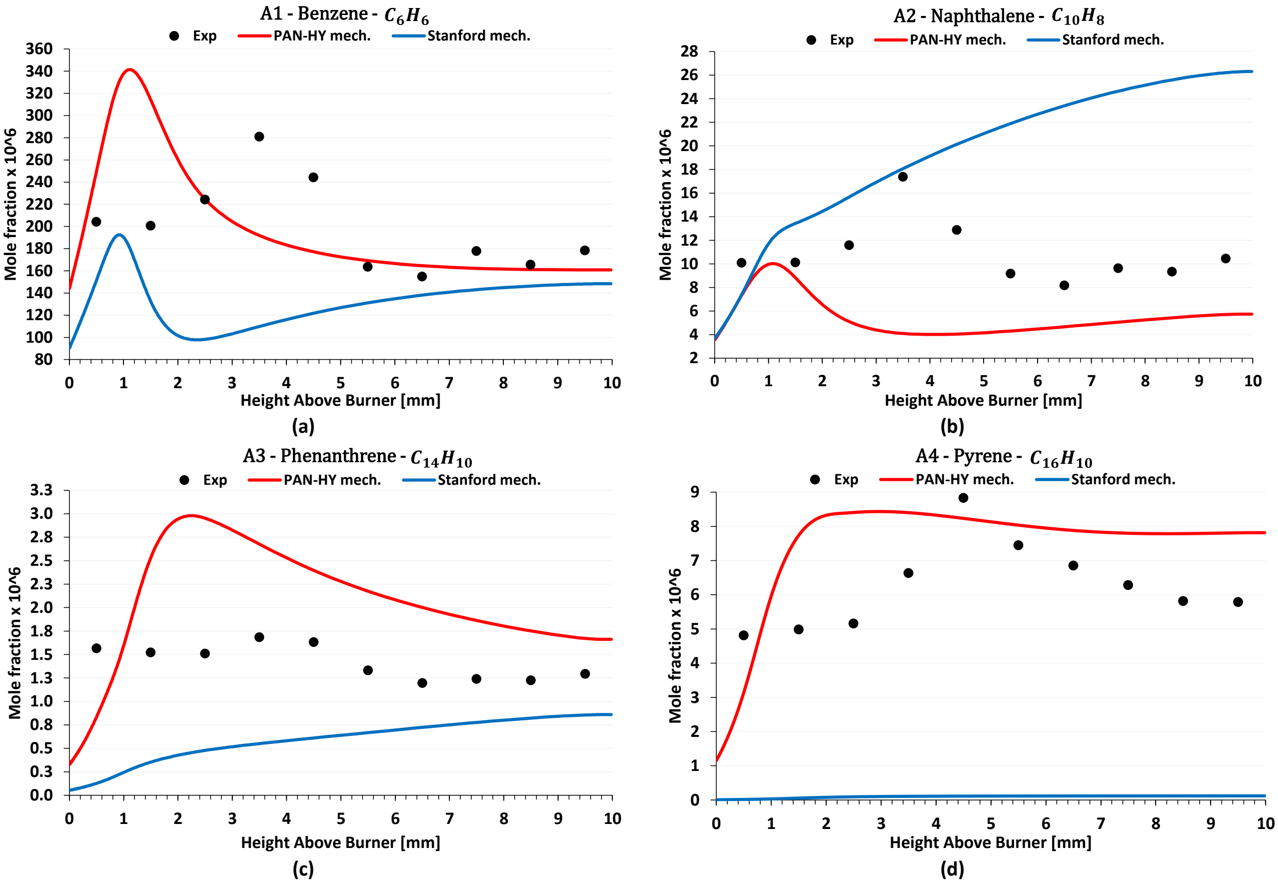

Figure 5.12. Main *PAH* species mole fraction profiles as a function of *HAB*: measured (dots), present mechanism PAN-HY (red solid line) and Stanford mechanism [132] (blue solid line) for **(a)** Benzene, **(b)** Naphthalene, **(c)** Phenanthrene and **(d)** Pyrene.

A particular focus is here devoted to the quantitative estimation of pyrene mole fraction profile, since the Sectional Method relies on the assumption that nucleation by two pyrene colliding molecules and quantitatively estimates *RPAH* based on pyrenyl radical $C_{16}H_9$ and acetylene C_2H_2 concentrations. In order to evaluate the accuracy of the investigated PAN-HY mechanism, the mechanism proposed by Blanquart et al. [132], here called "Stanford mech.", is also considered. While both mechanisms give a reasonable quantitative prediction of $A1$ and $A3$, a better prediction is given by PAN-HY for $A2$ and especially for $A4$. Despite constituting an interesting analysis, this validation activity should be extended to other relevant mechanisms found in literature and a wider number of validation cases in order to draw relevant conclusions for the research community. On the other hand, the analysis here presented demonstrates how *PAH* mechanisms are nowadays able to provide reasonable results considering laminar flames experiments at ambient conditions. Another key element has to be considered while choosing the chemical kinetics mechanism used to generate soot libraries. The chosen mechanism must contain and accurately describe the oxidation pathways of all pure compounds used in the fuel surrogates. Based on the results obtained in Paragraph 5.2 it is possible to conclude that ethanol content in the fuel surrogate is a key element deeply affecting soot formation at engine-like conditions. For this reason, none of the analysed mechanisms could be used to generate soot libraries since none of them model ethanol oxidation pathways. The mechanism proposed in 2019 by Cai et al. [134] and previously used in Paragraph 5.2 to generate the soot libraries is chosen as reference candidate to generate a dedicated soot library for ULG95 commercial gasoline, for the sake of the present study. As a final remark, this allows to use the *ETRF* surrogate generated in Paragraph 5.2, able to accurately mimic ULG95 *ST*. ULG95 gasoline was on purpose included in the analysis carried out in Paragraph 5.2 since it is deemed to well represent a European *RON*95 *E*5 commercial gasoline, such as the one used in the experiments. This aspect is of particular importance for the experimental-CFD comparison since surrogates composition was found, in Paragraph 5.2, to deeply affect ST on even stratification at spark timing.

⎔ 5.4.2 Soot Library Stepping Sensitivity

Since a suitable $ETRF$ chemical kinetics mechanism [134] and a $ETRF$ fuel surrogate (ULG95-Paragraph 5.2) were chosen, (p, T_u, ϕ, EGR) ranges and stepping are the only information missing to generate a soot library. While suitable ranges for each variable can be easily determined based on the thermodynamic history during the combustion process (p,T_u) and on ϕ and EGR scalar fields in the combustion chamber at spark onset, in the present paragraph a stepping sensitivity analysis is carried out to investigate the effect of localized refinements on $\widetilde{RPAH}, \tilde{k}_a, \tilde{k}_{rev}, \tilde{k}_{O_2}, \tilde{k}_{OH}$ prediction. In particular, this analysis is mainly focused on T_u stepping, being the main variable influencing mixture reactivity during combustion, and on ϕ, which is the main factor influencing ST. The influence of refinements in ϕ is of particular interest, considering that in the following paragraph three different injection strategies, leading to quite different mixture stratification at spark timing, are analysed in $3D$-CFD simulations. To perform such analysis, the following stepping have been adopted for equivalence ratio $\phi_{step} = 0.2$ and unburnt mixture temperature $T_{u,step} = 100\ K$. A variable stepping refinement with a base stepping $\phi_{step} = 0.1$ has been considered as a possible candidate to compare with the default strategy. A reference condition of $p = 24\ bar$ and progress variable $c = 0.5$ is chosen as representative of the $MFB10$-$MFB50$ portion of the engine cycle, which usually experiences the peak of soot formation. Moreover, since the main concern is the effect of stepping strategy on ST, $\widetilde{RPAH}$ sensitivity to these variations is analysed at first, as reported in Fig. 5.13.

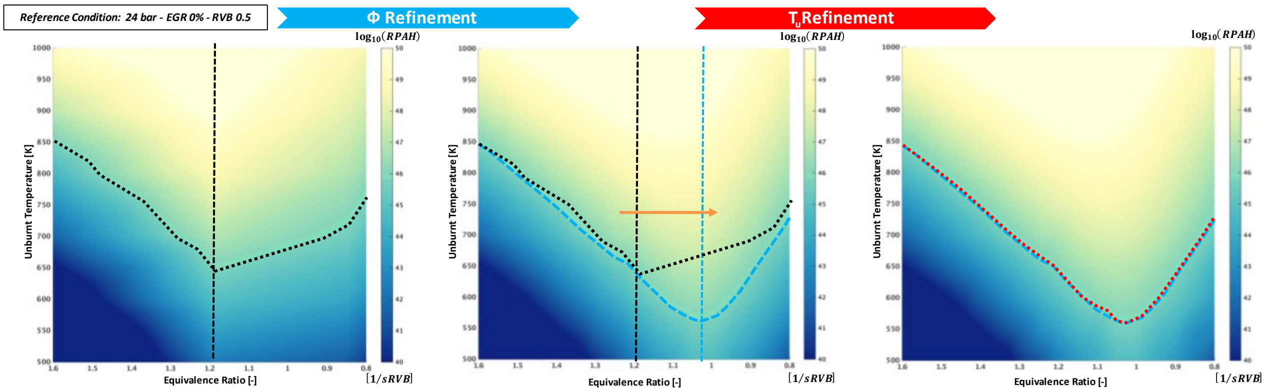

(a) (b) (c)

Figure 5.13. $\widetilde{RPAH}$ maps obtained with (a) default stepping (b) with a refinement in ϕ (c) with a refinement in ϕ, T_u.

As visible, a first refinement in ϕ changes both shape and local values of $\widetilde{RPAH}$. In particular, local $\widetilde{RPAH}$ maximum for $T_u = 750\ K$ is shifted from $\phi = 1.2$ to stoichiometric values. Conversely, a further refinement in terms of unburnt mixture temperature from $T_{u,step} = 100\ K$ to $T_{u,step} = 50\ K$ seems to have a limited effect on $\widetilde{RPAH}$. Maps in Fig. 5.13 are reported on a logarithmic scale since coefficients typically vary orders of magnitude. Therefore, small variations in colour might lead to big variations in terms of final source terms values. Based on these observations, a $\phi_{step} = 0.1$ is chosen as reference but local refinements around stoichiometry are adopted using a $\phi_{step} = 0.05$. In particular, in line with the findings reported in Paragraph 3.2, ϕ_{step} is found to be the key parameter influencing maps morphology rather than $T_{u,step}$. For the sake of brevity, results reporting ϕ_{step} refinement effect on the other coefficients is reported in Fig. 5.14.

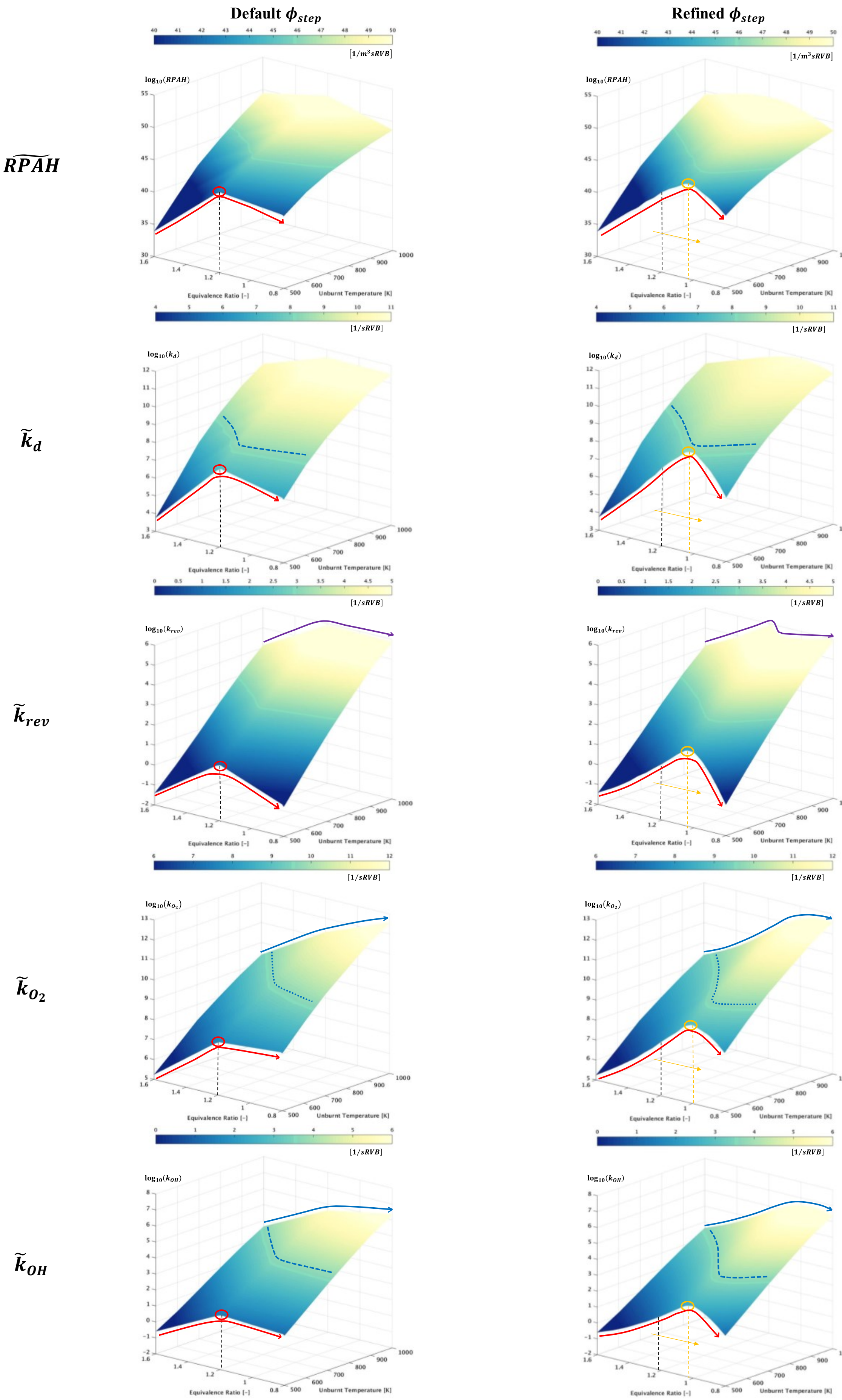

Figure 5.14. $\widetilde{RPAH}, \tilde{k}_d, \tilde{k}_{rev}, \tilde{k}_{O_2}, \tilde{k}_{OH}$ maps investigating the effect of default (left) and refined (right) ϕ_{step}.

As visible, similar results are found for the other coefficients and ϕ_{step} has to be considered as a key parameter when generating soot libraries. Considered that the proposed tabulated approach relies on CP reactors, the effect of EGR on combustion development and soot coefficients must be investigated. For this purpose, ϕ-T_u maps are represented in Fig. 5.15 for different EGR levels (namely: 5%, 20%, 40% and 60%) focusing $\tilde{k}_{O_2}$, since the detrimental effects of an increase in dilution rate is expected to influence the oxidative process towards combustion process completion, when reaction rates are smaller due to lower temperature levels.

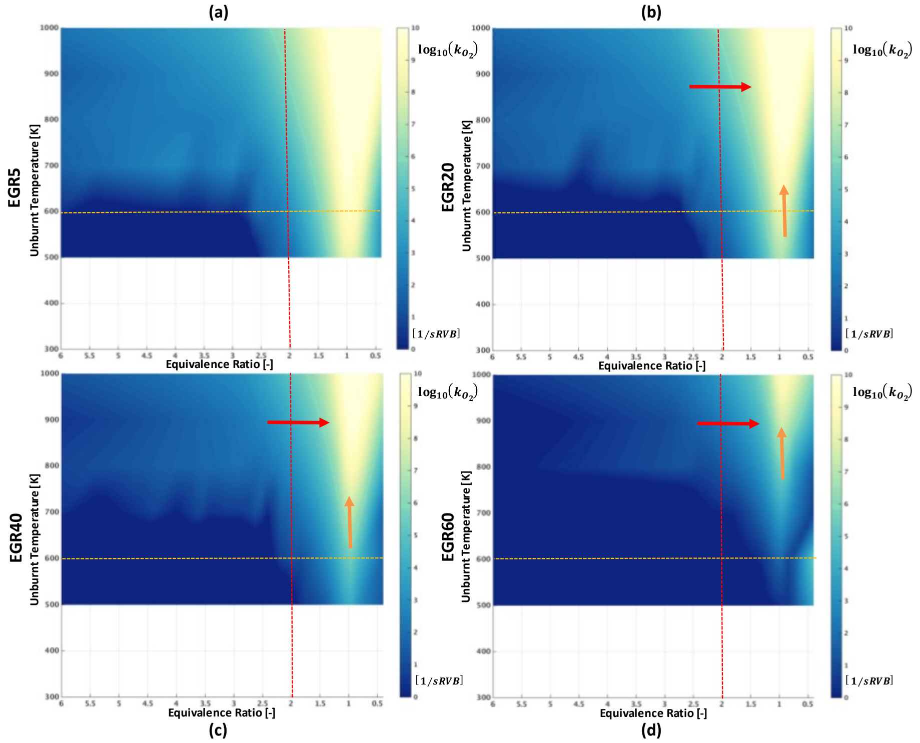

Figure 5.15. $\tilde{k}_{O_2}$ maps investigating the effect of different EGR levels: (a) 5% (b) 20% (c) 40% (d) 60%.

As expected, results clearly show that a general decrease of oxidation by O_2 is experienced on the entire ϕ-T_u conditions due to the detrimental effect on combustion of an increase in dilution levels. In particular, oxidation peak moves towards leaner conditions and higher T_u levels as EGR level increases, as shown by the arrows in Fig. 5.15. This is in line with the expectations, considering that T_f exhibits maximum values around stoichiometry. Therefore, results indicate that conditions starting from higher T_u levels and able to develop a high temperature combustion processes, depending on the original ϕ level, are likely to be more oxidizing. Similar results, not reported hereafter for the sake of brevity, are obtained for the other soot coefficients. It is therefore chosen to generate a soot library with a wide EGR range and an adequate stepping. Based on the results presented in this paragraph, a dedicated ULG95 gasoline soot library is generated with the ranges and stepping reported in Table 5.3.

$\boldsymbol{p}$ $[\boldsymbol{bar}]$	$0.5, 2, 5, 8, 12, 16, 20, 24, 28, 32, 36, 40, 44$
$\boldsymbol{T_u}$ $[\boldsymbol{K}]$	$500, 550, 600, 650, 700, 750, 800, 850, 900, 950, 1000$
$\boldsymbol{\phi}$ $[-]$	$0.4{:}\,0.05{:}\,2.0, 2.0{:}\,0.1{:}\,4.0, 4.0{:}\,0.2{:}\,6.0$
$\boldsymbol{EGR}$ $[\%]$	$0, 5, 10, 20, 30, 40, 50, 60$
Progress Variable c $[-]$	$0{:}\,0.01{:}\,1.0$

Table 5.3. ULG95 gasoline CP-based soot library ranges and stepping for a selection of engine-relevant (p, T_u, Φ, EGR) conditions

The pressure range is chosen to cover the entire in-cylinder conditions encountered during the cycle, including the cold part of the cycle where agglomeration phenomena, although negligible, may take place. Considering T_u, the range is limited to values actually experienced by flames in ICE. In order to double-check the validity of this assumption, Fig. 4.1 can be considered as reference. Focusing on ϕ, the range is extended to cover very rich mixtures that might generate from liquid film formed due to spray impingement on combustion chamber walls. Due to the important impact of ϕ, most of the points are spent to refine the entire range with variable stepping based on three main blocks. Finally, although the analysed engine OPs are characterized by standard valve strategies and the average EGR level is below 10%, the range is extended up to 60% to take into account for possible localized high EGR values. As a last comment, a variable stepping strategy allows to accurately represent high gradient regions while preserving cell-to-library access time during calculations.

5.5 IM-CNR Research Engine

In the present study, the proposed chemistry-based CFD methodologies are validated against dedicated experiments performed on an optically accessible $DISI$ engine at the Istituto Motori of the National Research Council ($IM\text{-}CNR$) in Naples, Italy. The engine, whose schematic representation is shown in Fig. 5.16(a), features a commercial cylinder head with 4 valves per cylinder, wall guided direct injection and centrally located spark plug. The optical access is ensured trough an 18 mm-thick fused silica window fixed on the piston crown featuring a Bowditch design [251] with a 45 degree UV-enhanced mirror fitted within the hollow piston as shown in Fig. 5.16(b).

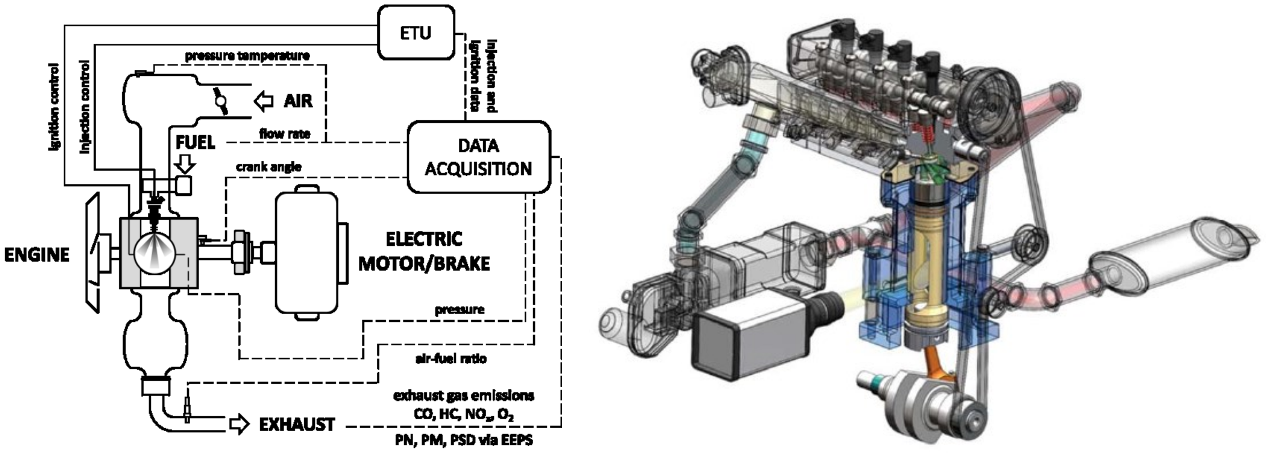

(a) (b)

Figure 5.16. (a) Illustration of the optical access (b) Schematic representation of the experimental setup.

The engine is equipped with self-lubricating piston rings, ensuring oil-less operation, thus contributing to have a higher degree of accuracy in the experiments, considering that oil consumption in the combustion chamber can heavily contribute to soot formation, as reported in [37,170,252]. As other optically accessible units, the engine suffers from non-negligible blow-by losses, a well-known for optically accessible units [253], due to the relatively high-volume crevices. In the experiments, coolant temperature was set at 325 K to allow longer combustion runs without risking piston thermal expansion close to the tolerance limit. The injection system features a six-hole injector, oriented so that spray impingement occurs mainly on the piston crown, for fuel delivery centred around halfway through the induction stroke. The experimental dataset was collected for a 2000 rpm Wide Open Throttle (WOT) operating condition and considering three different injection strategies: an optimized ($SOI300\ bTDC$), an advanced ($SOI340\ bTDC$) and a retarded ($SOI260\ bTDC$) injection strategies. Fuel was delivered in the combustion chamber thanks to a single pulse injection with the control signal generated by an Electronic Timing Unit (ETU), shown in Fig. 5.16(a). A $RON95$ $E5$ commercial gasoline was used as a reference fuel and stoichiometric fuelling strategy was adopted for the considered

SOIs. Close to stoichiometric operation was controlled via oxygen concentration measurements in the exhaust manifold, with an accuracy of ± 1%. In-cylinder pressure was measured with an accuracy of ± 1% by using a flush-mounted quartz piezo-electric transducer and traces were averaged over 200 consecutive cycles. An initial analysis of the pressure data showed a COV below 5%. Flame front propagation and fuel film oxidation evolution were investigated by a CMOS high-speed camera (Optronics CamRecord 5000) that featured a 16 µm × 16 µm pixel area that ensured good sensitivity in the visible wavelength range (9V/lux second at 550 nm). It was coupled with 50-mm focus Nikon lens (f/1.8D) and worked in full chip configuration (512 × 512 pixel), with an acquisition speed of 5000 fps and an exposure time of 200 µs. Synchronization of various control triggers for ignition, injection and camera was achieved using the optical encoder mounted on the crankshaft as an external clock connected to an AVL ETU. Lens f/stop was fixed at 5.6. In this way, the optical set-up gave a resolution of 190 µm per pixel, with a sufficient signal to noise ratio to allow the application of image processing for the analysis of flame front propagation, right from the early combustion stages. This configuration determined luminous saturation effects in the images detected during the late combustion phase which did not interfere with the analysis of the diffusive flames induced by liquid fuel film, since the related image processing was referred to binarized sequences. Flame evolution was analysed by a methodology developed by NI Vision Assistant software. The fundamental steps of the procedure are shown in Fig. 5.17.

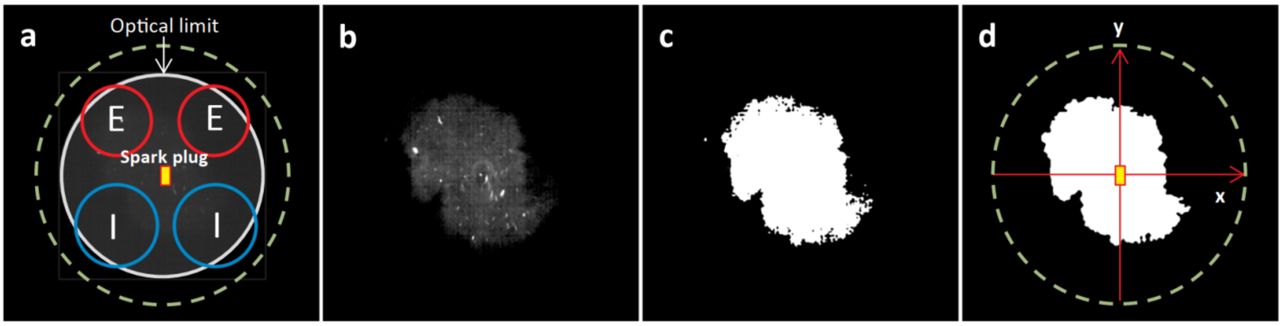

Figure 5.17. Sketch of the image processing steps for the analysis of SI flame morphology.

Specifically, a circular mask was applied to all the 256-grey scale image sequences, to cut reflections at the boundaries of the circular window of the piston crown, as shown in Fig. 5.17(a). Then, the gamma value, brightness and contrast levels were modified by using a double step Look-Up Table (LUT) function for highlighting the flame (foreground) with respect to the background (Fig. 5.17(b)). After this phase, binarized images were obtained by fixing the threshold at 32/ 256 (Fig. 5.17(c)). Advanced morphology operations performed on binary images allowed the removal of small spurious particles and filling holes in the foreground. Later, frequency filtering was applied to correct the drifts in the binary images. It consisted of three steps: first, the procedure finds the Fast Fourier transform (FFT) of the source image; then, the function filtered the complex image by applying 25% attenuation; finally, it computed the inverse FFT (Fig. 5.17(d)). After this phase, the coordinates of the centroid and the number of pixels in the foreground were stored. Flame area was normalized to the piston section. Flame displacement was estimated by considering the distance of border pixels from the combustion chamber centre along the x and y directions, as sketched in Fig. 5.17(d). The analysis of non-evaporated fuel distribution was performed by a second procedure developed with NI Vision Assistant that allowed to extract the luminous layer due to flames induced by fuel films [255]. In particular, after applying the circular mask (Fig. 5.18(a)), the 256-grey scale images were treated by a power LUT function (with constant 3) to increase the contrast in bright regions (Fig. 5.18(b)). This step highlighted the diffusive flames with respect to the luminosity induced by the spark ignited burned gas. The binary images were obtained by applying a 128/256 threshold (Fig. 5.18(c)).

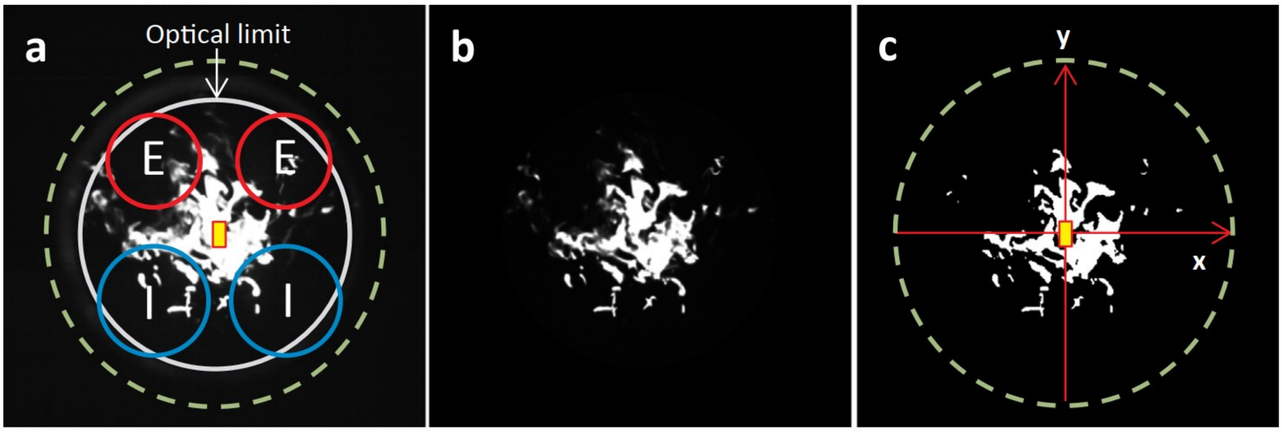

Figure 5.18. Sketch of the image processing steps for the analysis of flames induced by fuel films.

Pixel coordinates for this second category of flames were stored for all recorded sequences. They were used to evaluate the area of these regions and the distance from the combustion chamber centre. For each operative condition and fuel, the mean size and most probable location of the diffusive flames were obtained through the evaluation of Probability Density Functions (PDF) calculated by the cumulative of the areas and the distance from the centre of the centroid coordinates of all fuel film flames produced in the combustion chamber. This last experimental dataset is particularly useful for spray and liquid film modelling validation presented in the next paragraph. Regarding soot measurements at the exhaust, PN and $PSDF$ were measured by means of a TSI Engine Exhaust Particle Sizer 3090 ($EEPS$) through the electrical mobility methods. PM was calculated from PN measurements, taking into account for soot density decrease with increasing particle size, as suggested in [236,256,257]. In particular, PM and PN data are provided for the overall particle count and for the ultrafine particles, identified as the particle whose diameter is within the $30\,nm \leq d \leq 50nm$ range. The $EEPS$ measured particle size ranging from 5.6 to 560 nm, with a sizing resolution of 32 channels, providing results with an output frequency of 10 Hz. A sample of the exhaust gas was collected approximately 30 cm after the exhaust valve, passed through a 1.5 m long line heated at 150°C and diluted by means of a 10:1 ratio single stage dilution before entering the $EEPS$. The sampling period in the experiments was defined as the time required to have steady-state engine-out soot emissions. Therefore, the provided soot measurements should be considered as steady-state data representative of the average engine cycle. Further details on how soot experimental measurements were performed can be found in [130].

⎔ 5.6 3D-CFD Methodology for GDI Soot

⎔ 5.6.1 3D-CFD Model

The $3D$-CFD engine model is created using a customized version of SIEMENS Digital Industries Software STAR-CD v4.30. The combustion chamber and both the intake and exhaust ports are included in the model. As shown in Fig. 5.19, geometrical symmetry is exploited to reduce the computational effort, given the use of a $RANS$ modeling framework. This solution allows to counterbalance the very high computational cost introduced when adopting the Sectional Method and a multi-cycle simulation approach. As already reported in the previous paragraph, the GDI optical unit under investigation features a non-negligible crevice volume, which is included in the CFD model to account for compression ratio reduction and blow-by losses. The total number of fluid cells ranges from 1.2 to 0.4 million cells at TDC and BDC, respectively. The global average mesh size is around 0.8 mm for both combustion chamber and ports. A smaller average size of 0.1 mm is used in the crevice meshing strategy. All simulations are carried out using k-ε RNG turbulence model for compressible flows.

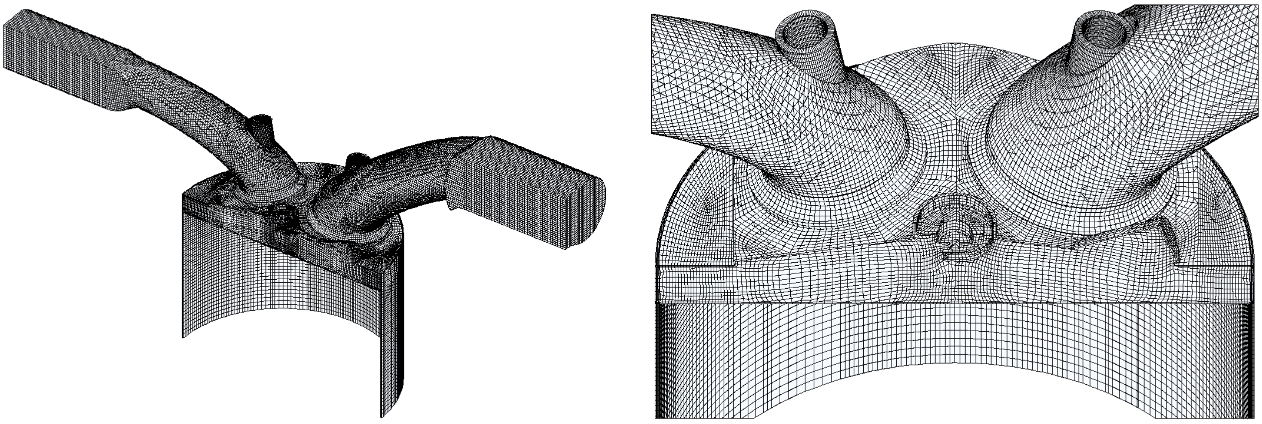
(a) (b)

Figure 5.19. (a) Model geometry including combustion chamber, manifolds and crevices (b) Detail of mesh topology and quality in the combustion chamber, ports and around the spark plug.

A dedicated $1D$ model of the engine was calibrated to derive time-varying pressure and temperature boundary conditions for both the intake and exhaust ports. An additional mass flow rate is applied at the annular area at the bottom of the crevice to model blow-by losses. Uniform wall temperatures are applied at each engine component facing the combustion chamber and the GruMo-UniMore wall heat transfer model [258] is used to estimate wall heat transfer. The approaches described in [259,260,261] are used to accurately describe spray evolution, whose validation is presented in detail in Paragraph 5.6.2 thanks to dedicated experiments performed in a constant-volume vessel. The importance of an accurate spray-wall interaction modelling for liquid film formation and evolution description on the engine cycle is granted by the use of Senda droplet-wall interaction model [262] in conjunction with Habchi model [263], for Leidenfrost temperature determination. Due to the marked influence of local liquid film deposits formation on engine-out PM, PN and $PSDF$, a dedicated validation of mixture stratification at spark timing for the three different SOIs is presented in Paragraph 5.6.3. Such validation is performed against the experimental PDF of local liquid film oxidation events obtained using the methodology described in the previous paragraph. $ECFM$-$3Z$ combustion model [39] is used to predict combustion process development using the dedicated part-load s_L correlation derived for ULG95 commercial gasoline in Chapter 4. The correlation was derived using the $ETRF$ fuel surrogate specifically formulated to mimic ULG95 commercial gasoline combustion-relevant properties with the methodology presented in Chapter 3. A simple flame kernel deposition model [264], based on Flame Surface Density (FSD), is chosen to model spark ignition. The Sectional Method is used to model soot formation based on the CP-based soot library with the approach discussed in Paragraph 5.4.2. The $ETRF$ fuel surrogate formulated in Chapter 3 targeting ULG95 ST was exploited to generate the soot library used in the simulations. The Sectional Method is here used in the configuration with 40 sections to widen the range of particle population covered by the simulation, for a consistent comparison with the experiments.

⬡ 5.6.2 Spray Modelling Validation

Soot formation is known to be a phenomena dependent on a complex interplay between different in-cylinder processes. In this context, spray evolution in the combustion chamber deeply influences mixture formation and the highest possible degree of accuracy is needed when describing the six-hole full-cone spray of the present engine case. The methodology presented in [259,260,261] for multi-hole GDI injectors up to 60 MPa of injection pressure is here used and the numerical spray is validated against experimental measurements carried out in a constant-volume vessel. In order to identify the engine-spray setup, the numerical spray parameters are tested via $3D$-CFD simulations in a quiescent vessel and numerical results are validated in terms of experimental liquid penetration and imaging. The operative conditions characterizing the spray are reported in Table 5.4.

Fuel Type	Fuel Pressure [MPa]	Fuel Temperature [K]	Ambient Pressure [MPa]	Ambient Temperature [K]
Gasoline1	10	300	0.1	293

Table 5.4. Investigated operating conditions for single component simulation.

The computational domain consists in a block- shaped vessel, whose characteristic dimensions are 120×120×120 mm. Due to the symmetrical pattern of the spray, only half domain is considered for the simulations, carried out in the $RANS$ framework. The numerical grid illustrated in Fig. 5.20 consists of hexahedral cells with cone-shaped refinements in the spray core region, whose minimum cell size is chosen according to the smallest cell dimension of the engine computational grid (i.e. 1mm). As for the turbulence model, k-ε RNG two-equations turbulence model is adopted [55]. A combined Eulerian-Lagrangian approach allows to properly account for both the vessel gaseous ambient and the dispersed liquid phase [265]. Apart from the top of the domain, which is modelled as a non-slip adiabatic wall, all other boundaries are set as pressure outlets. Experimental injection rate profiles are adopted as mass flow rates. Moreover, primary break-up is replaced by a simplified blob model, with an initial droplet diameter equal to the nozzle hole diameter (140 μm). As for the secondary break-up, Reitz's model [266] is adopted, and a calibration of the model constants was carried out to match the experimental outcomes.

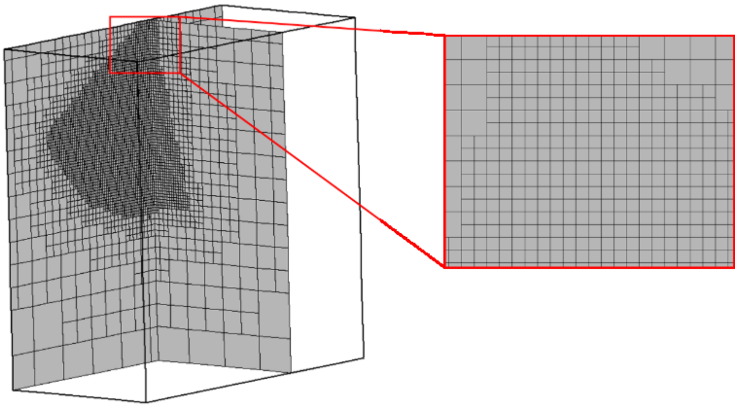

Figure 5.20. Numerical grid adopted in the simulation for spray validation.

While an accurate spray modelling approach is mandatory to predict spray penetration and spray plums pattern, qualitatively determining the critical regions for liquid film formation, an additional modelling effort is required to quantitatively predict the spray-wall interaction and estimate the critical conditions leading to liquid film formation. As previously mentioned, Senda droplet-wall interaction model [262] was used in conjunction with Habchi model [263] for this purpose. While previous investigations [267,268] clearly showed that a multicomponent approach is recommended to improve the prediction of pure and blended fuels spray, a single component approach is here used to reduce the overall computational cost of engine simulations while preserving the ability to estimate local fuel deposit formation [269,270]. Since fuel stratification at spark onset and local rich mixture pockets play a key role in soot formation and development during the combustion process, a simplified approach is used. In particular, the saturation pressure curve of gasoline1, the single component fuel used in the simulation, is scaled accordingly to match the reference multicomponent blend one. This workaround allows to recover the degree of accuracy typical of a multicomponent approach while retaining a single component setup. The first comparison between numerical and experimental data deals with liquid penetration, as reported in Fig. 5.21.

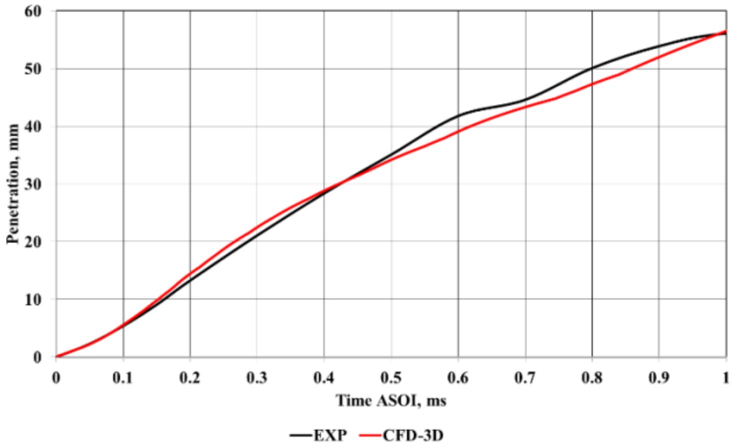

Figure 5.21. Comparison between numerical (solid red line) and experimental (solid black line) penetrations.

It is important to point out that liquid penetration is always determined considering the central plume, whose axis is almost coincident with the injector one. That said, a satisfying agreement between experimental and numerical data is achieved. To further validate the numerical spray, a further comparison between experimental and numerical data is carried out in terms of imaging: snapshots at 400 µs and 800 µs after the start of injection are shown in Fig.5.22(a)-(b).

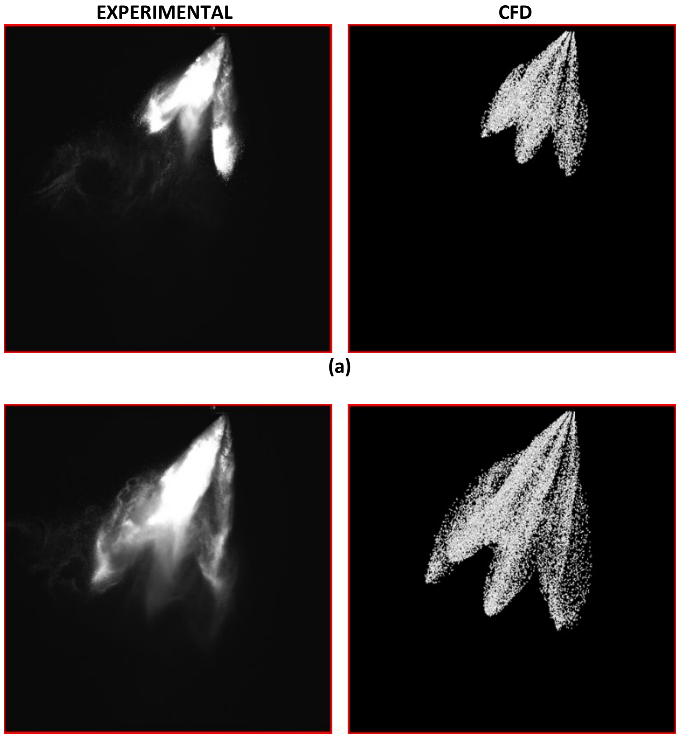

(a)

(b)

Figure 5.22. Spray shape comparison between experiments (left) and numerical simulation (right) at (a) 400 µs and (b) 800 µs.

Preliminary cold flow spray simulations were carried out on the engine using both approaches and a proper scaling was introduced in the saturation pressure curve of the single component CFD gasoline surrogate to match the amount and locations of liquid film formation predicted by the multicomponent model. In order to provide a further insight on the numerical spray behaviour on the engine case, numerical imaging resulting from the simulation of the three injection strategies is reported in Fig 5.23 and 5.24 for a side and top views, respectively. For the sake of brevity, advanced ($SOI340\ bTDC$), optimized ($SOI300\ bTDC$) and late ($SOI260\ bTDC$)injection strategies are hereafter referred to as $SOI340$, $SOI300$ and $SOI260$, respectively.

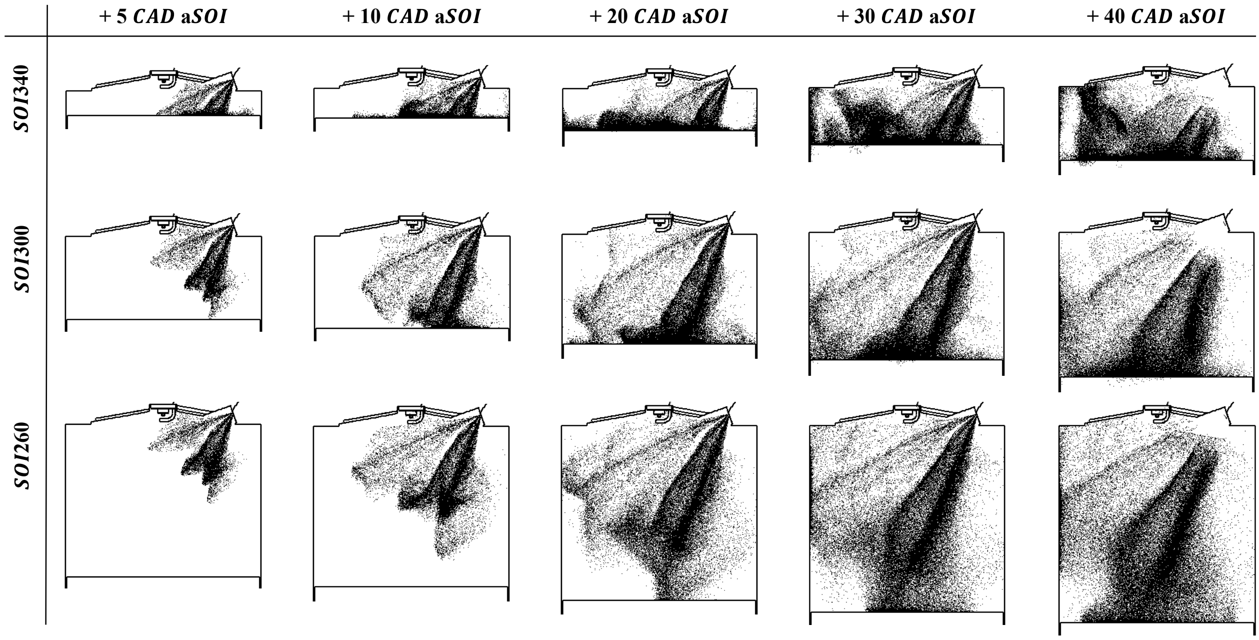

Figure 5.23. Side view: Spray evolution for the advanced (*SOI*340), optimized (*SOI*300) and late (*SOI*260) injection strategies analysed.

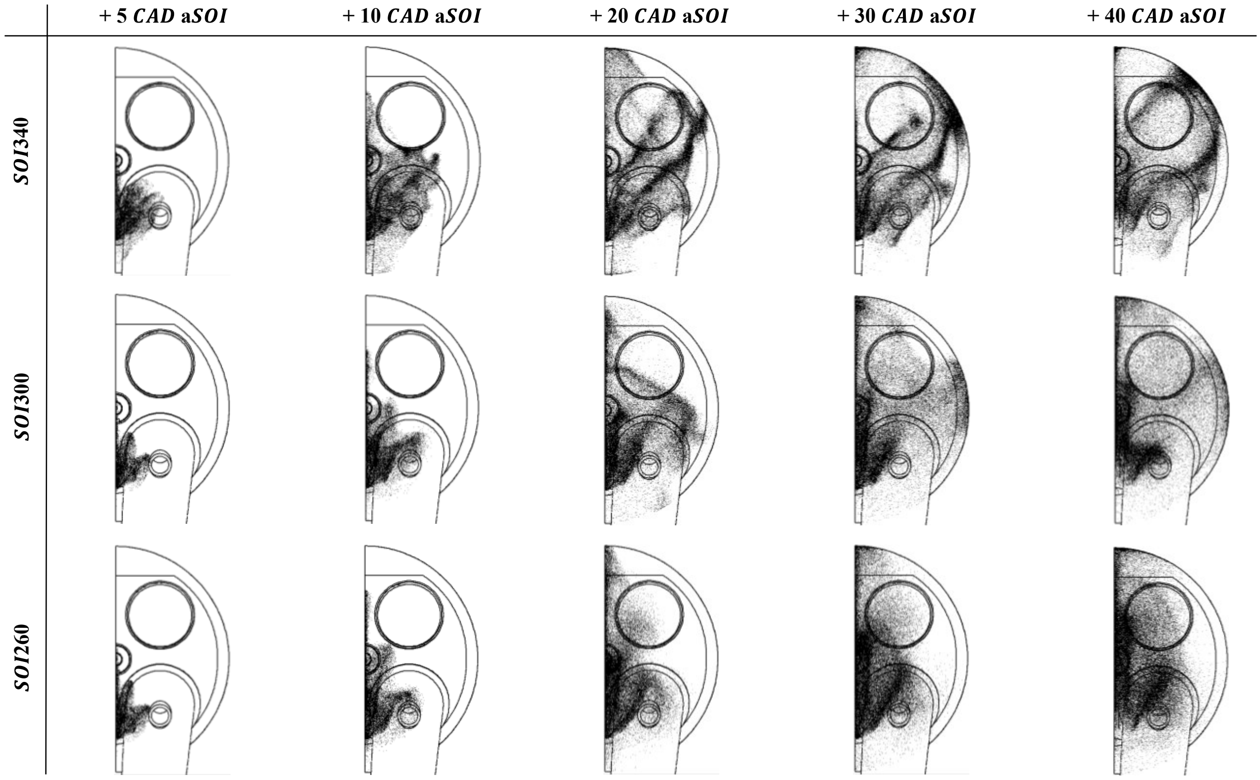

Figure 5.24. Top view: Spray evolution for the advanced (*SOI*340), optimized (*SOI*300) and late (*SOI*260) injection strategies analysed.

Analysing spray evolution and shape at 5 *CAD aSOI* it is possible to notice how spray behaves, for all the three injection strategies, as previously observed in the validation case in Fig. 5.22. Comparing spray evolution for the three different strategies, spray-wall interaction plays a key role in determining fuel distribution in the combustion chamber. The advanced injection strategy (*SOI*340) is characterized by a consistent fuel impingement on the piston crown which consequently leads to a partial rebound of fuel droplets. Focusing on the top view in Fig. 5.24, it is possible to notice how this chain of events leads to non-negligible amount of fuel being trapped in the exhaust-side crevice. The optimized injection strategy (*SOI*300) undergoes a similar evolution with a less marked fuel impingement on the piston crown.

This injection strategy also leads to a direct impact of fuel droplets on the liner, which is almost negligible for $SOI340$. Conversely, late injection strategy ($SOI260$) is characterized by a more pronounced spray-wall interaction taking place on the liner rather than on the piston crown, due to the increased distance between the injector and the former at SOI. This analysis is confirmed by the time-history of liquid film mass forming on the piston crown, liner and dome, reported in Fig. 5.25.

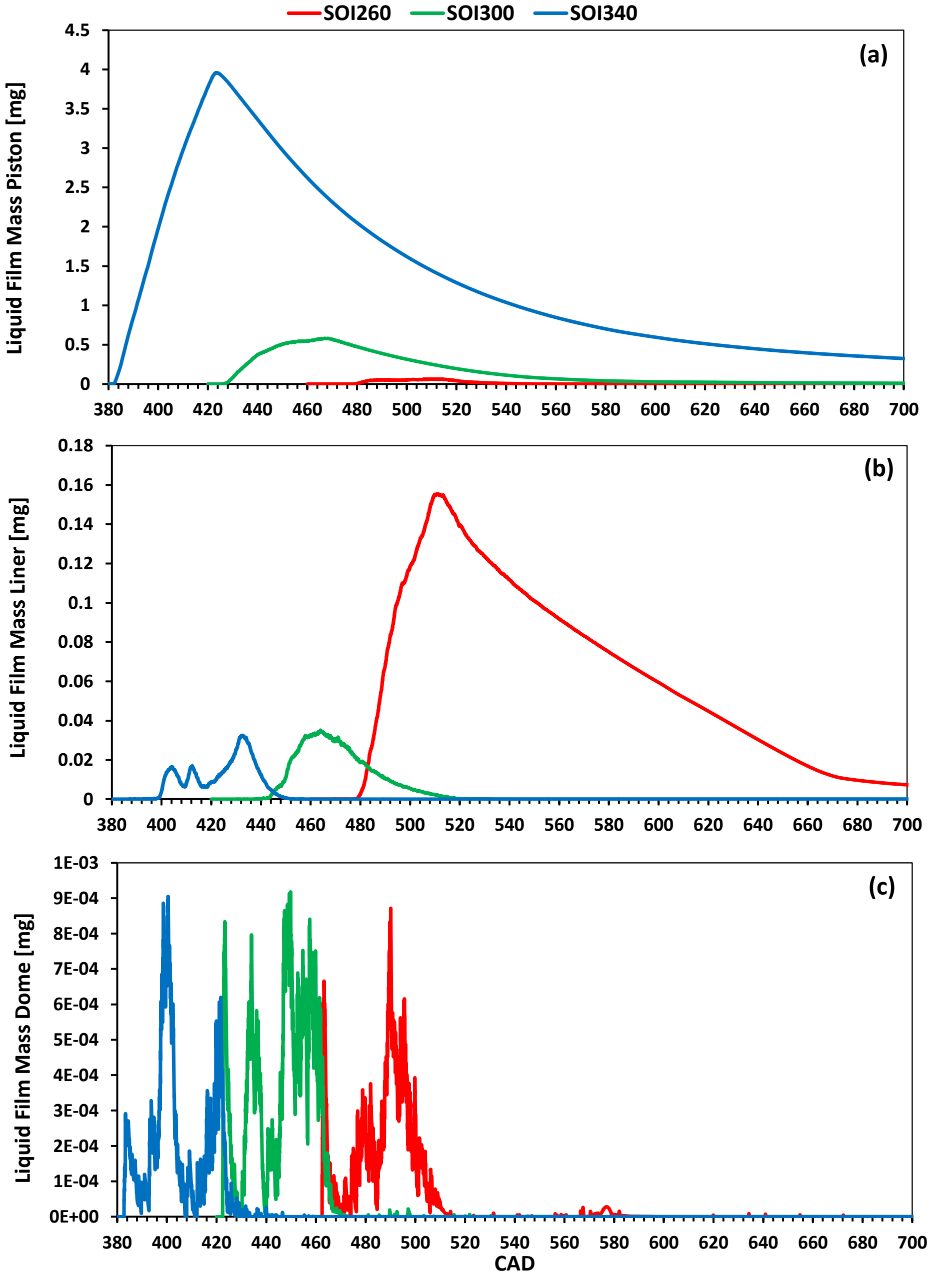

Figure 5.25. Liquid film mass time-history on (a) Piston (b) Liner and (c) Dome for $SOI260$ (ed line), $SOI300$ (green line), $SOI340$ (blue line).

As clearly visible in Fig. 5.25(a)-(b), the advanced and late injection strategies are characterised by a non-negligible amount of liquid film mass persisting on the piston crown and liner, respectively, at spark timing (705 CAD). Liquid film formation amount and location affects the formation of fuel-air mixture which result in different stratifications. This is confirmed by mixture stratifications, reported in Fig. 5.26 for the three SOIs at spark onset, in terms of ϕ scalar field in the combustion chamber and on the piston crown.

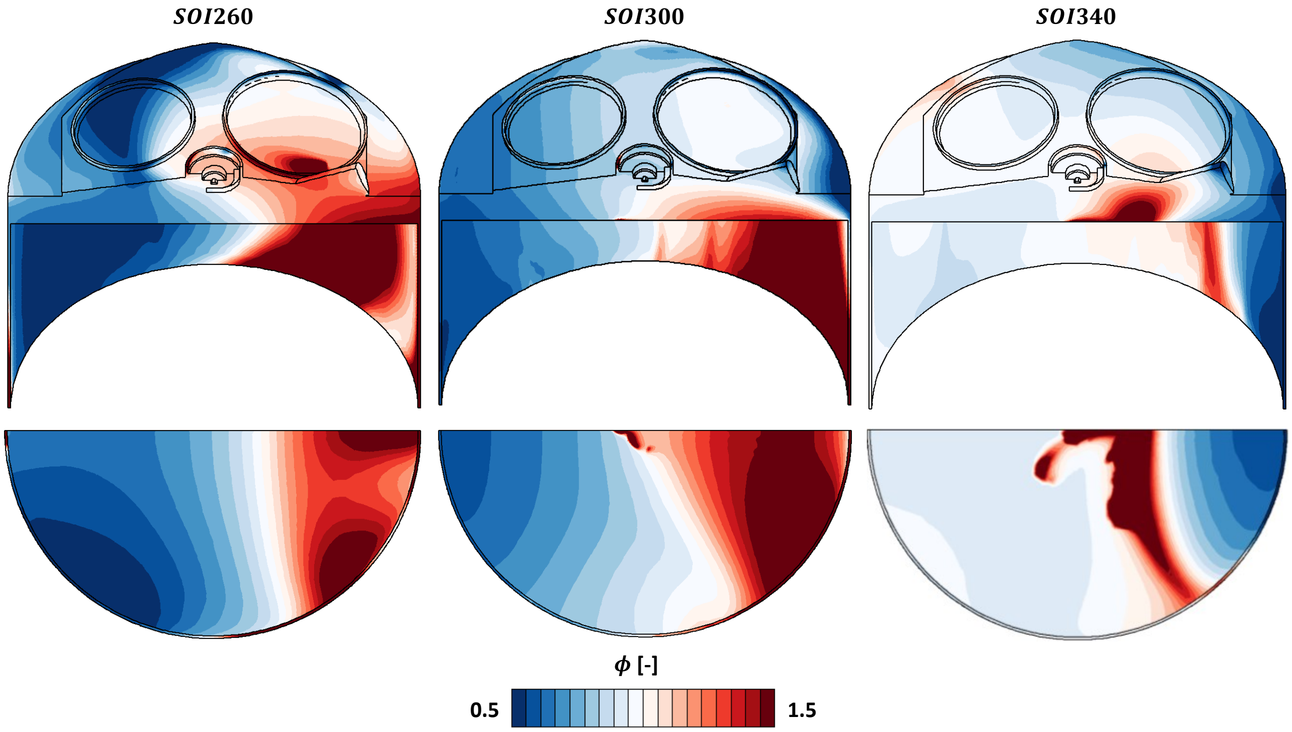

Figure 5.26. Mixture stratification at spark onset (705CAD) for the three injection strategies. A detail of the stratification on the piston is reported on the bottom row.

The advanced injection strategy ($SOI340$) exhibits a local rich pocket on the piston crown due to the high amount of liquid film formed during the injection process, confirmed by the results reported in Fig. 5.25 (a). The progressive evaporation of liquid film in this area forms a slightly rich mixture in the spark plug area. A rich pocket is also spotted in the exhaust-side crevice due to fuel droplets entrainment, clearly visible in Fig. 5.24 at 40 CAD aSOI. Coherently with the previous comments, liquid film persisting at SOC on the piston crown is the cause of the rich pockets extending from the spark plug region to the intake-side crevice. The late injection strategy ($SOI260$) is characterised by a severely inhomogeneous mixture, particularly rich on the intake side and lean on the exhaust side. Liquid film persisting at spark onset is located on the intake valve, as clearly visible in Fig. 5.26, and in the exhaust side crevice. Moreover, a consistent amount of fuel is trapped in the intake side crevice, due to tumble flow motion promoting fuel droplets entraining during the compression stroke. Moving to the last of the three cases, $SOI300$ is confirmed as optimized injection strategy since it is the least liquid film promoting case among the three considered, as confirmed by Fig. 5.25. In fact, an amount of liquid film persists in the spark plug region at spark onset but quantitatively in much lower values compared with the other strategies. Based on this analysis it is possible to conclude that injection timing deeply affects the mixture formation process and, consequently, mixture stratification at spark timing. As previously demonstrated in Paragraph 3.2, ST is strongly dependent on ϕ and slight variations of this parameter might result in dramatic differences in terms of soot formed during combustion on even initial thermodynamic conditions. For this reason, in the next paragraph, cycle-resolved flame visualizations obtained with the technique presented in Paragraph 5.5 are used to qualitatively validate the stratifications obtained for the three SOIs.

⬡ 5.6.3 Fuel Deposits-Mixture Stratification Analysis

In the present paragraph, experimental $PDFs$ of localized diffusive flames and premixed-based combustion phenomena originating from localized fuel-air mixing due to fuel trapped in the crevices, are used as reference for $3D$-CFD

stratification validation. It is important to point out that such PDFs are built tracking all the combustion phenomena apart from the main premixed flame front propagating from the spark plug to the end-gas region. Therefore, as already mentioned, combustion events such as fuel re-entering in the combustion chamber from the crevices and burning during the late stage of the power stroke are tracked as well. Due to the nature of these combustion events, it is expected that such phenomena are likely to take place in rich pockets throughout the combustion chamber. Based on this rationale, rich mixture pockets location at spark onset is qualitatively compared with the cycle-resolved experimental PDFs. In Fig. 5.27-5.28-5.29 such comparison is drawn for $SOI260$, $SOI300$ and $SOI340$ strategies, respectively.

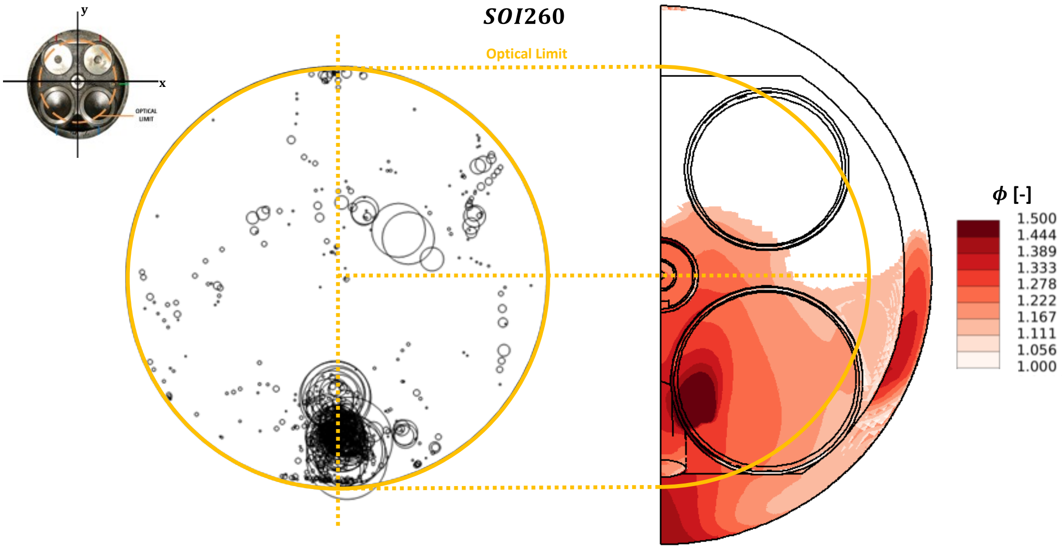

Figure 5.27. SOI260: Comparison between experimental cycle-resolved PDFs location of secondary combustion events and $3D\text{-}CFD$ prediction of rich mixture pockets at spark onset.

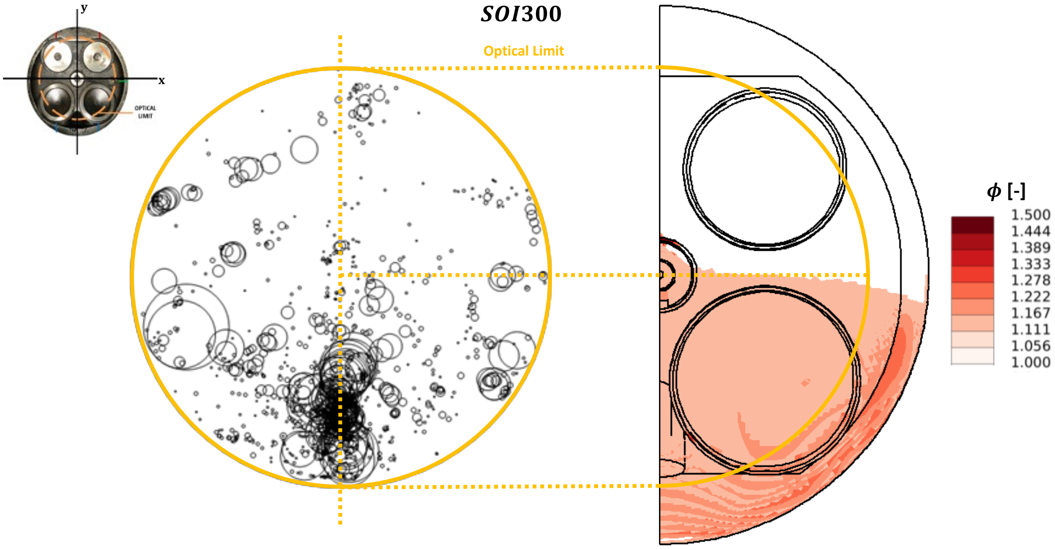

Figure 5.28. SOI300: Comparison between experimental cycle-resolved PDFs location of secondary combustion events and $3D\text{-}CFD$ prediction of rich mixture pockets at spark onset.

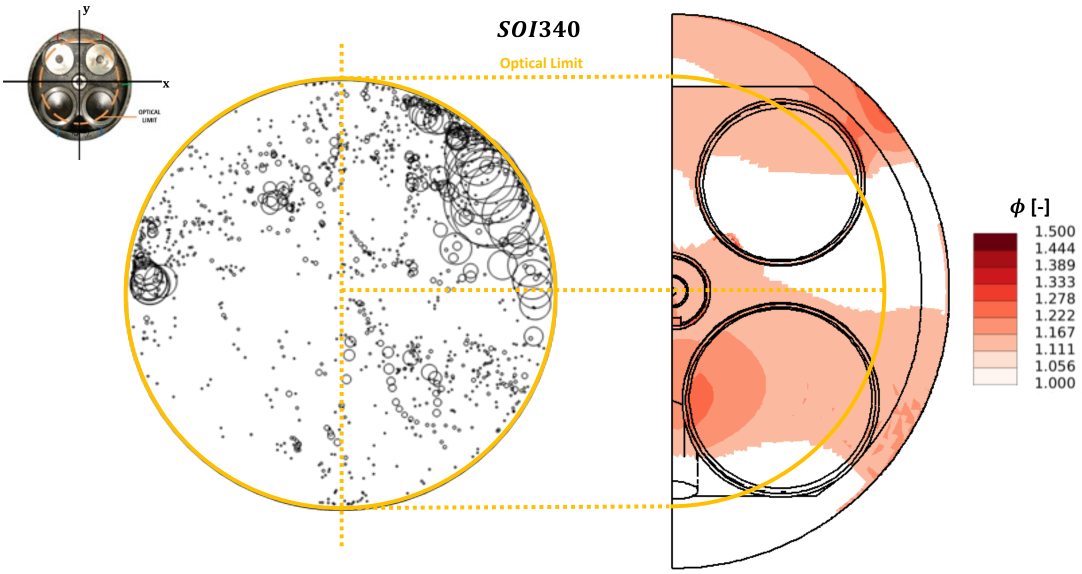

Figure 5.29. SOI340: Comparison between experimental cycle-resolved PDFs location of secondary combustion events and $3D$-CFD prediction of rich mixture pockets at spark onset.

In each figure, the experimental PDF, on the left-hand side, is compared with a subset of cells exceeding the thresholding value of $\phi = 1$, on the right-hand side. In this way, rich mixture pockets location predicted by CFD is clearly identified. It is important to point out that circles location in the experimental PDFs identify the position of the secondary combustion phenomena, while their occurrence over the cycles is reported based on the diameter. The bigger the diameter, the higher is the occurrence of localized combustion phenomena in that specific position over the cycles. Obviously, the entire combustion chamber has been considered for the experiments. Focusing, in the first place, on the experimental data it is immediate to notice how $SOI260$ and $SOI300$ exhibit a high occurrence of localized secondary burning phenomena towards the intake side. Conversely, $SOI340$ exhibits a high occurrence on the exhaust side mainly due to localized flames re-entering in the combustion chamber. This phenomena is clearly visible, cycle after cycle, analysing flame visualizations. Rich mixture pockets location predicted by CFD, are in quiet good agreement with the experimental data. A further confirmation of this is given by experimental PDFs in Fig. 5.30 reporting secondary combustion phenomena distribution as function of y-axis, depicted in the top-left images in Fig. 5.27-5.28-5.29. In other terms, y-axis evolves from the intake side (negative values) to the exhaust side (positive values).

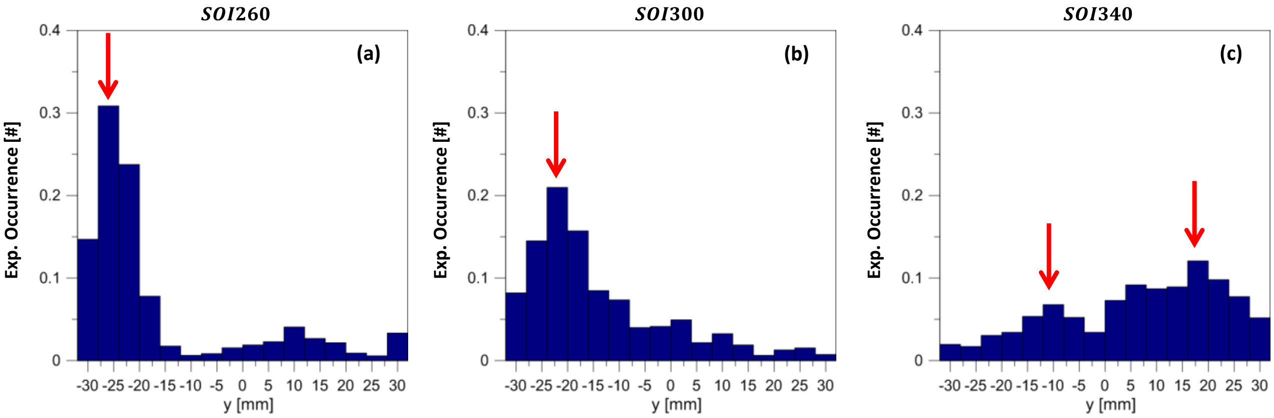

Figure 5.30. Normalized experimental occurrence of secondary combustion phenomena along the y-axis for (a) $SOI260$ (b) $SOI300$ and (c) $SOI340$.

Comparing the distributions in Fig. 5.30 with rich mixture pockets distribution predicted by CFD in Fig. 5.27-5.28-5.29, along the y-axis, a qualitative good correlation is found. In particular, CFD is able to qualitatively predict the bimodal distribution found for $SOI340$ and the unimodal distributions found for the other two strategies, highlighted by the red arrows in Fig. 5.30. Moreover, the absolute occurrence overall, found for $SOI260$ on the lean side, is particularly well correlated with the richest mixture pocket found for the same injection strategy on the intake side. Based on these results, $3D$-CFD prediction of mixture stratification at spark onset is deemed to be qualitatively reliable for the analysed cases. The three different CFD models are therefore used to simulate combustion process development and predict soot formation.

⎔ 5.6.4 Experimental-CFD Soot Comparison

In this last paragraph, a $3D$-CFD methodology is proposed to predict soot formation in GDI engines. For this purpose, an accurate $3D$-CFD modelling of all the in-cylinder phenomena prior to combustion is essential and this explains the double effort spent in the previous paragraph to validate spray modelling approach and the resulting stratification at spark onset. Starting from a solid $3D$-CFD modelling of fuel stratification, combustion simulation is the next step needed to accurately describe soot formation since most of the processes involved are chemistry-based, as extensively discussed in the previous paragraphs. All the previous studies found in literature focusing on soot formation using the Sectional Method [46,47,48,49,129] do not detail any precise strategy to perform soot simulations, apart from the Sectional Method setup used, and only a single one focuses on GDI soot. In particular, despite not being specifically reported, all of them seem to rely on a single combustion cycle to evaluate soot characteristic quantities. This choice is rather questionable for a series of reasons and particularly while focusing on SI engines simulations. In the first place, combustion-relevant quantities such as in-cylinder average ϕ, liquid film mass and patterns are not representative when evaluated at the first cycle. This is due to the fact that in-cylinder quantities in the first engine cycle are partially affected by the initial conditions. Moreover, it is common in GDI engines to have a backflow of fuel-air mixture in the intake manifold during the scavenging process, which usually re-enters in the combustion chamber at the following cycle. This leads to an underestimation of in-cylinder average ϕ at spark onset in the first engine-cycle. As extensively pointed out previously, the amount of soot formed might vary dramatically with slight variations in ϕ and for this reason it is advisable to start evaluating soot formation when the main combustion-relevant quantities have reached cyclic convergence. Secondly, a relevant error is introduced estimating soot quantities at the first cycle because of the total absence of any pre-existing soot particle in the combustion chamber at spark-onset. Undoubtedly, this assumption is far from being representative of the real scenario and deeply affects soot formation and evolution in many ways. For example, processes supporting soot accumulation mode (e.g. Condensation, Coagulation and Surface Growth) are widely underestimated since pre-existing particles are needed to trigger them. Furthermore, considering that the Sectional Method is based on a steady-state assumption between soot precursors formation rate (i.e. $\widetilde{RPAH}$) and consumption via Particle inception and Condensation, an underestimation of the second process (due to pre-existing particles underestimation) might lead to an overestimation of the first. Based on these considerations, a multi-cycle approach is adopted in the present work to correctly estimate PM, PN and $PSDF$ in two steps. At first, three consecutive cycles are carried out to reach convergence in terms of stratification and combustion-related quantities. In the second place, the Sectional Method model is activated and three additional cycles are performed to ensure a cyclic convergence of soot-related quantities. A total of six consecutive soot cycles is performed. For the sake of brevity, results supporting the need for a multi-cycle convergence are hereafter presented for a single injection strategy, specifically for $SOI340$. In Fig. 5.31, liquid film mass formation on the components facing the combustion chamber (Fig. 5.31(a)-(b)-(c)) and average in-cylinder ϕ (Fig. 5.31(d)) is analysed over the cycles. For the sake of clarity, the first three cycles and the last three cycles (with the Sectional Method active) are reported in black and red solid lines, respectively.

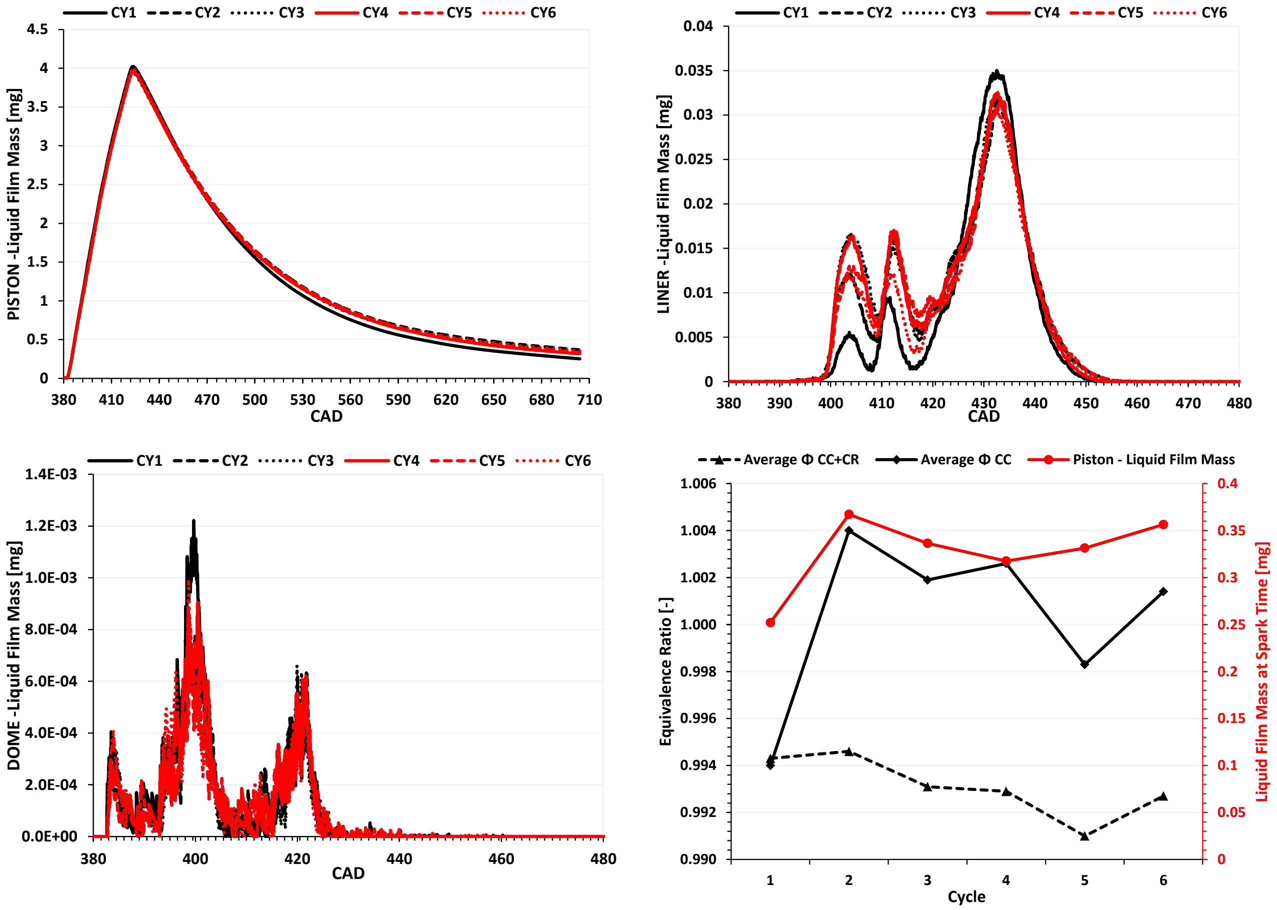

Figure 5.31. SOI340: Cycle-to-cycle evolution of: Liquid film mass on the piston crown (a), on the liner (b), and on the dome (c). Average equivalence ratio (d) in the combustion chamber (CC) and in the combustion chamber plus the crevices (CC+CR), and liquid film mass on the piston crown (red solid line) over the cycles at spark timing.

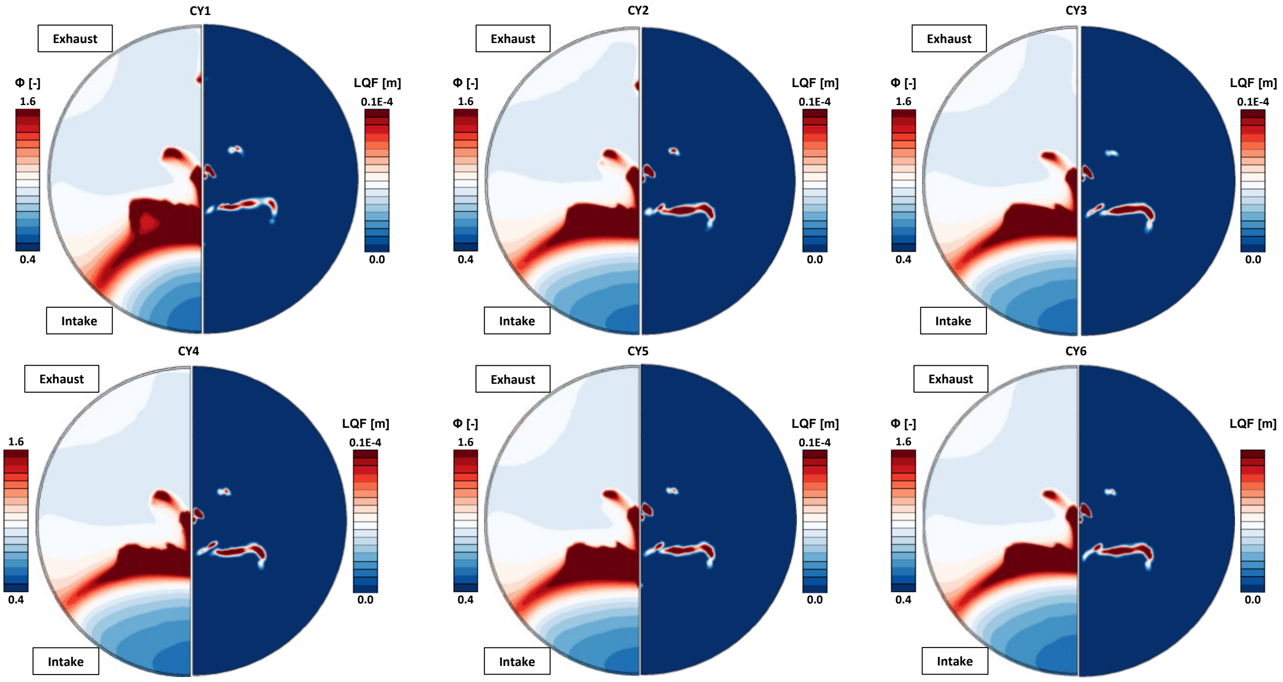

Figure 5.32. SOI340: Liquid film thickness pattern (right) and equivalence ratio field (left) on the piston crown at spark onset for the analysed cycles.

As clearly visible, a reasonable convergence is reached at the third engine cycle. This is particularly true for liquid film mass evolution on the piston crown (Fig. 5.31(a)) which is the driving factor influencing mixture formation during the cold part of the cycle. Liquid film mass and average ϕ at spark onset over the cycles, reported in Fig. 5.31 (d) confirm the aforementioned statement. As a further evidence, liquid film pattern on the piston crown at spark onset for the analysed cycles is also reported in Fig. 5.32. It is clearly visible, that a convergence is also reached at the third cycle in terms of liquid film pattern and ϕ on the piston crown. The number of cycles needed to reach convergence on all the combustion-relevant quantities might vary from case to case, but generally speaking, three cycles should be enough for any $RANS$-based $3D$-CFD engine simulation. Starting from the stabilized cycle (e.g. the third in this case), the Sectional Method is activated and three consecutive cycles are performed in order to reach convergence on soot characteristic quantities. Hereafter, combustion development results are reported for these last three cycles for two main reasons. Firstly, to discuss the ability of the CFD model to match to a satisfactory degree of accuracy the experiments, for the three injection strategies. Secondly, to further demonstrate the benefits deriving from the use of the dedicated part-load s_L correlation formulated with the methodology presented in Chapter 4. While analysing the results it useful to underline that a simple flame kernel deposition model is used [186], slightly adjusting the initial flame kernel diameter from case to case. Variations adopted for this parameter are in the order of tenth of millimetres. Results are reported as follows in terms of in-cylinder average pressure (Fig. 5.33), cumulative apparent HRR (Fig. 5.34) and main combustion indicators (Fig. 5.35).

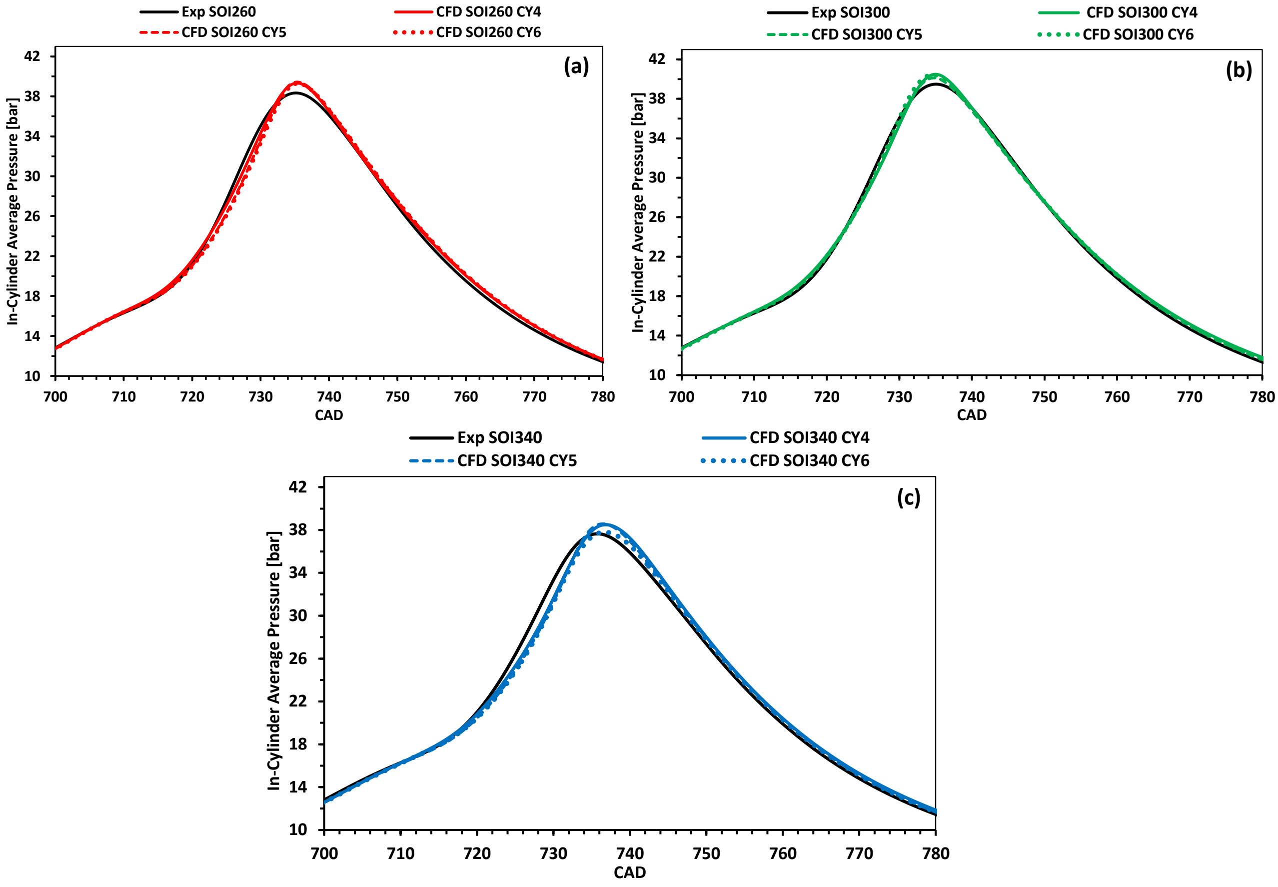

Figure 5.33. In-cylinder average pressure traces for (a) $SOI260$ (b) $SOI300$ (c) $SOI340$. Experiments (solid black line) and $3D$-CFD results (coloured solid and dashed lines) for the last three engine cycles (CY4,CY5,CY6).

Analysing Fig. 5.33, experiments are matched, in terms of peak pressure and phasing, with a good agreement by CFD simulations for all the three SOIs. $SOI340$ pressure increase in the early combustion stages is slightly underestimated

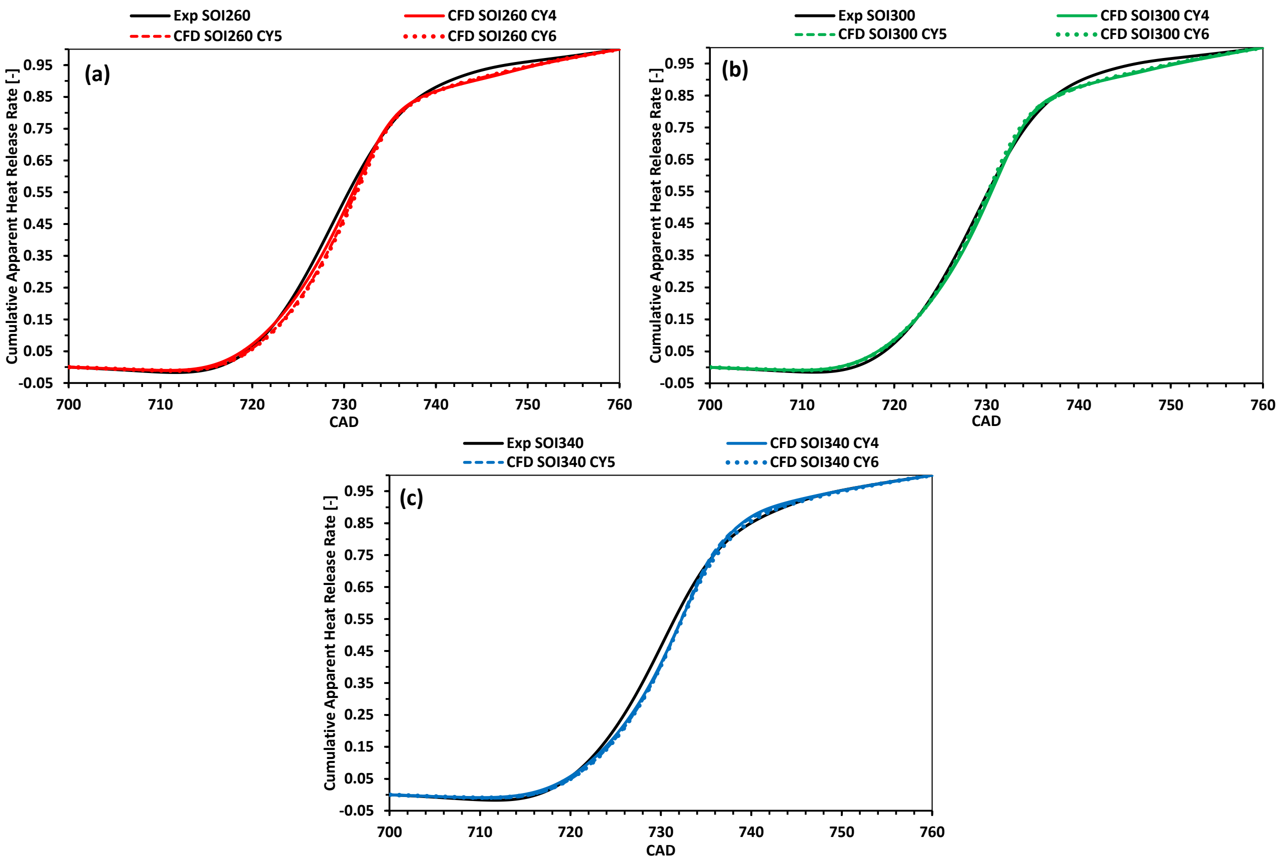

Figure 5.34. Cumulative apparent heat release rate for (a) $SOI260$ (b) $SOI300$ (c) $SOI340$. Experiments (solid black line) and $3D\text{-}CFD$ results (coloured solid and dashed lines) for the last three engine cycles (CY4,CY5,CY6).

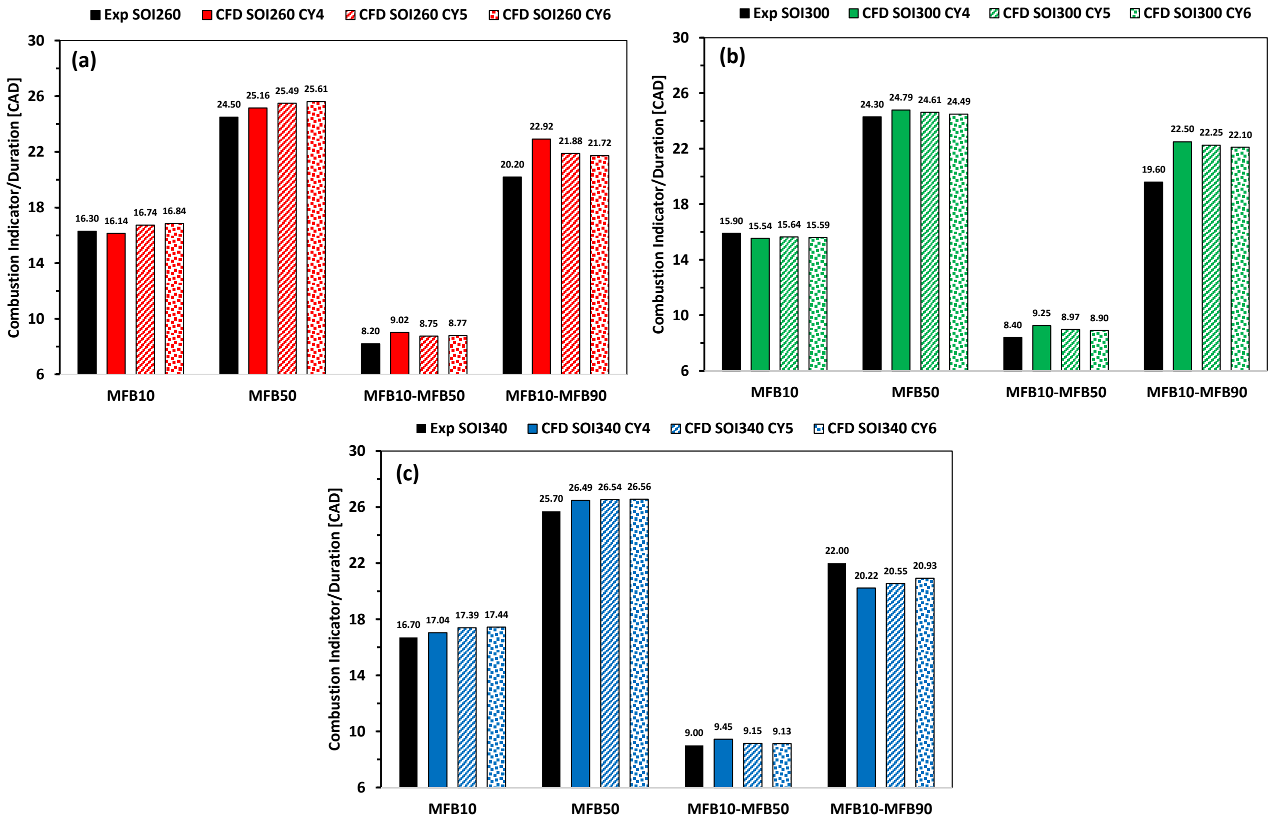

Figure 5.35. Combustion indicators for (a) $SOI260$ (b) $SOI300$ (c) $SOI340$. Experiments (black solid bar) and $3D\text{-}CFD$ results (coloured solid and dashed bars) for the last three engine cycles (CY4,CY5,CY6).

compared to the experiments but this results in an acceptable misalignments in terms of combustion indicators, as discussed in a few lines. It is also possible to notice that convergence is met, to an acceptable level, in terms of in-cylinder pressure history. Considering the results reported in Fig. Fig. 5.34-5.35, an overall good agreement with the experiments is found both in terms of cumulative apparent heat release rate and main combustion indicators. Generally speaking all the relevant combustion stages are quantitatively well-predicted. Despite the misalignments in the combustion completion stage, it can be concluded that the proposed modelling approach for s_L is proven to be a reliable tool which allows to enhance combustion development description, strongly reducing case-by-case tuning efforts. Furthermore, despite a slight overestimation of $MFB50$, which is still to be considered acceptable since quantitatively well within the engine COV in $IMEP$, the $3D\text{-}CFD$ model is able to correctly depict the relative trend among the cases, reported in Fig. 5.36.

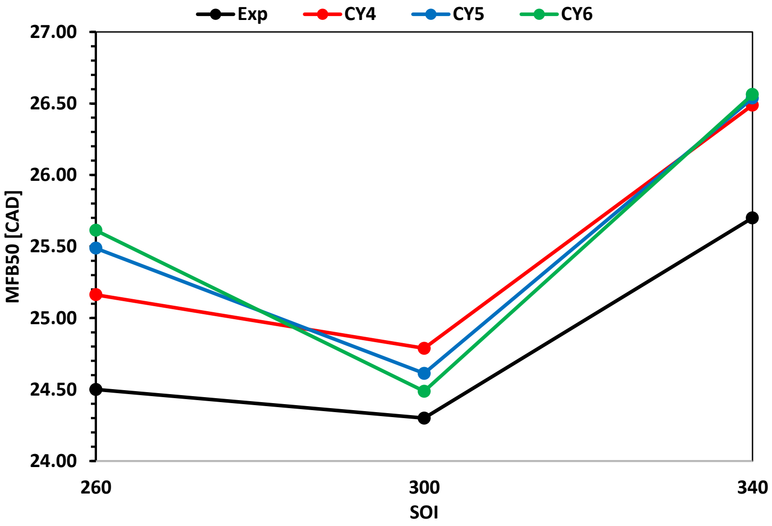

Figure 5.36. $MFB50$ relative trend for the three SOIs and cycles 4, 5, 6.

It can be concluded that combustion process development is described to a satisfactory degree of accuracy and soot formation and evolution can be therefore analysed. For the sake of brevity and the reasons previously outlined, the experimental-CFD comparison in terms of PM, PN and $PSDF$ is carried out based on the results obtained at the last simulated cycle (i.e. cycle 6). As suggested in previous studies, soot characteristic quantities are evaluated at EVO [48,49,129]. For different reasons, hereafter discussed, this is the only possible strategy to follow when quantitatively comparing CFD results and experimental engine-out soot emissions. Generally speaking, it is prohibitive to include the entire exhaust line in CFD simulations because this would lead to an unfeasible computational cost. This statement is particularly true for the present study, considering that a multi-cycle simulation approach is needed, as previously shown. Furthermore, it must be underlined that the Sectional Method alone introduces 40 transport equations to be additionally solved. Due to the impossibility of modelling the evolution of soot $PSDF$ in the exhaust line, the obvious choice is therefore to evaluate soot properties before the EVO event. This choice is equal to making the assumption that soot-related processes are considered frozen during the exhaust stroke. This assumption might seem severe but it is still considered to be acceptable since soot sampling point in the experimental layout is located 30 cm downstream of the exhaust valve seat. The experimental layout is sketched in Fig. 5.37 to support the discussion reported in the following lines. As visible in Fig. 5.37, soot travels through a 1.5 m long pipe heated at 423.15 K, it is diluted with a 1:10 ratio and subsequently enters in the $EEPS$ where PN and $PSDF$ are measured. As previously mentioned experimental PM is calculated imposing an array of soot densities based on particle sizes. This data is double-checked with the measurement provided by a smoke meter, whose sampling point is positioned further downstream in the exhaust line. Since $EEPS$ provides measurements in terms of concentrations (e.g. PM $[mg/m^3]$ and PN $[\#/cm^3]$), a methodology must be introduced to: 1) evaluate CFD results at EVO (e.g. PM $[mg]$, PN $[\#]$) in terms of concentrations 2) account for the different thermodynamic conditions found at EVO inside the combustion chamber (e.g. $p \approx 5\ bar, T \approx 1000\ K$) and the sampling conditions at the $EEPS$ (e.g. $p = 1\ bar, T \approx 313.15\ K$) and for the presence of a dilution process before soot measurement in the $EEPS$.

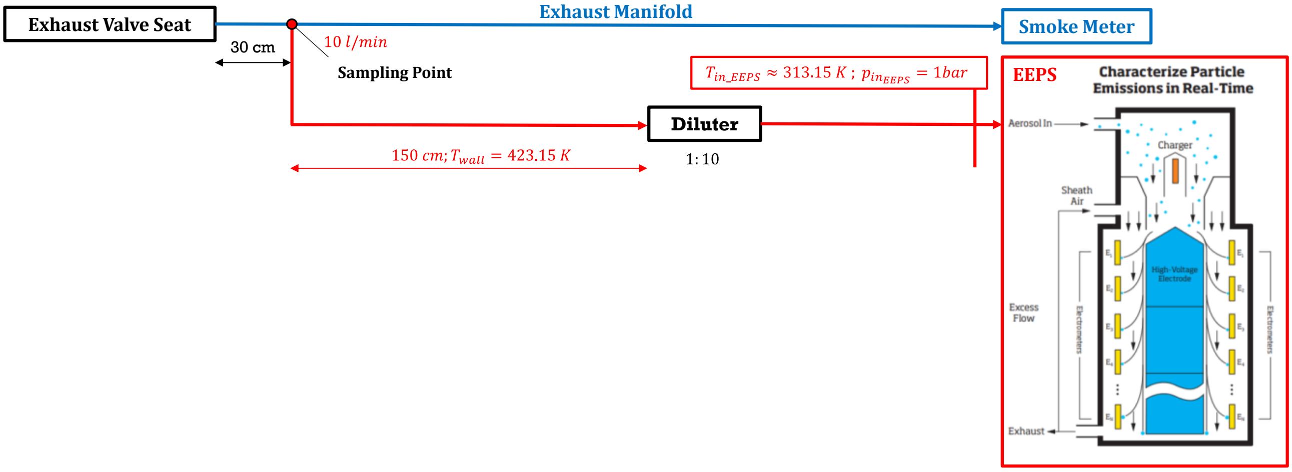

Figure 5.37. Schematic representation of the exhaust line and experimental layout for soot measurements.

In other words, pure CFD results need to be converted to concentrations using a reference volume but such volume must be calculated so that it corresponds to the thermodynamic conditions at the $EEPS$ inlet, in order to correctly compare results with experimental measurements. A methodology is therefore proposed and a number of assumptions is introduced. The initial reference volume is the combustion chamber volume at EVO, $V_{cc,EVO}$. The initial thermodynamic conditions are in-cylinder average pressure, $p_{cc,EVO}$, and temperature, $T_{cc,EVO}$, at EVO. Soot-related processes are considered to be frozen at EVO and possible PM, PN, $PSDF$ evolutions in the exhaust line are neglected. The exhaust gas are approximated to behave accordingly to the ideal gas law. Thanks to a temperature measurement provided by a probe located before the diluter, dilution is known to be responsible only for a flow rate increase and does not play a significant role in exhaust gas cooling which are found to be at thermodynamic conditions similar to those found at $EEPS$ inlet. As a matter of fact, exhaust gases are diluted to avoid water condensation on soot particles, which would lead to an overestimation of particle size during the measurement. Finally, only the section whose reference diameter is within the range effectively measured by the $EEPS$ are consider to compute PM and PN in the combustion chamber at EVO ($PM_{EVO}[mg]$, $PN_{EVO}[\#]$) . This means that only the sections between a lower s_{LOW} and upper s_{HIGH} boundaries are considered. Exploiting the ideal gas law and based on the aforementioned rationale, CFD results are reported to concentrations scaled to $EEPS$ inlet conditions via Eq. 5.35 and 5.36 for PM and PN, respectively.

$$PM_{in,EEPS}^{CFD} = \frac{PM_{EVO}}{V_{in,EEPS}} = \frac{\sum_{i=S_{LOW}}^{S_{HIGH}} s_{i,EVO} * 1e6}{V_{cc,EVO} \frac{p_{cc,evo}}{p_{in,EEPS}} \frac{T_{in,EEPS}}{T_{cc,EVO}} \frac{(m_{cc,EVO} d_r + m_{cc,EVO})}{m_{cc,EVO}}} \ [mg/m^3] \tag{5.35}$$

$$PN_{in,EEPS}^{CFD} = \frac{PN_{EVO}}{V_{in,EEPS}} = \frac{\sum_{i=S_{LOW}}^{S_{HIGH}} \frac{s_{i,EVO}}{\rho_s V_{m,i}} * 1e6}{V_{cc,EVO} \frac{p_{cc,evo}}{p_{in,EEPS}} \frac{T_{in,EEPS}}{T_{cc,EVO}} \frac{(m_{cc,EVO} d_r + m_{cc,EVO})}{m_{cc,EVO}} * 1e6} \ [\#/cm^3] \tag{5.36}$$

where $s_{i,EVO}$ is soot mass contained in the i^{th} section, $m_{cc,EVO}$ is in-cylinder gas mass and d_r is the dilution rate used in the diluter. PN in each section can be calculated using Eq. 5.36 on a single section. Once PN is calculated for each section, the normalized $PSDF$ predicted by CFD at EVO, is calculated using Eq. 5.1. Despite their simplicity, Eq. 5.35-5.36 allow a consistent comparison with the experimental measurements presented in a few lines. As a further comment, the advantage of carrying out such comparison on a single-cylinder engine is that no uncertainties are introduced by possible cylinder-to-cylinder interactions in terms of fluid dynamics and soot produced. All CFD results hereafter analysed, for the three SOIs, are scaled to the $EEPS$ inlet conditions using Eq. 5.35-5.36 and are therefore to be considered as equivalent CFD results at the exhaust. Furthermore, in order to consistently compare the calculated data with the experimental ones, the overall soot mass concentration is calculated considering only the sections whose mean diameter was included in the sampling diameter range of the instrument ($5\,nm \leq D_p \leq 560\,nm$), for the overall PM. Similarly, only the sections whose mean diameter is included in the $30\,nm \leq D_p \leq 50\,nm$ range are considered to calculate the ultrafine PM concentration. In the first place, a quantitative comparison of PM at the exhaust must be drawn. For the sake of clarity, PN and PM evolution over the engine cycle is reported up to EVO event. In Fig. 5.38(a), the evolution of in-cylinder PM during the sixth and last cycle simulated is compared for the three injection strategies, while Fig. 5.38(b) is focused on a quantitative comparison with the experimental measurements. For the sake of completeness, experimental and calculated values are reported in Table 5.5 for overall and ultrafine particles, in terms of PM and PN,

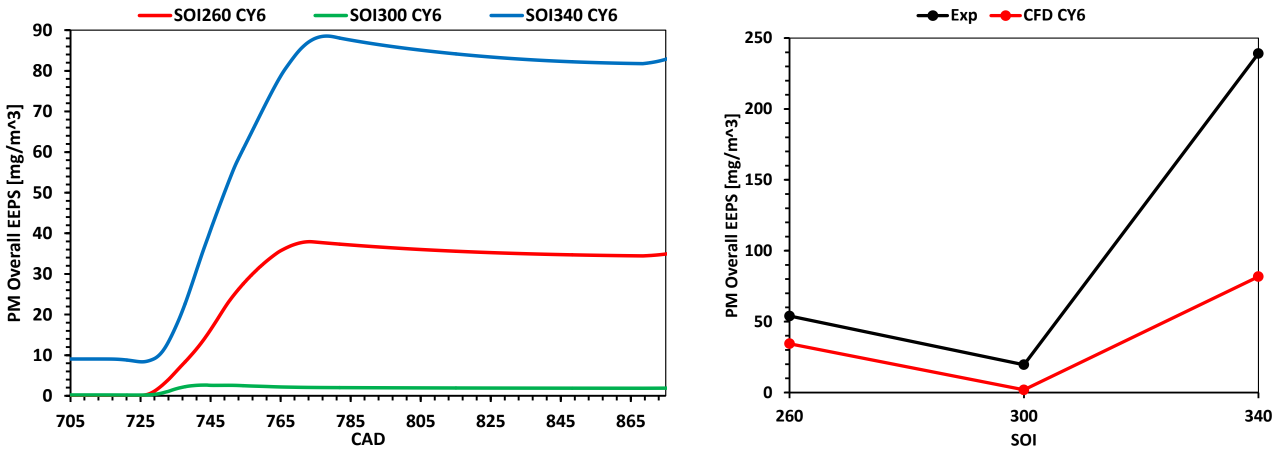

(a) **(b)**

Figure 5.38. (a) In-cylinder PM evolution, scaled to the $EEPS$ sampling conditions, for $SOI260$ (solid red line), $SOI300$ (solid green line) and $SOI340$ (solid blue line) for cycle 6 (b) Comparison between measured (solid black line) and predicted (solid red line) PM at the exhaust.

		PM Overall $EEPS$ $[mg/m^3]$	PM Ultrafine $EEPS$ $[mg/m^3]$	PN Overall $EEPS$ $[\#/cm^3]$	PN Ultrafine $EEPS$ $[\#/cm^3]$
$SOI260$	Exp	53.97	0.31	2.60E+06	2.86E+06
	CFD	34.44	4.28	6.28E+08	7.00E+07
$SOI300$	Exp	19.61	0.08	7.51E+06	7.37E+05
	CFD	1.87	0.82	6.21E+08	1.80E+07
$SOI340$	Exp	239.16	0.82	6.19E+06	8.86E+06
	CFD	81.76	10.60	5.95E+08	1.61E+08

Table 5.5. Experimental-CFD quantitative comparison in terms of PM and PN (Overall and Ultrafine).

Analysing CFD results it is immediate to notice how the CFD model is able to perfectly describe injection strategy dependence on SOI, confirming $SOI300$ as optimized injection strategy to minimize soot formation. In particular, it must be underlined that such results are obtained without any case-to-case calibration of the soot model, and with Sectional Method constants default values. To the author's best knowledge, this is an unprecedented result in the field of GDI soot modelling with the Sectional Method, since previous results reported in literature were obtained with a dedicated case-to-case tuning [129]. Quantitatively speaking, the CFD model generally underpredicts overall PM at the exhaust. On the other hand, results are promising in view of the fact that no soot model tuning was used and a series of assumptions were introduced. Further analysing the results, it straightforward to notice that a severe overestimation of PM ultrafine, PN overall and ultrafine is obtained in CFD simulations, as visible in Fig. 5.39 and Table 5.5. The reason for this is further discussed in a few lines. However, it is important to notice how the CFD model is able to correctly predict the sensitivity of PM and PN ultrafine to the injection strategy. In order to highlight this result, normalized values using $SOI300$ values as reference for both for experimental and CFD values, is reported in Fig. 5.39.

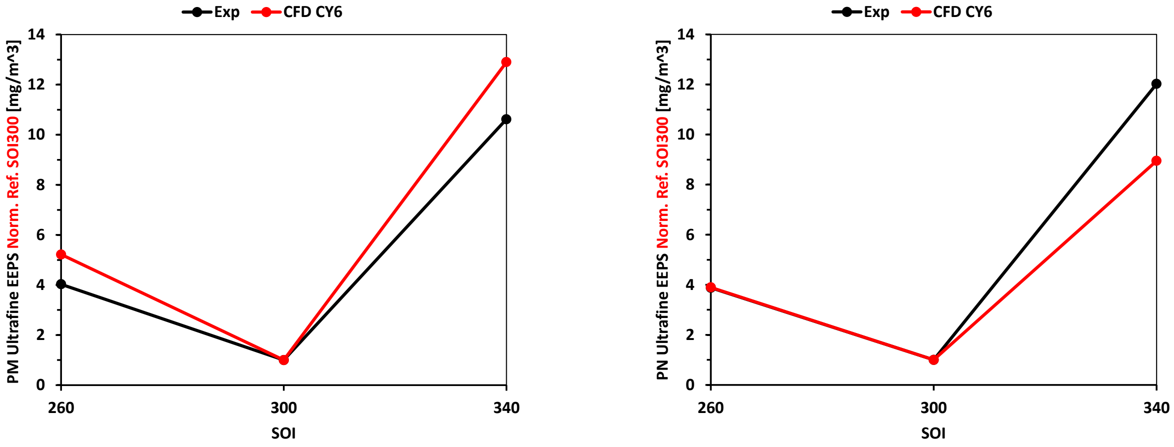

(a) **(b)**

Figure 5.39. (a) Comparison between measured (solid black line) and predicted (solid red line) (a) PM and (b) PN ultrafine normalized over yield values for $SOI300$ strategy.

These last results are deemed to be particularly interesting since the CFD model is at least able to predict, with a very good agreement, not only the qualitative trend but also the quantitative factors present among the strategies in terms of soot ultrafine emissions. Considering the huge concern related to ultrafine particle emissions, the ability to predict injection strategy sensitivity with such degree of accuracy is deemed to be a promising tool for researchers and engineers in the automotive industry. Conversely, overall PN predicted by CFD, reported in Fig. 5.40, is overestimated and the obtained trend appears to be not fully consistent with the experimental findings. Interestingly, a correct relative trend is captured in the main stage of the combustion process.

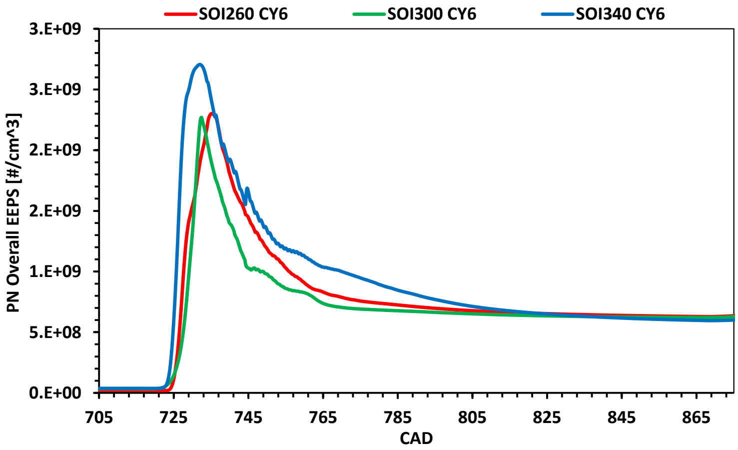

Figure 5.40. In-cylinder PN evolution, scaled to the $EEPS$ sampling conditions, for $SOI260$ (solid red line), $SOI300$ (solid green line) and $SOI340$ (solid blue line) for cycle 6.

Last but not least, a comparison in terms of measured and calculated $PSDF$ is portrayed in logarithmic and linear y-axis scale in Fig. 5.41(a)-(b). The results obtained in terms of $PSDF$ explain the quantitative results obtained in terms of PM and PN for both ultrafine and overall particles. The general underestimation in terms of PM and overestimation in terms of PN is apparently due to an underestimation of the accumulation processes (e.g. Condensation, Coagulation and Surface Growth) by which mass is moved from lower to higher sections, leading to PN reduction.

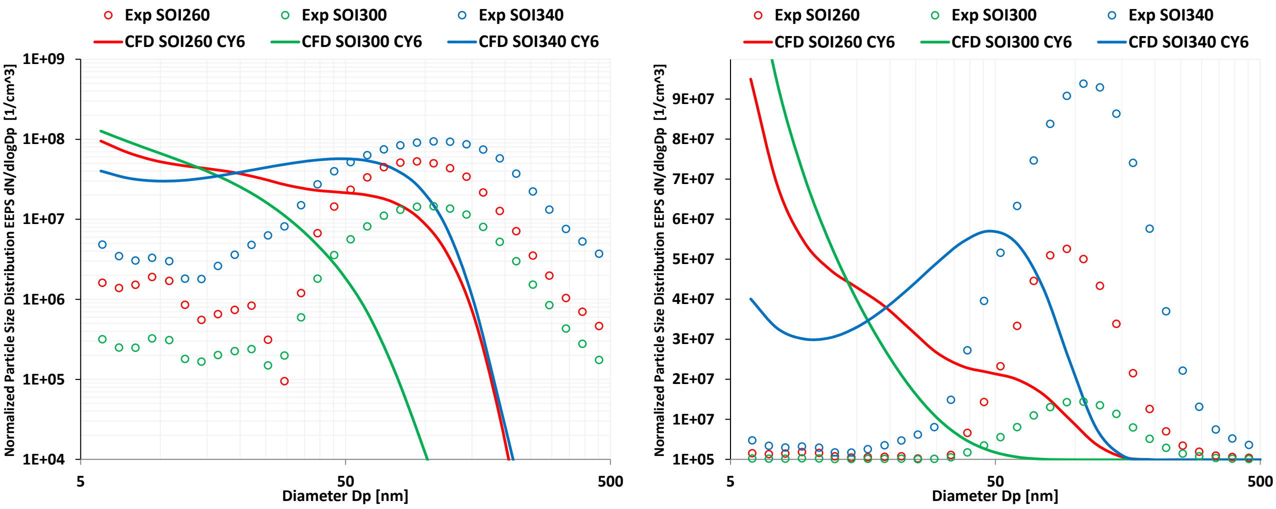

(a) (b)

Figure 5.41. Experimental (unfilled circles) and calculated (lines) normalized $PSDF$ on a logarithmic scale (a) and on a linear scale (b).

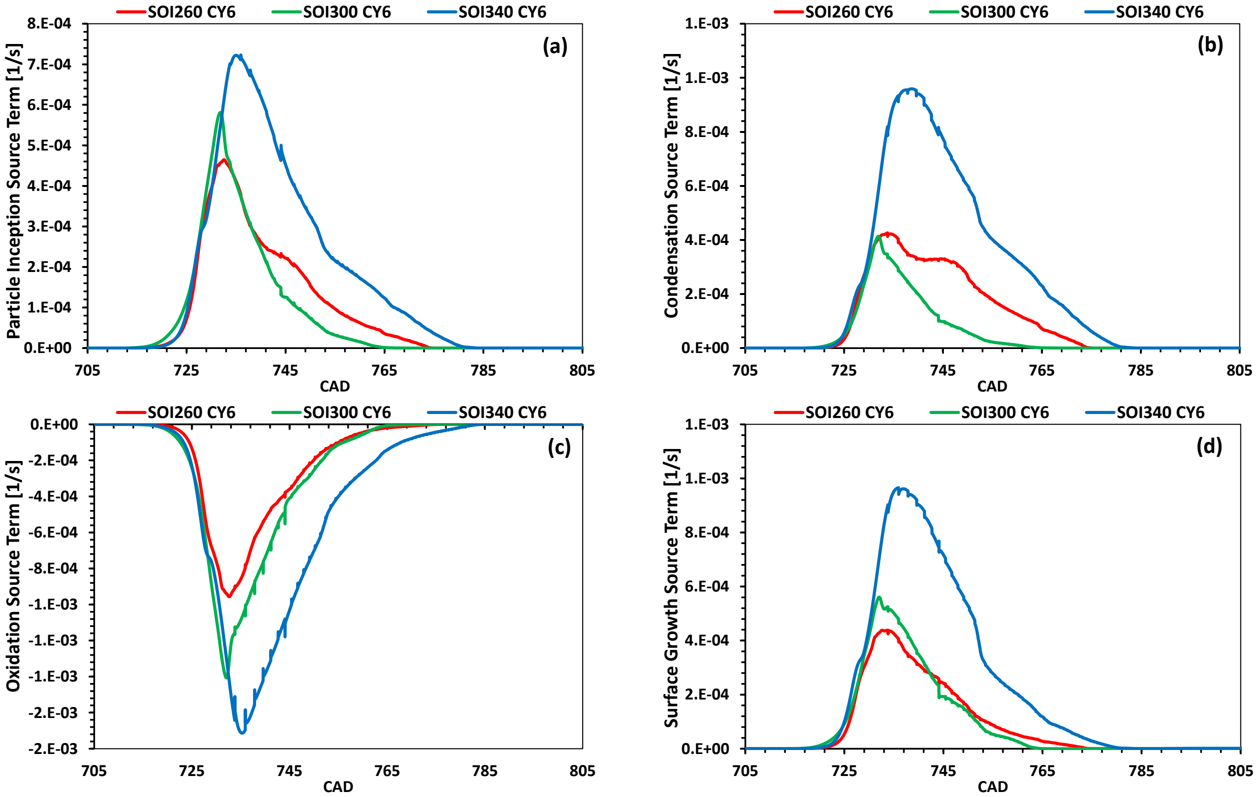

Figure 5.42. Particle inception (a), Condensation (b), Oxidation (c) and Surface Growth (d) source terms evolution during the engine cycle.

Despite being quantitatively more in line with the experiments, this behaviour is particularly evident for $SOI260$ and $SOI300$, whose $PSDF$s are clearly shifted towards small diameters and strongly overestimate PN. This conclusion is further confirmed by in-cylinder average source terms evolution over the cycle reported in Fig. 5.42 for all processes but Coagulation, whose total source terms across the section is by definition a numerical zero [47,48,49]. As a final remark, total soot source term Ω_{tot} scalar field evolution during the main combustion stage (740 CAD) is proposed in Fig. 5.43, to highlight local soot formation correlation with the stratification at spark onset for the three SOIs. Local blue spots, corresponding to negative Ω_{tot} values, identify regions in the combustion chamber where oxidation overcomes the other processes. Conversely, red spots, corresponding to positive Ω_{tot} values, identify regions where soot formation prevails. It is straightforward to notice how Ω_{tot} scalar field is strongly correlated with flame front position, dividing formation regions (unburnt gas-side) from oxidation regions (burnt gas-side).

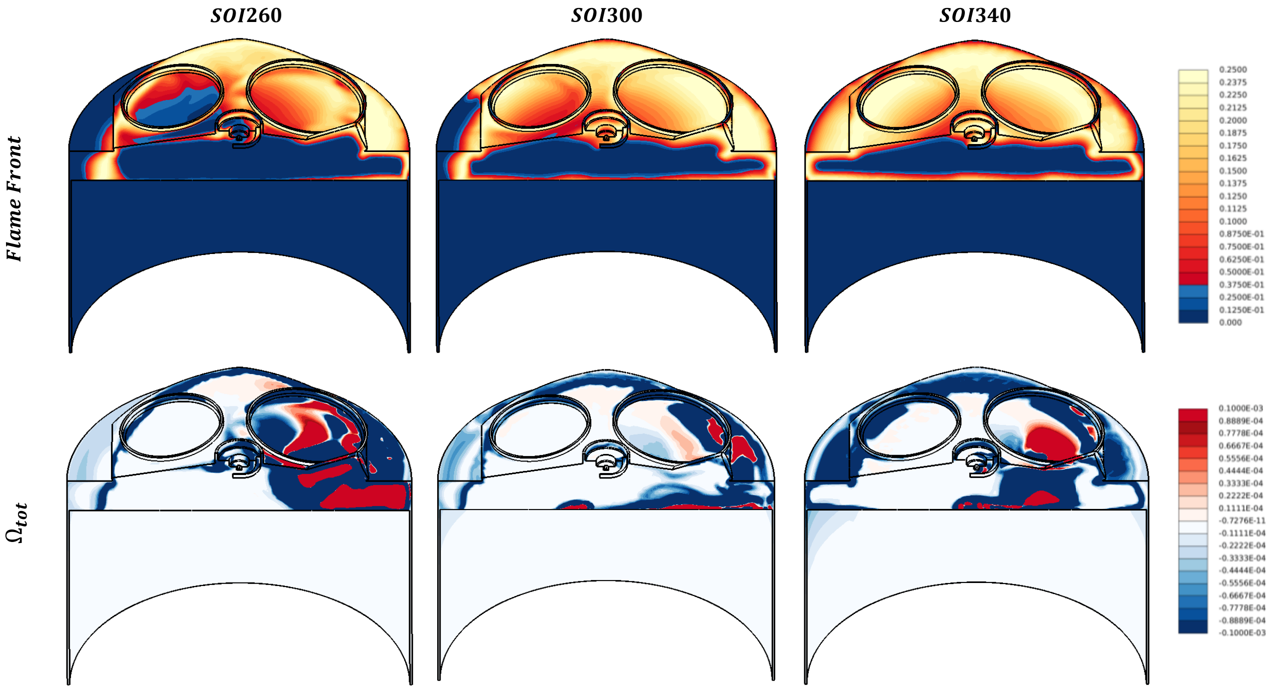

Figure 5.43. Flame front (top row) and Total soot source term Ω_{tot} scalar field at 740 CAD for the three injection strategies.

Several reasons might explain the underestimated accumulation mode shown by the CFD model. Firstly, the Sectional Method relies on the assumption of constant soot density ρ_s [47,48,49], which is in reality decreasing for an increasing particle size. This means that soot source terms mathematical formulation should be modified to account for this effect, which also influences surface reactions. In fact, surface reactivity is known to be decreasing with particle size, despite the increased surface area available [47]. Unfortunately, the Sectional Method relies on constant soot density ρ_s to simplify the mathematical formulation. As a matter of fact, writing the equations in terms of volume conservation allows to automatically conserve mass across the sections using the aforementioned assumption. A modified version of the model, accounting for ρ_s variation across the sections, is currently under study but such kind of modification is not trivial as mass flux conservation issues between sections and $PSDF$ concept itself are called into question. From another point of view, the underestimation might be due to the fact that CP-based soot libraries are not able to account for local diffusive flames phenomena, which might locally increase soot formation and accumulation processes. In this sense, an hybrid premixed-diffusive library could be considered to account for both combustion modes, selecting soot coefficients from the correct library based on a cell-wise evaluation of the flame index [271,272]. Last but not least, a dedicated methodology based on a set of assumptions was introduced to consistently compare experiments with CFD outcomes. Although being reasonable, some of these assumptions might be at least questionable and there is definitely room for improvement in this sense. For example, a detailed investigation of soot evolution in the exhaust line would help in understanding if the final result is more affected by the aforementioned approximations or by a lack of accuracy in modelling in-cylinder phenomena. That said, the proposed $3D$-CFD methodology for GDI soot prediction is, to the author’s best knowledge, the first study presenting such an extensive validation using a customized version of the Sectional Method. The author would like to stress the reader’s attention on the fact that results were obtained with default soot model constants and without any case-by-case tuning. In this scenario, the model correctly predicts trends for the analysed strategies in terms of PM overall and especially in terms of PM/PN for ultrafine particles, which are currently the biggest concern. Focusing on the quantitative estimation, PM overall is predicted to a satisfactory agreement considering the complexities arising while modelling soot formation. Therefore, such methodology is deemed to be sufficiently reliable to be potentially applied in $3D\text{-}CFD$ optimization procedures investigating new strategies aiming to further decrease engine-out soot emissions in production GDI units.

Conclusions

In the present PhD thesis, a comprehensive set of cost-effective methodologies were developed with the aim of integrating chemistry-relevant information in $3D\text{-}CFD$ combustion and soot simulations of GDI engines. All the methodologies were validated by means of $3D\text{-}CFD$ simulations against dedicated experiments carried out on a single-cylinder optically-accessible GDI research engine at the Istituto Motori-CNR. The present work covered a wide range of complementary aspects involving chemistry-based processes which were addressed in dedicated chapters. In Chapter 3, the importance of fuel surrogates modelling has been extensively discussed and two complementary fuel surrogates formulation methodologies were presented. At first, a novel methodology was proposed to formulate TRF, $ETRF$ and multicomponent fuel surrogates able to mimic the main chemico-physical properties, auto-ignition and flame propagation characteristics of a targeted commercial gasoline. This last aspect constitutes the element of novelty of the proposed approach which was extensively validated against auto-ignition delay and laminar flame speed experiments on a wide set of conditions. Secondly, a complementary fuel surrogate formulation methodology, relying on a purely mathematical approach, was proposed to estimate the sooting tendency of a real fuel based on basic compositional information and to generate $ETRF$ surrogates able to mimic this fuel property in a dominantly premixed combustion system. Despite its general validity, the methodology focused on commercial gasolines for the purpose of the present work. An extensive validation campaign, the last step of which consisted in dedicated $3D\text{-}CFD$ engine simulations aided by the Sectional Method, demonstrated the ability of the formulated surrogates to correctly model commercial gasolines sooting tendencies. This original methodology was developed by the author during a six-months period spent in SIEMENS Digital Industries Software office in London, as a PhD Intern. In view of the promising results obtained, constant-pressure based soot libraries for commercial gasolines, generated with the proposed approach, will be implemented in the commercial CFD code STAR-CDv2020.1. Furthermore, the presented fuel surrogate formulation methodology is adopted, at the time of writing, as state-of-the-art technique in SIEMENS Digital Industries Software. In Chapter 4, a chemistry-based methodology aiming to formulate laminar flame speed correlations valid at engine-relevant conditions was presented. The core of the methodology is the possibility to generate correlations based on laminar flame speed calculations carried out in a chemistry solver via $1D$ freely propagating simulations. This virtual dataset of flames is then fitted using a fifth order logarithmic polynomial correlation. This approach demonstrated to retain a high level of chemistry-fidelity while preserving CPU-efficiency compared to a tabulated approach, due to the adoption of a simple polynomial form. An additional methodology was presented to generate dedicated fitting extensions for lean and rich mixtures, taking into account the effect of both pressure and temperature on laminar flame speed scaling. A dedicated correlation was derived for $RON95$ $E5$ European commercial gasoline, based on a $ETRF$ surrogate specifically generated, for the purpose of this work. This correlation was tested, together with widespread empirical correlations, on a dedicated $3D\text{-}CFD$ engine case and validated against experimental data based on cycle-resolved in-cylinder flame visualizations from the analysed research engine. The results clearly demonstrated the enhanced and comprehensive combustion process description guaranteed by the proposed approach compared with empirical correlations. The methodologies introduced in Chapter 3 and Chapter 4 were essential steps needed to undertake the final modelling purpose of the whole work, which is the formulation of a solid methodology for GDI soot prediction using the Sectional Method, discussed in Chapter 5. In this chapter, a customized version of the Sectional Method, relying on a constant-pressure reactor-based tabulated approach is presented. The essential elements related to PAH chemistry were discussed and a precise tabulation strategy was adopted to ensure a proper description of chemistry-based phenomena involved in soot formation. The $3D\text{-}CFD$ model of the single-cylinder optically-accessible research engine was discussed in detail and dedicated validations of spray and liquid film modelling approaches were carried out due to the impact of these processes on mixture formation and, therefore, on soot formation. At first, the validity of the spray modelling approach was proven based on dedicated experiments carried out in a constant-volume vessel. Secondly, in-cylinder flame visualizations were used to track rich mixture locations during combustion to validate stratification at spark onset for the three injection strategies considered. A multi-cycle approach was then introduced to correctly evaluate PM, PN, $PSDF$ and a dedicated post-processing methodology was proposed to compare CFD and experimental data. $3D\text{-}CFD$ combustion results further confirmed the benefits introduced by the proposed chemistry-based laminar flame speed correlation in terms of combustion prediction. As a last step, a detailed comparison between soot experimental data and CFD simulations highlighted the capability of the proposed methodology to predict, to a satisfactory extent, engine-out PM, PN and $PSDF$ sensitivity to different injection strategies. The capability of predicting qualitative engine-out soot trends on multiple OPs, using the Sectional Method with default soot model constants and without any case-by-case tuning, constitutes an unprecedented result. $3D\text{-}CFD$ quantitative results were found to be promising, in terms of PM overall, considering that no tuning efforts were spent on purpose. Based on these results, the Sectional Method multi-cycle based approach, aided by constant-pressure soot libraries, is currently used as reference methodology for GDI soot modelling in SIEMENS Digital Industries Software. As a final remark, the present work clearly demonstrates the benefits deriving by the integration of chemistry-based methodologies in $3D\text{-}CFD$ in-cylinder combustion simulations.

Acknowledgements

Firstly, I would like to thank Professor Stefano Fontanesi (Ste) for offering me a position as a PhD student in the GRUppo MOtori research group. It has been an incredible journey that gave me the chance to grow both as an engineer and as a human being. I truly believe that this experience played a key role in helping me achieving my goals and a position that has always been the dream of a lifetime. For this reason and for the patience you have had during my endless presentations and our technical discussions, I am and always will be grateful to you!

In the second place, I have to thank Siemens Digital Industries Software in the person of Patrick Niven, Dr. Harry Lehtiniemi and Dr. Cedomir Kralj for giving me the possibility of joining STAR-CD Development Team in the London office. This opportunity has been fundamental for my professional growth and for the finalization of this PhD thesis. Special thanks to Dr. Cedomir Kralj, Dr. Jens Prager, Stefano Duranti and Yongjun Liang. Your continuous support during my stay in London has been really important to me. I would also like to thank all the guys and girls in the London office: Antonello, Gianluca, Leonardo, Mani, Massimo, Max, Phil, Rodolfo, Sava, Thomas, Virginia and all the others. You made me feel at home since day one and our renowned evenings at the pub did the rest. I found a true friend in each and every one of you. Thanks!

I indeed have to thank the Istituto Motori (IM-CNR) in the person of Dr. Simona Merola and Dr. Adrian Irimescu for providing the research engine experimental dataset used to validate the methodologies presented in this PhD thesis and for the time dedicated to me during our countless calls. I truly have to thank you for your willingness to discuss about the results and for your continuous support. Thanks!

Thanks are also due to Simone and Fabio, whose help has been fundamental to validate the spray modelling approach presented in this PhD thesis. Without your support I couldn't have achieved the results shown in the conclusion of this work. Thanks!

A massive thanks to Dr. Giuseppe Cicalese (Cica) for giving me the possibility of joining as a consultant the R&D CFD family. The projects I have been working on gave me the possibility to grow as an engineer and to cooperate with cutting edge companies, which is definitely something not happening on a daily basis. Thanks!

To all the guys and girls in the GRUppo MOtori and R&D CFD: Fabio, Ale, Clara, Vale, Simone, Alessio, Francesco, Matteo, Seba, Alfonsina, Fabri, Cristian, Mattia, Luca and Giovanni.. what can I say? It has been a pleasure to get to know you all, to work with you and to share many many adventures that I am sure I will always bring with me. In many of you I have found true and loyal friends and I really cannot thank you enough for your support during these tough years!

Special thanks goes to Vale: as a matter of fact without your endless help this last year it would have been impossible for me to finalize all the publications and I do know that working with me requires indeed a lot of patience! Special thanks goes to Fabio as well, for inspiring me to undertake the challenges of a research activity, for all of your support during my tough times and for being such a great friend. Special thanks also goes to Clara for being always supportive and for the endless sweets supply which has been crucial while working on the final draft of this work. Thank you guys!

To my former PhD colleague Fede, a thank you is not enough. Starting and ending this journey with you is priceless and I couldn't have asked for a better friend along the way. We have shared so many adventures and great moments together and you really have been an added value and a true friend. Without you it just wouldn't have been the same. Thanks for everything mate!

To Giacomo, Federica and all the good old friends back home: you represent my roots and just like a tree blown in the wind I made it through the storm thanks to your love and support. You really are my chosen family, thank you!

Last but not least, to my girlfriend Alessandra and my family: it is hard to find the words to express my gratitude for all the love and support that you gave me in these last three years. You have always believed in me and you really have been my first supporters with no exception. We really have been through some hard times and I do hope you all know how important you are to me. From the depths of my heart, thanks for being part of my life and for helping me during this journey!

Every single letter, word and page of this PhD thesis is dedicated to you Dad. You have always been my first supporter and we decided together to start this journey three and a half years ago. Unfortunately, life split us apart at the very beginning of this adventure and you couldn't see all of this. Countless times I would have liked to share the details of my adventures and successes with you. Making this journey without you, has been, by far, the hardest thing I have ever done. Despite your absence, you have been the reason that pushed me to get back up in my darkest hours. For this reason, all the words in this PhD thesis are as yours as mine. With all of my love, thanks for everything you have done.

Publications

The work presented in this PhD thesis led to the following publications:

- D'Adamo, A., Del Pecchia, M., Breda, S., Berni, F. et al., "Chemistry-Based Laminar Flame Speed Correlations for a Wide Range of Engine Conditions for Iso-Octane, n-Heptane, Toluene and Gasoline Surrogate Fuels," SAE Technical Paper 2017-01-2190, 2017, https://doi.org/10.4271/2017-01-2190.

- Breda, S., D'Adamo, A., Fontanesi, S., Del Pecchia, M. et al., "CFD Optimization of n-Butanol Mixture Preparation and Combustion in an Research GDI Engine," SAE Technical Paper 2017-24-0063, 2017, https://doi.org/10.4271/2017-24-0063.

- Del Pecchia, M., Breda, S., D'Adamo, A., Fontanesi, S. et al., "Development of Chemistry-Based Laminar Flame Speed Correlation for Part-Load SI Conditions and Validation in a GDI Research Engine," SAE Int. J. Engines 11(6):715-741, 2018, https://doi.org/10.4271/2018-01-0174.

- Del Pecchia, M., Pessina, V. Iacovano, C., Cantore, G. “Development of gasoline-ethanol blends laminar flame speed correlations at full-load SI conditions via 1D simulations”. AIP Conference Proceedings 2191, 020063 (2019); https://doi.org/10.1063/1.5138796.

- Del Pecchia, M., Sparacino, S., Breda, S., Cantore, G. “Validation of a sectional soot model based on a constant pressure tabulated chemistry approach for PM, PN and PSDF estimation in a GDI research engine”. AIP Conference Proceedings 2191, 020063 (2019); https:// doi.org/10.1063/1.5138797.

- Del Pecchia, M., Pessina, V., Berni, F., d’Adamo, A., Fontanesi, S. “Gasoline-ethanol blend formulation to mimic laminar flame speed and auto-ignition quality in automotive engines”, Fuel, Volume 264, 2020, 116741, ISSN 0016-2361, https://doi.org/10.1016/j.fuel.2019.116741.

- Del Pecchia, M., Sparacino, S., Breda, S., Cantore, G. “A 3D-CFD Methodology to Quantitatively Predict Engine-out Soot Emission in GDI Engines”, La Termotecnica, ISSN: 0040-3725, November 2019, Number 07, Pag. 48-56.

- Del Pecchia, M., Fontanesi, S. “A novel methodology to formulate comprehensive multicomponent gasoline fuel surrogates for 3D-CFD combustion and knock modelling simulations”, Fuel, JFUE-D-19-06973. *Under Review*

- Del Pecchia, M., Fontanesi, S., Prager, J., Kralj, C., Lehtiniemi, H. “A Threshold Soot Index-based Fuel Surrogate Formulation Methodology to Mimic Sooting Tendency of Real Fuels in 3D-CFD simulations”. Combustion & Flame, ISSN: 0010-2180. *To be Submitted*

- Del Pecchia, M., Pessina, V., Berni, F., Fontanesi, S., Merola, S.S. “A comprehensive CFD approach to quantitatively predict soot emission in GDI engines ”. Applied Energy, ISSN: 0306-2619. *To be submitted*

References

[1] International Agency for Research on Cancer (WHO), Press Release n.213, June 2012.

[2] Regulation of the European parliament and of the council, COM (2017) 676 final, 2017/0293 (COD)

[3] G.T. Kalghatgi. International Journal of Engine Research. (2014). 15. 10.1177/1468087414526189.

[4] G.T. Kalghatgi. Petroleum Technology Quarterly. 2016. 23-31.

[5] G.T. Kalghatgi et al. Petroleum Technology Quarterly. 2016. 17-23.

[6] S.Mani Sarathy et al. Prog. Energy Combust. Sci,Vol.65, 2018,Pag.67-108, 10.1016/j.pecs.2017.09.004.

[7] World Oil Outlook 2040. OPEC Secretariat, October 2017, ISBN 978-3-9503936-4-4.

[8] F. Zhao et al. SAE International,2002. ISBN 0-7680-0882-4.

[9] P. Leduc et al. Oil and Gas Science and Technology, Rev. IFP, vol.58, No.1, pp 115-127, 2003.

[10] F. Bozza et al. Energy Procedia, Volume 81, 2015, Pages 866-873, 10.1016/j.egypro.2015.12.134.

[11] ASTM D4814. West Conshohocken : PA : ASTM International, 2016.

[12] ASTM D2699. West Conshohocken : PA : ASTM International, 2012.

[13] ASTM D2700. West Conshohocken : PA : ASTM International, 2012.

[14] R. Nates et al. " SAE Technical Paper 942064, 1994, doi.org/10.4271/942064.

[15] J.B. Heywood. Second Edition, 2018 McGraw-Hill Education. ISBN 9781260116106.

[16] G.T. Kalghatgi. (2005). SAE Technical Paper. 10.4271/2005-01-0239.

[17] S. Martinez et al. Energies 2017, 10, 1337: doi: 10.3390/en10091337.

[18] M. Bunce et al. SAE Technical Paper 2014-01-2603, 2014, doi: 10.4271/2014-01-2603.

[19] W. Attard et al. SAE Technical Paper 2012-01-0823, 2012, doi: 10.4271/2012-01-0823.

[20] M. Bunce et al. SAE Technical Paper 2014-01-1195, 2014, doi: 10.4271/2014-01-1195.

[21] P. Chinnathambi et al. SAE Technical Paper 2015-01-0386, 2015, doi: 10.4271/2015-01-0386.

[22] M. Gholamisheeri et al. Combust. Flame 183 (2017) 194-206, doi: 10.1016/j.combustflame.2017.05.008.

[23] Directive 2018/2001. Official Journal of the European Union, L328/82, Volume 61, 2018, ISSN-1977-0677.

[24] T.W. Kuo., J. Eng. Gas Turbines Power 112:348-56 (1990).

[25] International Agency for Research on Cancer (WHO), Press Release n.213, June 2012.

[26] N.A.H. Janssen et al. World Health Organization Regional Office for Europe, ISBN: 978 92 890 0265 3.

[27] H.E. Wichmann. Inhal Toxicol. 2007;19 Suppl 1:241-4, doi 10.1080/08958370701498075.

[28] P. Thunis et al. Publications Office of the European Union, 2017, doi:10.2760/336669, JRC108595.

[29] H. Fuchsig et al. Emiss. Control Sci. Technol. (2017) 3:243-244.

[30] T.C. Bond et al. Journal of Geophysical Research: Atmospheres. (2013). doi: 10.1002/jgrd.50171.

[31] B. Liang et al. Journal of Aerosol Science, Vol 57, 2013, Pag 22-31, doi.org/10.1016/j.jaerosci.2012.11.008.

[32] J. Su et al. Journal of Engineering for Gas Turbines and Power. 136. 10.1115/ICEF2013-19157.

[33] C.L. Myung et al. Int. J. Automot. Technol. 2012;13(1):9-22. 10.1007/s12239-012-0002-y.

[34] V. Knop et al. SAE Int. J. Engines. 6. 941-952. 10.4271/2013-01-1103.

[35] H. Fu et al. SAE Technical Papers. 2014. 10.4271/2014-01-2836.

[36] X. He et al. Energy & Fuels - ENERG FUEL. 26. 2014-2027. doi:10.1021/ef201917p.

[37] M. Raza et al. (2018) Energies. 6. doi: 10.3390/en11061417.

[38] J. Qi et al. SAE Int. J. Engines, Vol. 8, no. 3, 2015, pp. 1322–1333.

[39] O. Colin et al. (2004) Oil Gas Sci. Technol. – Rev. IFP 59, 6, 593-609.

[40] N. Peters. “Turbulent Combustion”. Cambridge University Press, 2000.

[41] A. d'Adamo et al. SAE Int. J. Engines 9(1):618-630, 2016, doi:10.4271/2016-01-0581.

[42] A. d'Adamo et al. SAE Int. J. Engines 10(3):722-739, 2017, doi.org/10.4271/2017-01-0551.

[43] A. d’Adamo et al. Applied Energy Vol. 249, 2019, Pag. 126-142, doi.org/10.1016/j.apenergy.2019.04.093.

[44] C. Netzer et al. 8th European Combustion Meeting (ECM 2017), Dubrovnik, Croatia.
[45] C. Netzer et al. Int. Multidimensional Engine Modeling User's Group Meeting at the SAE Congress 2017.
[46] K. Netzell et al. Proc. Combust. Inst., Vol 31, Issue 1, 2007, Pag 667-674 doi.org/10.1016/j.proci.2006.08.081.
[47] K. Netzell. PhD Thesis, Lund Institute of Technology, 2006.
[48] C. Marchal. PhD Thesis, Université d'Orleans, 2008. https://tel.archives-ouvertes.fr/tel-00392316.
[49] D. Aubagnac-Karkar. PhD Thesis, Ecole Centrale Paris, 2014. https://tel.archives-ouvertes.fr/tel-01132323.
[50] T. Farrell et al. (2004).SAE Technical Papers. 10.4271/2004-01-2936.
[51] D. Witkowski et al. Combust Flame, Vol 160, Pag 1129-1141, doi.org/10.1016/ j.combustflame.2013.01. 027.
[52] C. Lee et al. Combust. Flame, Vol. 186, 2017, Pag. 114-128, doi.org/10.1016/j.combustflame.2017.07.034.
[53] K. Aikawa et al. SAE Int. J. Fuels Lubr. 3. 610-622. 10.4271/2010-01-2115.
[54] V. Yakhot et al. Journal of Scientific Computing, 1986. 1(1): p. 3-51.
[55] Z. Han et al. Combustion Science and Technology, 1995. 106(4-6): p. 267-295.
[56] V. Yakhot et al. Physics of Fluids A: Fluid Dynamics, 1992. 4(7): p. 1510-1520. END Chapter 1
[57] G.T. Kalghatgi. SAE 2001-01-3584, 2001, SAE – Journal of Fuels and Lubricants, Vol.110.
[58] M. Mehl et al. 10th US National Combustion Meeting, Lawrence Livermore National Laboratory, 2017.
[59] L. Cai et al. Combust. Flame 162 (2015) 1623–1637, doi.org/10.1016/j.combustflame.2014.11.018.
[60] J.C.G. Andrae et al. Combust. Flame,Vol.149, 2007, Pag.2-24, 10.1016/j.combustflame.2006.12.014.
[61] J.C.G. Andrae et al. Combust. Flame 156 (2009) 842-851.
[62] J.C.G. Andrae. Fuel, Vol. 107, 2013, Pag. 740-748, ISSN 0016-2361, doi.org/10.1016/j.fuel.2013.01.070.
[63] E. Ranzi et al. International Journal of Chemical Kinetics, doi:10.1002/kin.20867.
[64] S.R. Daly et al. Energy Fuels 2018, 32, 7916-7932, (2018).
[65] C. Pera et al. Fuel, Vol. 96, 2012, Pag. 59-69, ISSN 0016-2361, doi.org/10.1016/j.fuel.2012.01.008.
[66] M. Chaos et al. (2007). 5th US Combustion Meeting. 4. 25-28.
[67] R. Khan. M.Sc. thesis, Drexel University, Philadelphia, PA, USA, 1998.
[68] C. Naik et al.(2005). SAE Technical Papers. 2005-01-3741. 10.4271/2005-01-3741.
[69] B.M. Gauthier et al. Combust. Flame, Vol.139, 2004, Pag. 300-311, 10.1016/ j.combustflame.2004.08.015.
[70] G. Kukkadapu et al. Combust. Flame, Vol.159,2012,Pag.3066-3078, 10.1016/ j.combustflame.2012.05.008.
[71] S. Mani Sarathy et al. Combust. Flame, Vol.169,2016, Pag. 171-193, 10.1016/j.combustflame.2016.04.010.
[72] M. Mehl et al. (2011). Energy & Fuels. 25. 10.1021/ef201099y.
[73] O. Samimi Abianeh et al., Combust.Flame 162, 2015, 3773-3784, 10.1016/j.combustflame.2015.07.015.
[74] J. A. Piehl et al. Journal of Combustion, Article ID 8406754, 2018. doi.org/ 10.1155/2018/8406754.
[75] S. Jerzembeck et al. Combust and Flame 156 (2009) 292-301.
[76] P. Dirrenberger et al. (2014) Fuel. 115. 162-169. 10.1016/j.fuel.2013.07.015.
[77] L. Sileghem et al. Fuel, Volume 112, 2013, Pag. 355-365, https://doi.org/10.1016/j.fuel.2013.05.049.
[78] L. Sileghem et al. (2012). Energy & Fuels. 26. 4721–4727. 10.1021/ef300393h.
[79] M. Di Lorenzo. (2019). Fuel. 253. 1578-1588. 10.1016/j.fuel.2019.05.081.
[80] T. Lu et al. Prog. Energy Combust. Sci, Vol. 35, 2009, Pag. 192-215, doi.org/10.1016/j.pecs.2008.10.002.
[81] A. d'Adamo et al. SAE Technical Paper 2017-01-2190, 2017.
[82] M. Del Pecchia et al. (2018) SAE International Journal of Engines. 11. doi:10.4271/2018-01-017.
[83] M. Fatouraie et al. SAE Technical Paper 2018-01-0358, 2018, doi:10.4271/2018-01-0358.
[84] P.K. Kanaujia. Encyclopedia of Analytical Science, Academic Press, 2019, Pag. 217-231.
[85] E. Hu et al. Fuel, Volume 256, 2019, 115933, ISSN 0016-2361, doi.org/10.1016/j.fuel.2019.115933.
[86] A. Håkansson et al. (2001). Chemosphere. 44. 1243-52. 10.1016/S0045-6535(00)00481-1.
[87] A. Ahmed et al., Fuel, Vol. 143, 2015, Pag. 290-300, https://doi.org/10.1016/j.fuel.2014.11.022.
[88] F.L. Dryer. Proceedings of the Combustion Institute, Vol.35, No.11, pp. 7178-7193, 2014.
[89] C. K. Westbrook et al. Combustion and Flame, Vol.156, No.1, pp 181-199, 2009.

[90] L. Cai et al. Combustion and Flame, Vol.173, pp. 468-482, 2016.
[91] H.J. Curran et al. Combust Flame,Vol.129,Issue3, 2002, Pag. 253-280, 10.1016/S0010-2180(01)00373-X.
[92] M. Mehl et al. Proceedings of the European Combustion Meeting, Vienna, Austria, 2009.
[93] M. Mehl et al. SAE Technical Paper 2009-01-1806, 2009, doi.org/10.4271/2009-01-1806.
[94] Z. Tian et al. Proceedings of the Combustion Institute, Vol.33, No.1, pp.233-241, 2011.
[95] Y. Sakai et al. Proceedings of the Combustion Institute, Vol.32, pp. 411-418, 2009.
[96] Y.D. Liu et al. Energy & Fuels, Vol. 27, No. 1, pp.413-421, 2017.
[97] K. Natarajan et al. Proc. of the 13th International Shock Tube Symposium, p.834, Niagara Falls, 1981.
[98] F.N. Egolfopoulos et al. Proc. Symposium on combustion, Vol. 24, pp. 833-841, Elsevier, 1992.
[99] L.R. Cancino et al. Proc 27th International Symposium on Shock Waves, Petersburg, Russia, 2009.
[100] N.M. Marinov. International Journal of Chemical Kinetics, Vol.31, No. 2-3, pp. 183-220, 1999.
[101] M.P. Dunphy et al. Journal of the Chemical Society, Vol. 87, No. 11, pp.1691-1696, 1991.
[102] A. Frassoldati et al. Combustion Science and Technology, Vol. 182, No. 7, pp. 653-667, 2010.
[103] J. Li et al. Proceedings of the 5th US Combustion Meeting, pp. 25-28, Mar 25, 2007.
[104] H.R. Zhang et al. Proceeding of the Combustion Institute 2007;31:401-9.
[105] B. Sirjean et al. Proceedings of the Combustion Institute, Vol. 31, No. 1, pp. 277-284, 2007.
[106] O. Lemaire et al. Combustion and Flame, 2001; 127:1971-80.
[107] H.R. Zhang et al. Environmental Science Technology 2008;42:5615-21.
[108] S.M. Daley et al. International Journal of Chemical Kinetics, Vol. 40, No. 10, pp. 624-634, 2008.
[109] J.P. Orme et al. Proceedings of the European Combustion Meeting, Louvain-la-Neuve, Belgium, 2005.
[110] V. Simon et al. Canadian Journal of Chemistry, Vol. 75, No. 5, pp. 575-584, 1997.
[111] M.J. Al Rashidi et al. Proceedings of the Combustion Institute 2017; 36:469-77.
[112] J.R. Peterson. National Meeting of the American Chemical Society (ACS), Orlando, FL, 41, 25-30, 1996.
[113] W.G. Lovell. Industrial & Engineering Chemistry, Vol. 40, No. 12, pp. 2388-2438, Dec 1948.
[114] R. Minetti et al. Combustion and Flame, Vol. 118, No. 1-2, pp. 213-220, 1999.
[115] Y. Cheng et al. Proceedings of the Combustion Institute 2015; 35:365-75.
[116] N. Morgan et al. Combustion and Flame 2010;157:1122-31.
[117] P. Ghosh et al. Ind Eng Chem Res 2006;45:337-45.
[118] A. Alramadan et al. (2016). Fuel. 180. 175-186. 10.1016/j.fuel.2016.04.032.
[119] J. Badra et al. Applied Energy, Vol. 203, 2017, Pages 778-793, 10.1016/j.apenergy.2017.06.084.
[120] J.P.J. Van Lipzig. Division of Combustion Physics, Lund Institute of Technology, Sweden, MsC Thesis, 2010.
[121] H. Le Chatelier. “Estimation of firedamp by flammability limits”. Ann Mines 1891;19:388-95.
[122] V. Di Sarli et al. (2007) Int. J. of Hydrogen Energy. 32. 637-646. 10.1016/j.ijhydene.2006.05.016
[123] G. Pio et al. Chemical Engineering Transactions, Vol.67, 2018, doi.org/10.3303/CET1867001.
[124] L. Sileghem et al. Fuel, Volume 115, 2014, Pag. 32-40, doi.org/10.1016/j.fuel.2013.07.004.
[125] T. Hirasawa et al. Proc. Combust. Institute, Vol.29, Issue 2, 2002, Pag.1427-1434, 10.1016/S1540-7489(02)80175-4.
[126] M. Del Pecchia et al., Fuel, 2019, 116741, 10.1016/j.fuel.2019.116741.
[127] V.I. Kurganov et al. Chem Technol Fuels Oils (1975) 11: 639. https://doi.org/10.1007/BF00717294.
[128] B. Wang. Applied Energy. 163. 154-166. 10.1016/j.apenergy.2015.11.011.
[129] F. Bonatesta et al. SAE Technical Paper 2014-01-2569, 2014.
[130] A. Irimescu et al. Fuel. (2018) 216. 121-141. 10.1016/ j.fuel.2017.11.116.
[131] A. Überall et al. Fuel, Vol 147, 2015, Pag 203-207, ISSN 0016-2361, https://doi.org/10.1016/j.fuel.2015.01.012.
[132] G. Blanquart et al. Combust Flame, Vol 156, 2009, Pag 588-607, doi.org/10.1016/j.combustflame.2008.12.007.
[133] K. Narayanaswamy et al. Combust Flame, Vol 157, 2010, Pag 1879-1898, doi.org/10.1016/j.combustflame.2010.07. 009.
[134] L. Cai et al. Proc. Combust. Inst., Vol 37, 2019, Pag 639-647, doi.org/10.1016/j.proci.2018.05.032.
[135] C. Wang et al. Appl. Energy. 132. 178–191. 10.1016/j.apenergy.2014.06.012.

[136] P. Price et al. SAE Technical Paper 2007-01-0472, 2007, doi.org/10.4271/2007-01-0472.

[137] Y. Kobayashi et al. SAE Int. J. Engines. 9. 10.4271/2015-01-2024.

[138] E. Chapman et al. SAE Technical Paper 2016-01-2250, 2016, doi.org/10.4271/2016-01-2250.

[139] W. Yinhui et al. Fuel. 166. 10.1016/j.fuel.2015.11.019.

[140] J. Wittmann et al. SAE Int. J. Fuels Lubr. 10(3):2017, doi.org/10.4271/2017-01-9380.

[141] F. Leach et al. Proc. Inst. Mech. Eng. J. Part D: Journal of Automobile Engineering 231(6):717-730, 2017.

[142] S. Murad et al. SAE Technical Paper 2016-01-0991, doi: 10.4271/2016-01-0991.

[143] F. Leach et al. Institution of Mechanical Engineers – Internal Combustion Engines, 2015.

[144] D.D. Das et al. Fuel, Vol 197, 2017, Pag 445-458, doi.org/10.1016/j.fuel.2017.01.099.

[145] C.S. McEnally et al. Proc. Combust. Inst., Vol 37, Issue 1, 2019, Pag 961-968, doi.org/10.1016/ j.proci.2018.05.071.

[146] A. Mensch. MSc Thesis, Pennsylvania State University, 2009.

[147] M. Saffaripour et al. Energy & Fuels 2011 25 (12), 5584-5593, doi: 10.1021/ef201219v.

[148] M. Botero et al. Fuel. 126. 8-15. doi:10.1016/j.fuel.2014.02.005.

[149] Y. Yang et al. Combust Flame, Vol 149, 2007, Pag 191-205, doi.org/10.1016/j.combustflame.2006.11.007.

[150] R.J. Gill et al. (1984). 10.1115/84-GT-108.

[151] A. Mensch et al. Combust Flame, Vol 157, 2010, Pag 1097-1105, doi.org/1016/j.combustflame.2010.02.008.

[152] A.G. A. Jameel et al. Combust Flame, Vol 192, 2018, Pag 250-271, doi.org/10.1016/j.combustflame.2018.01.036.

[153] M. Storch et al. Appl. Energy, Vol 181, 2016, Pag 278-287, doi.org/10.1016/j.apenergy.2016.08.059.

[154] M. Maricq. Combust Flame, Vol 159, Pag 170-180, doi.org/10.1016/j.combustflame.2011.07.10.

[155] J. Barrientos et al. Combust Flame, Vol 167, 2016, Pag 308-319, doi.org/10.1016/j.combustflame.2016.01.034.

[156] M. Maricq et al. (2012) AEROSOL SCI TECH. 46. 10.1080/02786826.2011.648780.

[157] E. Barrientos et al. (2012) ASME Proceedings (IMECE). 6. 10.1115/IMECE2012-85745.

[158] M. Raza et al. (2018). Energies. 6. 10.3390/en11061417.

[159] ASTM D1322-18, ASTM International, doi: 10.1520/D1322-18.

[160] A.A. Akere. PhD Thesis, University of Cambridge, Department of Chemical Engineering, 2009.

[161] T.L. Berry et al. Combust Flame, Vol 145, 2006, Pag 571-578, doi.org/10.1016/j.combustflame.2005.12.010.

[162] S. Yan et al. (2005). Energy & Fuels. 19. doi: 10.1021/ef050107d.

[163] R.J. Watson et al. Fuel. 111. 120-130. 10.1016/j.fuel.2013.04.024.

[164] F.W. Rakowsky et al. Anal. Chem. 1956, 28, 10, 1583-1586.

[165] H.F. Calcote et al. Combust Flame, Vol 49, 1983, Pag 289-304, doi.org/10.1016/0010-2180(83)90172-4.

[166] D.B. Olson et al. Combust Flame, Vol 62, 1985, Pag 43-60, doi.org/10.1016/0010-2180(85)90092-6.

[167] R.J. Gill et al. (1984). Combust. Sci. Technol., 40:5-6, 307-315, doi: 10.1080/00102208408923814.

[168] P.A. Glaude. Fuel Processing Technology. 91. 229-235. 10.1016/j.fuproc.2009.10.002.

[169] K.G. Joback et al. (1987). Chemical Engineering Communications, 57, 233-243, doi.org/10.1080/0 0986448708960487.

[170] I. Glassman. Symp Combust Proc, Vol 22, 1989, Pag 295-311, doi.org/10.1016/S0082-0784(89)80036-0.

[171] H. Badshah et al. SAE Int. J. Engines 9(3):1775-1785, 2016, doi.org/10.4271/2016-01-0997.

[172] M. Frenklach et al. Proc. Comb. Inst. Vol 23, 1991, Pag 1559-1566, doi.org/10.1016/S0082-0784(06)80426-1.

[173] N.A. Slavinskaya et al.Combust Flame. 159. 979-995. 10.1016/j.combustflame.2011.10.005.

[174] N.A. Slavinskaya et al. Combust Flame. 156. 1705-1722, 10.1016/j.combustflame.2009.04.013.

[175] G. Blanquart et al. Combust Flame, Vol 156, 2009, 588-607, doi.org/10.1016/j.combustflame.2014.11.018.

[176] J.J. Hernandez et al. Energy Fuels 2006, 20, 2, 532-539, doi.org/10.1021/ef058025c.

[177] M.D. Hageman et al. Proc. Comb. Inst. Vol 35, 2015, Pag 2949-2956, doi.org/10.1016/j.proci.2014.06.105.

[178] A. Hamins. Chapter 3. CRC Press, Boca Rato, pp. 71-95.

[179] P. Pepiot-Desjardins et al. (2008). Combust Flame. 154. 191-205. 10.1016/j.combustflame.2008.03.017.

[180] J. Badra et al. (2015). Fuel. 160. 458-469.

[181] S. Breda et al. SAE Int. J. Engines 9(1):641-656,2016, doi:10.4271/2016-01-0601.

[182] S. Iaccarino et al. SAE Int. J. Engines 10(2):576-592,2017, doi:10.4271/2017-01-0555.
[183] S. Breda et al. SAE Int. J. Fuels Lubr. 10(1):2017, doi:10.4271/2017-01-0546.
[184] M. Del Pecchia et al. La Termotecnica, ISSN: 0040-3725, November 2019, Number 07, Pag. 48-56.
[185] M. Del Pecchia et al. AIP Conference Proceedings 2191, 020064 (2019); doi.org/10.1063/1.5138797.
[186] P. Boudier et al. Twenty-Fourth Symposium (International) on Combustion/The Combustion Institute, 1992/pp. 503-510.
[187] L.Tao et al. Biofuels, Bioprod Biorefin 2014; 8(1):30-48. 10.1002/bbb.1431.
[188] L.G. Pereira et al. Applied Energy 2015; 160:120-31. 10.1016/j.apenergy.2015.09.063.
[189] J. Rawat et al. SAE Technical Paper 2008-28-0125.
[190] P. Bielaczyc et al.. (2013) Fuel Processing Technology. 107. 50–63. 10.1016/j.fuproc.2012.07.030.
[191] L. De Simio et al. (2012) ISRN Renewable Energy. 2012. 10.5402/2012/219703.
[192] A. F. Kheiralla et al. (2011) University of Khartoum Engineering Journal (UKEJ).Vol. 1, Issue 2:22-28.
[193] D. H. Qi et al. (2014). International Journal of Sustainable Energy. 35. 1-16. (2014) 10.1080/14786451.2014.895004.
[194] P. Sakthivel et al. (2018) 146. 10.1016/j.applthermaleng.2018.10.035.
[195] P. Iodice et al. Applied Thermal Engineering. (2017) 130. 10.1016/j.applthermaleng.2017.11.090.
[196] W. Hsieh et al. Atmospheric Environment. 36. 403-410. (2002) 10.1016/S1352-2310(01)00508-8.
[197] R. Suarez-Bertoa et al. Fuel. 143. (2014) 10.1016/j.fuel.2014.10.076.
[198] F. Yüksel et al. Renewable Energy. (2004) 29. 1181-1191. 10.1016/j.renene.2003.11.012.
[199] T. Le Anh et al. (2011). The 4th AUN/SEED – Net Regional Conference on New and Renewable Energy.
[200] Official Journal of the European Union, L140, Volume 52, 5 June 2009, ISSN-1725-2555.
[201] F. Liu et al. Journal of the Energy Institute, Vol 91, 2018, Pag 997-1008, doi.org/10.1016/j.joei.2017.07.008.
[202] P. H. Truyen et al. School of Transportation Engineering – Hanoi University of Science and Technology (2012).
[203] J.E. Tibaquirá et al. Energies. (2018) 11. 221. 10.3390/en11010221.
[204] I. Schifter et al. (2018). Fuel. 219. 10.1016/J.FUEL.2018.01.118.
[205] C. Dardiotis et al. Fuel, Volume 140, 2015, Pages 531-540, ISSN 0016-2361, doi.org/10.1016/j.fuel.2014.09.085.
[206] Y. Barakat et al. Egyptian Journal of Petroleum, Vol 25, 2016, Pages 309-315, doi.org/10.1016/j.ejpe.2015.07.019.
[207] M. Eyidogan et al. Fuel, Vol 89, 2010, Pag 2713-2720, doi.org/10.1016/j.fuel.2010.01.032.
[208] I. Schifter et al. Fuel, Vol 90, 2011, Pag 3586-3592, doi.org/10.1016/j.fuel.2011.01.034.
[209] B. Doğan et al. (2017). Applied Thermal Engineering. 120, 10.1016/j.applthermaleng.2017.04.012.
[210] A. da Silva Jr. et al. Fuel, Vol 243, 2019, Pag 306-313, doi.org/10.1016/j.fuel.2019.01.068.
[211] T.M. Foong et al. Fuel, Vol 115, 2014, Pag 727-739, doi.org/10.1016/j.fuel.2013.07.105.
[212] J. E. Anderson et al. (2012). SAE Technical Papers. 10.4271/2012-01-1274.
[213] B. Waluyo et al. Fuel, Volume 215, 2018, Pag 178-186, doi.org/10.1016/j.fuel.2017.10.103.
[214] J. Warnatz et al. “Combustion”. 4th Edition, Springer, ISBN-10 3-540-25992-9.
[215] M. Metghalchi et al. Combust Flame, Vol. 48(1982), pp. 191-210.
[216] Ö.L. Gülder. Symposium (Int) on Combustion, Vol 19, 1982, Pag 275-281, doi.org/10.1016/S0082-0784(82)80198-7.
[217] G. Damkohler. “The Effect of Turbulence on the Flame Velocity in Gas Mixtures, “NACA TM 1112, 1947.
[218] R.G. Abdel-Gayed. Proc. R. Soc. Lond. A 414, 389-413 (1987).
[219] D. Bradley et al. Phil. Trans. R. Soc. Lond. A (1992) 338, 359-387.
[220] D.B. Rhodes et al. SAE Technical Paper 850047, 1985, doi.org/10.4271/850047.
[221] L. Gillespie et al. SAE Technical Paper 2000-01-0192, 2000, doi:10.4271/2000-01-0192.
[222] C. Xiouris et al. Combustion and Flame 163 (2016) 270–28.
[223] M. Lawes et al. Comb. Sc. and Techn., 177 (7). pp. 1273-1289 (2005).
[224] C. Wang et al. Combust Flame 113:242–248.
[225] R.J. Johnston et al. Proceedings of the Combustion Institute 30 (2005) 217–224.
[226] X. Gu et al. “Energy Fuels 2009, 23, 4900–4907, doi:10.1021/ef900378.
[227] E. Varea et al. Proceedings of the Combustion Institute 34 (2013) 735–744.

[228] K.J. Bosschaart et al. Combustion and Flame 136 (2004) 261–269.

[229] S. Verhelst et al. Proceedings of the Combustion Institute 30 (2005) 209–21.

[230] J. Vancoillie et al. Fuel 102 (2012) 460–469.

[231] J.P.J. Van Lipzig et al. Fuel 90 (2011) 2773–2781.

[232] M. Mehl et al. Proceedings of the Combustion Institute 33 (2011) 193–200.

[233] S. Brusca et al. Energy Procedia, Vol. 82, Pages 125-132, doi:10.1016/j.egypro.2015.12.004.

[234] S. Turns. "An introduction to Combustion". 3rd Edition, McGraw-Hill, ISBN10: 0073380199.

[235] Z. Meng et al. Fuel, Vol 37, Pag 630-636, doi.org/10.1016/j.fuel.2018.10.072.

[236] M. Matti Maricq et al. Journal of Aerosol Science, Vol 35, 2004, Pag 1251-1274, doi.org/10.1016/j.jaerosci.2004.05.002.

[237] P. Karjalainen et al. Atmospheric Environment, Vol 97, 2014, Pag 262-270, doi.org/10.1016/j.atmosenv.2014.08.025.

[238] A.S. Pfau et al. Combustion and Flame, Vol 121, 2020, Pag 430-444, doi.org/10.1016/j.combustflame.2019.10.020.

[239] W.C. Hinds. "Aerosol Technology", 1999, John Wiley & Sons, ISBN: 978-0-471-19410-1.

[240] M. Frenklach. Physical Chemistry chemical Physics 4 (11): 2008-2037 (2002).

[241] M.V. Smolochovski. Z. Phys. Chem., 92, p.129 (1917).

[242] N.A. Fuchs. "Mechanics of Aerosols", Pergamon, New York (1964).

[243] I. Kennedy. "Models of Soot Formation and oxidation", Prog. Energy Combust. Sci., Vol. 23, 95-132, (1997).

[244] F. Mauss. PhD Thesis, RWTH, Aachen, (1998).

[245] M. Balthasar. PhD Thesis, Lund University, (2000).

[246] H.Pitsch. PhD thesis, RWTH, Aachen, (1998).

[247] F. Inal, S.M. Senkan. (2002). Combustion and Flame. 131. 16-28. 10.1016/S0010-2180(02)00388-7.

[248] Y. An et al. Energy,Volume 94,2016,Pages 367-379, ISSN 0360-5442,https://doi.org/10.1016/j.energy.2015.11.014.

[249] A.T. Hartlieb, B. Atakan, K. Kohse-Hoeinghaus. Combust. Flame 121 (2000) 610-624.

[250] A. Tregrossi, A. Ciajolo, R. Barbella. Combust. Flame 117 (1999) 553-561.

[251] F. Bowditch. SAE Technical Paper 610002, 1961, doi:10.4271/610002.

[252] L. Pirjola et al. Environ. Sci. Technol. 2015, 49, 3644-3652.

[253] A. Irimescu et al. Appl. Energ. 157:777-788, 2015, doi:10.1016/j.apenergy.2015.02.050.

[254] A. Irimescu et al. SAE Technical Paper 2015-01-1887, 2015, doi:10.4271/2015-01-1887.

[255] S.S. Merola et al. Energies 2017; 10(7):832. doi: 10.3390/en10070832.

[256] K. Park et al. Environ. Sci. Technol. 37:577-583. doi.org/10.1021/es025960v.

[257] D.C. Quiros et al. J. Aeros. Sci., (83), 39-54. doi.org/10.1016/j.jaerosci.2014.12.004.

[258] G. Cicalese et al. SAE Int. J. Engines 9(1):601-617, 2016, doi:10.4271/2016-01-0578.

[259] L. Postrioti et al. SAE Technical Paper 2018-01-0271, 2018, doi.org/10.4271/2018-01-0271.

[260] S. Sparacino et al. Energies, 2019. 12(15), 2890, doi.org/10.3390/en12152890.

[261] A. Cavicchi et al. Fuel, 2019, 116657, doi: 10.1016/j.fuel.2019.116657.

[262] C. Lee et al. Numerical Heat Transfer, Part B: Fundamentals, 40:6, 495-513, doi: 10.1080/104077901753306610.

[263] C. Habchi. Oil & Gas Science and Technology. 65. 331-343. 10.2516/ogst/2009062.

[264] P. Boudier et al. Symposium (International) on Combustion, Vol 24, Pag 503-510, doi: 10.1016/S0082-0784(06)80064-0.

[265] Bracco, F.V. Modeling of Engine Sprays. SAE Int. 1985, doi:10.4271/850394.

[266] Reitz, R.D.; Diwaker, R. Effect of Drop Breakup on Fuel Sprays. SAE Int. 1986, doi:10.4271/86046.

[267] S. Malaguti et al. SAE Technical Paper 2013-24-0002, 2013, doi.org/10.4271/2013-24-0002.

[268] N. Giovannoni et al. SAE Technical Paper 2015-24-2408, 2015, doi.org/10.4271/2015-24-2408.

[269] S. Malaguti et al. (2009) SAE Technical Papers, DOI: 10.4271/2009-01-0704.

[270] S. Malaguti et al. (2010) SAE Technical Papers, DOI: 10.4271/2010-01-2123.

[271] D.A. Rosenberg et al. Combust. Flame, Vol 162, 2015, Pag 2808-2822, doi.org/10.1016/j.combustflame.2015.04.007.

[272] H. Yamashita et al. Symposium (Int.) on Combustion, Vol 26, Pag 27-34, doi.org/10.1016/S0082-0784(96)80196-2.

Nomenclature

EU	European Union	LES	Large Eddy Simulation
GHG	Greenhouse Gas	T	Absolute temperature
SI	Spark Ignition	ρ	Mass Density
BEV	Battery Electric Vehicle	t	Time
$OPEC$	Organization of the Petroleum Exporting Countries	x_i, x_j, x_k	Coordinates of a fluid element
ICE	Internal Combustion Engine	$\delta x_i, \delta x_j, \delta x_k$	Dimensions of a fluid element
DI	Direct Injection	u_i, u_j, u_k	Velocity Components
EGR	Exhaust Gas Recirculation	δV	Volume of a fluid element
GDI	Gasoline Direct Injection	τ	Shear stress or dimensionless time
COV	Coefficient Of Variation	E	Energy
$IMEP$	Indicated Mean Effective Pressure	Q	Heat transfer
TJI	Turbulent Jet Ignition	L	Work
UL	Ultra-Lean	R	Universal Gas Constant
$REDII$	Renewable Energy Directive	k	Turbulent Kinetic Energy
OEM	Original Equipment Manufacturers	ε	Specific Dissipation Rate
PM	Particulate Matter	RNG	ReNormalization Group
$IARC$	International Agency for Research on Cancer	μ	Molecular viscosity
WHO	World Health Organization	μ_t	Turbulent viscosity
$PM_{2.5}$	Ultrafine Particulate Matter	S, S_{ij}	Strain rate
PFI	Port Fuel Injection	σ_k, σ_ε, $\sigma_{h,t}$, $C_{\varepsilon1}$, $C_{\varepsilon2}$, $C_{\varepsilon3}$, $C_{\varepsilon4}$, η_0, β, C_μ	k-ε RNG turbulence model constants
PN	Particulate Number	Π	Stress tensor
DPF	Diesel Particulate Filter	N_A	Avogadro’s constant
$3D$-CFD	Multi-dimensional Computational Fluid Dynamics	x_i	Mole fraction of species i
$ECFM$-$3Z$	Extended Coherent Flame Model-3 Zones	n_i	Mole number of species i
s_L	Laminar Flame Speed	n	Total mole number
p	Absolute Pressure	w_i	Mass fraction of species i
T_u	Unburnt Temperature	m_i	Mass of species i
ϕ	Fuel Equivalence Ratio	m	Total mass
τ_{ig}	Ignition Delay Time	MW_i	Molecular Weight of species i
PAH	Polycyclic Aromatic Hydrocarbons	$\overline{MW}$	Mixture mean Molecular Weight
CP	Constant Pressure reactor	c	Molar density

$PSDF$	Particle Size Distribution Function	λ	Heat conductivity of the mixture
$RANS$	Reynolds-Averaged Navier-Stokes	u	Flow velocity
W	Density of a conserved variable	z	Spatial coordinate
J	Flux of a conserved variable	Q	Source or sink of a conserved variable
ρ_i	Partial density of species i	TRF	Toluene Reference Fuel
V_i	Diffusion velocity of species i	$ETRF$	Ethanol Toluene Reference Fuel
j_i	Diffusion flux of species i	SEN	Senary Multicomponent Fuel
h_j	Enthalpy of species j	ST	Shock-Tube
j_q	Heat flux	RCM	Rapid Compression Machine
D_{ij}	Multicomponent diffusion coefficients	$1D$	One-dimensional
D_i^T	Thermal diffusion coefficient	US	United States
D_i^M	Diffusion coefficient for species i	$EPIONA$	Ethanol/Paraffins/Iso-paraffins/Olefins/Naphtenes/Aromatics
$c_{p,j}$	Specific heat capacity of the mixture at constant pressure	DHA	Detailed Hydrocarbon Analysis
ρ_u	Density of unburnt gases	$MTBE$	Methyl-T-Butyl Ether
ρ_b	Density of burnt gases	GC	Gas Chromatography
u_u	Velocity of unburnt gases	MW	Molecular Weight
u_b	Velocity of burnt gases	$ETBE$	Ethyl T-Butyl Ether
ω_i	Net reaction rate associate with species i	$TAME$	T-Amyl Methyl Ether
Y_i	Mass fraction of species i	$DIPE$	DiIsoPropyl Ether
E	Total energy of a system	T_b	Boiling Point
$\dot{Q}$	Heat transfer rate between control volume and environment	T_f	Adiabatic Flame Temperature
$\dot{W}$	Work transfer rate between control volume and environment	ON	Octane Number
h	Specific enthalpy	MR	Mixing Rule
e_k	Specific kinetic energy	$s^*_{L,target}$	Experimental $\mathrm{s_L}$ targeted value
e_p	Specific potential energy	$s^*_{L,iso}$	Chemistry-based $\mathrm{s_L}$ for Iso-octane
U	Internal energy of the system	$s^*_{L,nhept}$	Chemistry-based s_L for n-Heptane
σ	Boltzmann's constant	$s^*_{L,tol}$	Chemistry-based s_L for Toluene
T_w	Wall temperature	x_{iso}	Iso-octane molar fraction
CV	Constant Volume reactor	x_{nhept}	n-Heptane molar fraction
H/C	Hydrogen to Carbon ratio	x_{tol}	Toluene molar fraction
O/C	Oxygen to Carbon ratio	$\bar{x}^m$	m^{th} surrogate composition vector
LHV	Lower Heating Value	$\bar{x}^{m,norm}$	Norm. m^{th} surrogate composition vector
RON	Research Octane Number	ρ	Density

MON	Motor Octane Number	ρ_s	Soot density
x_{nhept}^{f}	Final surrogate n-Heptane content	x_{iso}^{f}	Final surrogate Iso-octane content
S	Sensitivity $S = RON - MON$	M_1	Second Moment
AKI	Anti-Knock Index AKI = $\mathrm{RON} + \mathrm{MON}/2$	f_v	Soot volume fraction
α_s	Stoichiometric Air-to-Fuel ratio	x_{tol}^{f}	Final surrogate Toluene content
$\bar{x}_f$	Final surrogate composition vector	$0D$	Zero-dimensional
x_{eth}	Ethanol molar fraction	Y_{soot}^{max}	Maximum Soot Mass Fraction
$s_{L,eth}^{*}$	Chemistry-based s_L for Ethanol	STR_{av}	Average Sooting Tendency Rate
NTC	Negative Temperature Coefficient	τ_f	Final Simulation Time
x_{1pen}	1-Pentene molar fraction	Y_{soot}	Soot Mass Fraction
$s_{L,1pen}^{*}$	Chemistry-based s_L for 1-Pentene	$NSTR_{av}$	Normalized Average Sooting Tendency Rate
x_{cpen}	Cyclopentane molar fraction	TSI_1	TSI Blend No 1
$s_{L,1pen}^{*}$	Chemistry-based s_L for Cyclopentane	$FACE$	Fuels for Advanced Combustion Engines
ACA	Average Carbon Atoms Number	HRR	Heat Release Rate
AHA	Average Hydrogen Atoms Number	c	Progress variable
AOA	Average Oxygen Atoms Number	$h_{298}(t)$	Current enthalpy of formation
CV	Constant Volume	h_{298}^{in}	Initial enthalpy of formation
$KLSA$	Knock Limited Spark Advance	h_{298}^{eq}	Equilibrium composition enthalpy of formation
ST	Sooting Tendency	$IM\text{-}CNR$	Istituto Motori of the National Research Council of Italy
TSI	Threshold Soot Index	SOI	Start Of Injection
SP	Smoke Point	EVO	Exhaust Valve Opening
a, b	Apparatus-dependent constants for TSI	IVO	Intake Valve Opening
TSI_i	ith pure compound TSI	EVC	Exhaust Valve Closing
YSI	Yield Soot Index	IVC	Intake Valve Closing
LII	Laser Induced Incandescence	TDC	Top Dead Center
$QSPR$	Quantitative Structure-Property Relationships	BDC	Bottom Dead Center
sp_k	Contribution from the kth group in Joback's method	WOT	Wide Open Throttle
PRF	Primary Reference Fuel	$FSD\ /\ \Sigma$	Flame Surface Density
N_i	Number density of soot particles of size class i	d	Particle diameter
m_i	Mass of soot particles of size class i	$d_{PSDF,max}$	$PSDF$ peak location in terms of diameter
m_1	Soot mass gap in adjacent soot sizes	PM_i^{EVO}	PM evaluated at EVO for the i^{th} fuel

M_0	First Moment	$NPM\text{-}CFD_i$	PM evaluated at EVO for the i^{th} fuel surrogate normalized over Tier 2 surrogate one
$DISI$	Direct-Injection Spark-Ignition	p_{ref}	Reference pressure for s_L fitting
ECU	Electronic Control Unit	T_{ref}	Reference temperature for s_L fitting
OP	Operating Point	PSF	Pressure Scaling Factor
UHC	Unburnt Hydrocarbons	m	Slope coefficient
E	Ethanol content in %vol	q	y-axis intercept coefficient
$ECFM$	Extended Coherent Flame Model	m_{LOW}^{lean}	Slope coefficients for lean-side low temperature level
G, G'	G-equation model passive scalars	m_{MED}^{lean}	Slope coefficients for lean-side medium temperature level
ω	Turbulent Burn Rate	m_{HIGH}^{lean}	Slope coefficients for lean-side high temperature level
Y_F	Fuel Mass Fraction	q_{LOW}^{lean}	Y-axis intercept coefficients for lean-side low temperature level
s_T	Turbulent Flame Speed	q_{MED}^{lean}	Y-axis intercept coefficients for lean-side medium temperature level
u'	Turbulence Intensity	q_{HIGH}^{lean}	Y-axis intercept coefficients for lean-side high temperature level
Y_{res}	Residuals mass farction	lml_2, lml_1, lml_0	m_{LOW}^{lean} fitting coefficients
$s_{L,0}$	s_L at ambient conditions	lmm_2, lmm_1, lmm_0	m_{MED}^{lean} fitting coefficients
α	Temperature exponent	lmh_2, lmh_1, lmh_0	m_{HIGH}^{lean} fitting coefficients
β	Pressure exponent	lql_2, lql_1, lql_0	q_{LOW}^{lean} fitting coefficients
δ_L	Flame thickness	lqm_2, lqm_1, lqm_0	q_{MED}^{lean} fitting coefficients
c_P	Isobaric mixture specific heat	lqh_2, lqh_1, lqh_0	q_{HIGH}^{lean} fitting coefficients
c_V	Isochoric mixture specific heat	TSF	Temperature Scaling Factor
γ	c_P/c_V	TSF_{LOW}^{lean}	TSF for lean mixtures at low temperature levels
EC	Engine Condition	TSF_{MED}^{lean}	TSF for lean mixtures at medium temperature levels
SOC	Start Of Combustion	TSF_{HIGH}^{lean}	TSF for high mixtures at medium temperature levels
a_i, b_i, c_i	Fitting coefficient expressing s_L dependence on ϕ, T_u, p	p_W	Weight coefficient for pressure

T_W	Weight coefficient for temperature	TEM	Transmission Electron Microscopy
PS	Pressure Scaling	$NEDC$	New European Driving Cycle
TPS	Temperature-Pressure Scaling	D_p	Soot Particle Diameter
m_{LOW}^{rich}	Slope coefficients for rich-side low temperature level	dN	Particle Concentration
m_{MED}^{rich}	Slope coefficients for rich-side medium temperature level	D_p	Midpoint channel particle diameter
m_{HIGH}^{rich}	Slope coefficients for rich-side high temperature level	$D_{p,u}$	Upper channel particle diameter
q_{LOW}^{rich}	Y-axis intercept coefficients for rich-side low temperature level	$D_{p,l}$	Lower channel particle diameter
q_{MED}^{rich}	Y-axis intercept coefficients for rich-side medium temperature level	$dlogD_p$	$logD_{p,u} - logD_{p,l}$
q_{HIGH}^{rich}	Y-axis intercept coefficients for rich-side high temperature level	$dN/dlogD_p$	Normalized particle concentration
$rml_4, rml_3, rml_2,$ rml_1, rml_0	m_{LOW}^{rich} fitting coefficients	BSF	Burner Stabilized Flames
$rmm_4, rmm_3, rmm_2,$ rmm_1, rmm_0	m_{MED}^{rich} fitting coefficients	N_i	Number or particles of size i
$rmh_4, rmh_3, rmh_2,$ rmh_1, rmh_0	m_{HIGH}^{rich} fitting coefficients	$\dot{N}_i$	N_i time rate of change
$rql_4, rql_3, rql_2,$ rql_1, rql_0	q_{LOW}^{rich} fitting coefficients	$\beta_{i,j}$	Collision frequency factor between two particles of sizes i and j
$rqm_4, rqm_3, rqm_2,$ rqm_1, rqm_0	q_{MED}^{rich} fitting coefficients	N_{PAH}	Number density of PAH molecules
$rqh_4, rqh_3, rqh_2,$ rqh_1, rqh_0	q_{HIGH}^{rich} fitting coefficients	$\beta_{i,j}^{fm}$	Collision frequency in the free molecular regime
TSF	Temperature Scaling Factor	k_b	Boltzmann's constant
TSF_{LOW}^{rich}	TSF for rich mixtures at low temperature levels	$\mu_{i,j}$	Reduced colliding particles (i,j) mass
TSF_{MED}^{rich}	TSF for rich mixtures at medium temperature levels	r_i	Soot particle radius i^{th} size
TSF_{HIGH}^{rich}	TSF for rich mixtures at medium temperature levels	$\varepsilon_{i,j}$	Size-dependent coagulation enhancement factor
$ASOS$	After Start Of Spark	Kn	Knudsen number
PM_{10}	Fine Particulate Matter	λ_{gas}	Gas mean free path
AQG	Air Quality Directive	$\beta_{i,j}^{c}$	Collision frequency in the continuum regime
η	Gas viscosity	C_i	Cunningham slip correction factor for particles with Knudsen number Kn_i

$\beta_{i,j}^{tr}$	Collision frequency in the transition regime	$\widetilde{RPAH}$	Polycyclic Aromatic Hydrocarbons Formation Rate
α	Fraction of active sites	k_{pi}	Nucleation frequency collision factor
χ_{soot}	Number of sites per unit area	k_{cond}	Condensation frequency collision factor
S_i	Surface area of the i^{th} site	$\tilde{k}_d$	Forward reaction rate constant for the $HACARC$ mechanism
θ	Fractal dimension	$\tilde{k}_{rev}$	Backward reaction rate constant for the $HACARC$ mechanism
v	Soot particle volume	$\tilde{k}_{O_2}$	Reaction rate constant for oxidation via O_2
Q/sfv	Soot Volume Fraction	$\tilde{k}_{OH}$	Reaction rate constant for oxidation via OH
v_{MIN}	Volume of the smallest soot particle	Da_s	Damköhler number for soot
v_{MAX}	Volume of the largest soot particle	Da_{comb}	Damköhler number for combustion
$v_{i,max}$	Maximum volume in the i^{th} section	$\tau_{turbulence}$	Turbulence characteristic time scale
$v_{i,min}$	Minimum volume in the i^{th} section	$\tau_{soot\ chemistry}$	Soot chemistry characteristic time scale
$v_{i,m}$	Average volume in the i^{th} section	$\tau_{fuel\ oxidation}$	Fuel oxidation characteristic time scale
v_{PAH}	Volume of the reference soot precursor	WOT	Wide Open Throttle
$q_i(v)$	Soot volume fraction density in the i^{th} section	ETU	Electronic Timing Unit
Q_i	Soot volume fraction in the i^{th} section	LUT	Look-Up Table
$\tilde{Y}_{s,i}$	Soot mass fraction in the i^{th} section	FFT	Fast Fourier Transform
$\bar{\rho}$	Average gas phase density	PDF	Probability Density Function
$D_{t,s}$	Soot turbulent diffusion coefficient	$EEPS$	Engine Exhaust Particle Sizer
i_{max}	Number of sections	FSD	Flame Surface Density
$\Omega_{s,i}$	Soot source term in the i^{th} section	CC	Combustion Chamber
$\tilde{\Omega}_{pi,i}$	Particle inception source term in the i^{th} section	CR	Crevices
$\tilde{\Omega}_{cond,i}$	Condensation source term in the i^{th} section	$V_{cc,EVO}$	Combustion chamber volume at EVO
$\tilde{\Omega}_{coag,i}$	Coagulation source term in the i^{th} section	$p_{cc,EVO}$	In-cylinder average pressure at EVO
$\tilde{\Omega}_{sg,i}$	Surface Growth source term in the i^{th} section	$T_{cc,EVO}$	In-cylinder average temperature at EVO
$\tilde{\Omega}_{ox,i}$	Oxidation source term in the i^{th} section	s_{LOW}	Lower section considered to compute $PM, PN, PSDF$

s_{HIGH}	Upper section considered to compute PM, PN, $PSDF$	d_r	Dilution rate
$s_{i,EVO}$	Soot mass in the i^{th} section at EVO	Ω_{tot}	Total soot source term
$m_{cc,EVO}$	In-cylinder gas mass at EVO		